A STUDY OF METAL-ORGANIC FRAMEWORKS FOR THE STORAGE AND RELEASE OF MEDICAL GASES
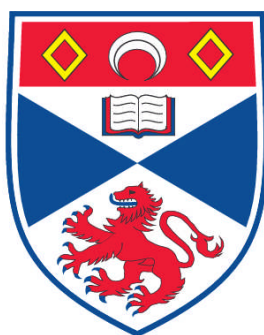
Phoebe Kate Allan

A Thesis Submitted for the Degree of PhD
at the
University of St. Andrews

2012

**Full metadata for this item is available in
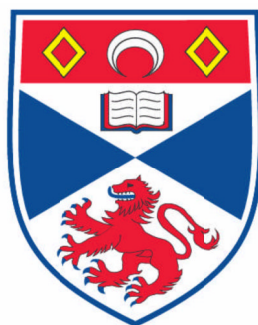Research@StAndrews:FullText
at:
http://research-repository.st-andrews.ac.uk/**

**Please use this identifier to cite or link to this item:
http://hdl.handle.net/10023/3198**

A Study of Metal-Organic Frameworks for the Storage and Release of Medical Gases

Phoebe Kate Allan

This thesis is submitted in partial fulfilment for the degree of PhD
at the University of St Andrews

7$^{\text{th}}$ June 2012

Declarations

I, Phoebe Kate Allan, hereby certify that this thesis, which is approximately 68000 words in length, has been written by me, that it is the record of work carried out by me and that it has not been submitted in any previous application for a higher degree.

I was admitted as a research student in September 2008 and as a candidate for the degree of PhD in September 2009; the higher study for which this is a record was carried out in the University of St Andrews between 2008 and 2012.

Date   Signature of candidate

I hereby certify that the candidate has fulfilled the conditions of the Resolution and Regulations appropriate for the degree of PhD in the University of St Andrews and that the candidate is qualified to submit this thesis in application for that degree.

Date   Signature of supervisor

Courses Attended

The School of Chemistry at the University of St. Andrews requires that a postgraduate attend a number of taught courses. The courses attended were:

Crystallography

Frontiers in Main Group Chemistry

EastChem Paper writing course

EastChem Thesis writing course

Abstract

This thesis presents a study of the interaction of medical gases nitric oxide, carbon monoxide and hydrogen sulfide with metal-organic framework materials. Most analysis is performed via single-crystal X-ray diffraction and Rietveld and pair distribution function analysis of powder X-ray diffraction data. A background to the field and the experimental methods used are described in Chapters 1 and 3.

The use of a specially designed static environmental gas cell to assess the role of coordinatively unsaturated metal sites in nitric oxide storage in Co-CPO-27 via *in situ* single-crystal structure determination is described in Chapter 4. Nitric oxide was shown to bind to the Co-centre of the material in a bent geometry in an approximately 1:1 Co:NO ratio.

A multi-technique study was conducted on the framework Cu-SIP-3 in Chapters 5 and 6, utilising both single-crystal X-ray diffraction and pair distribution function analysis to obtain complementary information about atomic movements during a thermally active single-crystal to single-crystal transition. These techniques were further applied during *in situ* gas-loading experiments on the same framework.

Application of the pair distribution function technique to metal-organic frameworks is described in Chapter 7, where refinements of both known and unknown metal-organic framework structures are presented. Partial PDFs are used to determine the secondary building block of a new metal-organic framework and verify the structural solution determined from powder X-ray diffraction data.

Chapter 8 presents the study of the M-CPO-27 isostructural series for the adsorption and release of hydrogen sulfide and carbon monoxide. Gas adsorption isotherms and release measurements are correlated with the structure of the Ni-CPO-27 hydrogen sulfide-adduct determined by both powder X-ray diffraction and differential pair distribution function methods which reveal the open-metal site as the primary adsorption interaction in the material. The hydrogen sulfide released from Zn-CPO-27 is determined to be biologically active through vasodilatation experiments.

Table of contents

1 Introduction

This thesis examines the interaction of the medical gases nitric oxide (NO), carbon monoxide (CO) and hydrogen sulfide (H_2S) with metal-organic frameworks. In the following introduction the chemistry, endogenous production and biological actions of these gases are reviewed, and current technologies for implementing their use in medicine are presented. Subsequently, a background to the field of metal-organic frameworks is presented with consideration of why these materials present a promising technology for storing and delivering biological gases. Finally, the importance of crystallographic studies in revealing the structural details associated with gas adsorption in materials is discussed and previous studies in this area are described.

1.1 Gaseous Signalling Molecules

Cells signal to each other in order to coordinate cellular actions. This intercellular signalling takes place through the use of neurotransmitters. Chemicals traditionally recognised as neurotransmitters are compounds produced by neurons and stored in vesicles until stimulation of the neurons trigger their release (Figure 1-1a). They bind to specific membrane receptors in a neighbouring cell to produce a physiological effect. 'Gasotransmitters' are a group of small gaseous molecules that exhibit a similar signalling function in the body but through a different mechanism. They function without receptors because they are freely permeable to cell membranes (Figure 1-1b).[1] The term gasotransmitter was first used in a paper by Rui Wang in 2002,[2] in order to distinguish the receptor-independent signalling nature of these molecules from that of traditional neurotransmitters. Wang suggested that for a molecule to be considered a gasotransmitter, a number of criteria must be met (Table 1).[1] Most importantly, the molecule must be produced endogenously (within the body) for a specific biological function. The term gasotransmitter additionally serves to recognise the similarities between signalling methods employed by each of the gasotransmitter molecules and to group the molecules together. The similarities and differences between the actions of each gasotransmitter are discussed in section 1.4.3.

To date, three gasotransmitter molecules have been proposed; nitric oxide, carbon monoxide and hydrogen sulfide. Ironically, considering this biological role, the

1

reputation of all of these gases is for being detrimental to health; inhalation of high concentrations of any of the three can be lethal. Nitric oxide is best known for being an atmospheric pollutant as part of NO_x, a component of smog. Carbon monoxide is a common household hazard produced by incomplete combustion of fossil fuels, and is undetectable by the human senses making it known as the 'silent killer'. Hydrogen sulfide has a toxicity of similar potency to cyanide and is responsible for the characteristic smell of rotten eggs.

Neurotransmitter is produced in transmitting neuron and stored in vesicles until required

Transmitting neuron

Vesicle

Neurotransmitters cross synapse and bind to receptor

Synapse

Receptor

Receiving neuron

Gasotransmitter synthesised in neuron but not stored

Transmitting neuron

NOS

NO

NO

NO
NO

NO

NO

Gasotransmitter permeates cell membrane without need for receptor

Synapse

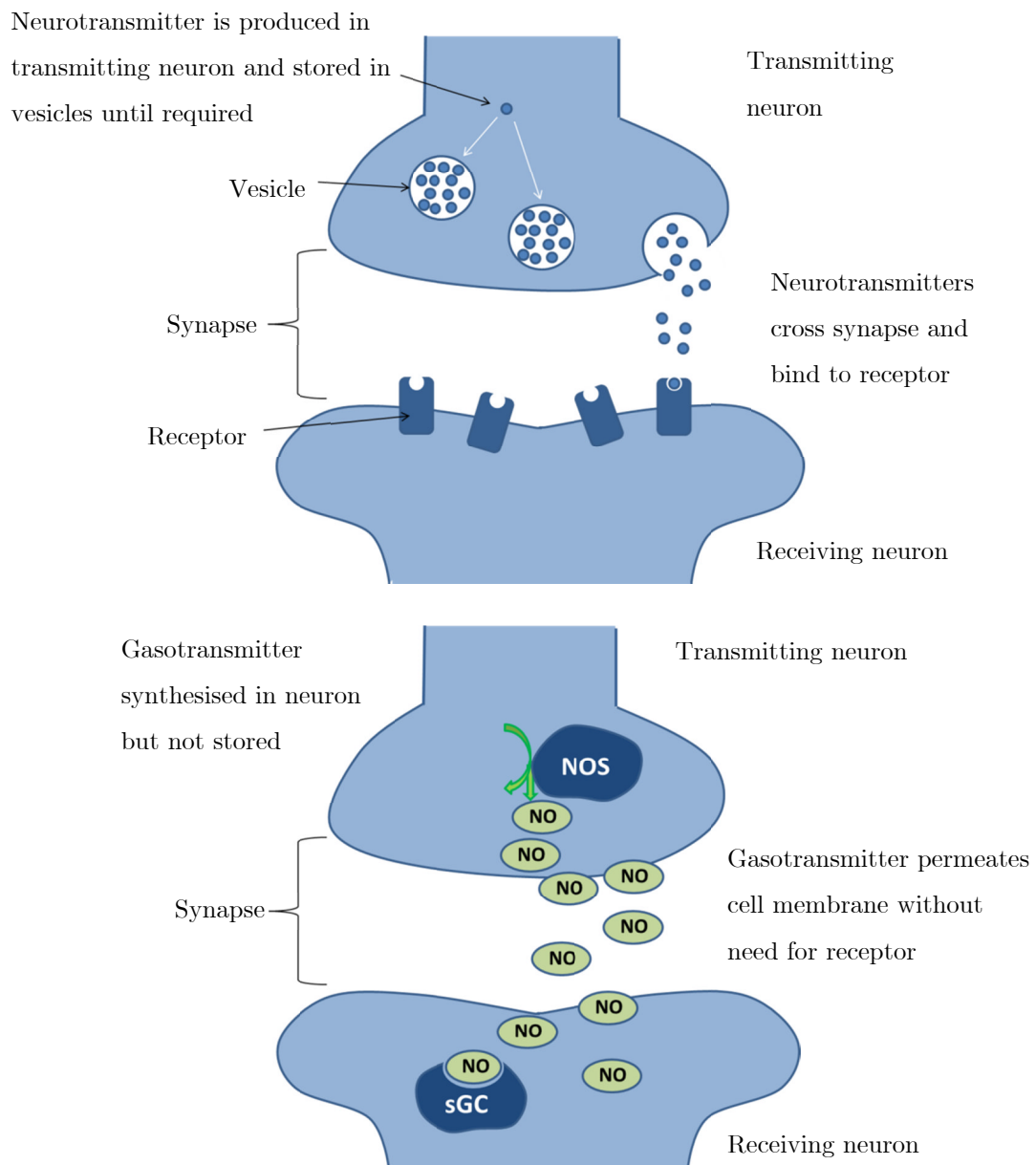NO

NO

NO

NO

sGC

NO

Receiving neuron

Figure 1-1: Schematics of mechanism of neurotransmitter (1-1a, top) and gasotransmitter (1-1b, bottom) action.

Table 1: Criteria for gasotransmitters.[1]

1. They are small, gaseous molecules.

2. They are freely permeable to cell membranes.

3. They are endogenously and enzymatically produced and regulated.

4. They have well defined and specific biological roles at specific concentrations.

5. Their functions can be mimicked by the same molecules dosed exogenously.

However dangerous large doses of these gases are, it has been shown that small amounts of all three gases are actually vital to human health. In fact, the body produces a small but biologically significant amount of all three gases and they are known to modulate cellular functions by influencing a range of intercellular signalling processes. The significance of this discovery was reflected in the award of the 1998 Nobel Prize for physiology to the three American scientists, Murad, Furchgott and Ignarro for the discovery of the endogenous production of NO. In addition to the three accepted gasotransmitter molecules, recent reports suggest that the small gaseous sulfur dioxide molecule also plays a gasotransmitter role within the body[3, 4], and other gases such as carbonyl sulfide[5] and nitrous oxide[6] have been suggested for investigation.

1.2 Structure and chemistry of nitric oxide, carbon monoxide and hydrogen sulfide

1.2.1 Nitric oxide

Nitric oxide, or nitrogen monoxide, is a diatomic molecule with the chemical structure NO. The ground state molecular orbital (MO) diagram for nitric oxide is shown in Figure 1-2. NO has 11 valence electrons, to which nitrogen donates five electrons and oxygen six electrons. There is significant sp-mixing in nitric oxide, which leads to the 1π orbital lying lower than the 3σ and a ground state configuration of $1\sigma^2 2\sigma^2 1\pi^4 3\sigma^2 2\pi^1$. The antibonding 2π orbital is both the highest occupied molecular orbital (HOMO) and lowest unoccupied molecular orbital (LUMO) and, due to the electronegativity differences between nitrogen and oxygen, has mostly nitrogen character. The formal bond order of the N-O bond is 2.5 and the N-O bond length (1.15 Å)[7] lies between that of a dinitrogen triple N≡N bond (1.098 Å)[7] and a dioxygen double O=O bond (1.48 Å).[7]
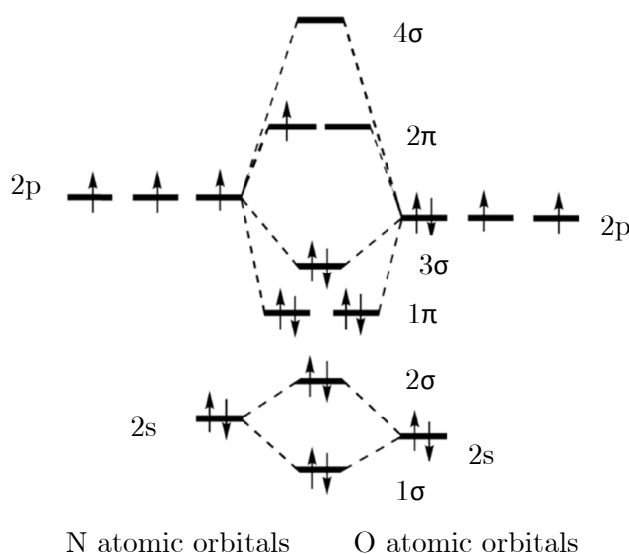
Figure 1-2: MO diagram for nitric oxide.

Nitric oxide is a radical species with an unpaired electron in the antibonding 2π orbital. NO is uncharged and is highly soluble in hydrophobic environments. The latter property may allow free diffusion across biological membranes, accounting for its role as a biological signalling molecule. NO does not dimerise significantly to ON-NO in the gaseous form because, although this would eliminate the unpaired electrons, the loss of entropy associated with the dimerization is large compared with the weak N-N bond in the dimer.[8] The unpaired electron can easily be lost to form $[NO]^+$ or an electron can be gained to form $[NO]^-$, meaning that nitric oxide is relatively reactive.

NO reacts very readily with oxygen to form nitrogen dioxide, NO_2, a brown gas. Together with NO, NO_2 makes up NO_x, an atmospheric pollutant responsible for a large component of smog. Nitric oxide reacts with transition metals to give complexes called metal nitrosyls. Where bonding proceeds though coordination of the nitrogen to metal centres there are two common metal-nitrosyl bonding modes corresponding to nitric oxide acting as either a one-electron or three-electron donor (Figure 1-3). In the case of a three-electron donor, an electron is notionally donated to the metal, reducing the metal and oxidising the nitric oxide to NO^+. The nitric oxide now acts as a σ-donor from the *sp* orbital, of which the main component is on the nitrogen atom, donating a total of 3 electrons. The NO is also a π-acceptor into the antibonding 2π orbitals. The bond order

of the nitric oxide in this nitrosyl is 3 and in order for the correct orbital overlap to happen, the M-N-O bonding must be linear.

In the case of a one-electron donor, the nitric oxide notionally accepts an electron from the metal centre into the π^* orbital. The nitric oxide rehybridises to sp^2 with two lone pairs on the nitrogen atom. One of these lone pairs is donated to the metal centre though only one of the electrons originally comes from the NO; the other is inert and points away from the metal. The bond order of the N-O bond in the nitrosyl complex is 2, and the M-N-O bond angle of these complexes is between 120 and 140°. In addition to this, isonitrosyl and side-on nitrosyl compounds are known and are common in photolytic studies of linker isomerism.[9]

Similar to carbon monoxide, the infra-red (IR) stretch of the NO bond is very sensitive to the electronic state of the NO; free NO has a stretch of 1876 cm^{-1}, NO$^+$ = 2205 cm^{-1}, NO$^+$ complexes have stretches in the range of 1900 – 1600 cm^{-1} and NO$^-$ complexes 1600 – 1500 cm^{-1}.[10]
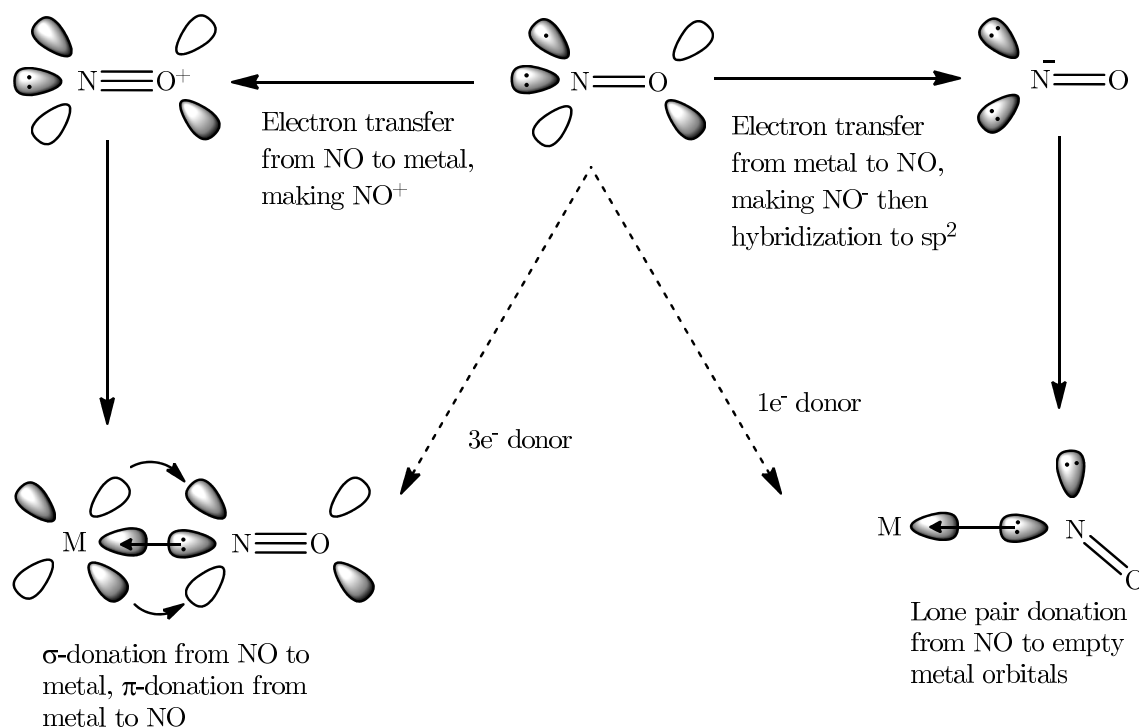

Figure 1-3: The relationship between linear and bent nitrosyl complexes (Figure adapted from reference 8).

1.2.2 Carbon monoxide

Carbon monoxide is a colourless, odourless gas which is slightly lighter than air. The main source of carbon monoxide is the incomplete combustion of carbon-containing compounds. Naturally occurring carbon monoxide is made by photochemical reactions in the troposphere.

Like nitric oxide, carbon monoxide is a diatomic molecule, with formula CO. The carbon and oxygen atoms are bonded together with a triple bond. CO shows similarity with nitrogen, N_2; both gases have a formal bond order of three, have the same number of electrons and have very similar boiling points. Differences in properties arise from the asymmetry of CO compared with N_2. Each nitrogen atom donates five valence electrons to the dinitrogen structure, resulting in symmetrical molecular orbitals with electrons equally distributed over each atom. Carbon and oxygen are located on either side of nitrogen in groups IV and VI respectively, meaning that carbon donates four electrons to the structure and oxygen six. Like nitrogen, there is significant s-p mixing resulting in the 1π orbitals lying lower than the 3σ, thus the ground state configuration is $1\sigma^2 2\sigma^2 1\pi^4 3\sigma^2$. The molecular orbital is shown in Figure 1-4. The HOMO is the non-bonding 3σ which, due to electronegativity differences between carbon and oxygen, is located mainly on the carbon atom. The LUMO is the 2π system showing mainly C-$2p$ character[11]. The bond length is 1.128 Å in free CO.[7]

Carbon monoxide reacts with late transition metal centres to form metal-carbonyl complexes. Carbon monoxide acts as a σ-donor and π-acceptor (Figure 1-5). The non-bonding 3σ of CO donates electrons into the orbitals on the metal centre with σ-symmetry. This leads to an excess of electron density on the metal centre, so the metal pushes electron density back from the t_{2g}-orbitals into the empty anti-bonding 2π-orbitals on CO. In order for these orbitals to overlap correctly, the coordination mode must be linear. σ−donation takes place from the bonding σ-orbital. Donation from a bonding orbital makes it weakly antibonding from CO, weakening the C-O bond. The π-acceptance interaction is into an antibonding orbital and this weakens the C-O bond further.
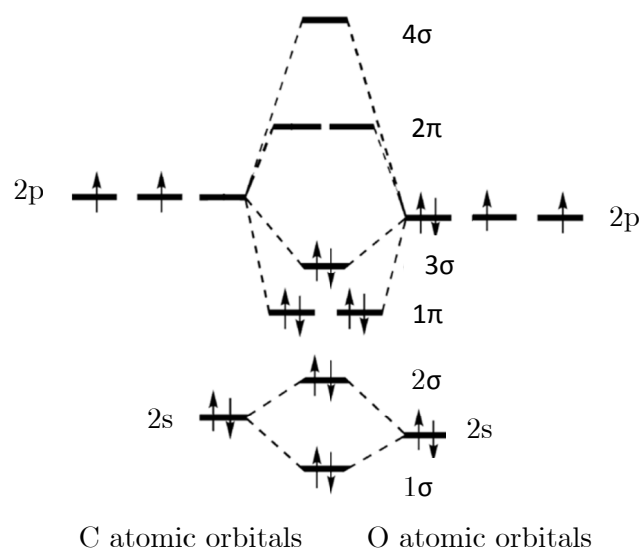
Figure 1-4: MO diagram for carbon monoxide.
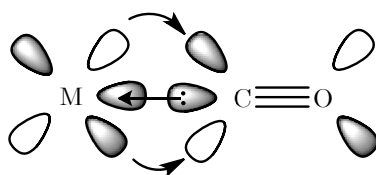
Figure 1-5: Carbon monoxide acts a σ-donor π-acceptor.

The C-O bond strength is dependent on the amount of σ-donation and π-acceptance, and therefore also dependent on the oxidation state of the metal and the properties of the other ligands on the metal centre. This can be monitored crystallographically or by using IR. The latter technique is particularly useful as the C-O bond is polarized and independent of any other stretches in the complex. Free carbon monoxide has an IR stretch of 2143 cm^{-1} and weakening of the C-O bond decreases the frequency of the stretch, usually below 2100 cm^{-1}.

1.2.3   Hydrogen sulfide

Hydrogen sulfide is a colourless gas with the strong characteristic smell of rotten eggs. Hydrogen sulfide has the chemical formula H_2S. The sulfur is bonded to two

hydrogen atoms and has two lone pairs, giving the molecule bent molecular geometry with a H-S-H angle of 92.1° and a H-S bond length of 1.336 Å.[7] In nature, H_2S is produced primarily by the decomposition of organic matter and is found in natural gas, petroleum, volcanic, and sulfur-spring emissions. Hydrogen sulfide has long been associated with decay, probably because many sulphate-reducing bacteria in low-oxygen conditions obtain energy by the oxidization of organic matter, producing hydrogen sulfide.

Hydrogen sulfide is a reducing species. In solution it is known to dissociate into hydrosulfide, HS^-, and sulfide, S^{2-}, anions in equilibrium:

$$H_2S \rightleftharpoons HS^- \rightleftharpoons S^{2-} \qquad\qquad 1.1$$

The pK_a of HS^- is 7.04 and of S^{2-} is 11.96, meaning that in solution at pH 7.4 it is known that approximately 18-33% is H_2S and 67-81% is HS^-, depending on temperature.[12] H_2S is highly soluble in both lipids and water meaning that it can diffuse easily throughout the body.

1.3 Endogenous production of NO, CO and H_2S

Endogenous production of nitric oxide was suggested in 1987 when reports from the groups of Louis Ignarro and Salvador Moncada suggested that nitric oxide was responsible for the relaxation of endothelial cells[i] in blood vessels.[13, 14] Direct evidence that endogenous nitric oxide production was responsible for this effect was given shortly thereafter by the use of isotopic labelling of nitrogen in arginine in endothelium cell cultures.[15]

It is now well established that the bulk of endogenous nitric oxide is formed by the reaction of the amino acid L-arginine (which provides the nitrogen of the NO) with oxygen gas to form citrulline and nitric oxide. The reaction is shown in Figure 1-6. This reaction is catalysed by the family of enzymes called nitric oxide synthase (NOS). There are several isoforms of NOS; the constitutive forms, eNOS and nNOS, which are expressed within tissues in all physiological conditions, and an inducible form, iNOS,

---

[i] In blood vessels, endothelial cells exist in the endothelium, which is the single-layer of cells between the hole through the middle of blood vessels where blood flows (the lumen) and the exterior wall of the blood vessel (smooth muscle layer). Relaxation of the muscle layer increases the size of the lumen and allows more blood to flow through the vessel, which is called dilation of the blood vessel (vasodilation).

which only exists when induced by the switching on of a central gene. All forms involve a central metal ion such as zinc, copper or iron within a haem moiety.

The mechanism by which nitric oxide is formed is similar for all types of NOS.[16] Electrons are required for the conversion and these are provided by the chemical nicotinamide adenine dinucleotide phosphate (NADPH) which, whilst not part of the NOS enzyme itself, is essential to the enzyme activity. NOS has two distinct domains which take part in the conversion of L-arginine: reductase and oxygenase. The reductase domain contains two cofactors[ii], flavin mononucleotide (FMN) and flavin adenine dinucleotide (FAD), which receive the electrons from the NADPH and pass them, via calmodulin, to the oxygenase domain. The oxygenase domain contains, in addition to the NADPH, two cofactors; haem, where the substrate oxygen binds to the iron before reacting with the L-arginine, and BH_4, whose role is currently unknown. The electrons from the reductase domain activate the oxygen attached to the haem moiety and facilitate attack of the arginine. Whilst most nitric oxide is produced by the method above, other sources of nitric oxide within the body are also known, such as S-nitrosothiols.

The endogenous concentration of nitric oxide has been estimated to be in the nanomolar concentration range,[17] which is quite low for something to show significant biological activity. However, as NO is reactive and its lifetime in the body is thought to be a few seconds at the most, there would not be much free nitric oxide in tissues to be detected.[13]
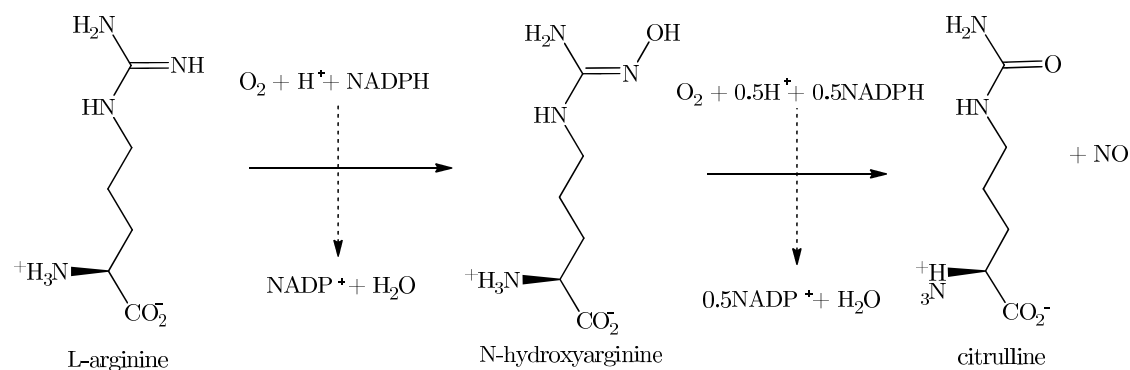
Figure 1-6: Nitric oxide production via the conversion of L-arginine to citrulline.[18]

[ii] Cofactors are "helper molecules" for enzymes - chemical compounds which are not part of the enzyme itself but are required for the enzyme to catalyse biochemical processes.

Endogenous carbon monoxide production was postulated by Saint-Martin and Nicloux in 1898.[19] The first experimental evidence was published in two papers by Sjostrand in 1949 and 1951.[20, 21] It has also been known since the 1950s that breakdown of haem results in the production of carbon monoxide in the body, and in 1968 these facts were linked by the discovery of the enzyme haem oxyegnase (HO), the main source of endogenous carbon monoxide, accounting for over 80% of endogenous production.[22] HO exists as HO-1, an inducible form only present when stimulated by some kind of physiological stress,[23] and HO-2/3 which are constitutive forms present in tissues at all times without a specific stimulus. Only HO-1 and HO-2 are known to be active in carbon monoxide production. Haem oxygenase catalyses the first step of the haem-degradation process;[24] it breaks down the porphyrin ring at the alpha-methane bridge to produce Fe(II), a green pigment open-chain tetrapyrrole called biliverdin, and carbon monoxide, using, as in the production of nitric oxide, oxygen and NADPH as cofactors.[25] Biliverdin is quickly degraded to bilirubin, a yellow pigment, and removed from the bloodstream.

Carbon monoxide production is visible to anyone who has ever had a bruise. This process is illustrated in Figure 1-8. Injury to a tissue results in free haem being released from haemoglobin forming a dark red patch (oxyhaemoglobin). Free haem does not occur in healthy tissue and is toxic, so it is broken down by the body. HO catalyses the oxidation of haem, producing first biliverdin (green) and then bilirubin (yellow) and carbon monoxide. This carbon monoxide coordinates to haem to give a bright red colour. The blue colour seen as the bruise develops is deoxygenated venous blood as the degradation of each haem requires three equivalents of dioxygen.

Most endogenous CO is part of the bloodstream, meaning that in the absence of significant ambient CO, blood Hb-CO levels are around 0.4–1% of the total Hb content.[26] The stability of carbon monoxide means that elimination of CO from the bodies of mammals occurs strictly through exhalation from the lungs with no further metabolism.
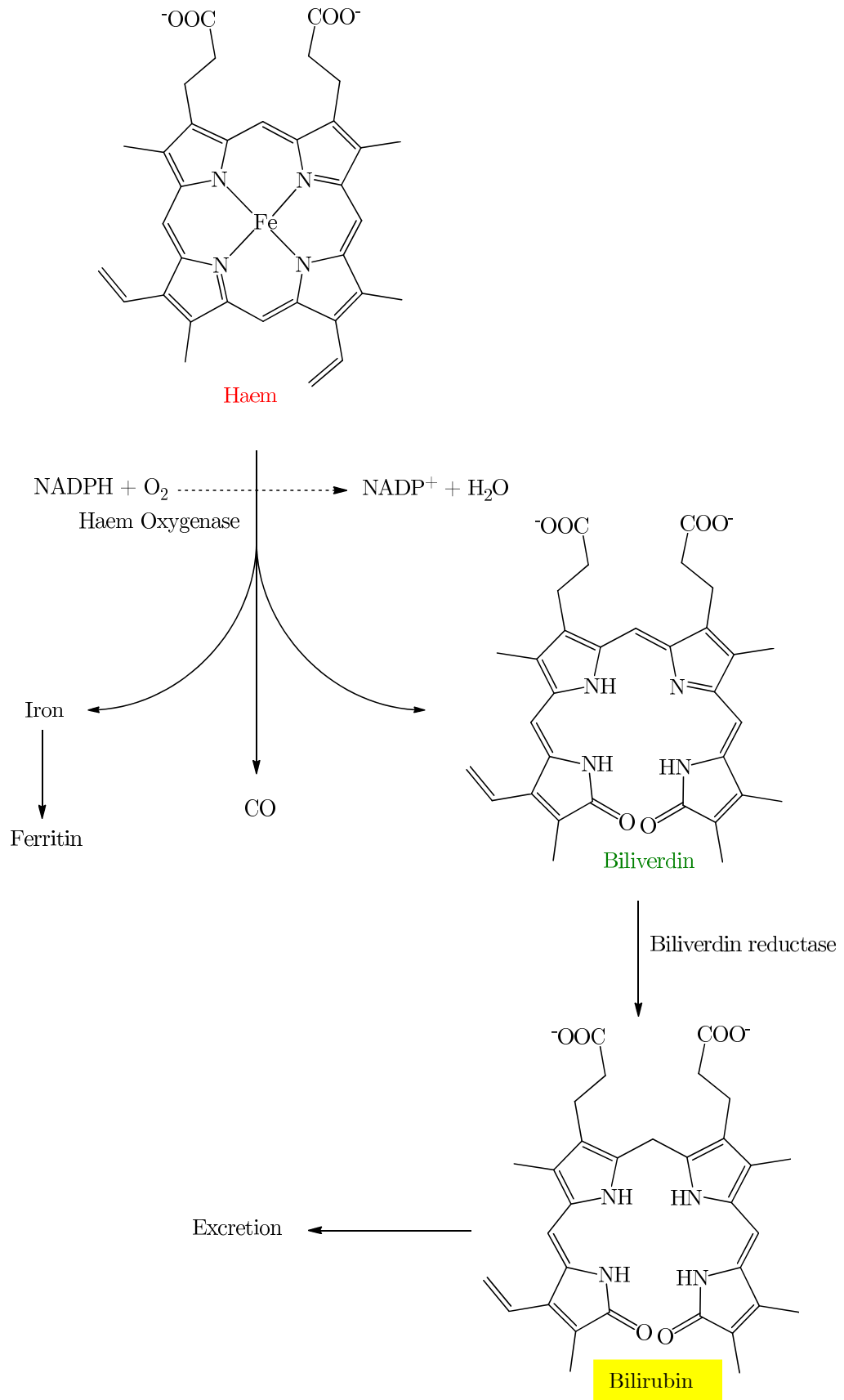
Figure 1-7: Oxidation of haem to produce carbon monoxide as a by-product.

Free haem (red)

Deoxygenated blood (Blue)

Biliverdin (green)

Bilirubin (yellow)
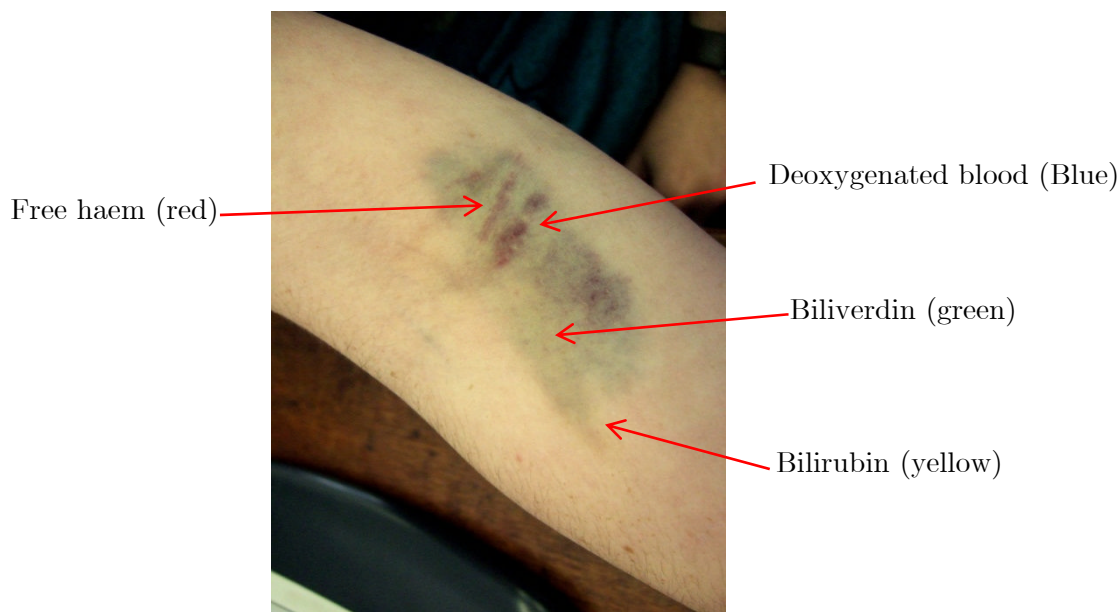
Figure 1-8: Bruising is an example of endogenous CO production.

Hydrogen sulfide is produced by both enzymatic and non-enzymatic pathways.[27] There are four enzymatic pathways which are known to produce hydrogen sulfide from cysteine derivatives. Of these, the bulk of endogenous H_2S is produced by the enzymes cystathionine-β-synthase (CBS) and cystathionine-γ-lyase (CSE).[28] L-cysteine is hydrolysed by cystathionine-β-synthase (CBS) to produce equimolar amounts of H_2S and L-serine. CBS is responsible for the bulk of H_2S production in the brain and central nervous system, whereas CSE is expressed largely in endothelial and smooth muscle cells in the cardiovascular system.

Several estimates of endogenous hydrogen sulfide levels have been made. Many of these show relatively high levels of hydrogen sulfide (50 – 160 μM concentrations in brain tissue[29]), but figures should be approached with caution as their measurement involves an assay which is also sensitive to HS^- and S^{2-}.[30, 31] Recent estimates of H_2S put levels much lower, for example in a mouse brain the concentration is thought to be 15 nM.[30, 32] As for NO, these low levels are not necessarily a marker of biological inactivity, but are more of an indication that biological activity takes place rapidly upon production of the H_2S.[7] More accurate methods of measuring endogenous H_2S production is an area of current research.[33]

Once produced, hydrogen sulfide is quickly metabolised by a number of pathways meaning that its lifetime in the body is fairly short with a half-life of the order of minutes[34]. Metabolism takes place mainly in the kidneys through oxidation by mitochondria yielding thiosulfate ($S_2O_3^{2-}$), sulfite (SO_3^{2-}) and sulfate (SO_4^{2-}), by methylation to dimethyl sulfide, or by reaction with metallo- or disulfide-containing molecules.[2, 35] One of these metalloproteins - the interaction with haemoglobin - is of particular interest, as this molecule is a common sink for both NO and CO. Interaction of H_2S with porphyrin forms the green sulfhemoglobin, and its formation could significantly alter the binding capacity for other gases.[2]

1.4 Biological actions of NO, CO and H_2S

1.4.1 Toxicity

The direct toxicity of nitric oxide is modest, but is greatly enhanced by it reacting with superoxide to form peroxynitrite (ONOO-).[36] The generation of excess $ONOO^-$ leads to oxidative injury and lung damage culminating, at high dosages, in pulmonary oedema. On contact with oxygen, NO spontaneously produces NO_2 which is considerably more toxic than nitric oxide itself.

The toxicity of carbon monoxide is has been known since Roman and Greek times when the gas was used for judicial executions.[37] Carbon monoxide's affinity for the iron in haemoglobin, the blood's oxygen carrier, is 220 times greater than that of oxygen, meaning that it competitively binds to the metal site in the haem moiety to form carboxy-haemoglobin (HbCO) instead of the oxy-haemoglobin (OxHb) required to transport oxygen from the lungs to other organs. The danger this poses is double-pronged: first, with carbon monoxide carried on the metal site there is a decreased capacity of the blood to carry oxygen. Secondly, the coordination of carbon monoxide to one site in haemoglobin molecule decreases the affinity of the other three oxygen-binding sites, compounding the reduction in oxygen content. Hence, exposure to carbon monoxide can lead to tissue hypoxia and ultimately suffocation. In addition to Hb, CO can bind to other proteins such as myoglobin and this can, at high concentrations, have a toxic effect on the cells. This effect, however, is generally superseded by the Hb binding.

The human nose is a very sensitive hydrogen sulfide detector, sensing it at concentrations as low as 0.0047 parts per million (ppm). This concentration is lower than the harmful threshold. Despite the strong characteristic odour, the sense of smell is severely impaired after exposure to higher levels (100 ppm) of the gas,[38] meaning that many exposed individuals are unaware of its presence. Hydrogen sulfide is toxic through the same mechanism as cyanide; both poisons inhibit cytochrome *c* oxide, the enzyme responsible for cellular respiration, via coordination to the enzyme's copper-centre. [39] The level of toxicity is highly dependent on the concentration and time of exposure.

1.4.2 Biological effects

NO, CO and H_2S have been connected to a large number of biological processes.[18,30,40] Nitric oxide has been the subject of the most studies, and hydrogen sulfide the subject of least. Research is only in its infancy, and in many areas there is not a clear consensus of the exact roles these gases perform, with many contradictory accounts of their effects being reported. Part of the reason for this is that endogenous levels of the gases must strike a very fine balance; for example, nitric oxide deficiency can cause unwanted effects such as hypertension, thrombosis, and a reduced ability to fight infection and heal wounds[41] whilst overproduction of NO has been linked to conditions such as septic shock and inflammation.[42] Similarly, enhanced H_2S production has been identified in conditions such as pancreatitis, diabetes and inflammation, whereas low levels of H_2S are associated with hypertension and asthma.[30]

Despite this complexity, some patterns are becoming clear. All three gases are known to be vasodilators through the relaxation of vascular smooth muscle cells (see footnote on page 7). Both NO and CO impart this activity with a concentration in the nanomolar range whilst a considerably higher concentration (micromolar) of hydrogen sulfide is required for the same effect.[27] Both nitric oxide and carbon monoxide are produced in endothelial cells and diffuse into the smooth muscle to signal for the conversion of guanosine-5-triphosphate (GTP) into cyclic guanosine-3,5-monophosphate (cGMP) via the activation of the enzyme guanylate cyclase (cGC) which causes relaxation.[15]

Both endothelial cells and smooth muscle cells are known to contain the enzyme CSE and therefore produce H_2S. H_2S-induced vasodilation appears to occur through an entirely different, cGC-independent pathway. Specifically, it appears that H_2S activates

proteins called K_{ATP} channels that control the flow of potassium ions out of smooth muscle cells within blood vessels. The potassium ion flow generates electric currents that limit the number of calcium ions that can enter the cells. The lower Ca^{2+} level leads to relaxation of the muscles and dilation of vessels.

The role of gasotransmitters in inflammation is complex, and is both tissue- and concentration-dependent. Nitric oxide is generally labelled as pro-inflammatory, and the overproduction of NO by the inducible form of NOS (iNOS) has been implicated in pro-inflammatory conditions such as rheumatoid arthritis. Despite being pro-inflammatory, NO produced by eNOS is essential to wound repair and the growth of new blood vessels in the area affected by inflammation, meaning that therapies involving the inhibition of all NO production would not necessarily improve inflammatory conditions. Drugs which down-regulate iNOS-induced nitric oxide production without stopping production of eNOS-NO may possibly improve inflammatory conditions, and the subtle structural differences between the enzymes may mean that this level of selectivity is possible.[43]

Similar, seemingly contradictory, effects are also reported for hydrogen sulfide. The concentration of H_2S in plasma and tissue, and the levels of CSE expression in those tissues, are all increased in animal models of inflammation.[30] Both H_2S-releasing derivatives of diclofenac (10-50 µmol/kg) and the slow-release H_2S donor GYY4137 (133 µmol/kg) have both shown anti-inflammatory effects,[44, 45] but NaHS injection showed pro-inflammatory effects.

1.4.2.1 Nitric oxide, platelet aggregation and antibacterial activity

NO produced in the endothelium prevents platelet aggregation in healthy blood vessels through a cGC-derived mechanism, implicating NO in wound healing and thrombosis.[46] This effect is only observed with NO; weak effects are shown by CO and H_2S but only at pharmacological concentrations of the gas (high millimolar concentrations).

When the endothelium of a blood vessel is damaged, the level of NO produced is lowered and platelet aggregation is no longer prevented. This leads to platelet aggregation clotting and healing of the vessel. NO is known to regulate the growth of new blood vessels and may regulate the production of new skin cells during wound healing.[47] This, coupled with the roles NO plays in fighting infection and in clotting, means that the endogenous dosage of nitric oxide has been suggested to improve wound

healing, particularly in situations where the body's wound healing mechanisms are lowered (such as in diabetic ulcers). There are growing reports that H$_2$S, like nitric oxide, has therapeutic potential in the angiogenesis/wound healing area. *In vitro* studies demonstrate that hydrogen sulfide induces angiogenesis and stimulates gastric ulcer healing in rodent models.[34, 48, 49]

In cases where platelet aggregation is not associated with a wound, there is a danger of clots which can prevent blood flow to key organs. This danger is increased when foreign matter, which does not produce NO, is inserted into the blood vessels, as is the case when stents are used to alleviate stenosis. Stenosis, the narrowing of the blood vessels by fatty lipid deposits, is a very dangerous condition which can increase blood pressure and strain on the heart. A stent at the end of a catheter is inserted into the vessel and a balloon is inflated to increase the size of the lumen and increase blood flow. This procedure can damage the endothelium, lowering NO levels and increasing risk of clots on the surface of the stent, forming a thrombosis. Using stent materials which produce NO to mimic endothelial action could have a role in preventing thrombosis.

NO is a known antibacterial agent. Macrophages, which are scavenger cells and part of the immune system, protect the body from infection by killing and digesting microbes via the production of toxic chemicals to destroy the microbe cells. These chemicals are quickly removed from the body by enzymes, preventing them from damaging cells of the host tissue. NO is known to be one of the chemicals produced by macrophages and is involved in cell death, both necrosis[iii] and apoptosis,[iv] in its produced form and via conversion to peroxynitrite and nitrate.[18] NO-induced necrosis has also been suggested as the mechanism by which nitric oxide attacks tumour cells, although the role of nitric oxide in cancer is neither simple nor well understood at present.[40]

1.4.2.2   Carbon monoxide and organ transplantation

Organ transplantation is used routinely as a treatment for end-stage organ disease. A major challenge associated with the process of cold storage and warm

---

[iii] Necrosis is cell death caused by factors external to the cell or tissue, such as infection, toxins, or trauma. It is generally 'messy' leaving behind debris in the body, and is normally detrimental to tissue.
[iv] Apoptosis is programmed cell death. It results in cell fragments which can be engulfed and removed from the body before the contents of the cell can spill out onto surrounding cells and cause damage.

reperfusion is ischemia/reperfusion injury[v] (I/R injury) which affects the short-term and long-term outcomes of transplants. Lack of oxygen to the tissue leads to increased expression of anaerobic mediators which, when combined with reoxygenated blood can lead to an excess of oxygen and radical oxygenating species (ROS)[vi]. This causes damage to the organ[50, 51] leading to chronic deterioration of the graft, infection and ultimately graft rejection. [50, 51,52] A shortage of suitable donors leads to the use of more 'marginal' organs[52] which are more susceptible to I/R injury and chronic deterioration, and makes patients more likely to suffer post-transplant complications.

The haem oxygenase system has been shown to have cytoprotective effects in transplantation using a number of disease models, and several papers have postulated that it is carbon monoxide generation which underlies this cytoprotective effect.[52-54] Transplants of organs from patients who have died from carbon monoxide poisoning have been successful and have shown reduced susceptibility to I/R injury.[55] Exogenous dosage of carbon monoxide has been shown to have a protective effect against I/R injury in many transplant models, including liver, intestinal, kidney, heart, and lung grafts. Increased survival rates in CO-dosed animals have been reported, indicating that carbon monoxide could be an exciting potential therapeutic in this area.[52, 54, 56-59] More recently, hydrogen sulfide has been suggested to have a similar role in I/R injury models.[60, 61]

1.4.2.3 Hydrogen sulfide and suspended animation

Hydrogen sulfide has been shown to have an effect on metabolism and help survival in very low oxygen conditions. Administration of low levels (80 ppm) of hydrogen sulfide to mice led to a suspended animation or "H_2S hibernation" state where the body maintains a baseline metabolism that protects the vital organs from damage until energy supply levels and the heart rate returns to normal.[62, 63] These results indicate that H_2S may be able to protect against some of the effects of hypoxia[vii], but experiments using larger animals such as sheep[64, 65] and piglets[66] have not seen the same effect, and whether H_2S could induce a hibernation-like state in humans is unknown.

---

[v] Ischemia is a state of tissue oxygen deprivation through loss of blood flow to an organ. Reperfusion is the restoration of blood flow to an ischemic tissue.
[vi] Reactive oxygenating species are intermediates formed by the incomplete one-electron reduction of molecular oxygen and include singlet oxygen, superoxides, peroxides and hydroxyl radicals. They have crucial roles in oxidative stress, signal transduction, regulation of gene expression and host defence.
[vii] Hypoxia is a state when a tissue has an inadequate oxygen supply to allow normal cellular processes to take place.

Nevertheless, this raises the possibility that H$_2$S may be of value in transplantation surgery where excessive cell death in low oxygen conditions has an impact on the success of the procedure.[60, 61]

1.4.3   Interactions between gasotransmitters

As more research appears in the literature it is becoming clearer that NO, CO and H$_2$S all interact with each other and, to some extent, mediate the function of one another at many different levels.[27] There are at least two common sites of action for the three gases involving interaction with haem moieties; all three gases are known to bind to iron in haemoglobin and both CO and NO are known to interact with cGC, an enzyme involved in vasodilation.   There are reports that the presence of more than one gasotransmitter has different effects to each gasotransmitter alone, depending on the location and conditions. Each gas appears to be able to regulate the expression of the other two gases, and the best known of these currently is that NO-donors up-regulate HO-1, increasing the synthesis of carbon monoxide in blood vessels. The activity of CBS, an H$_2$S producing enzyme, can be directly inhibited by both nitric oxide and carbon monoxide.[34]   H$_2$S can also induce an up-regulation of anti-inflammatory and cytoprotective genes including haem oxygenase.   The interactions of the three gases are likely to be complex and highly dependent on the tissue and the absolute and relative concentrations of the gases involved.

1.5   Potential of gasotransmitters as therapeutics

1.5.1   What is required?

NO, CO and H$_2$S are exciting potential therapeutics.   The required concentrations of gas molecules for particular biological applications are starting to be realised. It is thought, for example, that for antiplatelet action very low concentrations of nitric oxide, of the order of nano- to pico-molar, are required.[67] For antibacterial action, much higher concentrations (milli-molar) are needed.   The biological effects are highly dependent on the concentration of the molecule, meaning that potential therapies require a method that allows delivery of the exact amount of gas appropriate to the therapy at the desired rate.

There are number of difficulties with the dosage of these molecules, firstly because all three are gases at room temperature and pressure. Secondly, all are lethal in

high doses, meaning that the use of gas cylinders would have to be very tightly controlled and dosing an appropriately small amount would be awkward and difficult. In the case of NO, any exposure to oxygen causes immediate conversion to the extremely toxic NO_2. Inhalation of NO has been used extensively in biological experiments and, in fact, has met with some success in the treatment of infants with respiratory failure.[68] Recently, a delivery system specifically for dosing inhaled carbon monoxide (CO) has been developed by Ikaria to provide quantitative delivery of pharmaceutical-grade CO for inhalation in proportion to the subject's body weight.[69]

Another issue is that the short lifetimes *in vivo* of NO and H_2S mean that systemic delivery may not be able to dose the gas to the correct areas. Particularly for applications such as wound healing, direct delivery of the gas to a targeted area is desirable, and this would further avoid unwanted side effects of the gas's action in other parts of the body.

1.5.2   Current therapies

Outside of inhalation, chemical compounds which release the gas when exposed to a specific stimulus are the most widely researched source of gasotransmitters. NO donors are a growing area of research. Exogenous sources of NO have unwittingly been used as therapies for centuries; there are reports of potassium nitrate, which is broken down by NOS to produce NO, being used to treat the discomfort and pain associated with angina as early as 800 AD.[18]   Glyceryl trinitrate, which is thought to be metabolised to form nitric oxide is the most common treatment for angina[viii].[70] Diazeniumdiolate compounds (NONOates, section 1.8.1.2) release nitric oxide in a first order, proton-mediated reaction, and the rate of gas release from compounds can be chemically controlled.[71] The drug Viagra works by prolonging the effect of NO in the penis, where the gas acts to relax the vessels, thereby enhancing blood flow.[72] S-nitrosothiols, when used as NO donor drugs, break down to form NO.

Carbon monoxide is commonly dosed through the liver metabolism of methylene chloride (dichloromethane). Recently developed carbon monoxide-releasing molecules (CORMs) are transition metal carbonyl complexes which release carbon monoxide by

---

[viii] Angina is a condition caused by constriction of the arteries supplying the heart, putting increased strain on the heart to maintain the same level of blood flow. Its symptoms are chest pain and choking.

ligand dissociation, with chemically tailorable half-lives of release.[69, 73] The biological activity of these molecules has been extensively studied[69] and it has been shown that CORM derived CO can be delivered to organs without a large increase in blood HbCO levels, meaning that CORMs present an exciting possibility of targeted delivery. Concerns do remain though; it is not known whether the release of gas from CORMs mimics its production from endogenous sources[69] and all CORM molecules are based on heavy metal atoms, meaning that the by-products of carbon monoxide release could have their own, possibly competitive, side effects.[69]

Most reported experiments dose H_2S via the dissociation of NaHS.[34] The release from NaHS is rapid as the equilibrium in equation 1.1 is reached quickly. It is not known whether NaHS releases mainly H_2S or HS^- in each biological situation, and whether the quick burst of H_2S from NaHS mimics the endogenous production accurately. Additionally, it is not known which component of the equilibrium has the biological effect; contradictory reports suggest that it is possible that one, the other or both do so in particular situations.

Reports of other chemical methods of dosing hydrogen sulfide and the consequential biological effects are growing.[30,74] These can be loosely divided into 4 areas (1) Lawesson's reagent (2,4-bis(4-methoxyphenyl)-1,3,2,4-dithiadiphosphetane-2,4-dithione) and derivatives such as GYY4137 release H_2S in aqueous solution.[75] (2) Co-drugs of 5-(4-hydroxyphenyl)-3H-1,2-dithiol-3-thione (ADT-OH) such as S-diclofenac and S-mesalamine break at the ester linkage to form ADT-OH which breaks down to release hydrogen sulfide.[44, 45] (3) Garlic derived polysulfide compounds[76] (4) Cysteine-activated donors based on N-mercapto compounds, whose release kinetics can be controlled by chemical substituents on the benzene ring.[77]

The donor that mimics endogenous production of each gas most accurately is, as yet, unknown and the donor (or more likely, the release rate) has been shown to have remarkable influence over the biology. For example, Moore and co-workers found that a slow-release H_2S-donor gave anti-inflammatory effects whilst the same dosage of NaHS increased inflammation.[78]

Some uses such as wound healing applications require topical delivery of the gas. Topical delivery of nitric oxide has received the most attention. Acidified nitrite creams have improved the wound healing time in both normal and diabetic mice, but there is

some concern with regard to skin inflammation. Dressings with NO-releasing materials improved the wound healing time in diabetic mice.[79]

Coatings for stents and catheters which release nitric oxide and better mimic endothelial nitric oxide production have been shown to decrease thrombosis formation.[80-83] This technology also requires materials which can release nitric oxide at a rate which mimics endogenous production. Porous materials are known to adsorb nitric oxide, carbon monoxide and hydrogen sulfide, and this is reviewed in section 1.8.1.2.

1.6 Metal-organic frameworks

Metal-organic frameworks (MOFs), also known as coordination polymers, are extended materials which consist of metal ions or clusters which act as polyhedral 'nodes', connected by multi-dentate ligand molecules acting as linkers. Frameworks are formed by coordinate bonds into infinite arrays, sometimes forming crystalline solids. The first MOF crystal structure was reported in 1959,[84] although significant research into the science and applications of MOFs started in the 1990s. To date, several thousand metal-organic frameworks have been synthesised, usually via hydrothermal and solvothermal methods (section 2.1) but increasingly using other techniques such as microwaves and electrochemistry.[67]

1.6.1 Synthesis and general features

MOFs can exist as one dimensional chains, two-dimensional sheets or three dimensional frameworks. 2D and 3D structures can exhibit pores or channels running through them which are usually filled with solvent molecules from the synthesis. Many frameworks have fairly low thermal stability, but those which show higher stability can have guest molecules removed from pores by exposing the material to a vacuum or to heat. This results in materials with large pore volumes and high surface areas of thousands of square meters per gram. This compares favourably with several hundred $m^2 g^{-1}$ for the most porous zeolites (the maximum surface area is zeolite Y, at $904 \, m^2 g^{-1}$) and activated carbons which have a theoretical maximum surface area of $2630 \, m^2 g^{-1}$.[85] The highest reported MOF surface area (BET) to date is $6240 \, m^2/g$, shown by MIL-200.[86]

The connectivities and topologies of MOF structures are dependent on coordination preferences of the synthetic conditions. Metals provide coordination sites for linkers and the geometry of the metal caused by oxidation states and coordination numbers determines the shape of the node and therefore the geometry of the framework. Linkers have multiple functional groups in order to act as a bridge between metal centres. The most common linker atoms are oxygen and nitrogen - carboxylates, phenol, pyridine, and imidazole donors are by far the most common donor groups reported, though the use of more 'exotic' functional groups such as sulfonates, nitrates and phosphonates are becoming increasingly common as the search for new frameworks continues. Rigid linkers, where the movement of the lone pair is restricted, increase the predictability of reactions and act as rods between metal nodes which can lead to robust frameworks with permanent porosity. Linkers with flexible binding modes have the potential to act as hemi-labile ligands and can lead to coordinative flexibility in the framework. Counter anions from regents and solvents can act as reactants; both can take an active part in the framework, or act as template ions. Reaction conditions are also known to have a determining effect on the structure.

The range of metals and organic linkers available and the ability to change experimental conditions gives potential for a seemingly infinite number of framework topologies. However, in practice, the chemistry of these systems favour the *in situ* generation of particular polyatomic metal units, meaning that the same so-called 'secondary building units' (SBUs) are seen over and over again.[87] This is analogous to aluminosilicate zeolite chemistry, where a description of the structure can be given in terms of nine SBUs based on tetrahedral AlO_4 and SiO_4 primary building units.[88] Some common secondary building units - the Zn_4O-cluster, the copper paddlewheel dimer, and $Cr_3(OH)$-trimer - are shown in Figure 1-9.

It is possible to tailor the structure and properties of a framework. Firstly, knowledge of SBU formation can be applied in order to design frameworks with the same topology but utilising different ligands, resulting in different pore sizes and surface areas. The best known example of this 'isoreticular synthesis' is the IRMOFs reported by Yaghi and co-workers which use the same Zn_4O-cluster with different linkers to form a series of frameworks based on the same cubic topology but with different pore sizes and chemical functionality and thus varying gas adsorption properties.[89, 90] In a similar manner, the

same framework topology can be created with different metals, as demonstrated by the M-CPO-27 framework (Chapter 4), where metals (Ni, Co, Zn, Mn, Mg, Fe) are linked by 2,5,-dihydroxyterephthalic acid into a 3-D honeycomb framework, and the $[M_3(btc)_2]$ framework, based on M_2-paddle-wheel units linked by benzenetricarboxylic acid (btc) which can be synthesised with M = Cu (where it is commonly called HKUST-1) Fe, Cr, Mo (Figure 1-10).[91-94]

In addition to the range of frameworks which can be synthesised directly, it is also possible to modify the framework after the initial synthesis. This strategy of post-synthetic modification is frequently used to introduce functionalities to the pores and channels of the material required for specific purposes.[95] Post-synthetic modification can take several forms; removal of guest solvent molecules through the application of heat could be described as the most simple of post-synthetic modification procedures. Others include carrying out organic reactions on functional groups within the framework, grafting functional groups either onto the linker group or onto open metal sites in the material, or adding metal ions, clusters or other species into the pores in order to enhance a particular characteristic of the material.

This ability to tailor a MOF's structure to specific needs and requirements makes them exciting for a range of applications. Initially, the high porosity of the materials focused attention onto gas adsorption (see below), but MOFs have since been suggested for potential applications in areas such as gas separation,[96, 97] catalysis,[98-100] luminescence and sensing,[101, 102] magnetism,[103] and medicine (see section 1.8).

1.7 Gas storage in porous materials

Gas storage is a topical issue; with the projected exhaustion of fossil fuels, the urgency of our search for new energy sources has increased, and porous materials have been highlighted as a possible storage medium. Gas storage in zeolites has been studied extensively, especially in those materials with extra-framework ions which can interact with guest species.[88] Some MOFs have large surface areas and high porosity and this means that they have the potential to store significant amounts of gas in their pores. Most work to-date has concentrated on gas storage for environmental applications, and this can be broadly split into adsorption of potential fuel gases, hydrogen and methane,[104-108] and the capture of carbon dioxide and other hazardous gases.[109, 110]

There are several potential advantages of using MOFs for gas storage compared to gas cylinders. Firstly, there can be an increased storage density when compared with gas cylinders, zeolites and activated carbons.[106] Secondly, in applications where only a small amount of gas is required, it could be easier to handle the gas in the form of solid pellets with adsorbed gas whose capacity can be tailored for application. Lastly, it might be safer to handle a gas when it is adsorbed in a solid, especially if higher pressures can be avoided. This is particularly applicable in the case of biological gases, where very controlled delivery of the gas is required.

Storage of a gas in a MOF requires large enough pore windows to allow the gas molecules to diffuse into the material and an ability to keep the molecule in the material through the interaction of the gas and the framework's internal surface. Storage implies that the gas can be removed when required, meaning the ability to trigger the release of the gas from the material is necessary. Gas adsorption capacity is generally reported as adsorption isotherms, which quantify the amount of gas that a material adsorbs as a function of partial pressure of the gas (section 3.8). In general, few gas release experiments are performed, meaning that in reality if the delivery of gas is incomplete, the deliverable storage capacity may be less than the adsorption values reported.

1.7.1 Methods of gas storage

When gas molecules enter the material, they can bind to sites on its internal surface. This is adsorption. Adsorption is loosely divided into physical adsorption, or physisorption, and chemical adsorption, or chemisorption. Physisorption is generally weak, is due to induced or permanent dipoles and is generally observed at low temperatures with reduced capacity at higher temperature. Chemisorption involves the exchange of electrons (formation of chemical bonds) between adsorbate and adsorbant and is a much stronger interaction. Whilst physisorption tends to be completely reversible on the decrease in partial pressure, species chemisorbed to a surface are likely to need an extra driving force such as heat for their removal.

For an uncharged gas molecule, the main interaction with the framework surface is via physisorption. Because of this, uptake is generally correlated with higher surface area, though this is not necessarily the only factor. The strength of interactions between the framework and gases can be reflected by isosteric heats of adsorption, Q_{st}.[111] When van der Waals interactions dominate, Q_{st} values are generally small; for hydrogen gas, for

example, the Q_{st} for interaction with frameworks is typically in the range of $4 - 7$ kJmol^{-1}.[112] For larger molecules such as methane, the Columbic portion of the interaction is larger, meaning that the gas is more 'sticky'. The relatively weak interaction between the framework and the gas molecules is often the limiting factor with regard to gas adsorption capacity, but there are a number of ways in which this interaction energy can be increased through functionalization of the framework surface.

Unlike zeolites, where metal ions exchanged into the framework sit extra- to the framework and are readily available for interaction with guest species, the metal ions within metal-organic frameworks are an integral part of the structure. This means that in many cases their coordination sphere is made up entirely of strong ligand bonds and so they are unable to interact with guest species without breakdown of the framework. However, in some cases where one or more coordination site is taken up by solvent molecules from the synthesis, their removal leaves the structure with metals which are not coordinatively saturated. These metals with empty sites in their coordination spheres are named coordinatively unsaturated sites (CUS), or open metal sites. They can be very reactive with a high affinity for guest molecules and can become involved in chemisorption processes. CUS have been shown to enhance gas storage in a number of systems.[104] The Cu-framework HKUST-1 ($[Cu_3(btc)_2(H_2O)_3]$) shown at the bottom of Figure 1-10 was the first example of functionalisable CUS. The aqua ligands from the Cu-site can be removed upon heating, and replaced by other groups such as pyridine.[91] The Mn-framework $Mn_3[(Mn_4Cl)_3(BTT)_8]_2$ (BTT = 1,3,5-benzenetristetrazolate) was reported by Dinca et $al.$ to contain open Mn^{2+} coordination sites. Interaction with D_2 gives a Q_{st} value of 10.1 kJ mol^{-1} at zero coverage at 77 K, with a Mn-D_2 bond length (2.27 Å) much shorter than would be expected for physisorption.[113] Similarly, the interaction of H_2 with the open Ni-sites in Ni-CPO-27 was shown to give $Q_{st} = 13$ kJ mol^{-1} at low coverages, the highest framework-H_2 interaction energy to date.[114]
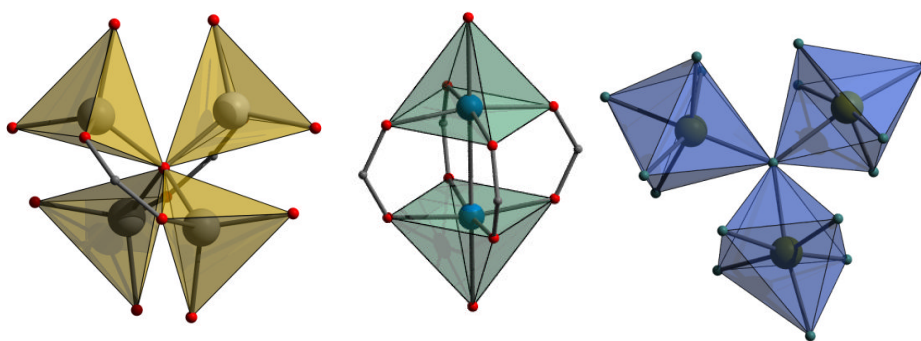
Figure 1-9: Common secondary building units for MOFs: Zn$_4$O-cluster used in MOF-5 and IRMOFs (left); Cu-paddlewheel dimer seen in HKUST-1 (middle); Cr-trimer found in MIL-101 (right).
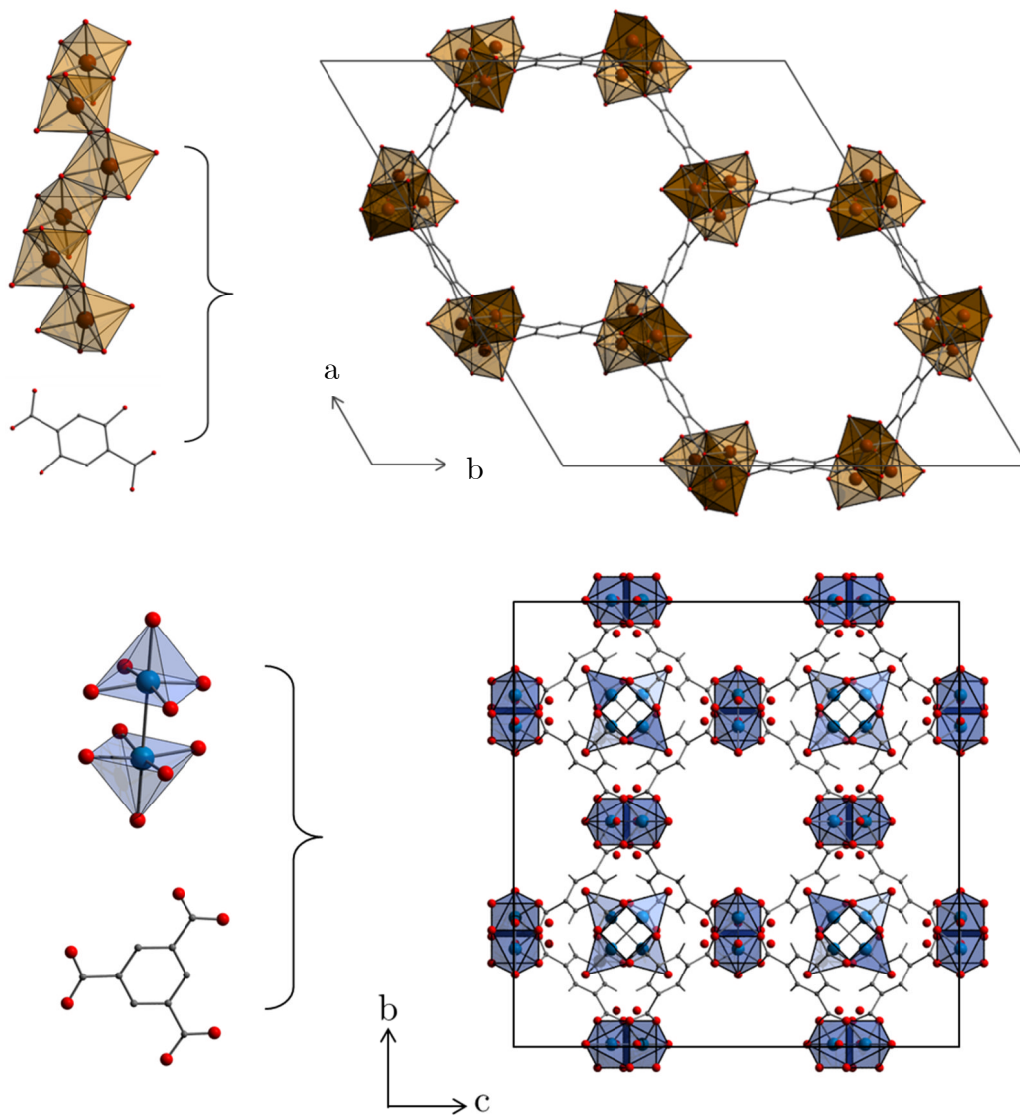

Figure 1-10: M-CPO-27 (top) and M$_3$(btc)$_2$ (bottom) framework topologies.

Interaction of a guest with the ligand can also increase the energy of adsorption. The higher methane capacity of IRMOF-6 compared to the other IRMOFs was ascribed to interaction with the cyclobutyl 1,4-benzenedicarboxylate ligand.[89] PCN-14, which combines both copper open metal sites and additional adsorption sites interacting with the anthracene ligand, shows the highest interaction energy and adsorption capacity for methane to date.[115, 116] Use of amine-based ligands has been shown to greatly increase the interaction of CO_2 with the framework. Interaction with organic groups can be increased further by grafting pendant functionalities onto the surface; this strategy to introduce alkylamine functionality onto bridging ligands or onto open metal-sites can result in the increased uptake of carbon dioxide.[110]

Gas storage by framework flexibility has been reported for several frameworks.[85, 117-122] These transformations can include stretching, 'breathing' and rotation and in some cases the selective induction of framework transitions can lead to selective gas adsorption properties through size selectivity or thermodynamic effects.

1.7.2   Structural studies of gas adsorption in metal-organic frameworks

In order to understand the storage of gas in a material clearly, it is important to know the way in which gas molecules interact with the framework. Knowledge of where gases bind in known materials is essential in order to understand how the characteristics of binding sites relate to the physical properties displayed by the materials. This should aid the design of materials with gas binding sites known to induce specific adsorption properties. This is particularly important for the design of materials with specific and tailored adsorption properties, whether those properties be adsorption capacity, selectivity of one gas over another, or release rate of gas from the material on exposure to a stimulus. For medical gases the rate of release is of critical importance to their safety and function, and this is directly affected by the nature of the binding sites in the material. In order to characterise how gas is released from the materials, it is first necessary to understand where gases bind, and, if possible, monitor the structure of the material through the full adsorption-release cycle.

There are number of characterisation methods which have been used to probe the nature of gas-adducts in MOFs, including IR spectroscopy, EXAFS and inelastic scattering.[94, 123-129] Infrared spectroscopy is useful for gases that show very specific IR modes that are sensitive to interaction with metal ions or framework features, such as

carbon monoxide and nitric oxide and work in this area has been published by Bordiga and co-workers.[123, 125] Crystallographic techniques (single-crystal and powder X-ray and neutron diffraction) are among the most useful, as these can give structural information about where the gas appears in the structure, and, by interpretation, information about binding strengths. Many MOFs are crystalline solids meaning they are suitable for crystallographic analysis. Coupled with the wide range of structures available and the ability to tailor structural features, this makes these materials ideal for the study of structure-property relationships. An increasing number of structural studies determining the gas adsorption sites in a number of MOF materials have been reported in recent years.[93, 113-115, 130-135]

MOF-5, which does not have CUS but has large pores with the potential for gas adsorption has been extensively studied. Single crystals of the material were placed in capillaries activated and backfilled with either Ar, N_2[136] or H_2[137] before neutron diffraction data were collected for the samples. At higher temperatures (293 K) no significant Fourier peaks could be located in the channels to be attributed to guests. At 30 K eight symmetry-independent adsorption sites could be located, five primary adsorption sites close to the framework and three secondary adsorption sites forming a second layer of gas within the pore. The site showing greatest occupancy in all data sets lies on a triangular face of the octahedron whose vertices are defined by the carboxylate-C atoms ($\alpha(CO_2)_3$ site, Figure 1-11).

Structural studies have characterised CUS as the primary adsorption interaction in a number of MOFs. Hydrogen storage in HKUST-1 was studied by Kepert and co-workers using neutron powder diffraction.[131, 134] Six distinct D_2 sites were identified within the structure which are progressively filled on increasing pressure of hydrogen. The highest energy is on the CUS on the axial sites of the SBU. The Cu-H distance is 2.39(1) Å at 4 K indicating that there is significant interaction between the copper centre and the hydrogen, consistent with the IR data on the same compound.[127] Similarly, for methane adsorption, powder X-ray diffraction data indicate that the gas interacts with the copper-sites in the framework.[138]

The interaction of gases with the M-CPO-27 series has been reported for a number of gases.[93, 115, 126, 139, 140] For all gases, the primary adsorption site was found to be the open metal site on the apex of the MO_5 square pyramid, changing the metal-

coordination to octahedral. Powder diffraction studies have been used to characterise the metal-gas binding mode. This is further discussed in section 4.2.2
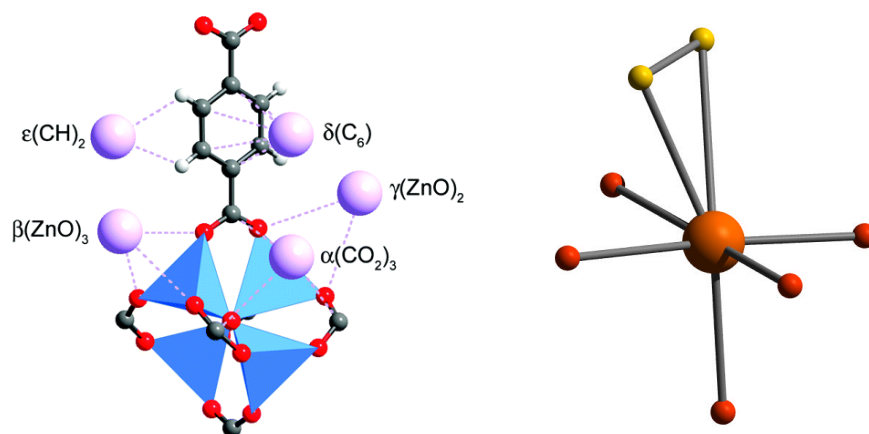

Figure 1-11: Gas binding sites in MOFs determined by diffraction studies. Left: H_2 binding sites (purple spheres) in IRMOF-1 determined by single crystal neutron diffraction. Adapted with permission from Roswell et al.,[136] Copyright (2012) American Chemical Society. Right: O_2-binding site on the base of the MO_5 square pyramidal face of Fe-CPO-27 as determined from Rietveld analysis of powder neutron diffraction. O_2 is shown in yellow.[93]

1.8 MOFs for biological applications

In recent years a growing area of research has involved MOFs for biological applications.[67] The use of MOFs for biomedical purposes is attractive for a number of reasons. MOFs are generally quite biodegradable because of the relatively labile nature of the coordination linkages holding the materials together, and this feature can be modified by the careful choice of metal and linker. Additionally, there is a wide range of MOFs available including those which use non-toxic components. This range lends itself to the idea that a MOF could be tailored for a specific therapeutic purpose.

Several ways in which MOFs could be used for biological applications have been suggested. Firstly, MOFs could be used as a container to store and deliver biologically active guests. Alternatively, the MOFs themselves could be biologically active or could be used as a diagnostic for applications such as imaging within the body. These three areas are outlined in the following sections.

1.8.1 MOFs as a delivery method

Metal-organic frameworks have many interesting features which make them potentially useful as a delivery device. The high porosity shown by many frameworks means that they have the potential to carry a large volume of any guest. Additionally, coordinatively unsaturated metal sites can increase the interaction of the framework with guest molecules. The ability to tune MOFs by choice of component can lead to very specific binding interactions of the host framework with the guest and so lead the ability to tailor delivery. The flexibility of some frameworks gives interesting delivery properties.

1.8.1.1 MOFs for drug delivery

The use of many active pharmaceutical ingredients (APIs) is limited by their hydrophobicity or lack of solubility making them difficult to dose in the correct concentrations.[67] Materials used as delivery capsules or vessels to transport the drug into the body and to the site of interest before releasing them are a method of improving the use of these compounds. The most commonly researched have been lipids and polymers which generally show high capacities but low control over release rates. Zeolites[141] and mesoporous silicas[142] have also been reported as nanocarriers which show better control over release kinetics but generally show poorer capacities.

MOFs were first suggested as nanocarriers for drug by Horcajada *et al.* who reported the encapsulation and delivery of the anti-inflammatory drug ibuprofen in two Cr-frameworks, MIL-100 and MIL-101.[143] Drug encapsulation in MOFs is attractive because of the range of MOFs available, with an increasing number of them made from non-toxic metals and many being biodegradable.[144] Encapsulation is also fairly simple, involving impregnation of the previously dehydrated framework in a solution of the drug. In recent years, a range of drugs have been encapsulated in MOFs reviewed in the recent article by Horcajada *et al.*[67]

The uptake of drug molecules appears to be highly dependent on the framework properties. Of the three Cr-MOFs which were studied for ibuprofen uptake, MIL-101(Cr) showed uptake of 1.4 g of ibuprofen per gram of dehydrated MOF,[145] which is substantially larger than both MIL-100(Cr) (0.35 g/g)[143] and MIL-53(Cr) (0.22 g/g).[146] MIL-100 has much smaller windows (~5 Å and ~8.5 Å) than MIL-101 (~12 Å and ~16 Å) meaning that the diffusion of drug into the framework is severely impaired. Similarly, MIL-53 has a much lower pore volume than MIL-101 which does not allow the

same high uptake of drug molecules.[67] The nature of the metal (Fe vs. Cr) in MIL-53 does not have an effect on the amount of drug taken up.[145]

The use of ionic interactions can increase drug uptake; the cationic drug procainamide has been adsorbed in the anionic framework BioMOF-1, which uses an adenine linker, in much larger quantities than reported for other materials.[147] The anti-cancer drug nimesulfide has been stored in a nanocomposite material formed of the Cu-framework HKUST-1 and Fe_3O_4 nanorods.[148]

The way in which a drug is delivered is very important; a quick initial delivery called the "burst effect" could be a waste of expensive ingredient or potentially be very dangerous to the patient. The delivery from MOFs has been characterized by submersing the drug-loaded framework in a solvent medium, and has been shown to be dependent on a number of factors.[67] The size of the window into the pores of the material determines whether the molecules reside in the pores of the framework or on the surface. Surface storage, such as that displayed when AZT-TP is stored in smaller pored-MIL-53, results in a quick burst of drug being released into solution. Slower delivery is achieved if the drug has to diffuse out of the solid as is the case with the same drug in MIL-100 which takes 5 days to release.[67, 149] The interaction of the framework with the drug molecule can determine how tightly held the molecule is and so how quickly it can diffuse out.

The rigidity of the framework is also key to the rate of drug release. In rigid MIL-100 and MIL-101, the ibuprofen release is complete in 3 and 6 days respectively, and the release profile shows a distinct stage for each of the three different ibuprofen-framework interactions.[150] In the case of flexible MIL-53, the release profile showed concentration-independent zero order kinetics as a consequence of the flexibility of the framework. The framework adapts its pore size to the dimensions of the drug to optimize drug-matrix interactions and shows partial pore-opening upon incorporation of ibuprofen into the pore. ^{1}H NMR indicates that there are strong interactions between the hydroxyl group of the linker and the carboxylic acid groups of ibuprofen molecules.[146]

Finally, the stability of the framework in the aqueous medium can determine delivery rate. Frameworks which show low stability release their drugs much quicker than those which are very stable in the aqueous medium used. Taylor-Pashow *et. al.*

coated their MIL-101(Fe) nanoparticles in silica in order to protect them from immediate degradation in the phosphate buffer, and this resulted in increased delivery times.[151]

1.8.1.2 MOFs for storage of biological gases

The exogenous dosage of gasotransmitter molecules has been shown to have beneficial medical effects. Unlike with gas storage and release for energy applications, it is not the amount of the gas stored but the release amounts and rate which are key.[105]

1.8.1.2.1 Nitric oxide in zeolites and MOFs

Both zeolites and MOFs have been shown to store and release NO. There are two ways of storing NO in a structure (Figure 1-12). The first is through the formation of diazeniumdiolate (or NONOates), which can deliver nitric oxide on exposure to water, and the second is by coordination of nitric oxide to a metal.

1.8.1.2.2 Zeolites

The interaction of NO with zeolite materials is well characterised due to their use as deNOx catalysts to remove the NO and NO_2 molecules from car exhaust fumes. Some of the NO is bound weakly by physisorption and some binds to the metal site making a strong, chemisorption interaction. The chemisorbed nitric oxide is not released from the material even at low pressures, making the adsorption irreversible. Both single crystal experiments[152] and IR studies indicate that this chemisorption component involves the interaction of nitric oxide with the metal sites in the zeolite.[152-154]
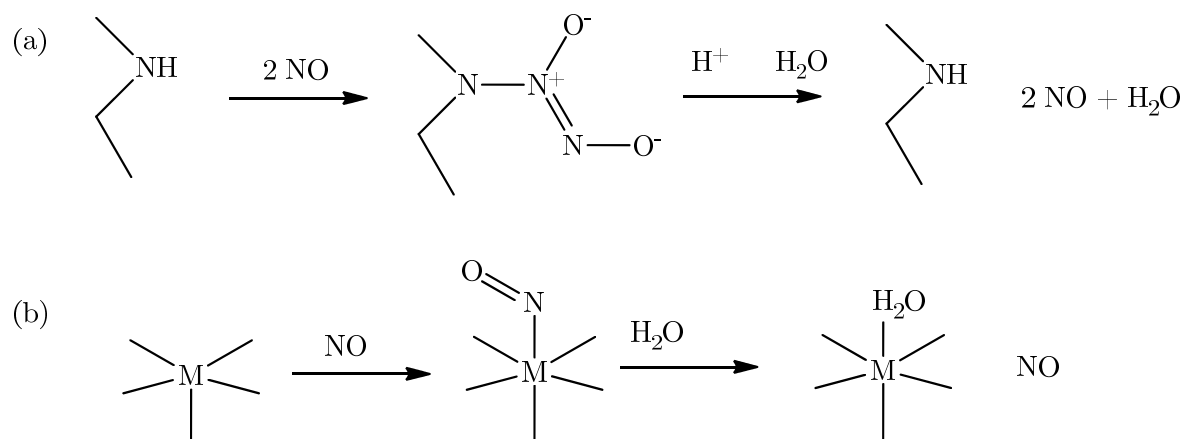

Figure 1-12: Methods of storing nitric oxide in a zeolite or MOF (a) formation of diazeniumdiolates (b) coordination to a metal ion.

32

Work by Wheatley *et al.*[155, 156] probed the effect that zeolite topology and extra-framework cations had on NO adsorption and release, and concluded that the most effective framework topology was LTA. Different metal cations within the same zeolite framework topology (LTA) gave rise to differing adsorption capacities and rates of release, with cobalt showing the best characteristics - adsorption of 1.7 mmolg^{-1} of nitric oxide at 1 atmosphere of NO and at room temperature.

On the reduction of pressure, the weakly held physisorbed nitric oxide was removed leaving the irreversible chemisorbed content within the material. Upon exposure to moisture, water replaces the NO on the extra cation site and the nitric oxide is released. The zeolites show release of NO that is comparable in quantity to the adsorption process, although the total amount which is adsorbed is not released.

The toxic nature of cobalt makes it unsuitable for some applications, so the much less toxic zinc framework, despite showing less ideal adsorption and desorption characteristics, has been used in several biological experiments. The nitric oxide released from these materials has been shown to have antithrombotic effects.[157] The well characterised low toxicity of zeolites makes them ideal for use in dermatological applications, and the sensitive nature of the delivery method compared favourably to other nitric oxide donors; nitric oxide from a zeolite showed increased blood flow to the skin (due to the vasodilatory effect) without the redness from irritation found from acidified nitrate.[157]

1.8.1.2.3 MOFs

Several framework materials have been studied for nitric oxide adsorption and release. The storage of nitric oxide in MOFs can take place via either mechanism shown in Figure 1-12. MOFs with open metal sites have shown much stronger adsorption of nitric oxide than those without.[158] Every MOF with open metal sites appears to store nitric oxide to some degree due to interaction of the gas molecule with the open metal site. The first studied MOF for NO adsorption, HKUST-1, adsorbs around 3 mmolg^{-1} of nitric oxide at room temperature and pressure.[159]

The behaviour of the CPO-27 isostructural series of frameworks for nitric oxide adsorption and release has been extensively studied.[158] McKinlay *et al.* report that both Ni-CPO-27 and Co-CPO-27 store considerable amounts of nitric oxide, with up to 8

mmolg^{-1} via coordination of the nitric oxide to the metal site resulting in octahedral geometry.

Storage of NO via the formation of diethylenetiamines, or NONOates was reported by Rosseinsky *et al.* who used post-synthetic modification of the open-metal site of HKUST-1.[160] However, on immersion in water, nitric oxide was released, but the amines were also leeched from the metal sites. Cohen and co-workers use a similar method for functionalising MOFs with NONOates by conversion of secondary amines from the functionalised ligands in MOFs rather than the open metal sites, thus improving the stability of the grafted amine species.[161]

Nitric oxide can bind strongly to frameworks in comparison with other gaseous species. This means that it can be selectively adsorbed over other species that form weaker bonds. The Cu-SIP-3 framework on which much of this thesis is based has shown ultra-selective uptake of nitric oxide because of the way in which the nitric oxide interacts with the framework. Similarly, the zinc-tetracyanoquinodimethane framework has shown extremely selective NO and O$_2$ adsorption because of their ability to undergo electron transfer with the framework ligand.[162]

For biological applications, the release of nitric oxide is very important. In structures which chemisorb nitric oxide, reduction in gas pressure is not enough to induce release of the nitric oxide molecule. Nitric oxide can be released on heating the material, or photolytically, but the most common method of release is exposure to water. If the framework-nitrosyl compound is susceptible to water, water replaces the nitric oxide on the framework binding site and the nitric oxide is released. The amount of nitric oxide released is dependent on how susceptible the framework is to moisture. For example, HKUST-1, which chemisorbs 3 mmolg^{-1} of NO at room temperature, releases only a tiny fraction because the nitrosyl complex is too stable.[156] However, even this small amount of NO has shown antiplatelet behaviour in biological testing.[67]

The release of nitric oxide from M-CPO-27 was studied by Dr Alistair McKinlay. Where M = Ni or Co, the materials show exceptional release capabilities and the full adsorbed capacity is released on exposure to water.[163] The other members of the series also store and release nitric oxide but without the same exceptional release capacities.[158] The release capacities of these materials appear to be in some way correlated with the ease of dehydration and the stability of the open-metal sites.[67] The NO released from

this material has shown both vasodilatory and antibacterial actions.[67, 163] Between these two extremes lie other MOFs with open metal sites which release a portion of their adsorbed amounts of nitric oxide.

Harding *et al.* recently reported the generation of nitric oxide via the MOF-catalysed reaction of S-nitrosocysteine. At the peak of nitric oxide production, 200 picomolar concentrations were released whereas control experiments without the MOF present did not yield appreciable NO generation.[164]

1.8.1.2.4 Carbon monoxide adsorption and release using MOFs

There is less literature describing the interaction of carbon monoxide with metal-organic frameworks and work focuses on the adsorption into frameworks. To date, there are no reports of quantification of the release of carbon monoxide from metal organic frameworks or of the CO released being used for biological applications. The crystallographic structures of adsorbed carbon monoxide has been reported in several zeolites but in no MOF materials to-date.[165]

Unsaturated Lewis acid sites in some copper and nickel frameworks have been studied for the catalytic oxidation of carbon monoxide to carbon dioxide, and the catalytic activity of the frameworks has been shown to be superior to that of zeolites but inferior to oxides of the same metal.[166-168] Loading of nanoparticles of gold or Co_3O_4 into ZIF-8 have also been reported to improve catalytic CO oxidation.[169, 170]

CO adsorption has also been reported in some MOFs, although adsorption capacity has tended to be low. Both the zinc-framework PCN-13[171] and $Mg_3(NDC)_3$, where NCD = 2,6-naphthalenedicarboxylate,[172] are selective for nitrogen adsorption over carbon monoxide adsorption due to minor kinetic diameter differences. The isoreticular MOF series (IRMOFs) showed no retention of carbon monoxide.[173]

The characteristic IR stretching frequency of CO is strongly dependent on the bonding environment. For this reason CO is commonly used as a probe molecule to understand structural features of materials. Several MOFs have been studied in this manner. For example, the relative abundance of reduced Fe^{2+} and Fe^{3+} in MIL-100 was determined by use of a CO probe.[174]

Carbon monoxide interaction with HKUST-1 has been studied by several research groups. The IR stretch of CO is able to differentiate between different Cu-sites in the

material; the formation of Cu^{2+}-CO monoadducts on the open metal sites after dehydration is the main interaction and this is corroborated by computational studies.[124, 175] The adsorption enthalpy for this site is reported to be approximately 17.5 kJmol^{-1}. Dicarbonyl species on Cu-defects in the structure are also reported. Alaerts *et al.* report that there are no interactions of CO with the organic surface, though recent reports by Drenchev *et al.* dispute this claim.[176, 177] Experimental and computational adsorption isotherms on HKUST-1 report an uptake of approximately 1 mmolg^{-1} at atmospheric pressure, and computational data show a further uptake at higher pressures of up to 11 mmolg^{-1} at 4 MPa pressure. Separation studies show a slight preference for CO retention over other small molecule gases.

CO interaction with the M-CPO-27 series has been studied by both IR and computational methods.[125, 129, 178] UV, XANES and computational data indicate that, like HKUST-1, open metal sites are the main site of adsorption for the Ni, Mg and Zn materials. IR studies on Ni-CPO-27 reported strong 1:1 Ni-CO interactions on 80% of the Ni-sites at 60 mbar which could only be removed at room temperature under persistent vacuum. These values give a theoretical adsorption value of 5.1 mmolg^{-1} at 60 mbar and an adsorption enthalpy of approximately 58 kJmol^{-1} as determined by microcalorimetry. A linear slow decline of this value at higher pressures is characteristic of having a single adsorption site. Computational values of adsorption enthalpies on the same material were slightly lower.[179] EXAFS data indicate that π-backdonation from the metal in the Ni-material might be a factor, so a deviation from linear M-C-O bonding could take place. The Ni-C distance from computational data is reduced compared to the Mg-C and Zn-C distance giving further weight to this theory.

The addition of $Cr(CO)_3$ in η^6-fashion to the benzene rings of MOF-5 by post-synthetic modification followed by heating resulted in complete decarboxylation of the cobalt and the release of carbon monoxide. The carbon monoxide release was not quantified.[180]

1.8.1.2.5 Hydrogen sulfide

Interest in hydrogen sulfide loading in metal-organic frameworks is relatively recent and focuses on the removal of hydrogen sulfide from gas streams. Few MOFs have been characterised for hydrogen sulfide adsorption and none for the release of the gas. MOFs do show good adsorption capacities, with 40 mmol g^{-1} in MIL-101(Cr) at 2

MPa pressure being the best reported to date.[181] Framework structure has a profound effect on adsorption; flexible MIL-53 showed pronounced steps in adsorption isotherms while rigid MIL-47, MIL-100 and MIL-101 showed Type 1 isotherms. The interaction between MIL-47(V) and H_2S was determined by computational methods and IR studies and was found to be through hydrogen bond donation from the H_2S to the V=O⋯V units in the framework. The calculated enthalpy of this adsorption was low at 27-29 kJ mol^{-1}. In comparison, flexible MIL-53 showed a two-step adsorption process characterised by the IR modes from the terephthalic acid linker. Firstly, the large pore open structure changed to a narrow pore closed structure at low pressures of H_2S, presumably to maximise the interaction of the guest with the framework. Secondly, swelling of the framework to its large pore mode occurred at high pressures to accommodate more H_2S molecules.

Adsorption of H_2S in both MIL-100 and MIL-101 appears to be partially irreversible, either because of partial destruction of the framework or because of strong interactions between the framework and the H_2S molecules. The open metal sites in these materials could account for some of the irreversibility.

Recently, relatively good adsorption uptake was reported for HKUST-1, which could be improved by making composites of the MOFs with graphene oxide.[182] Interaction of hydrogen sulfide with the Cu-sites in HKUST-1 resulted in progressive and permanent framework degradation to form copper sulfide.

1.8.2 Bioactive MOFs

Whilst MOFs have been used to encapsulate drug molecules, another strategy is to make the MOFs themselves biologically active. MOF materials may be degraded in the body and release the components into the body. In this area, porosity is not an important factor; instead factors of biodegradability of the MOF are key.

One method is to link an active organic linker with a non-toxic metal. The framework's degradation can be used to control the release kinetics of the active molecule, which is a technique used in pharmaceutics through co-crystallisation.[183] There are several reports of naturally occurring ligands being used in frameworks. Amino acid-based (tryptophan[184, 185], histidine,[143] phenylalanine,[186] tyrosine, aspartate[187,188] and proline[189]) and nucleotide-based (adenine, fumerate) frameworks have been reported.[94, 190]

Synthetic peptides and dipeptides[191-194] were used to form metal peptide frameworks (MPF) with both copper and calcium ions.[195] Cyclodextrin-based MOFs based on ionic interactions have been reported and this approach to 'edible' MOFs could be used for further biomedical applications in the future.[196] The biological effects of these frameworks have, so far, not been reported.

Using drugs as the linker molecules in a MOF is an elegant approach which is rarely employed. MOFs using the molecule nicotinic acid (vitamin B3), which possesses vasodilatory properties and is an essential nutrient for health, have been reported but always use toxic metals which limits their potential as therapeutics.[197, 198] BioMIL-1, an Fe-framework which is based on nicotinic acid, is an example of a three-dimensional bioactive MOF.[199] The effective drug loading in this material is close to 72%. The fast release of the drug is achieved through the degradation of the MOF in phosphate buffer solution (PBS) at 37 °C. The use of glutamic acid, an experimental drug, as a linker has been reported.[200] Methotrexate, a small molecule chemotherapeutic agent which contains two carboxylic acid groups at either end of the molecule, has been used as a linker in zinc and gallium frameworks.[201] This framework was subsequently incorporated into a functionalised lipid bilayer, which ensured that the material targeted cancer cells. The framework showed superior cytotoxicity efficacy compared to the as-synthesized particles or free drug molecules.

It is also possible to use a biologically active metal. For example, silver is a known antibacterial metal and is currently found in a range of antibacterial applications in items ranging from dental materials to socks. Several silver MOFs have been reported,[202-204] and the silver released from a MOF has been found to have antibacterial properties.[205, 206] The antibacterial role of zinc is an area of current research.

1.8.3 Imaging/Diagnostics

As well as a therapeutic role, there are several reports of MOFs being used in non-invasive diagnostics in medicine. The method which has received the most attention is the use of MOFs in magnetic resonance imaging (MRI) which has been reviewed by Lin and co-workers.[207, 208] MRI uses strong magnetic fields to form detailed internal images which, unlike X-ray techniques, give good contrast between different soft tissues. Protons with more rapid longitudinal relaxation times relax back to their equilibrium state faster, yielding higher net electromagnetic signals and brighter MRI images. The

contrast of these images is generally low, but can be greatly improved by the use of contrast agents (CA), which decrease the longitudinal relaxation time allowing greater resolution to the images. Currently, small molecule gadolinium(III) compounds are the most common and must be used in large doses to provide the necessary contrast, despite the high toxicity of any free gadolinium leached into tissue. Current contrast agents are fairly inefficient with low retention times, requiring high dosages, and non-specific in their target, meaning that there is intense research into new CAs. Nanomaterials, and in particular nanoparticle metal organic frameworks (nanoMOFs), have been intensively researched as potential CAs.

Gd-based compounds such as $Gd(BDC)_{1.5}(H_2O)_2$ nanorods show very high relaxivity, r_1, values[ix].[209] Other Gd-based nanoMOFs have also been reported. Both the particle size and surface modification reportedly affects the relaxivity.[210] The stability of these materials *in vivo* can be improved by coating the nanoparticles in silica[211] or biocompatible polymers.[210] The choice of polymer also has a significant effect on the relaxivity.[208] Reports of CAs using Mn-nanorods were reported to improve contrast, but with a much lower r_1 time than for the Gd-materials.[212] However, the decreased toxicity of these materials means that higher doses could be used to overcome this problem. Iron carboxylates (MILs) have also been studied as contrast agents.[149] Encapsulating CAs within a MOF has also been suggested and recently nanorods of Fe_2O_4 were encapsulated in HKUST-1. The CA-potential has not yet been tested.[148]

MOFs have been suggested for application in other diagnostic techniques. High Z compounds, such as those containing iodine and bismuth, are used to increase contrast in computer topography and can be attached to the linker of a MOF or encapsulated within the framework. These have shown slightly higher contrast than commercial CAs.[213] Optical imaging uses differential dye uptake to determine the nature of tissues. MOF materials which use dye components as linker molecules and those which can encapsulate fluorescent dyes for optical imaging have been reported to increase the contrast of these scans.[214] The dual-loading of drugs and imaging agents could have exciting potential in the area of theranostics, where the path of a drug through the body is monitored.[67, 151]

[ix] relaxivity, r_1, is used as a measure of how strong a contrast agent is, with stronger contrast reflected in higher relaxivity values.

1.9 References

1.   R. Wang, *Signal transduction and the gasotransmitters: NO, CO, and H₂S in biology and medicine,* Humana Press, Totowa, N.J., 2004.

2.   R. Wang, *FASEB J.*, 2002, **16**, 1792-1798.

3.   N. D. Mathew, D. I. Schlipalius and P. R. Ebert, *J. Toxicol.*, 2011, **2011**.

4.   X. B. Wang, H. F. Jin, C. S. Tang and J. B. Du, *Eur. J. Pharmacol.*, 2011, **670**, 1-6.

5.   M. Balazy, I. A. Abu-Yousef, D. N. Harpp and J. Park, *Biochem. Biophys. Res. Commun.*, 2003, **311**, 728-734.

6.   M. A. Gillman, *Lancet,* 1992, **339**, 307-307.

7.   *CRC Handbook of Chemistry and Physics*, CRC Press, Cleveland, Ohio, Editon edn., 1977, p. v.

8.   R. H. Crabtree, *The organometallic chemistry of the transition metals, 4th edn., John Wiley*, Hoboken, N.J., 2005.

9.   B. Thomas E, *Coord. Chem. Rev.*, 2006, **250**, 1196-1207.

10.   J. A. McCleverty, *Chemistry of the first-row transition metals*, Oxford University Press, Oxford ; New York, 1999.

11.   H. H. Jaffé and M. Orchin, *Tetrahedron,* 1960, **10**, 212-214.

12.   R. A. Dombkowski, M. J. Russell and K. R. Olson, *Am. J. Physiol.*, 2004, **286**, R678-R685.

13.   R. M. J. Palmer, A. G. Ferrige and S. Moncada, *Nature,* 1987, **327**, 524-526.

14.   L. J. Ignarro, G. M. Buga, K. S. Wood, R. E. Byrns and G. Chaudhuri, *Proc. Natl. Acad. Sci. U. S. A.*, 1987, **84**, 9265-9269.

15.   R. M. J. Palmer, D. S. Ashton and S. Moncada, *Nature*, 1988, **333**, 664-666.

16.   H. Y. Li and T. L. Poulos, *J. Inorg. Biochem.*, 2005, **99**, 293-305.

17.   C. N. Hall and J. Garthwaite, *Nitric Oxide*, 2009, **21**, 92-103.

18.   A. Butler and R. Nicholson, *Life, death, and nitric oxide,* RSC, Cambridge, UK, 2003.

19.   L. Y. Wu and R. Wang, *Pharmacological Reviews*, 2005, **57**, 585-630.

20.   T. Sjostrand, *Acta. Physiol. Scand.*, 1951, **22**, 137-141.

21.   T. Sjostrand, *Nature*, 1949, **164**, 580.

22.   R. Tenhunen, H. S. Marver and R. Schmid, *Proc. Natl. Acad. Sci. U. S. A.*, 1968, **61**, 748-755.

23.   M. D. Maines and A. Kappas, *Proc. Natl. Acad. Sci. U. S. A.*, 1974, **71**, 4293-4297.

24.   R. Tenhunen, H. S. Marver and R. Schmid, *J. Biol. Chem.*, 1969, **244**, 6388-6394.

25.   R. Motterlini, J. E. Clark, R. Foresti, P. Sarathchandra, B. E. Mann and C. J. Green, *Circ. Res.*, 2002, **90**, E17-E24.

26.   D. R. Von Burg, *J. Appl. Toxicol.*, 1999, **19**, 379-386.

27.   L. Li, A. Hsu and P. K. Moore, *Pharmacol. Ther.*, 2009, **123**, 386-400.

28.   S. Awata, K. Nakayama, I. Suzuki, K. Sugahara and H. Kodama, *Biochem. Mol. Biol. Int.,* 1995, **35**, 1331-1338.

29.   K. Abe and H. Kimura, *J. Neurosci.*, 1996, **16**, 1066-1071.

30.   L. Li, P. Rose and P. K. Moore, *Annu. Rev. Pharmacol. Toxicol.*, 2011, **51**, 169-187.

31.   T. Albert, *J. Chromatogr., B: Anal. Technol. Biomed. Life Sci.*, 2009, **877**, 3366-3377.

32.   J. Furne, A. Saeed and M. D. Levitt, *Am. J. Physiol.*, 2008, **295**, R1479-R1485.

33.   K. Sasakura, K. Hanaoka, N. Shibuya, Y. Mikami, Y. Kimura, T. Komatsu, T. Ueno, T. Terai, H. Kimura and T. Nagano, *J. Am. Chem. Soc.*, 2011, **133**, 18003-18005.

34.   C. Szabo, *Nat. Rev. Drug Discovery*, 2007, **6**, 917-935.

35.   R. O. Beauchamp, J. S. Bus, J. A. Popp, C. J. Boreiko and D. A. Andjelkovich, *Crc. Cr. Rev. Toxicol.*, 1984, **13**, 25-97.

36.   J. S. Beckman and W. H. Koppenol, *Am. J. Physiol. - Cell Physiol.,* 1996, **271**, C1424-C1437.

37.   G. L. Sternbach and J. Varon, *Resuscitation*, 2003, **58**, 127-130.

38.   R. J. Reiffenstein, W. C. Hulbert and S. H. Roth, *Annu. Rev. Pharmacol. Toxicol.*, 1992, **32**, 109-134.

39.   P. Nicholls and J. K. Kim, *Can. J. Biochem.*, 1982, **60**, 613-623.

40.   S. W. Ryter, J. Alam and A. M. Choi, *Physiol. Rev.*, 2006, **86**, 583-650.

41.   L. K. Keefer, *Nat. Mater.*, 2003, **2**, 357-358.

42.   J. Loscalzo and G. Welch, *Prog. Cardiovasc. Dis.*, 1995, **38**, 87-104.

43.   A. Pautz, J. Art, S. Hahn, S. Nowag, C. Voss and H. Kleinert, *Nitric Oxide-Biol. Ch.*, 2010, **23**, 75-93.

44.   L. Li, G. Rossoni, A. Sparatore, L. C. Lee, P. Del Soldato and P. K. Moore, *Free Radical Biol. Med.*, 2007, **42**, 706-719.

45.   J. L. Wallace, G. Caliendo, V. Santagada, G. Cirino and S. Fiorucci, *Gastroenterology*, 2007, **132**, 261-271.

46.   M. W. Radomski, R. M. J. Palmer and S. Moncada, *Trends Pharmacol. Sci.*, *1991*, **12**, 87-88.

47.   M. R. Schaffer, U. Tantry, S. S. Gross, H. L. Wasserkrug and A. Barbul, *J. Sur. Res.*, 1996, **63**, 237-240.

48.   A. Papapetropoulos, A. Pyriochou, Z. Altaany, G. D. Yang, A. Marazioti, Z. M. Zhou, M. G. Jeschke, L. K. Branski, D. N. Herndon, R. Wang and C. Szabo, *Proc. Natl. Acad. Sci. U. S. A.*, 2009, **106**, 21972-21977.

49.   J. L. Wallace, M. Dicay, W. McKnight and G. R. Martin, *FASEB J.,* 2007, **21**, 4070-4076.

50.   H. Jaeschke, *J. Hepatol.*, 1996, **25**, 774-780.

51.   P. A. Clavien, P. R. C. Harvey and S. M. Strasberg, *Transplantation*, 1992, **53**, 957-978.

52.   A. Nakao, A. M. K. Choi and N. Murase, *J. Cell. Mol. Med.*, 2006, **10**, 650-671.

53.   N. G. Abraham and A. Kappas, *Free Radical Biol. Med.*, 2005, **39**, 1-25.

54.   A. Nakao, L. E. Otterbein, M. Overhaus, J. K. Sarady, A. Tsung, K. Kimizuka, M. A. Nalesnik, T. Kaizu, T. Uchiyama, F. Liu, N. Murase, A. J. Bauer and F. H. Bach, *Gastroenterology*, 2004, **127**, 595-606.

55.   H. Luckraz, S. S. Tsui, J. Parameshwar, J. Wallwork and S. R. Large, *Annals of Thoracic Surgery*, 2001, **72**, 709-713.

56.   A. Nakao, K. Kimizuka, D. B. Stolz, J. S. Neto, T. Kaizu, A. M. Choi, T. Uchiyama, B. S. Zuckerbraun, A. J. Bauer, N. A. Nalesnik, L. E. Otterbein, D. A. Geller and N. Murase, *Surgery*, 2003, **134**, 285-292.

57.   A. Nakao, K. Kimizuka, D. B. Stolz, J. S. Neto, T. Kaizu, A. M. K. Choi, T. Uchiyama, B. S. Zuckerbraun, M. A. Nalesnik, L. E. Otterbein and N. Murase, *Am. J. Pathol.*, 2003, **163**, 1587-1598.

58. A. Nakao, H. Toyokawa, K. Kimizuka, T. Kiyomoto, R. J. Bailey, M. A. Nalesnik and N. Murase, *Am. J. Transplant.*, 2004, **4**, 461-461.

59. A. Nakao, H. Toyokawa, A. Tsung, M. A. Nalesnik, D. B. Stolz, J. Kohmoto, A. Ikeda, K. Tomiyama, T. Harada, T. Takahashi, R. Yang, M. P. Fink, K. Morita, A. M. K. Choi and N. Murase, *Am. J. Transplant.*, 2006, **6**, 2243-2255.

60. F. Wagner, P. Asfar, E. Calzia, P. Radermacher and C. Szabo, *Crit. Care*, 2009, **13**.

61. E. Lowicka and J. Beltowski, *Pharmacol. Rep.*, 2007, **59**, 4-24.

62. E. Blackstone, M. Morrison and M. B. Roth, *Science*, 2005, **308**, 518-518.

63. R. Dagani, *Chem. Eng. News*, 2005, **83**, 8-8.

64. P. Haouzi, V. Notet, B. Chenuel, B. Chalon, I. Sponne, V. Ogier and B. Bihain, *Resp. Physiol. Neurobi.*, 2008, **160**, 109-115.

65. P. Haouzi, H. Bell and M. Philmon, *Resp. Physiol. Neurobi.*, 2011, *177*, 273-283.

66. J. Li, G. Zhang, S. Cai and A. N. Redington, *Pediatric Critical Care Medicine*, 2008, **9**, 110-112.

67. P. Horcajada, R. Gref, T. Baati, P. K. Allan, G. Maurin, P. Couvreur, G. Férey, R. E. Morris and C. Serre, *Chem. Rev.*, 2012, **112**, 1232–1268.

68. N. N. Finer, P. C. Etches, B. Kamstra, A. J. Tierney, A. Peliowski and C. A. Ryan, *J. Pediatr.*, 1994, **124**, 302-308.

69. R. Motterlini and L. E. Otterbein, *Nat. Rev. Drug Discovery*, 2010, **9**, 728-U724.

70. Z. Q. Chen, J. Zhang and J. S. Stamler, *Proc. Natl. Acad. Sci. U. S. A.*, 2002, **99**, 8306-8311.

71. L. K. Keefer, *Chemtech,* 1998, **28**, 30-35.

72. M. Boolell, M. J. Allen, S. A. Ballard, S. Gepi-Attee, G. J. Muirhead, A. M. Naylor, I. H. Osterloh and C. Gingell, *Int. J. Impot. Res.*, 1996, **8**, 47-52.

73. R. Alberto and R. Motterlini, *Dalton Trans.*, 2007, **17**, 1651-1660.

74. E. Distrutti, L. Sediari, A. Mencarelli, B. Renga, S. Orlandi, G. Russo, G. Caliendo, V. Santagada, G. Cirino, J. L. Wallace and S. Fiorucci, *J. Pharmacol. Exp. Ther.*, 2006, **319**, 447-458.

75. L. Li, M. Whiteman, Y. Y. Guan, K. L. Neo, Y. Cheng, S. W. Lee, Y. Zhao, R. Baskar, C.-H. Tan and P. K. Moore, *Circulation,* 2008, **117**, 2351-2360.

76. G. A. Benavides, G. L. Squadrito, R. W. Mills, H. D. Patel, T. S. Isbell, R. P. Patel, V. M. Darley-Usmar, J. E. Doeller and D. W. Kraus, *Proc. Natl. Acad. Sci. U. S. A.*, 2007, **104**, 17977-17982.

77. Y. Zhao, H. Wang and M. Xian, *J. Am. Chem. Soc.*, 2010, **133**, 15-17.

78. M. Whiteman, L. Li, P. Rose, C. H. Tan, D. B. Parkinson and P. K. Moore, *Antioxid. Redox Signal.*, 2010, **12**, 1147-1154.

79. K. S. B. Masters, S. J. Leibovich, P. Belem, J. L. West and L. A. Poole-Warren, *Wound Repair Regen.*, 2002, *10*, 286-294.

80. H. Zhao, Y. Feng and J. Guo, *J. Appl. Polym. Sci.*, 2011, **122**, 1712-1721.

81. K. S. Bohl and J. L. West, *Biomaterials*, 2000, **21**, 2273-2278.

82. M. Kushwaha, J. M. Anderson, C. A. Bosworth, A. Andukuri, W. P. Minor, J. R. Lancaster Jr, P. G. Anderson, B. C. Brott and H.-W. Jun, *Biomaterials*, 2010, **31**, 1502-1508.

83. D. A. Riccio, K. P. Dobmeier, E. M. Hetrick, B. J. Privett, H. S. Paul and M. H. Schoenfisch, *Biomaterials*, 2009, **30**, 4494-4502.

84. Y. Kinoshita, I. Matsubara, T. Higuciu, and Y. Saito, *Bull. Chem. Soc. Japan.*, *1959*, **32**, 1221.

85. A. J. Fletcher, K. M. Thomas and M. J. Rosseinsky, *J. Solid State Chem.*, 2005, **178**, 2491-2510.

86. H. Furukawa, N. Ko, Y. B. Go, N. Aratani, S. B. Choi, E. Choi, A. Ö. Yazaydin, R. Q. Snurr, M. O'Keeffe, J. Kim and O. M. Yaghi, *Science*, 2010, **329**, 424-428.

87. M. Eddaoudi, D. B. Moler, H. L. Li, B. L. Chen, T. M. Reineke, M. O'Keeffe and O. M. Yaghi, *Acc. Chem. Res.*, 2001, **34**, 319-330.

88. P. A. Wright, *Microporous framework solids*, RSC Publishing, Cambridge, U.K., 2008.

89. M. Eddaoudi, J. Kim, N. Rosi, D. Vodak, J. Wachter, M. O'Keeffe and O. M. Yaghi, *Science*, 2002, **295**, 469-472.

90. N. L. Rosi, J. Eckert, M. Eddaoudi, D. T. Vodak, J. Kim, M. O'Keeffe and O. M. Yaghi, *Science*, 2003, **300**, 1127-1129.

91. S. S. Y. Chui, S. M. F. Lo, J. P. H. Charmant, A. G. Orpen and I. D. Williams, *Science*, 1999, **283**, 1148-1150.

92. P. J. Byrne, PhD Thesis, *St Andrews*, 2009.

93. M. Kramer, U. Schwarz and S. Kaskel, *Journal of Materials Chemistry*, 2006, **16**, 2245-2248.

94.   L. J., Murray, M. Dincǎ, J. Yano, S. Chavan, S Bordiga, C. M. Brown, J. R. Long, *J. Am. Chem. Soc.* **2010**, *132*, 7856-7857.

95.   S. M. Cohen, *Chem. Rev.*, 2011., **12**, 970–1000

96.   J.-R. Li, R. J. Kuppler and H.-C. Zhou, *Chem. Soc. Rev.*, 2009, **38**, 1477-1504.

97.   J.-R. Li, J. Sculley and H.-C. Zhou, *Chem. Rev.*, 2012 **112**, 869–932.

98.   J. Lee, O. K. Farha, J. Roberts, K. A. Scheidt, S. T. Nguyen and J. T. Hupp, *Chem. Soc. Rev.*, 2009, **38**, 1450-1459.

99.   M. Yoon, R. Srirambalaji and K. Kim, *Chem. Rev.*, 2012, **112**, 1196–1231

100. A. Corma, H. Garcia and F. X. Llabres i Xamena, *Chem. Rev.*, 2010, **110**, 4606-4655.

101. M. D. Allendorf, C. A. Bauer, R. K. Bhakta and R. J. T. Houk, *Chem. Soc. Rev.*, 2009, **38**, 1330-1352.

102. L. E. Kreno, K. Leong, O. K. Farha, M. Allendorf, R. P. Van Duyne and J. T. Hupp, *Chem. Rev.*, 2012, **112**, 1105–1125.

103. M. Kurmoo, *Chem. Soc. Rev.*, 2009, **38**, 1353-1379.

104. S. Ma and H. C. Zhou, *Chem. Commun.*, 2010, **46**, 44-53.

105. R. E. Morris and P. S. Wheatley, *Angew. Chem. Int. Ed.*, 2008, **47**, 4966-4981.

106. U. Mueller, M. Schubert, F. Teich, H. Puetter, K. Schierle-Arndt and J. Pastre, *J. Mater. Chem.*, 2006, **16**, 626-636.

107. P. K. Thallapally, K. A. Kirby and J. L. Atwood, *New J. Chem.*, 2007, **31**, 628-630.

108. M. P. Suh, H. J. Park, T. K. Prasad and D.-W. Lim, *Chem. Rev.*, 2012, **112**, 782–835.

109. Z. R. Herm, J. A. Swisher, B. Smit, R. Krishna and J. R. Long, *J. Am. Chem. Soc.*, 2011, **133**, 5664-5667.

110. K. Sumida, D. L. Rogow, J. A. Mason, T. M. McDonald, E. D. Bloch, Z. R. Herm, T.-H. Bae and J. R. Long, *Chem. Rev.*, 2012, **112**, 724–781.

111. F. o. Rouquerol, J. Rouquerol and K. S. W. Sing, *Adsorption by powders and porous solids : principles, methodology and applications*, Academic Press, San Diego, Calif.; London, 1999.

112. L. J. Murray, M. Dinca and J. R. Long, *Chem. Soc. Rev.*, 2009, **38**, 1294-1314.

113. M. Dinca and J. R. Long, *J. Am. Chem. Soc.*, 2007, **129**, 11172-11176.

114. W. Zhou, H. Wu and T. Yildirim, *J. Am. Chem. Soc.*, 2008, **130**, 15268-15269.

115. H. Wu, J. M. Simmons, Y. Liu, C. M. Brown, X. S. Wang, S. Ma, V. K. Peterson, P. D. Southon, C. J. Kepert, H. C. Zhou, T. Yildirim and W. Zhou, *Chemistry*, 2010, **16**, 5205-5214.

116. S. Ma, D. Sun, J. M. Simmons, C. D. Collier, D. Yuan and H.-C. Zhou, *J. Am. Chem. Soc.*, 2008, **130**, 1012-1016.

117. C. Serre, C. Mellot-Draznieks, S. Surble, N. Audebrand, Y. Filinchuk and G. Ferey, *Science*, 2007, **315**, 1828-1831.

118. D. Tanaka, K. Nakagawa, M. Higuchi, S. Horike, Y. Kubota, Tatsuo C. Kobayashi, M. Takata and S. Kitagawa, *Angew. Chem. Int. Ed.*, 2008, **47**, 3914-3918.

119. T. Fukushima, S. Horike, Y. Inubushi, K. Nakagawa, Y. Kubota, M. Takata and S. Kitagawa, *Angew. Chem. Int. Ed.*, 2010, **49**, 4820-4824.

120. S. Horike, Y. Inubushi, T. Hori, T. Fukushima and S. Kitagawa, *Chem. Sci.*, 2012, *3*.

121. Y. Cheng, H. Kajiro, H. Noguchi, A. Kondo, T. Ohba, Y. Hattori, K. Kaneko and H. Kanoh, *Langmuir*, 2011, **27**, 6905-6909.

122. S. Uchida, R. Kawamoto, H. Tagami, Y. Nakagawa and N. Mizuno, *J. Am. Chem. Soc.*, 2008, **130**, 12370-12376.

123. F. Bonino, S. Chavan, J. G. Vitillo, E. Groppo, G. Agostini, C. Lamberti, P. D. C. Dietzel, C. Prestipino and S. Bordiga, *Chem. Mater.*, 2008, **20**, 4957-4968.

124. S. Bordiga, L. Regli, F. Bonino, E. Groppo, C. Lamberti, B. Xiao, P. S. Wheatley, R. E. Morris and A. Zecchina, *Phys. Chem. Chem. Phys*, 2007, **9**, 2676-2685.

125. S. Chavan, J. G. Vitillo, E. Groppo, F. Bonino, C. Lamberti, P. D. C. Dietzel and S. Bordiga, *J. Phys. Chem. C*, 2009, **113**, 3292-3299.

126. P. D. C. Dietzel, R. E. Johnsen, H. Fjellvag, S. Bordiga, E. Groppo, S. Chavan and R. Blom, *Chem. Comm.*, 2008, **41**, 5125-5127.

127. C. Prestipino, L. Regli, J. G. Vitillo, F. Bonino, A. Damin, C. Lamberti, A. Zecchina, P. L. Solari, K. O. Kongshaug and S. Bordiga, *Chem. Mater.*, 2006, **18**, 1337-1346.

128. K. Sumida, C. M. Brown, Z. R. Herm, S. Chavan, S. Bordiga and J. R. Long, *Chem. Comm*, 2011, **47**, 1157-1159.

129. L. Valenzano, B. Civalleri, S. Chavan, G. T. Palomino, C. O. Areán and S. Bordiga, *J. Phys. Chem. C.*, 2010, **114**, 11185-11191.

130. E. C. Spencer, J. A. K. Howard, G. J. McIntyre, J. L. C. Rowsell and O. M. Yaghi, *Chem. Comm*, 2006, 278-280.

131. C. M. Brown, Y. Liu, T. Yildirim, V. K. Peterson and C. J. Kepert, *Nanotechnology*, 2009, **20**, 204025.

132. H. Wu, W. Zhou and T. Yildirim, *J. Am. Chem. Soc.*, 2009, **131**, 4995-5000.

133. T. Yildirim and M. R. Hartman, *Phys. Rev. Lett.*, 2005, **95**.

134. V. K. Peterson, Y. Liu, C. M. Brown and C. J. Kepert, *J. Am. Chem. Soc.*, 2006, **128**, 15578-15579.

135. R. Vaidhyanathan, S. S. Iremonger, G. K. H. Shimizu, P. G. Boyd, S. Alavi and T. K. Woo, *Science*, 2010, **330**, 650-653.

136. J. L. Rowsell, E. C. Spencer, J. Eckert, J. A. Howard and O. M. Yaghi, *Science*, 2005, **309**, 1350-1354.

137. E. C. Spencer, J. A. Howard, G. J. McIntyre, J. L. Rowsell and O. M. Yaghi, *Chem. Comm*, 2006, 278-280.

138. J. Getzschmann, I. Senkovska, D. Wallacher, M. Tovar, D. Fairen-Jimenez, T. Duren, J. M. van Baten, R. Krishna and S. Kaskel, *Microporous Mesoporous Mater.*, 2010, **136**, 50-58.

139. S. R. Caskey, A. G. Wong-Foy and A. J. Matzger, *J. Am. Chem. Soc.*, 2008, **130**, 10870-10871.

140. P. D. C. Dietzel, P. A. Georgiev, J. Eckert, R. Blom, T. Strassle and T. Unruh, *Chem. Comm*, 2010, **46**, 4962-4964.

141. A. Rivera and T. Farías, *Microporous Mesoporous Mater.*, 2005, **80**, 337-346.

142. M. Vallet-Regi, A. Rámila, R. P. del Real and J. Pérez-Pariente, *Chem. Mater.*, 2000, **13**, 308-311.

143. P. Horcajada, C. Serre, M. Vallet-Regí, M. Sebban, F. Taulelle and G. Férey, *Angew. Chem. Int. Ed.*, 2006, **118**, 6120-6124.

144. A. C. McKinlay, R. E. Morris, P. Horcajada, G. Ferey, R. Gref, P. Couvreur and C. Serre, *Angew. Chem. Int. Ed.,* 2010, **49**, 6260-6266.

145. P. Horcajada, C. Serre, G. Maurin, N. A. Ramsahye, F. Balas, M. Vallet-Regi, M. Sebban, F. Taulelle and G. Ferey, *J. Am. Chem. Soc.*, 2008, **130**, 6774-6780.

146. P. Horcajada, C. Serre, G. Maurin, N. A. Ramsahye, F. Balas, M. a. Vallet-Regí, M. Sebban, F. Taulelle and G. R. Férey, *J. Am. Chem. Soc.*, 2008, **130**, 6774-6780.

147. J. An, S. J. Geib and N. L. Rosi, *J. Am. Chem. Soc.*, 2009, **131**, 8376-8377.

148. F. Ke, Y.-P. Yuan, L.-G. Qiu, Y.-H. Shen, A.-J. Xie, J.-F. Zhu, X.-Y. Tian and L.-D. Zhang, *J. Mat. Chem.*, 2011, **21**, 3843-3848.

149. P. Horcajada, T. Chalati, C. Serre, B. Gillet, C. Sebrie, T. Baati, J. F. Eubank, D. Heurtaux, P. Clayette, C. Kreuz, J.-S. Chang, Y. K. Hwang, V. Marsaud, P.-N. Bories, L. Cynober, S. Gil, G. Ferey, P. Couvreur and R. Gref, *Nat. Mater.*, 2010, **9**, 172-178.

150. P. Horcajada, C. Serre, M. Vallet-Regi, M. Sebban, F. Taulelle and G. Ferey, *Angew. Chem. Int. Ed.*, 2006, **45**, 5974-5978.

151. K. M. L. Taylor-Pashow, J. D. Rocca, Z. Xie, S. Tran and W. Lin, *J. Am. Chem. Soc.*, 2009, **131**, 14261-14263.

152. W. V. Cruz, P. C. W. Leung and K. Seff, *Inorg. Chem.*, 1979, **18**, 1692-1696.

153. G. H. Jeong, Y. Kim and K. Seff, *Microporous Mesoporous Mater.*, 2006, **93**, 12-22.

154. Y. M. Lee, Y. Kim and K. Seff, *J. Phys. Chem. B*, 2005, **109**, 4900-4908.

155. P. S. Wheatley, A. R. Butler, M. S. Crane, S. Fox, B. Xiao, A. G. Rossi, I. L. Megson and R. E. Morris, *J. Am. Chem. Soc.*, 2006, **128**, 502-509.

156. P. S. Wheatley, A. C. McKinlay and R. E. Morris, in *Studies in Surface Science and Catalysis,* eds. P. M. Antoine Gédéon and B. Florence, Elsevier, Editon edn., 2008, vol. Volume 174, Part A, pp. 441-446.

157. P. S. Wheatley, A. R. Butler, M. S. Crane, S. Fox, B. Xiao, A. G. Rossi, I. L. Megson and R. E. Morris, *J. Am. Chem. Soc.*, 2006, **128**, 502-509.

158. A. C. McKinlay, PhD Thesis, *University of St Andrews*, 2010.

159. B. Xiao, P. S. Wheatley, X. B. Zhao, A. J. Fletcher, S. Fox, A. G. Rossi, I. L. Megson, S. Bordiga, L. Regli, K. M. Thomas and R. E. Morris, *J. Am. Chem. Soc.*, 2007, **129**, 1203-1209.

160. M. J. Ingleson, R. Heck, J. A. Gould and M. J. Rosseinsky, *Inorg. Chem.*, 2009, **48**, 9986-9988.

161. J. G. Nguyen, K. K. Tanabe and S. M. Cohen, *Crystengcomm*, 2010, **12**, 2335-2338.

162. S. Shimomura, M. Higuchi, R. Matsuda, K. Yoneda, Y. Hijikata, Y. Kubota, Y. Mita, J. Kim, M. Takata and S. Kitagawa, *Nat. Chem.*, 2010, **2**, 633-637.

163. A. C. McKinlay, B. Xiao, D. S. Wragg, P. S. Wheatley, I. L. Megson and R. E. Morris, *J. Am. Chem. Soc.*, 2008, **130**, 10440-10444.

164. J. L. Harding and M. M. Reynolds, *J. Am. Chem. Soc.*, 2012.

165.   P. E. Riley and K. Seff, *Inorg. Chem.*, 1974, **13**, 1355-1360.

166.   R.-Q. Zou, H. Sakurai and Q. Xu, *Angew. Chem. Int. Ed.*, 2006, **45**, 2542-2546.

167.   R.-Q. Zou, H. Sakurai, S. Han, R.-Q. Zhong and Q. Xu, *J. Am. Chem. Soc.*, 2007, **129**, 8402-8403.

168.   Y. Zhao, M. Padmanabhan, Q. Gong, N. Tsumori, Q. Xu and J. Li, *Chem. Comm*, 2011, **47**, 6377-6379.

169.   H.-L. Jiang, B. Liu, T. Akita, M. Haruta, H. Sakurai and Q. Xu, *J. Am. Chem. Soc.*, 2009, **131**, 11302-11303.

170.   W. Wang, Y. Li, R. Zhang, D. He, H. Liu and S. Liao, *Catal. Commun.*, 2011, **12**, 875-879.

171.   S. Ma, X.-S. Wang, C. D. Collier, E. S. Manis and H.-C. Zhou, *Inorg. Chem.*, 2007, **46**, 8499-8501.

172.   M. Dincǎ and J. R. Long, *J. Am. Chem. Soc.*, 2005, **127**, 9376-9377.

173.   D. Britt, D. Tranchemontagne and O. M. Yaghi, *Proc. Natl. Acad. Sci. U. S. A.*, 2008, **105**, 11623-11627.

174.   H. Leclerc, A. Vimont, J.-C. Lavalley, M. Daturi, A. D. Wiersum, P. L. Llwellyn, P. Horcajada, G. Ferey and C. Serre, *Phys. Chem. Chem. Phys.*, 2011, **13**, 11748-11756.

175.   J. R. Karra and K. S. Walton, *Langmuir*, 2008, **24**, 8620-8626.

176.   L. Alaerts, E. Seguin, H. Poelman, F. Thibault-Starzyk, P. A. Jacobs and D. E. De Vos, *Chem.--Eur. J.*, 2006, **12**, 7353-7363.

177.   N. Drenchev, E. Ivanova, M. Mihaylov and K. Hadjiivanov, *Phys. Chem. Chem. Phys.* 2010, **12**, 6423-6427.

178.   L. Valenzano, J. G. Vitillo, S. Chavan, B. Civalleri, F. Bonino, S. Bordiga and C. Lamberti, *Catal. Today.*, 2012, **182**, 67–79

179.   L. Valenzano, B. Civalleri, K. Sillar and J. Sauer, *J. Phys. Chem. C.*, 2011, **115**, 21777-21784.

180.   S. S. Kaye and J. R. Long, *J. Am. Chem. Soc.*, 2008, **130**, 806–807

181.   L. Hamon, C. Serre, T. Devic, T. Loiseau, F. Millange, G. Ferey and G. De Weireld, *J. Am. Chem. Soc.*, 2009, **131**, 8775.

182.   C. Petit, B. Mendoza and T. J. Bandosz, *ChemPhysChem*, 2010, **11**, 3678-3684.

183.   D. J. Good and N. R. Rodríguez-Hornedo, *Cryst. Growth Des.*, 2009, **9**, 2252-2264.

184.   Y. Xie, H.-H. Wu, G.-P. Yong and Z.-Y. Wang, *Acta Crystallogr., Sect. E: Struct. Rep. Online*, 2006, **62**, m2089-m2090.

185.   Y. Xie, Y. Yan, H.-H. Wu, G.-P. Yong, Y. Cui, Z.-Y. Wang, L. Pan, J. Li, R. Fan, R.-P. Li, Y.-C. Tian, G.-Q. Pan, L.-S. Sheng and X. Li, *Inorg. Chim. Acta*, 2007, **360**, 1669-1677.

186.   Y. Xie, Z. Yu, X. Huang, Z. Wang, L. Niu, M. Teng and J. Li, *Chem.--Eur. J.*, 2007, **13**, 9399-9405.

187.   E. V. Anokhina, Y. B. Go, Y. Lee, T. Vogt and A. J. Jacobson, *J. Am. Chem. Soc.*, 2006, **128**, 9957-9962.

188.   R. Vaidhyanathan, D. Bradshaw, J.-N. Rebilly, J. P. Barrio, J. A. Gould, N. G. Berry and M. J. Rosseinsky, *Angew. Chem. Int. Ed.*, 2006, **45**, 6495-6499.

189.   M. J. Ingleson, J. Bacsa and M. J. Rosseinsky, *Chem. Comm*, 2007, 3036-3038.

190.   J. P. García-Terán, O. Castillo, A. Luque, U. García-Couceiro, P. Román and L. Lezama, *Inorg. Chem.*, 2004, **43**, 4549-4551.

191.   J. Rabone, Y.-F. Yue, S. Y. Chong, K. C. Stylianou, J. Bacsa, D. Bradshaw, G. R. Darling, N. G. Berry, Y. Z. Khimyak, A. Y. Ganin, P. Wiper, J. B. Claridge and M. J. Rosseinsky, *Science*, 2010, **329**, 1053-1057.

192.   P. A. Wright, *Science*, 2010, **329**, 1025-1026.

193.   A. Comotti, S. Bracco, G. Distefano and P. Sozzani, *Chem. Comm*, 2009, 284-286.

194.   D. V. Soldatov, I. L. Moudrakovski and J. A. Ripmeester, *Angew. Chem. Int. Ed.*, 2004, **43**, 6308-6311.

195.   A. Mantion, L. Massüger, P. Rabu, C. Palivan, L. B. McCusker and A. Taubert, *J. Am. Chem. Soc.*, 2008, **130**, 2517-2526.

196.   R. A. Smaldone, R. S. Forgan, H. Furukawa, J. J. Gassensmith, A. M. Z. Slawin, O. M. Yaghi and J. F. Stoddart, *Angew. Chem. Int. Ed.*, 2010, **49**, 8630-8634.

197.   J. Y. Lu and A. M. Babb, *Inorg. Chem. Commun.*, 2001, **4**, 716-718.

198.   Y.-S. Song, B. Yan and Z.-X. Chen, *J. Solid State Chem.*, 2006, **179**, 4037-4046.

199.   S. R. Miller, D. Heurtaux, T. Baati, P. Horcajada, J.-M. Greneche and C. Serre, *Chem. Comm*, 2010, **46**, 4526-4528.

200.   S. R. Miller, P. Horcajada and C. Serre, *CrystEngComm*, 2011, **13**, 1894-1898.

201.   R. C. Huxford, K. E. deKrafft, W. S. Boyle, D. Liu and W. Lin, *Chem. Sci.*, 2012, **3**, 198-204.

202. S. R. Halper, L. Do, J. R. Stork and S. M. Cohen, *J. Am. Chem. Soc.,* 2006, **128**, 15255-15268.

203. J.-P. Zou, Q. Peng, Z. Wen, G.-S. Zeng, Q.-J. Xing and G.-C. Guo, *Cryst. Growth Des.*, 2010, **10**, 2613-2619.

204. M.-S. Wang, S.-P. Guo, Y. Li, L.-Z. Cai, J.-P. Zou, G. Xu, W.-W. Zhou, F.-K. Zheng and G.-C. Guo, *J. Am. Chem. Soc.*, 2009, **131**, 13572-13573.

205. R. Singleton, J. Bye, J. Dyson, G. Baker, R. M. Ranson and G. B. Hix, *Dalton Trans.*, 2010, **39**, 6024-6030.

206. M. Berchel, T. L. Gall, C. Denis, S. L. Hir, F. Quentel, C. Elleouet, T. Montier, J.-M. Rueff, J.-Y. Salaun, J.-P. Haelters, G. B. Hix, P. Lehn and P.-A. Jaffres, *New J. Chem.*, 2011, **35**, 1000-1003.

207. J. Della Rocca, D. Liu and W. Lin, *Acc. Chem. Res.*, 2011, **44**, 957-968.

208. J. Della Rocca and W. Lin, *Eur. J. Inorg. Chem.*, 2010, **2010**, 3725-3734.

209. W. J. Rieter, K. M. L. Taylor, H. An, W. Lin and W. Lin, *J. Am. Chem. Soc.*, 2006, **128**, 9024-9025.

210. M. D. Rowe, D. H. Thamm, S. L. Kraft and S. G. Boyes, *Biomacromolecules*, 2009, **10**, 983-993.

211. W. J. Rieter, K. M. L. Taylor and W. Lin, *J. Am. Chem. Soc.*, 2007, **129**, 9852-9853.

212. K. M. L. Taylor, W. J. Rieter and W. B. Lin, *J. Am. Chem. Soc.*, 2008, **130**, 14358.

213. K. E. deKrafft, Z. Xie, G. Cao, S. Tran, L. Ma, Otto Z. Zhou and W. Lin, *Angew. Chem. Int. Ed.*, 2009, **48**, 9901-9904.

214. R. Nishiyabu, N. Hashimoto, T. Cho, K. Watanabe, T. Yasunaga, A. Endo, K. Kaneko, T. Niidome, M. Murata, C. Adachi, Y. Katayama, M. Hashizume and N. Kimizuka, *J. Am. Chem. Soc.*, 2009, **131**, 2151-2158.

2 Aims

Chapter 1 outlined the potential of nitric oxide, carbon monoxide and hydrogen sulfide as therapeutics, and how metal-organic frameworks represent a potential delivery method. The storage and delivery of nitric oxide from some MOFs has been well characterised, but whether suitable amounts of hydrogen sulfide and carbon monoxide can be released from MOFs is currently unknown. In order for these materials to be used for the storage and delivery of these gases, more needs to be known about the physical properties of the framework materials; how much of each gas each material can store; whether all of the stored gas can be delivered, and at what rate; and whether the frameworks degrade over storage periods. Ideally, these questions should be answered with reference to the structural properties of the material and how gases interact with the structure. Therefore, the main objective of this thesis is to gain a greater understanding of the way in which nitric oxide, carbon monoxide and hydrogen sulfide interact with metal-organic frameworks in order to assess their potential as gas storage and release media.

Gas adsorption and release measurements for materials with the potential for the storage of these gases will be correlated with crystallographic analysis; both Bragg techniques (single-crystal X-ray diffraction and Rietveld analysis of powder X-ray diffraction data) and total-scattering methods (X-ray pair distribution functions), to obtain information about where in the structure gases bind and how the structure of a material influences its interaction with gases. *In situ* gas-loading crystallographic experiments will be used to link these two analyses and observe framework material throughout the activation, gas adsorption and release processes. This thesis also aims to develop methods to study gas adsorption in these materials; some development of an environmental gas cell for *in situ* crystallographic studies will be undertaken, and the potential of total-scattering methods for studying a number of metal-organic framework transitions and gas adsorption will be analysed.

3 Experimental Methods

3.1 Solvothermal Synthesis[1]

Solvothermal synthesis is a method of producing solid, often crystalline, materials through carrying out reactions in solvents heated above their normal boiling point by containing the material in a vessel which can withstand high pressure. The decreased viscosity of the solvent at these temperatures promotes diffusion, meaning that a large range of materials can be synthesised which are not able to be synthesised in normal conditions. A pre-weighed amount of reactant is dissolved in a solvent and placed in a Telfon-lined autoclave (Figure 3-1). This is encased in a steel-bomb and heated to the desired temperature for a period of hours or days. Solvothermal synthesis has become a common method of synthesising porous materials.

Figure 3-1 Teflon-lined autoclaves used for solvothermal synthesis. Left: steel-bomb with lid. Middle: steel autoclave unit. Right: Teflon liner.

3.2 The crystalline state[2-4]

A crystal is made up of a very large number of molecules arranged in an ordered array which is repeated in all directions. The complete structure of a crystal can be stated by describing the contents of the repeating unit (the unit cell) and the way in which it is repeated by translational symmetry (described by the lattice). The lattice is an array of symmetry-equivalent points, called lattice points which are related by translational symmetry. A parallelepiped can be chosen with lattice points at each corner. This is called the unit cell and is the smallest repeat unit within the crystal which contains all symmetry elements of the structure. The unit cell is defined by six lattice parameters; three non-coplanar axes, a, b, c, corresponding to the vectors between lattice points, and three interstitial angles, α, β, γ, where α is the angle between the b- and c-axes (Figure 3-2). The lattice parameters can take any values, but if there are additional symmetry elements present in the structure (see below) restrictions are imposed on these parameters. Unit cell symmetry is broadly divided into seven crystal systems (Table 1).

A primitive unit cell has lattice points at each corner of the cell, which is equivalent to having one lattice point per cell. For some systems which possess more symmetry elements it is often more convenient to understand the structure by defining a unit cell with more than one lattice point per cell. This is called lattice centring. Possible centrings are shown in Figure 3-3. Combination of the lattice centring with the constraints on the unit cell expands the seven crystal systems into fourteen unique Bravais lattice types.

3.2.1 Point and space symmetry:

The unit cell can contain additional symmetry elements. These can be divided into symmetry elements which act through a point (point symmetry) – reflection and rotation - and those which involve point symmetry with additional translation (space symmetry) – glide planes and screw axes. All point symmetry can be divided into proper and improper rotations. Proper rotations involve rotation by a fraction of 360° around an axis and retain the handedness of the molecule. Improper rotations involve rotation by a fraction of 360° around an axis with a simultaneous inversion in a plane perpendicular to rotation axis, and subsequently change the handedness of the molecule. The asymmetric unit is the unique part of the unit cell, no part of which can regenerated by application of symmetry elements to another part.
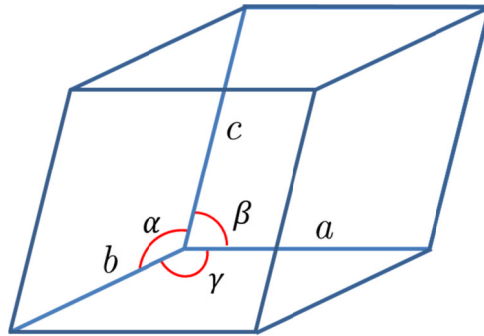
Figure 3-2 A unit cell.
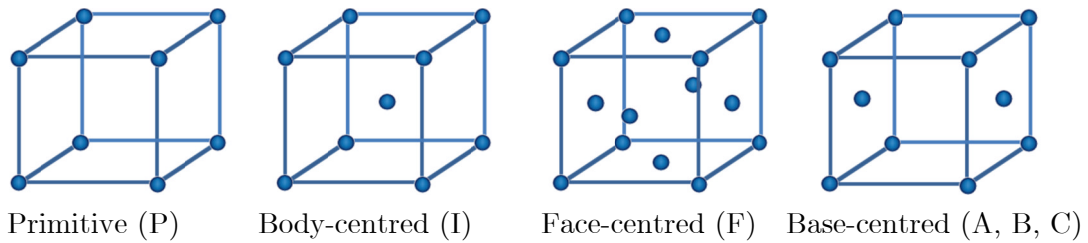

Primitive (P)   Body-centred (I)   Face-centred (F)   Base-centred (A, B, C)

Figure 3-3: Types of lattice centring.
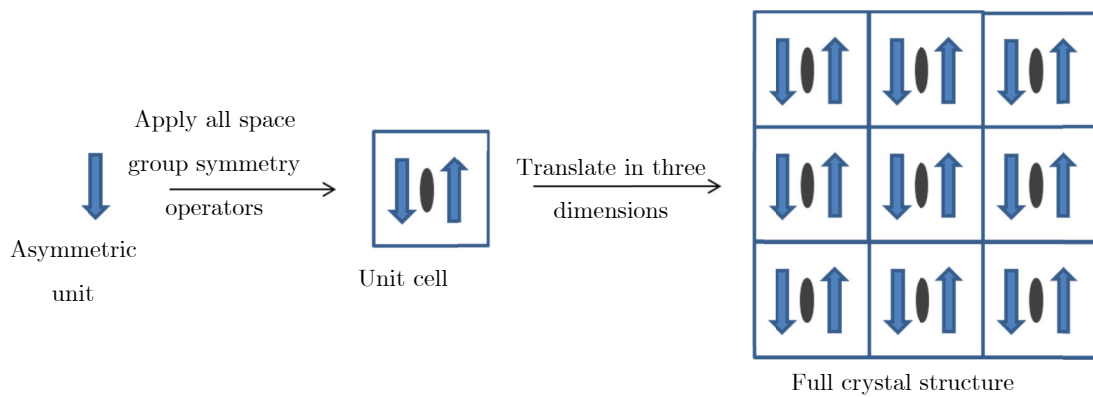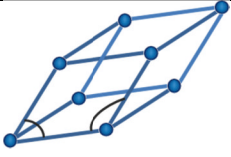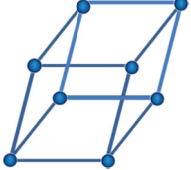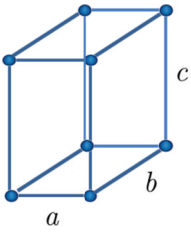
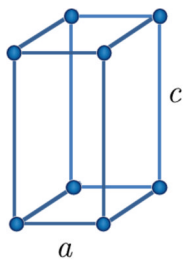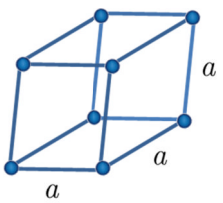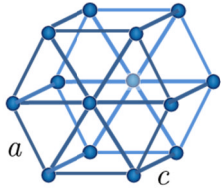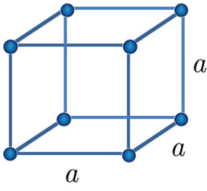**Figure 3-4: A full description of all atom positions in a crystal can be gained by first taking the atomic positions for the asymmetric unit, applying all symmetry elements to generate the atomic positions for the unit cell and then translating unit cells in three dimensions.**

Table 1: The seven crystal systems with essential symmetry and unit cell restrictions.

Crystal System	Essential Symmetry	Restrictions on unit cell	
Triclinic	None	None	
Monoclinic	One two-fold rotation and/or mirror plane	$\alpha = \gamma = 90°$	
Orthorhombic	Three two-fold rotations and/or mirror planes	$\alpha = \beta = \gamma = 90°$	
Tetragonal	One four-fold rotation	$a = b; \alpha = \beta = \gamma = 90°$	
Trigonal	One three-fold rotation	$a = b = c;$ $\alpha = \beta = \gamma \, (\neq 90°)$	
Hexagonal	One six-fold rotation	$a = b;$ $\alpha = \beta = 90°; \gamma = 120°$	
Cubic	Four three-fold rotation axes	$a = b = c; \alpha = \beta = \gamma$	

A complete assembly of all combinations of symmetry elements passing through a central point is given by a point group. There are 32 possible point groups for crystal symmetry, generated using the seven crystal systems with their possible point symmetries. In the solid state, not all symmetry elements pass through a single point. Instead they are arranged in space around the translational symmetry of the lattice. There are 230 possible arrangements for symmetry elements in the solid state called space groups. A crystal space group will give a full description of all symmetry elements in the crystal and, when combined with the atomic positions of the asymmetric unit, can generate atomic positions for every atom in the unit cell. When combined with translational symmetry this produces the full crystal structure (Figure 3-4).[5]

3.3 X-ray diffraction[2, 6, 7]

X-rays are electromagnetic waves which consist of electric and magnetic fields which vary sinusoidally with time in directions orthogonal to both each other and to the direction of their propagation. The wavelengths generally used for diffraction experiments vary between 0.4 and 2 Å (Figure 3-5).

X-rays have a refractive index very close to unity in most cases, meaning that they cannot be focused using lenses in the ways that visible light or electrons can. There is, therefore, no equivalent to the electron microscope for X-rays. However, when X-rays interact with matter they can be either scattered (diffracted) or absorbed. X-ray diffraction experiments measure the intensity of the X-rays scattered by electrons bound to atoms in an object. The waves which are emitted from the object by diffraction of an X-ray beam can undergo interference. Interference can be constructive (wave planes add up to give a higher intensity) or destructive (waves cancel out) depending on the phase relationship between the waves. Waves scattered by atoms at different positions will arrive at the detector with a different phase shift. The interference between waves can yield information about these relative atomic positions.
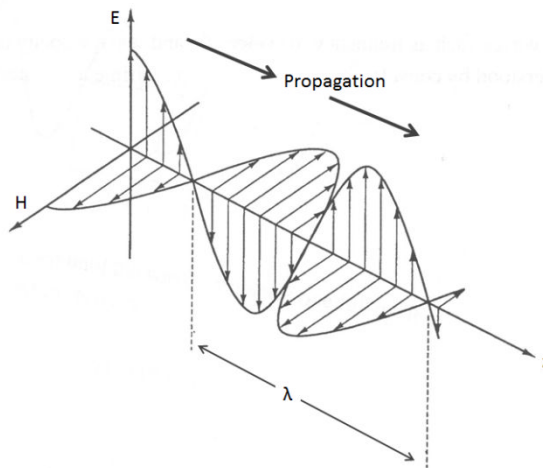
Figure 3-5: Schematic of an electromagnetic wave. E represents the electric field, H represents the magnetic field and λ depicts the wavelength of the radiation.

3.3.1 Diffraction from atoms and arrangements of atoms

The scattering amplitude of diffraction from a general object can be described by the equation:

$$F(\boldsymbol{S}) = A_0 \int \rho(\boldsymbol{r})\exp(2\pi i \boldsymbol{r} \cdot \boldsymbol{S})dV_r \qquad (3.1)$$

where $\boldsymbol{r}$ is the vector between two point scatterers, A_0 is maximum amplitude of the wave and $\rho(\boldsymbol{r})$ is the number of electrons in the volume dV_r. $\boldsymbol{S}$ is the scattering vector, defined as $\frac{1}{\lambda}(\boldsymbol{s} - \boldsymbol{s_0})$.[i] The angle between $\boldsymbol{s}$ and $\boldsymbol{s_0}$ is 2θ, making the value of the magnitude of $S = |\boldsymbol{S}| = 2\sin\theta/\lambda$. Equation 3.1 is in the form of a mathematical operation, where the scattering amplitude from a material is the Fourier transform of the electron density. The theory of Fourier transforms means that the electron density from a sample can be calculated from the inverse Fourier transform of the amplitude of the scattered wave:

$$\rho(\boldsymbol{r}) = FT[F(\boldsymbol{S})]^{-1} = \int_V F(\boldsymbol{S})\exp(2\pi i \, \boldsymbol{r} \cdot \boldsymbol{S})dV_r \qquad (3.2)$$

---

[i] Chemists tend to use S to denote the scattering vector, whilst other branches of science, such as physics (including the Total Scattering community) use Q.

For an arrangement of atoms the overall structure factor can be calculated by summing over all N atoms in the sample:

$$F(\boldsymbol{S}) = \sum_{j=1}^{N} f_j(S)\exp(2\pi i \boldsymbol{r_j} \cdot \boldsymbol{S})$$

(3.3)

where $f_j(S)$ is the atomic scattering factor for the jth atom in the structure and $\boldsymbol{r_j}$ is the position vector for the jth atom relative to a fixed origin. The electron density of a material can be calculated by doing the Fourier transform of the equation above. Therefore, if we know the form of the scattering factor then we should be able to work out the electron density, and therefore the structure of the material. However, when the scattering is measured the intensity of the X-rays reaching the detector at a given time is proportional to $F(\boldsymbol{S})F^*(\boldsymbol{S})$, and we can only measure the modulus – the amplitude but no phases. These missing phases make it impossible to carry out the Fourier transform in Equation 3.3 directly, and this is known as the "phase problem". In order to solve the crystal structure a method of solving the phase problem must be found. Two common ways in which this is done are outlined in section 3.1.3.

3.3.2   Diffraction from crystalline materials

In a crystal, atoms diffract incoming radiation. As shown in Figure 3-7, a row of regularly spaced atoms separated by distance, a, scatter incoming radiation with wavelength, λ. The scattered waves can interact with each other, causing interference. In order for constructive interference between the beams to occur, the path difference between them must be an integer number of wavelengths:

$$\text{Path difference} = a \cos \alpha - a \cos \alpha_0 = h\lambda \qquad (3.4)$$

where α and α_0 are the angles of the scattered and incoming radiation respectively and h is an integer. In vector notation:

$$\boldsymbol{a} \cdot \boldsymbol{s} - \boldsymbol{a} \cdot \boldsymbol{s_0} = h\lambda \qquad (3.5)$$

$$\boldsymbol{a} \cdot \frac{(\boldsymbol{s} - \boldsymbol{s_0})}{\lambda} = \boldsymbol{a} \cdot \boldsymbol{S} = h \qquad (3.6)$$

For a three dimensional solid there are three equations which outline the diffraction conditions, called the Laue equations:

$$\boldsymbol{a} \cdot \boldsymbol{S} = h, \boldsymbol{b} \cdot \boldsymbol{S} = k, \boldsymbol{c} \cdot \boldsymbol{S} = l \qquad (3.7)$$

where h, k and l are all integers. For a large number of scatterers, such as in a crystal, destructive interference means that the diffracted intensity is essentially zero in directions other than where the conditions in equation 3.7 are met. Therefore, in a three dimensional solid, all three of the Laue equations must be satisfied simultaneously in order for diffraction to occur and this restricts the scattering vector, $\boldsymbol{S}$, to be of the form:

$$\boldsymbol{S} = h\boldsymbol{a}^* + k\boldsymbol{b}^* + l\boldsymbol{c}^* \qquad (3.8)$$

where $\boldsymbol{a}^* \cdot \boldsymbol{a} = 1$ and $\boldsymbol{a}^* \cdot \boldsymbol{b} = 0$. The effect of this is that the possible values for $\boldsymbol{S}$ form a reciprocal lattice.
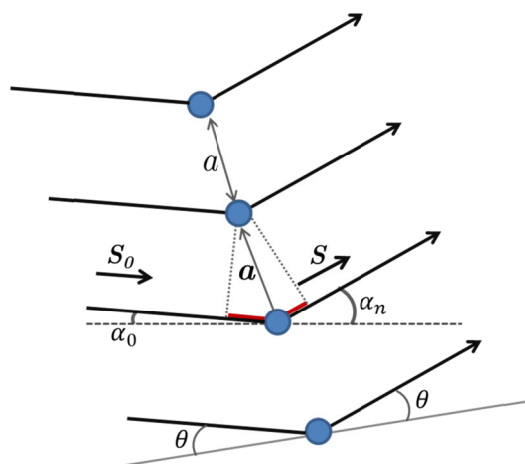

Figure 3-6 Scattering from a row of atoms.

In a three dimensional crystal, the repeat arrangement of atoms in the unit cell can constrain the value of the vector $\boldsymbol{r_j}$ to being of the form:

$$\boldsymbol{r_j} = x_j\boldsymbol{a} + y_j\boldsymbol{b} + z_j\boldsymbol{c} \qquad (3.9)$$

where $\boldsymbol{a}$, $\boldsymbol{b}$ and $\boldsymbol{c}$ are unit cell vectors, and x_j, y_j and z_j are the fractional atomic coordinates of each atom in the unit cell.

Now, both $\boldsymbol{r_j}$ and $\boldsymbol{S}$ are constrained to integer values, so equation 3.3 becomes:

$$
\begin{aligned}
F(\boldsymbol{S}) &= \sum_{j=1}^{N} f_j(S)\exp\left(2\pi i \boldsymbol{r_j} \cdot \boldsymbol{S}\right) \\
&= \sum_{j=1}^{N} f_j(S)\exp\left(2\pi i (x_j \boldsymbol{a} + y_j \boldsymbol{b} + z_j \boldsymbol{c}) \cdot (h\boldsymbol{a}^* + k\boldsymbol{b}^* + l\boldsymbol{c}^*)\right) \\
&= \sum_{j=1}^{N} f_j(S)\exp\left(2\pi i (hx_j + ky_j + lz_j)\right) = F(hkl)
\end{aligned}
$$

$$(3.10)$$

When W. L. Bragg considered diffraction in 1912 he described the change in direction of the scattered wave geometrically as though it were a reflection from sets of parallel planes in the crystal (Figure 3-7). Here, the path difference which must be an integer number of wavelengths is given again by $AO + OB = d_{hkl}sin\theta + d_{hkl}sin\theta$, which gives Bragg's Law:

$$2d_{hkl}sin\theta = n\lambda \qquad\qquad (3.11)$$

The planes from which these reflections can occur are described by Miller planes. Each Miller plane has three values, h, k and l, describing its orientation within the unit cell (Figure 3-8). The distance between each plane is given by the magnitude of the scattering vector, d_{hkl}, where $|d_{hkl}| = \sqrt{\left(\frac{h}{a}\right)^2 + \left(\frac{k}{b}\right)^2 + \left(\frac{l}{c}\right)^2}$. For diffraction to occur, the Bragg equation must be satisfied so the set of planes, hkl, must lie at the correct angle to the incident radiation.

The structure factor has both amplitude ($|F(hkl)|$) and phase (φ_{hkl}) so can be expressed as $F(hkl) = |F(hkl)|\exp(i\varphi_{hkl})$. In a diffraction experiment, the modulus structure factors, $|F(hkl)|$, as reflections from planes are obtained by collecting the intensity of diffraction spots from a crystal. This process is used for both single-crystal and powder X-ray diffraction.
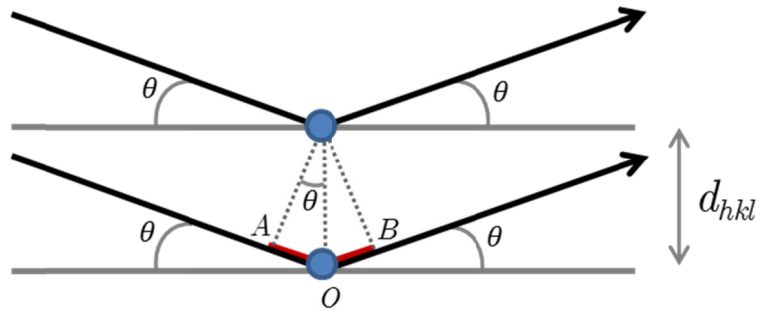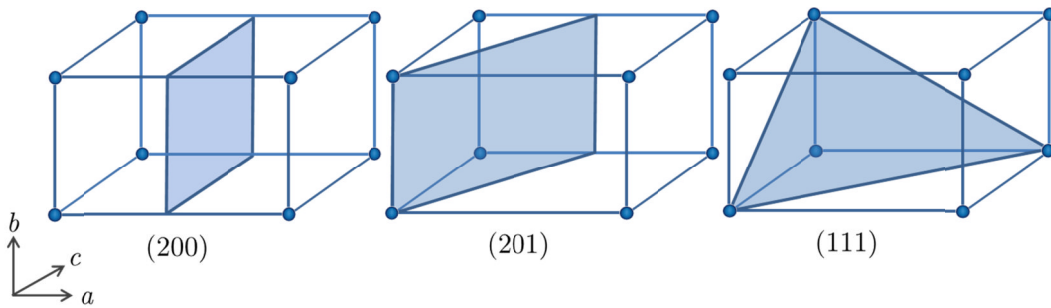
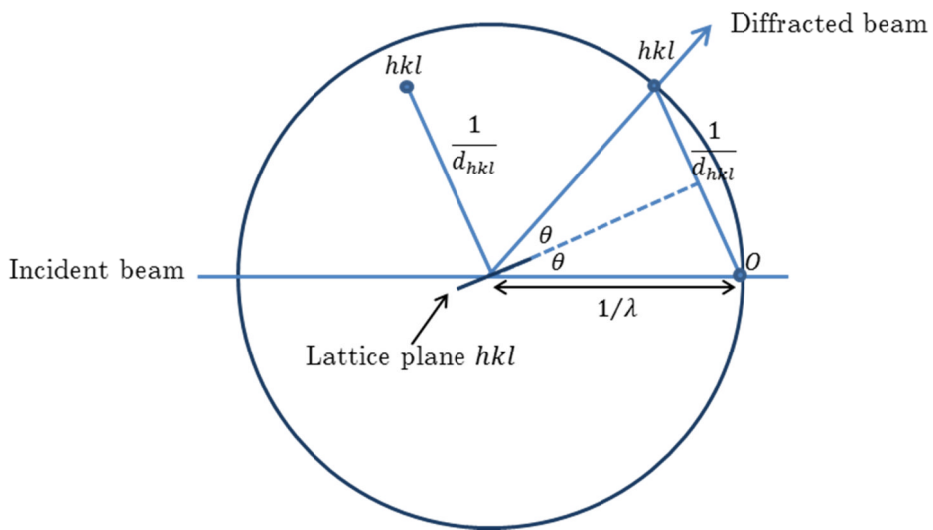**Figure 3-7: Bragg's Law.**

Figure 3-8 Examples of Miller planes.

Figure 3-9: The Ewald sphere.

3.3.2.1   The Ewald sphere

Consider a crystal with the correct orientation for diffraction from the *hkl* plane.   The reciprocal lattice vector which lies perpendicular to this set of planes has length $1/d_{hkl}$. A sphere with radius $1/\lambda$ can be drawn (Figure 3-9).   Bragg's Law is satisfied when the reciprocal lattice point for the set of planes lies on the Ewald reflecting sphere. Examination of the Ewald sphere can tell us the angle at which the crystal must be in order to get diffraction and the direction in which the diffraction will be observed. If we change the reciprocal lattice point which lies on the Ewald sphere, then the reflections observed will change. Therefore, rotating the crystal through the X-ray beam will rotate the Ewald sphere, and so vary the observed reflections.   Those reciprocal lattice points which lie outside the Ewald sphere can never be observed; the sphere with diameter $2/\lambda$ is called the limiting sphere for the wavelength or radiation used.

3.3.3   Diffraction from disordered or amorphous materials:

In an amorphous material there is little long range order, meaning that there need not necessarily be any restriction on $\boldsymbol{r}$ or $\boldsymbol{S}.$ The intensity of scattering from a material is given by:

$$I(S) = NF(S)F^*(S) \tag{3.12}$$

$$= N \sum_j f_j(S) \exp\big(2\pi i \boldsymbol{r_j} \cdot \boldsymbol{S}\big) \sum_k f_k(S)\big(-\exp(2\pi i \boldsymbol{r_k} \cdot \boldsymbol{S})\big)$$

$$= N \sum_j \sum_k f_j(S) f_k(S) \exp\big(2\pi i \boldsymbol{r_{jk}} \cdot \boldsymbol{S}\big)$$

where N is the total number of scatters, $\boldsymbol{r_j}$ and $\boldsymbol{r_k}$ are the positions of atoms j and k respectively, and $\boldsymbol{r_{jk}}$ is the separation vector, $\boldsymbol{r_j} - \boldsymbol{r_k}.$ Where materials can be assumed to be isotropic, this can be written as:

$$I(S) = \sum_j F_j^2(S) + \sum_{j \neq} \sum_k f_j(S) f_k(S) \frac{\sin(Sr)}{Sr} \tag{3.13}$$

which can be related to the interference function, $S(S)$, defined as:

$$S(S) = 1 + \frac{1}{N}\sum_{j \neq}\sum_{k}\frac{\sin(Sr)}{Sr} \tag{3.14}$$

by: $I(S) = NF^2(S)S(S)$. Therefore, the interference function is experimentally accessible as the corrected and normalised scattering intensity. The probability of finding each molecule in a radial element, δr, of volume $4\pi r^2 \frac{\delta r}{V}$ is given by:

$$4\pi r^2 \frac{\delta r}{V}g(r) \tag{3.15}$$

where $g(r)$ is the probability of finding an atom at distance, r, from the origin. This makes the interference function:

$$S(S) \ = \ 1 \ + \ \frac{N}{V}\int_{r}4\pi r^2 g(r)\frac{\sin(Sr)}{Sr}dr \tag{3.16}$$

$(g(r) - 1)$ is related to the corrected, normalised total scattering intensity, or interference function, $(S(S) - 1)$, by a Fourier transform:

$$g(r) \ = \ 1 + \frac{1}{n_0}\int_{o}^{\infty}4\pi Q^2(S(S) - 1)\frac{\sin(Sr)}{Sr}dS \tag{3.17}$$

where $n_0 = N/V$, the number density. It is this relationship which is used in the pair distribution function technique (Section 3.6).

3.4 X-ray generation and synchrotrons[6, 8]

Most laboratory-X-ray sources are produced in an X-ray tube. A source of more intense X-rays is a synchrotron. Synchtoron radiation was first observed as an unwanted loss of intensity in Bevatron experiments.[8] It was found that when an electric charge is accelerated in an electromagnetic field, an electromagnetic wave is emitted. The frequency of the emitted radiation is determined by the oscillation frequency of the charge. By accelerating the electrons close to the speed of light the spectrum of electromagnetic radiation which can be produced is stretched into the X-ray region.

In a synchrotron (Figure 3-10), electrons are produced in an electron gun and accelerated using a high potential in a linear accelerator. The electrons are injected into a booster synchrotron where they are accelerated by an electric field close to the speed of light. These high-velocity electrons are injected into the synchrotron storage ring, a tube under high vacuum consisting of straight sections and curved sections to make up a continuous path in which bending magnets make the electrons circulate many times a second. Undulators or wigglers are installed along the straight sections of the storage ring – magnetic structures which make the electron beam undulate. This deviation from linearity constitutes acceleration, which stimulates the electron beam to emit radiation. The electrons are also accelerated in the curved sections of the storage ring by the bending magnets and so radiation is produced here too. X-rays travel tangentially from the ring in the direction of travel at the time of the acceleration and are collected by beamlines where they are conditioned ready for use by experimental users. There are many of these insertion devices placed around the storage ring so many beams of X-rays are produced simultaneously allowing many simultaneous experiments.

The X-rays which are produced have a range of wavelengths and must be monochromated before use. The most common way in which this is done is by using a crystal or pair of crystals set at a certain angle next to a slit, meaning that only radiation of a certain wavelength reflects at the correct angle to pass through the slit. The rest of the radiation is absorbed.

The light produced by a synchrotron has intensity and brightness many orders of magnitude greater than a conventional lab source. This increases the intensity of scattering from a material so reduces data collection times considerably. Crystal samples which are too small or weakly diffracting to be able to be run on a lab source are able to be run at a synchrotron. In addition to this, the shorter data collection times make it possible for much more complex experiments to be carried out on a sensible time scale. This has been utilised extensively for this work, where many of the single-crystal gas cell collections would not have been possible without the use of a high intensity X-ray source. A synchrotron source can also achieve lower divergence, which improves spot shape and aids in the deconvolution of twinned species. The synchrotron has other advantages not so pressing for this thesis, such as the ability to tune the wavelength of the X-rays and direct more than one pulse of electrons around the ring at the same time allowing for time-resolved experiments.

Synchrotron sources are expensive to set up and to run. For this reason, they are usually national or international facilities which allocate experimental time via a peer-review system. Anyone can submit a proposal to use the facility and proposals are ranked by a peer review panel. Synchrotrons are run 24 hours a day and because of the large amount of data which can be collected quickly, experimental time runs typically from 24 hours to 1 week. The characteristics of the beamlines used for this work are described in sections 3.1.8, 3.2.1 and 3.6.4.
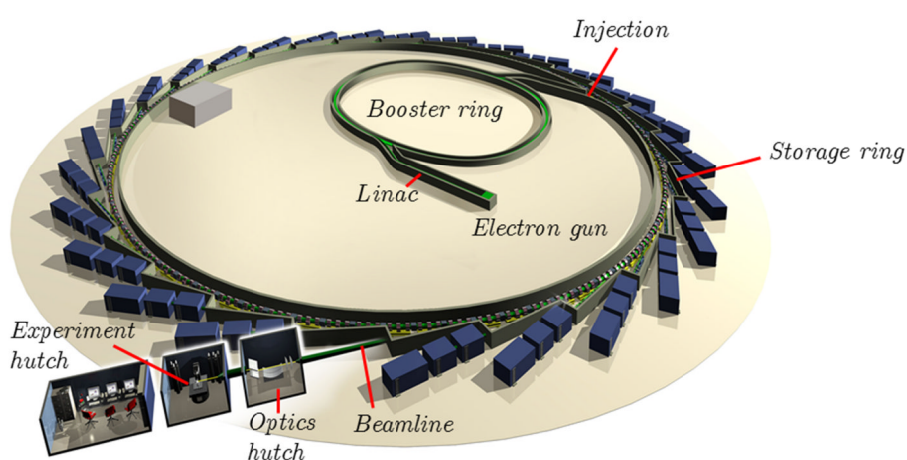

Figure 3-10: Diagram of a synchrotron (altered from http://www.diamond.ac.uk/Home/Technology/Components/booster.html)

3.5 Single-crystal X-ray diffraction (SCXRD)

X-ray diffraction experiments can be performed on both single-crystals and powder samples. Single-crystal X-ray diffraction involves collecting the intensity of diffraction spots from a crystal rotated in the X-ray beam, and relating them back to the structure factors in order to perform a Fourier transform to calculate the electron density of a material, and hence the structure.

3.5.1 Choosing a good crystal

The first stage in any successful structure solution is to select the best possible crystal in which all the unit cells are in the same orientation, so that diffracted beams will interfere

correctly to give an easily interpreted diffraction pattern. Crystals are examined under an optical microscope and a crystal which appears to be isolated and not split is chosen. A regular shape is indicative but not definitive of a good crystal. Once a possible crystal is identified it is examined under a polarizing filter (Figure 3-11). A single crystal should extinguish polarized light uniformly every 90° when rotated (although because of the symmetry requirements this does not apply for crystals with cubic symmetry or along certain high symmetry axes). If different parts of the crystal extinguish light at different angles when rotated then the sample is probably not single and therefore not appropriate for data collection.
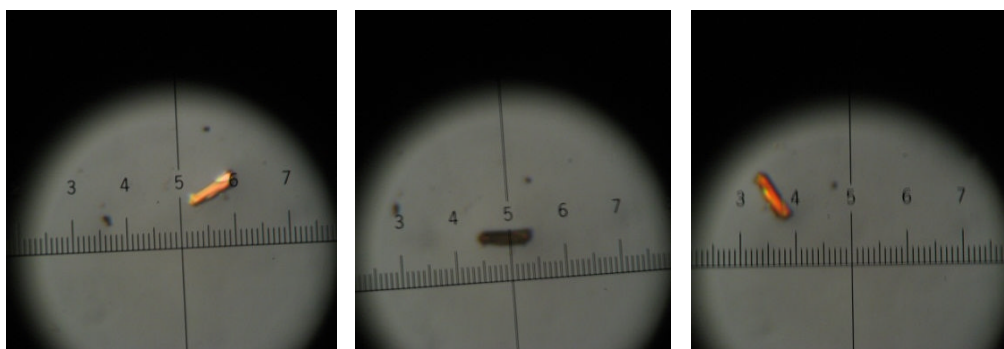

Figure 3-11: A crystal under a microscope under (a) polarized light, (b) polarized light rotated by 90° and (c) polarized light rotated by 180°.

The size of the crystal required depends on the X-ray source which is being used and the elemental composition of the material. Systematic errors in the data increase when the whole crystal is not present in the X-ray beam at all times; therefore crystals with an axis larger than 1 mm are avoided. Heavier elements scatter more strongly so smaller crystals of materials that contain them are suitable. On a conventional lab source, crystals with dimensions of as little as 0.1 mm can be accommodated. Using a synchrotron, data can be collected for crystals with dimensions of 10 μm.

When a suitable crystal is identified, oil or glue is used to attach the crystal to a glass fibre or a MicroMount (Figure 3-12), and also to protect it from beam damage throughout the collection. The mount is attached to a goniometer head which ensures

that the crystal remains firmly in place on the machine during the data collection so there is no unwanted movement to confuse the assignment of intensities. The XYZ positions of the crystal on the goniometer head can be adjusted to centre the crystal in the beam. Data are usually collected at low temperatures (100 – 150 K) to reduce radiation damage, and the crystal is cooled using a stream of nitrogen gas.
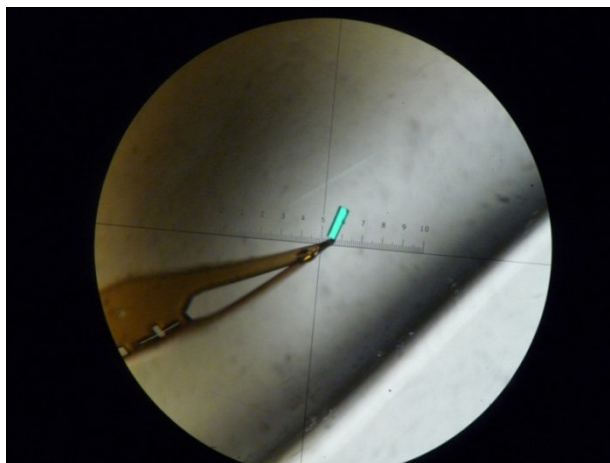

Figure 3-12: Crystal mounted on a MiTiGen Micromount (Photograph: Simon Teat).

3.5.2   Diffractometers

Early data collections were done using photographic film which blackens on exposure to X-rays.   Modern day collections are carried out using diffractometers. These are computer controlled and comprise of a system to control the movement of the crystal and a detector which can quantify the intensity of X-rays it receives.   To form a good model from the data it is necessary to collect information about reflections from all crystal planes (up to a sensible value), meaning it is necessary to rotate the crystal during the data collection to move all reciprocal lattice points through the Ewald sphere. To do this a diffractometer can move through two or three independent circles to rotate the sample in addition to moving the detector with respect to the incident beam. (Figure 3-13).
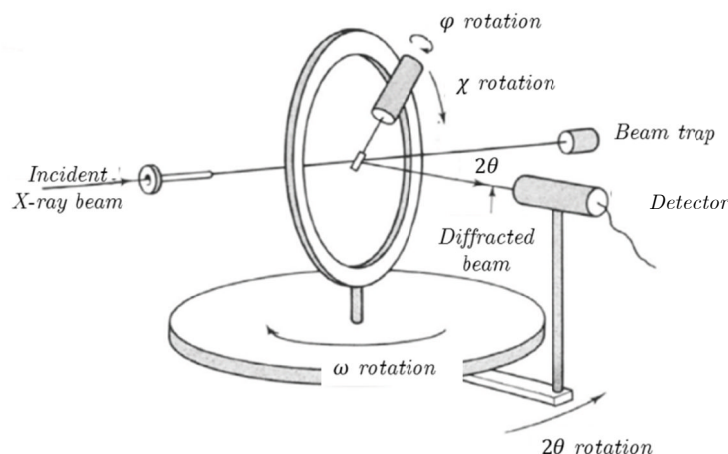
Figure 3-13: Four-circle diffractometer (image altered from ref 9). χ is fixed at 54.74° in a three circle diffractometer.

3.5.3   Initial images and calculation of the orientation matrix

It is said that the "proof of the pudding is in the eating," and for crystal quality this is the diffraction pattern which is obtained. Initial images are collected to determine the scattering capability of the sample and whether the crystal is suitable for a full data collection. In an ideal crystal with no thermal motion, reflections would be delta functions. In reality this is not possible, but a good crystal should have discrete, unsplit spots which are spherical in 3D, at a good distance from each other out to a large scattering angle. Figure 3-14 shows diffraction patterns from a highly crystalline sample suitable for collection and from a poor crystal that was deemed unsuitable.

The initial images also allow the determination of the orientation of the crystal on the diffractometer. When the crystal is mounted its orientation with respect to the diffractometer is random and a matrix must be determined in order to assign the collected reflections to *hkl* planes in the crystal. This is determined from the high intensity reflections in the initial images and by using this, along with calculated Bragg angles, a unit cell can be determined. It is useful to check whether the unit cell parameters are in keeping with information already known about the sample (for example, it is unlikely that a large pore metal-organic framework will have a unit cell with cell parameters of 3 Å). At this point the unit cell parameters can be checked against already reported values to avoid recollecting a known structure.

3.1.1 Data collection Strategies

If a crystal is suitable for a full data collection then a data collection strategy must be carefully thought out. Data at higher angles will greatly improve the quality of the crystal structure solution obtained, but have a much weaker intensity so require longer collection times. The symmetry of the structure is an important consideration; fewer spheres of data can be collected for a crystal with high symmetry as more of the reflections can be generated by symmetry. Low symmetry structures must be collected with as many spheres of data as possible to ensure that enough data is collected for a good structure to be obtained. A typical data collection run is shown in Table 2; 600 frames of data are collected in each of four or more ω-scans collected at different ϕ and θ values, with a frame width of 0.3°. Each frame takes typically 1 – 20 seconds on a synchrotron source, resulting in a data collection time ranging from 90 minutes for a high symmetry, strongly diffracting crystal to 24 hours in the case of a low symmetry, weakly diffracting sample.
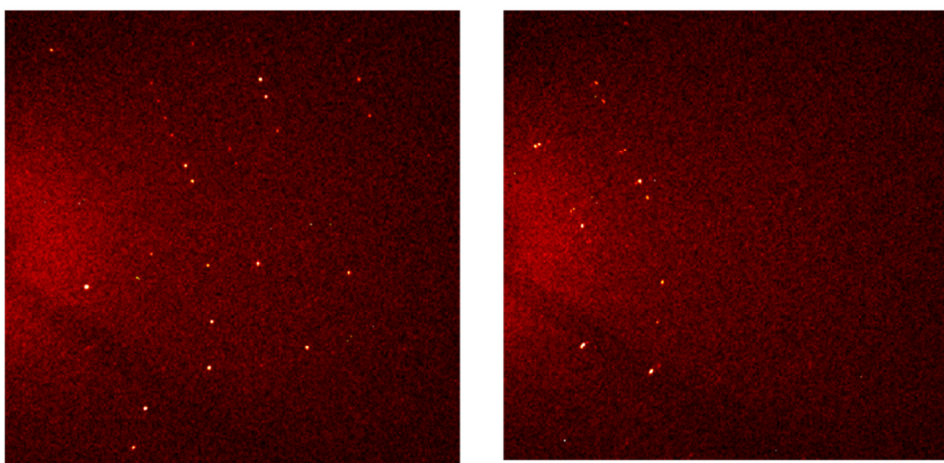

Figure 3-14 Diffraction images from a single, highly crystalline sample (left) and a poor sample unsuitable for data collection (right).

Table 2: Typical full-sphere data collection at Beamline 11.3.1 at the ALS.

Operation	Distance (mm)	2theta deg)	Omega (deg)	Phi (deg)	Chi (deg)	Time (sec)	Width (deg)	Sweep (deg)	Direction
Omega Scan	50	-36	-36	0	54.71	default	0.3	180	negative
Omega Scan	50	-36	-36	90	54.71	default	0.3	180	negative
Omega Scan	50	-36	-36	180	54.71	default	0.3	180	negative
Omega Scan	50	-36	-36	270	54.71	default	0.3	180	negative

3.1.2 Data integration and reduction

Once diffraction frames have been collected, the intensity information is extracted in a process called integration. The position of each *hkl* reflection is calculated from the orientation matrix, and the pixels associated with the reflection are summed. The unit cell is recalculated from the full data set and symmetry-equivalent reflections are merged. The intensity data must be corrected for a number of systematic errors to generate a final set of $|F(hkl)|^2$ or $|F_{obs}|^2$. Effects due to the polarization of the beam and Lorentz effects, correcting for the different lengths of time which reciprocal lattice points spend passing through the Ewald sphere, vary for the machine used and for the data scan carried out, so are applied by the integration software. Absorption corrections are necessary to account for the fact that different diffracted beams will travel a different distance through the crystal resulting in different amounts of beam adsorption and, in the case of X-ray sources whose intensity decays with time, the differing intensities of X-rays. Absorption effects are accounted for using the program SADABS. Output from the data reduction usually gives information about the data completeness, redundancy and significance, and this can be examined to decide whether additional collection or reprocessing is required. The corrected intensity data are displayed in a *.hkl* file which consists of a one line per reflection format with values for h, k, l, F_{obs}^2 and $\sigma(F_{obs}^2)$. Crystal data, atom coordinates and refinement instructions are given in the instrument *.ins* file.

3.1.3 Solving the structure – getting around the phase problem

As mentioned in section 3.3.1, it is the intensity of diffracted waves which is measured experimentally, and in doing so we lose the information about the phases of the waves.

These phases must be generated in order to solve the crystal structure. The two most common methods of generating the phases are Patterson methods and Direct methods.

3.1.3.1 Patterson Methods[4, 9]

A Patterson function is the convolution of the electron density with its inverse, and is experimentally accessible by the Fourier transform of the observed intensity:

$$P(xyz) = FT^{-1}[|F(hkl)|]^2 \qquad (3.18)$$

$$= \int\limits_{x'} \int\limits_{y'} \int\limits_{z'} \rho(x', y', z') \rho(x' + x, y' + y, z' + z) dx' dy' dz'$$

The Patterson map integrates the degree of overlap between the structure and its complex conjugate, and consists of a series of peaks representing the interatomic vectors of the original electron density. If there are N atoms in the unit cell then there will be N^2 peaks in the Patterson synthesis, N of which superimpose at the origin with peak weightings proportional to the areas of electron density which produce them. Therefore for heavier atoms we expect intense peaks in the Patterson map. The positions of heavy atoms in the structure can be assigned and then removed from the Patterson map to leave a map where the heaviest peaks are due to the next heaviest atoms. This method is ideal for solution of a structure that contains an atom which is much heavier than most of the rest of the structure, for example a heavy metal salt or coordination compound with an organic ligand. Patterson methods are also a useful method for validating space groups.

3.1.3.2 Direct Methods[4, 10]

Direct methods use the little information that is already known about both the electron density and the measured phases. The electron density must always be positive or zero, and it must exist in specific regions. These conditions put restrictions on the relationships between phases of strong reflections. Centrosymmetric structures have an additional requirement of the potential phases being 0 or π. Direct methods work out the probable relationship between the strongest reflections and try different possible phases to find the most promising combinations of phases for the reflections. These phases are used in a Fourier transform to find electron density patterns which resemble atomic arrangements.

3.1.4 Refining the structure

The initial atomic positions solved from the crystal data may not be entirely correct and some atoms, especially lighter atoms such as hydrogen, may not be placed in the solution. It is therefore necessary to improve the accuracy of the model through refinement. In this process, the atomic positions from the model allow more accurate phases to be calculated, meaning more atomic positions can be assigned with more certainty. To improve it, the fit of the experimental model to the data must be analysed, and the model must be changed only in ways that improve the accuracy. The most common way to do this is least squares refinement, where the structure factors for the model are calculated through a Fourier transform of the calculated electron density and compared with the observed data. Experimental parameters, atomic positions and unit cell parameters can all be changed in order to find the model which minimises the difference between the theoretical structure factors and the experimental structure factors:

$$ M = \sum w(F_o^2 - F_c^2)^2 \qquad (3.19) $$

where F_o is the observed structure function and F_c is the structure function calculated from the structural model. w is a weighting factor, which indicates how accurate the measurement is likely to be based on its standard uncertainty.

Where the refinement highlights an area of high electron density which is unassigned in the original model, new atoms can be introduced. Erroneous atoms can be removed or changed in the same way. Each atom in the model on a general position has three atomic coordinates and one or six atomic displacement parameters (ADPs) for an isotropic or anisotropic refinement respectively. In addition to these parameters, there are site occupancy parameters for each atom, scale parameters and atom types which can also be refined. Refinement of the structures presented in this thesis is done using the SHELX suite.[11]

3.1.5 Residual factors

The fit of the refined model with the experimental data is measured using residual factors (R-factors). A low R-factor indicates a sensible model. The most commonly used residual, mainly for historical reasons, is the unweighted R-factor, R_1, based on F, given by:

$$R_1 = \frac{\sum ||F_o| - |F_c||}{\sum |F_o|} \tag{3.20}$$

The weighted R-factor is based on F^2, where w is the weighting of each measured reflection based on uncertainties:

$$wR = \left[\frac{\sum w(F_o^2 - F_c^2)^2}{\sum w(F_o^2)^2} \right]^{\frac{1}{2}} \tag{3.21}$$

Finally, the goodness of fit, S, should be close to 1 for a properly weighted refinement. If S is less than 1 then the model is better than the data, indicating that there are problems with either the data or the refinement:

$$S = \left[\frac{\sum w(F_o^2 - F_c^2)^2}{(N_R - N_P)} \right]^{\frac{1}{2}} \tag{3.22}$$

where N_R is the number of independent reflections and N_P represents the number of refined parameters.

Whilst a low R-factor is a good indication of the sense of the model, it is also important that the model makes chemical sense. Coordination number of atoms, bond lengths and angles should all be able to be rationalised by the chemistry of the compound.

3.5.4   Atomic displacement parameters and occupancy factors

In addition to atomic positions and cell parameters, several other parameters can be refined. At any temperature above absolute zero, atoms will vibrate and move off their crystallographic positions. This movement is described by atomic displacement parameters (ADPs). ADPs are the isotropic mean-square amplitude of vibration of the atom; and are represented graphically as spheres or ellipsoids.[3]   In isotropic refinement the atoms are assumed to be spherical and vibrate equally in all directions. Three positional parameters, x, y and z and a displacement parameter, U, are refined using least squares analysis. This scheme is usually assumed for light atoms such as hydrogen due to the relatively weak scattering of these atoms.[12]   U shows a strong temperature-

dependence; it is expected to increase with higher temperatures as increased vibration of the structure leads to greater uncertainty as to the position of the atom.

A more accurate description of thermal motion is obtained by refining the atoms anisotropically. In this scheme six U parameters are defined for each atom in a matrix, one in each direction and three off-diagonal terms. In order for U_1 (defined as the direction in which there is largest mean-square displacement), U_2 and U_3 to be calculated, this matrix must be diagonalised. This is done by SHELXL during the refinement. The value of U_{eq} (the radius of a sphere which would have the same volume as the ellipsoid defined by U_1, U_2 and U_3) can also be calculated for anisotropic displacement and can be used as a simplification of the magnitude of movement for comparison.

If an atom is present on a site in every unit cell, then the site occupancy factor (SOF) of this atom is unity. When an atom sits on a special position, the occupancy can be less than 1 because the other portions of the occupancy are generated by symmetry operators. Occupancy can also be lower if the site is not occupied by an atom in every single unit cell. This is often the case with solvent molecules, which are not always present in every cell. The single-crystal structure averages out the occupied and non-occupied sites, resulting in an occupancy less than one. In a desolvation experiment at variable temperature data where the occupancy of solvent is expected to decrease with temperature, it is helpful to allow the SOF values of solvent molecules to freely refine. This can be done by changing the SOF in the *.ins* file from 11.000 to 1.000 which allows free refinement of the parameter.

3.1.6 Constraints and restraints

Constraints and restraints are extra information that is given to the refinement to help it on its way. A constraint reduces the number of independent parameters to be refined by rigidly equating parameters with each other or to a certain number instead of the value which is in best agreement between observed and calculated observations. Hydrogen atoms, for example, are routinely constrained to move the non-hydrogen atom to which they are attached. A restraint gives extra experimental observations to the refinement such a known bond lengths or angles. This forces the least-squared refinement towards convergence. They are also used to impose non-crystallographic symmetry, e.g. making the bond lengths in benzene equal.

3.1.7 Publication (CIFs and cifcheck)

When the refinement has converged to an acceptable R-factor (usually $R < 7\%$ is required for publication) it is important to make sure that the structure makes chemical sense. The final structure can be reported in a crystallographic information file (CIF) which provides a standard way to archive crystal structures and reports all atomic positions and geometries in the crystal as well as details about the data collection and refinement. Computer databases are available to upload and download CIF files; the most widely used are the Cambridge Structural Database[13] which draws crystal structures from scientific literature and the Inorganic Crystal Structure database (ICSD).[14]

3.1.8 Equipment used for SCXRD

All single-crystal data presented in this thesis were collected on a synchrotron source. Unless noted, data was collected at beamline 11.3.1 at the Advanced Light Source, Lawrence Berkeley National Laboratories. The beamline receives beam from a bending magnet in the energy range of 6-18.5 keV (0.73-2.07 Å). The beam is monochromated to a wavelength of 0.77490 Å using a channel-cut Si(111) monochromator located 6 m away from the X-ray source. The final beam size is 100 microns, with a flux of 10^{10} ph/s at sample location. The beamline uses an Apex II 3-circle diffractometer and CCD detector. The sample can be placed in the temperature range of 100 – 500 K using an Oxford Cryosystem 700 Plus device. The single-crystal setup on this beamline is shown in Figure 3-15.
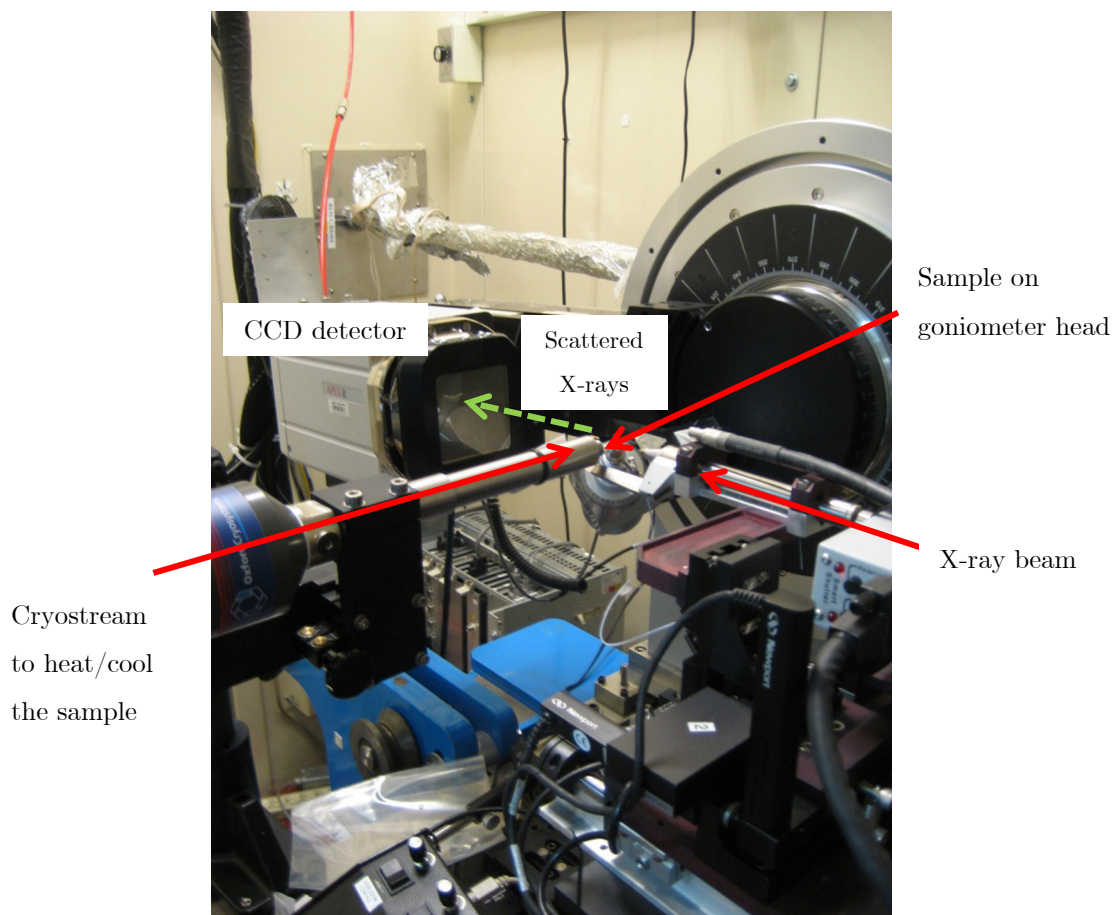
Figure 3-15: Single-crystal X-ray diffraction experimental setup at Beamline 11.3.1 at the Advanced Light Source.

3.2 Powder X-ray diffraction[15, 16]

Single-crystal X-ray diffraction allows the structure of a crystal to be solved. That single crystal may have the same composition as every crystal in the sample, or it may represent a minor phase or impurity. It is necessary to analyse the bulk of the material to tell this. Sometimes it is not possible to obtain a single crystal of a material for analysis. In both these cases, powder X-ray diffraction (PXRD) is a powerful analytical technique. PXRD experiments, like single-crystal experiments, involve analysing the diffraction from a sample irradiated with X-rays. If several crystallites in different orientations are irradiated by an X-ray beam simultaneously, several Miller planes may be in the correct orientation for diffraction and each crystallite will give an individual diffraction pattern; these are overlaid on each other on the detector. A crystalline

powder is made up of many small crystallites in random orientations and the overlaid diffraction spots of all of the crystals orientated correctly for Bragg's Law to be satisfied results in a diffraction pattern. This is made up of cones of diffraction at angle 2θ to the incident beam direction (Figure 3-16). Circles of intensity are produced on the detector perpendicular to the incident beam. The intensity of a cross section of the circles can be extracted and intensity plotted as a function of 2θ, compressing the three-dimensional diffraction pattern into a one-dimensional pattern (Figure 3-17). In a PXRD experiment, the sample is rotated in a capillary but it remains stationary with respect to the X-ray beam, whilst the detector is moved through space through 2θ angles. The intensity of diffraction at different 2θ values is recorded and output as plot of the intensity versus 2θ.

Figure 3-16: Schematic showing the diffraction spots from a single crystal (left), several crystallites (middle) and diffraction rings from a crystalline powder (right).
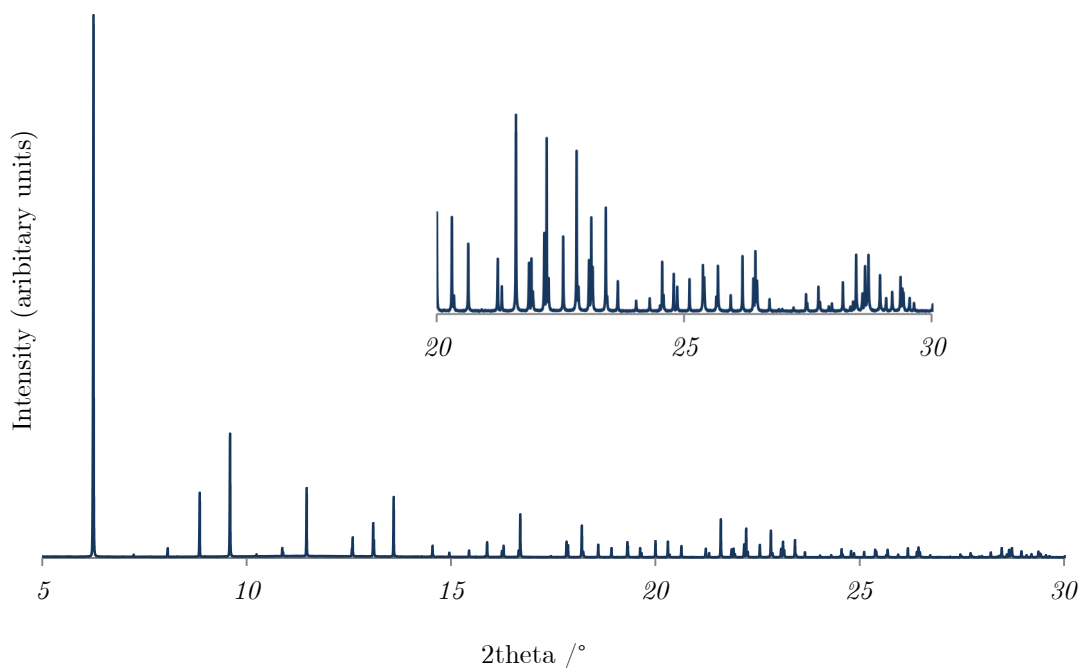
Figure 3-17: Typical powder pattern of intensity plotted as a function of scattering angle, 2theta, with inset of high-angle region.

The PXRD pattern is unique to a particular structure meaning this method can be used as a fingerprinting method for crystalline materials. Data can be generated quickly in-house and compared to patterns generated for single-crystal structures, or patterns downloaded from databases such as the ICSD.[14]

The positions of the peaks are determined very accurately by PXRD due to the large number of diffraction spots which make up the diffraction rings. However the intensity of individual peaks, especially those at higher angles where there can be significant peak overlap can be hard to determine. The effect of this is that unit cell parameters which are calculated using only peak positions can be determined very accurately from high quality PXRD, but the loss of intensity information makes solving a structure from PXRD data without some prior knowledge of the structure difficult. Much progress has been made in recent years thanks to the combination of advances in computational power and facilities where high resolution data can be collected meaning that solution by PXRD models is becoming routine, albeit time-consuming and tricky.

3.5.4.1   The Rietveld Method[16-18]

If reasonable approximations for unit cell and atomic parameters can be made for a material then a model structure can be refined using the Rietveld method.[17] Introduced in 1966 by H. M. Rietveld, this involves a full-profile refinement in which a model is fitted to the experimental PXRD data without the extraction of individual intensities from the data. In doing so, the problems associated with peak overlap are minimised. During a refinement, non-linear least squares is used to minimise the function:

$$\Phi = \sum_{i=1}^{n} w_i (Y_i^{obs} - Y_i^{calc})^2$$

(3.23)

where Y_i^{obs} is the observed intensity and Y_i^{calc} is the intensity calculated from a model structure at point i in the diffraction pattern, n is the total number of data points and w_i is the weight given to point i in the diffraction pattern based on experimental uncertainty. This function is minimised by the refinement of parameters such as background, peak shape, unit cell parameters and, later in the refinement, atomic positions and thermal parameters.

The reliability of the refinement can be estimated using residual factors. R_p is a measure of how well a model and experimental pattern fit:

$$R_p = \frac{\sum_{i=1}^{n} |Y_i^{obs} - Y_i^{calc}|}{\sum_{i=1}^{n} Y_i^{obs}}$$

(3.24)

The weighted R-factor, R_{wp}, gives a weight to each point dependent on its statistical quality:

$$R_{wp} = \left[\frac{\sum_{i=1}^{n} w_i (Y_i^{obs} - Y_i^{calc})^2}{\sum_{i=1}^{n} w (Y_i^{obs})^2} \right]^{1/2}$$

(3.25)

The Goodness of Fit is estimated using χ^2,

$$\chi^2 = \frac{\sum_{i=1}^{n} w_i (Y_i^{obs} - Y_i^{calc})^2}{N - P + C}$$

(3.26)

where N denotes the number of observations, P is the number of refined parameters and C is the number of constraints. These numbers are useful comparisons for refinements but are potentially misleading. The refinement should be plotted and viewed to check for discrepancies in the refinement. The quality of the refinement using the Rietveld method is highly dependent on the quality of the PXRD data. For this reason it is often preferable to use a synchrotron source to collect data (sPXRD) which, because of the lower divergence and high intensity, results in data with better defined peaks where it is easier to assign intensities to particular reflections.

Were a crystal infinite then the diffraction pattern would consist of delta functions at specific Bragg angles.[15] As no crystals are infinite, and thermal energy makes atoms vibrate off their ideal crystallographic positions, peaks are broadened and this broadening increases as crystallite size decreases. Hence, PXRD is a convenient way to calculate the mean crystallite size in a material with crystallite sizes of up to approximately 200 nm. This is done using the Scherrer equation:[15]

$$\tau = \frac{K\lambda}{\beta \cos\theta} \tag{3.27}$$

where τ is the mean particle size of the crystallite domain, λ is the wavelength of the radiation used, K is the shape factor (shape dependant but generally a value of around 0.9), β is the width of the Bragg peak at full width half maximum (FWHM) and θ is the angle at which the Bragg peak appears.

3.2.1   Equipment used for PXRD, in-house and beamline I11

Data for fingerprinting were collected in-house on three PXRD machines: a Phillips XPERT machine in reflection geometry, STOE STADIP diffractometer using monochromated Cu $K_{\alpha 1}$ radiation working in transmission mode, and PANalytical in reflection mode.

High resolution sPXRD data for structure refinement were collected at beamline, I11 at the Diamond Light Source.[19] Samples were packed in 0.5mm diameter borosilicate capillaries and fixed to a magnetic mount to go on the diffractometer. Data were collected at room temperature in Debye-Sherrer geometry using monochromated X-rays

of wavelength 0.827439(1) Å. Measurements were done at 300 K or 150 K depending on the sample. Data were collected between 2 and 150 degrees in 2theta. Analysis was performed using the GSAS suite.[20, 21]

3.6 Pair Distribution Function (PDF) analysis[15, 22-27]

3.6.1 Crystallographically challenged materials

Whilst many materials take an ordered form defined by the repeating unit cell of atoms, other materials show little long-range order. A good example of this is in a glass where the first coordination sphere of molecules tends to be well defined but higher coordination spheres show little order. In the solid state, nanoparticles, mesoporous materials and bulk crystals with short-range structural fluctuations are all examples of crystallographically challenged materials. The result of PXRD on these materials is a continuous distribution of scattering intensity over the angle range which cannot be analysed by Bragg methods.

Pair distribution function (PDF) analysis is a total scattering method that does not rely on having Bragg diffraction from a material. The PDF technique has historically been applied to glasses and liquids. For solid materials, the limited Q-ranges accessible on typical X-ray sources lead to very large termination errors which limit the applicability of the PDF technique.[25] However, recent developments in synchrotron technology mean that PDF is increasingly used to study solid materials.

3.6.2 Total scattering and relation to the functions S(Q), F(Q) and G(r)

The total scattering from a material consists of Bragg scattering and diffuse scattering. In section 3.3.2, the Bragg scattering was described as sharp peaks of diffracted intensity resulting from the constructive interference of parallel diffracted beams. The constructive interference is a product of having long-range order in the material. Therefore, when there is a deviation in long-range order, the conditions for Bragg diffraction are broken. The intensity of the Bragg diffraction is weakened, and the scattering is redistributed in reciprocal space around the Bragg peaks. This redistribution is dependent on the correlation length of the material; a very crystalline sample will have an almost infinite correlation length and therefore diffuse scattering will be almost completely overwhelmed by the Bragg peaks. A less crystalline sample will show some

diffuse scattering around the Bragg peaks and an amorphous material will show large amounts of diffuse scattering. Figure 3-18 shows scattering from a single crystal in which sharp Bragg peaks and weaker diffuse scattering can be seen.
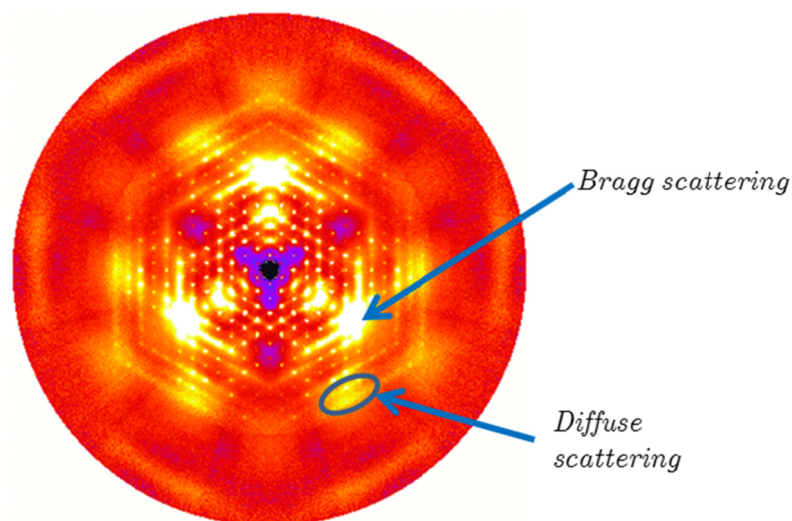

Bragg scattering

Diffuse scattering

Figure 3-18: Diffuse scattering from a single crystal.[28]

Diffuse scattering is much weaker than Bragg scattering, and in the conventional crystallographic analysis of a well-ordered material it is subtracted as background intensity. However, in the PDF technique, the Bragg scattering and the diffuse scattering are treated with equal weight during analysis. This means that the crystallinity of the material is taken into account throughout the analysis of Bragg scattering, but the deviations from the long-range order are also analysed through use of the diffuse scattering.

The scattering from an object where there is no restriction on the values that the scattering vector can take was outlined in section 3.3.3. A total scattering experiment monitors the scattering intensity variation with scattering vector. In chemical crystallography, the scattering vector is named S, but in total scattering, Q is used, which is related to S by a factor of 2π. Because all total scattering literature and

software uses Q for the scattering vector, this convention will be followed in the following section. Experimental intensity data, $I_{\text{experimental}}(Q)$ has several components:

$$I_{\text{experimental}}(Q) = I_{\text{coh}}(Q) + I_{\text{incoh}}(Q) + I_{\text{MS}}(Q) + I_{\text{BG}}(Q) \qquad (3.28)$$

where $I_{\text{coh}}(Q)$ is the coherent scattering, $I_{\text{incoh}}(Q)$ is the incoherent scattering, $I_{\text{MS}}(Q)$ is the multiple scattering and $I_{\text{BG}}(Q)$ is the scattering from the background. Structural information is contained only in the coherent portion of the scattering, meaning that the other components of the scattering must be removed before the Fourier transform can be performed. This is removed by the various corrections applied to the data during processing (section 3.6.5). The intensity data are also formalised to give a function with units of scattering-per-atom by dividing the initial intensity by the number of scatterers, N, and the average scattering power per atom to give $S(Q)$ which is known as the structure function, or interference function:

$$S(Q) = \frac{I^{coh}(Q) - \sum c_i |f_i(Q)|^2}{|\sum c_i f_i(Q)|^2} + 1 \qquad (3.29)$$

c_i is the concentration of atom species, i, and f_i is the X-ray form factor of atom species, i.

An example of S(Q) for a crystalline fcc nickel sample is shown in Figure 3-19. This function oscillates around 1 at high Q, and $\langle S(Q) \rangle = 1$ meaning $S(Q)$ essentially represents a powder pattern which has been corrected for experimental artefacts then normalised so $\langle S(Q) \rangle = 1$. The intensity of peaks in the structure function decreases with increasing Q due to the Debye-Waller factor. $S(Q)$ contains both sharp peaks from the Bragg intensity at low Q-values, and wider peaks due to diffuse scattering at higher Q-values.

More commonly reported than $S(Q)$ is the reduced structure factor, $F(Q)$. The two functions are related by the simple relationship:

$$F(Q) = Q(S(Q) - 1) \qquad (3.30)$$

The reason that this function, which does not add any extra information to the function but is merely a different way of expressing the same information, is much more widely

quoted is that this function is exactly related to the reduced pair distribution function, $G(r)$, via a Fourier transform.

3.6.3 The pair distribution function, g(r), G(r) and R(r)

There are three main forms of the pair distribution function which will be considered: the atomic pair distribution function, $g(r)$, the reduced pair distribution function, $G(r)$, and the radial distribution function, $R(r)$. All three functions are accessible from experimental data and can be converted to one another through the addition and multiplication of various constants.

The reduced pair distribution function, $G(r)$ is the function most easily accessible from experimental data as it is the Fourier transform of the reduced structure function, $F(Q)$:

$$G(r) = \frac{2}{\pi} \int_0^\infty F(Q) \sin(Qr) \, dQ \tag{3.31}$$

$$= \frac{2}{\pi} \int_0^\infty Q[S(Q) - 1] \sin(Qr) \, dQ$$

where $S(Q)$ is the normalised corrected coherent scattering intensity from equation 3.35. In reality, it is not possible to measure data with Q-values up to ∞, but up to a maximum value, Q_{max}, making the expression for $G(r)$:

$$G(r) = \frac{2}{\pi} \int_{Q_{min}}^{Q_{max}} Q[S(Q) - 1] \sin(Qr) \, dQ \tag{3.32}$$

When the total scattering is measured we get a continuous function, $I(Q)$, with sharp features (Bragg peaks) and broad underlying features (diffuse scattering). Figure 3-19 shows the form of the raw data, normalised total scattering function and atomic pair distribution function for crystalline nickel.

$G(r)$ is related to the atomic pair distribution function, $g(r)$, by a factor of $4\pi r \rho_0$:

$$G(r) = 4\pi r \rho_0 [g(r) - 1] \tag{3.33}$$

where r is the radial distance, ρ_0 is the average number density of the material and $g(r)$ represents the probability of finding two atoms at a certain separation, r. $g(r)$ oscillates around 1 at high r, and tends to zero as $r \rightarrow 0$. Multiplying it by the average number density, ρ_0, gives the probability of a pair of atoms being at this separation in the sample.

The radial distribution function (RDF) is the most physically intuitive of the three functions described here. It describes the number of atoms present in a ring with thickness dr at distance r from another atom in the structure:

$$R(r) \;=\; 4\pi r^2 \rho_0 g(r) \tag{3.34}$$

$G(r)$ is the most commonly used version of the PDF. There are several reasons for this. Firstly, $R(r)$, whilst physically intuitive, scales with r^2 so is hard to interpret visually at high r-values. $G(r)$ is the direct Fourier transform of the corrected scattering data so there is no need to know, or estimate, extra constants for multiplication such as ρ_0. Finally, the function $g(r)$ is weighted by the function 1/r. This means that the errors on the data are much greater at low-r values, making interpretation very difficult. The errors of the function $G(r)$ are weighted equally throughout the r-range, making the PDF much easier to interpret and model. In this thesis, all the pair distribution functions which have been analysed have been the reduced PDF, $G(r)$, and the term PDF is used exclusively to refer to $G(r)$.
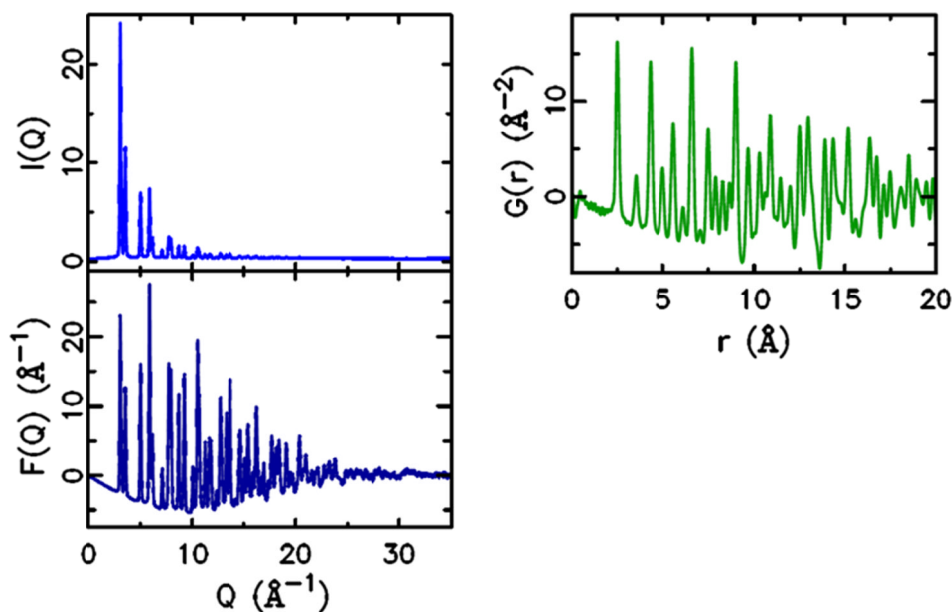
Figure 3-19: Raw intensity data [I(Q)] (top left), the normalised reduced scattering function, [F(Q)], (bottom left) and the atomic pair distribution function, [G(R)] (top right) for fcc nickel. Figure taken from PDFGetX2 user guide.[29]

3.6.4   Data collection

In a typical total scattering experiment, the intensity of scattered radiation is monitored as a function of the scattering vector, Q. It is desirable to collect total scattering for a wide Q-range (a range of $25 - 50$ Å^{-1}) in order to minimise Fourier termination errors which manifest as extra ripples in the $G(r)$ function and confuse interpretation. The Q-range for an experiment is determined by the wavelength:

$$Q_{max} = \frac{4\pi \sin \theta}{\lambda} \qquad (3.35)$$

For lab-based sources using typical copper, molybdenum or silver radiation, the obtainable Q_{max} values are ~8Å^{-1}, ~16 Å^{-1} and ~20 Å^{-1} respectively. This produces data which are usually acceptable for initial examination, but insufficient for any detailed analysis and modelling. Much higher Q-values resulting in higher-space resolution data can be collected using a synchrotron or neutron source. It is also important to collect good quality data at higher Q-values because of the way that the data is normalised. Equation 3.30 shows that the data is divided by $|\sum c_i f_i(Q)|^2$. This becomes very small at high Q-values due to the Debye-Waller factor so has the effect of amplifying the high-Q

data. Optimally, therefore, data is collected using synchrotron sources with large Q-ranges and good counting statistics.

Data can be collected in a very similar way to powder-diffraction experiments (section 3.2.1) using a 1D detector in Debye-Scherrer mode and then processing the data for total-scattering analysis, but it is increasingly common to use rapid acquisition PDF measurements (RAPDF).[26] In this setup (Figure 3-20) PDF data is collected in a single shot. A well-ground powder sample is placed in a polyimide capillary. High energy X-rays are fired through the sample and a 2D large-area detector placed perpendicular to the incoming beam records the scattering. Scattering appears as rings of data at a distance from the centre of the detector (Figure 3-21).

A large area detector is able to catch the many rings of scattering data at once, making data collection relatively quick. Data collection times vary depending on the crystallinity, chemical composition of the sample and beam intensity, from 30 ms to several minutes. This is much quicker than the collection of a full powder pattern which is typically 30 - 90 minutes at its quickest. RAPDF measurements are therefore ideal for studying materials in time-resolved experiments or through phase transitions. Because all the detected scattering from these images is used in later analysis, explicit measurements for background and sample holder scattering must be made before data collection and then subtracted from the measured intensity later in the data processing.[26]

Beamline 11-ID-B at the Advanced Photon Source has been dedicated to the collection of PDF data. The beamline operates at two fixed energies, ~58 keV and ~90 keV, giving a choice of wavelengths depending on the scattering power of the sample. X-rays are produced via an insertion device and monochromated using a Si(511) crystal. X-rays pass through the sample which is placed in a Kapton or quartz capillary and the scattered X-rays are collected by a General Electric amorphous silicon detector placed perpendicular to the incident beam.
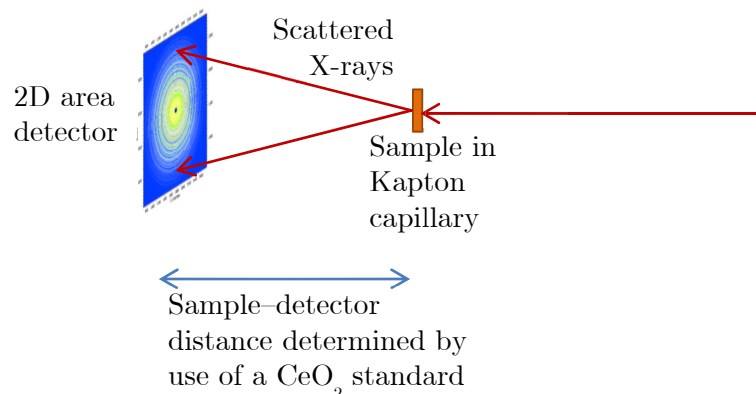
Figure 3-20: Schematic of RA-PDF setup.

3.6.5   Data processing

Once total scattering data have been collected it is necessary to integrate the 2-dimensional data from the area detector to produce a 1-dimensional graph of $I(Q)$ shown in Figure 3-19 (top). The distance between the sample and the detector can be determined by using a CeO_2 standard for which the distance between diffraction rings is tabulated. This distance can then be used to convert the distance of the ring from the centre of the detector to the 2θ angle from which it is scattered. This is done using the program FIT2D.[30] A sample data frame is shown in Figure 3-21. The output of this process is a *.chi* file which contains intensity information as a function of scattering angle, or Q-value.

As outlined in equation 3-28, the experiential intensity has several components, of which only the coherent scattering gives structural information. Other components of the scattering must be removed before the Fourier transform can be performed. In addition to the removal of these components, the data must be corrected for the reduction in intensity due to absorption of some X-rays by the sample and for the change in intensity due to polarization of the diffracted intensity. These corrections are done using tabulated values using the program PDFGetX2.[29] Here, information about the sample background (from the explicit measurement made during data collection), chemical composition and experiment geometry are inputted to produce corrected and normalised intensity plots, $S(Q)$.

The background of the sample is measured separately to the sample data, so it is possible that the beam intensity will have changed throughout the data collection. Therefore, it is necessary to scale the background appropriately by the visual examination of the $S(Q)$ function. For the properly subtracted background the first Bragg peak of the function should have a minimum of close to the baseline of the function. The position of the minima should then rise quickly and the function should oscillate around at 1.0 at longer Q-values and tend to 1 at the high end of the Q-scale. The value for the background scaling can be changed until the value for $S(Q)$ looks correct. Once the function $S(Q)$ looks correct, it is necessary to obtain the best $G(r)$ function possible by altering the background multiplication by small amounts to minimise the intensity of the peaks obtained below 1.3 Å. The presence of these peaks is due to the finite Fourier termination; the Fourier transform performed on intensity data is limited by the Q-range of the experiment to between the values of Q_{min} and Q_{max}. The consequence of doing this finite Fourier transform is that termination ripples appear in the PDF with wavelength $\sim 2\pi/Q_{max}$. Using the largest value of Q_{max} which can be increased through longer collection times, removal of experimental artefacts and good instrument alignment can decrease these errors. In addition, the intensity of these peaks can be minimised by the correct subtraction of background. Close to the correct value of the background multiplication, there can be considerable variation of the intensity of the low-r peaks and these must be minimised as far as possible. Finally, the data is Fourier transformed using PDFGetX2 to produce $G(r)$.

3.6.6 Interpretation and modelling

The PDF is a probability distribution showing the likelihood of finding an atom pair separated by a certain distance. Therefore, the PDF is a weighted histogram of atom-atom distances in a sample. Where an atom pair is likely we find a sharp peak, and where there is little probability of an atom pair the function returns to the baseline of -$4\pi r\rho_0$. Conceptually, PDF can be thought of as the result of choosing an atom randomly in the sample and plotting on a graph the distance from this atom to every other atom out to a certain distance. Next, another atom is chosen and the process is repeated. This is done for all the atoms in the sample. Each point which is plotted in the histogram is weighted by the scattering factor of the atoms involved. After all these atom-atom distances are summed, the result is the PDF.
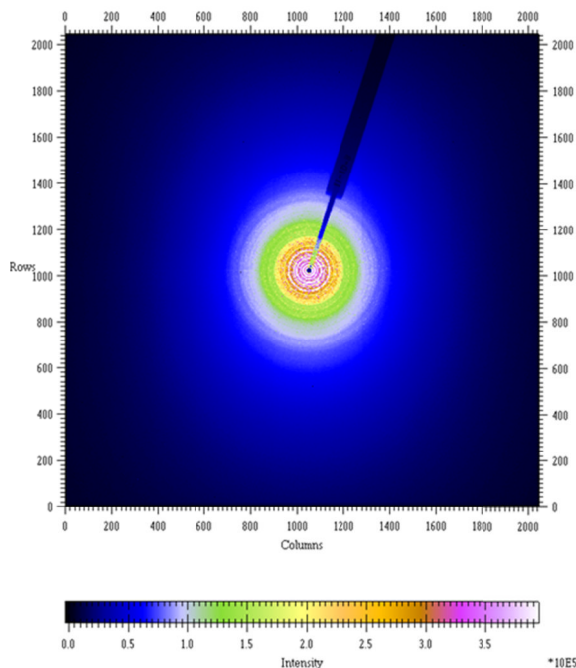
Figure 3-21: Sample integration frame from FIT2D.

The advantage of looking at the PDF is that it is not dependent on the positions of any one atom in the crystal structure but is instead dependant on the separation between them. This means that for structures without long-range order it is still possible to gain information about the structure without the necessity of Bragg scattering. The other advantage of PDF is that it amplifies the data at high Q-values, data which in conventional crystallographic methods is too weak to be used. Random uncertainties are constant with r, making $G(r)$ resilient to random errors in the data.

An example PDF for face-centred nickel is shown in Figure 3-19. Below 2 Å there are no peaks because this is less than the nearest neighbour distance for nickel, so atoms cannot approach this closely. Any peaks in experimental data in this region are the result of Fourier truncation errors and are a good indication of the quality of the data. The first peak features at 2.6 Å, relating to the nearest neighbour distance. The peaks at 3.6 Å and 4.2 Å represent next nearest neighbour distances.

3.6.6.1 Model independent information[15]

Much of the information which is extracted from the experimental PDF is done using modelling (see below). Some information, however, can be extracted directly from the experimental $G(r)$ (Figure 3-22):

(1) r_{max} = crystallinity

The value to which peaks are discernible above noise gives an indication of the crystallinity in a sample. A well-ordered sample will have defined atom-atom distances out to large distances (>100Å) and so have sharp peaks in the PDF. Less crystalline samples will have few recognisable peaks after the first coordination sphere as there is little long-range order between two points. PDFs for crystalline and amorphous ZIF-8 shown in Figure 3-23 illustrate this.

(2) Peak position = bond lengths or atom-atom distances

The position of a peak in the PDF at distance r indicates that there are two atoms separated at this distance in the sample. This feature is particularly useful in monitoring changes in structure with outside influence (heat, or gaseous guest molecules) as a change in a PDF peak position shows a change in bond-length in the sample.

(3) Peak width = Thermal or static disorder

For a structure with perfect structural coherence at absolute zero the peaks in $G(r)$ would extend to infinity. As this is never the case, all peaks are of a finite height. More disordered materials will have wider peaks compared to very ordered materials. Higher temperatures result in increased movement of atoms, so a larger range of interatomic distances are possible, broadening peaks. Peak width is also dependent on the Q_{max} value used for the Fourier transform.

(4) Peak integration = coordination number

For a well-defined peak with known chemical origin (therefore known weighting factor) it is possible to understand something about the coordination number of the origin of the peak. For example, if the peak is known to be a Ni-Ni coordination then integration of the PDF peak can tell you the coordination number. However,

especially in higher-r regions, peak overlap makes the PDF quite complicated and this simple approach is inadequate. In these cases structural models are used to understand the integrals of the peak.

3.6.6.2   Modelling the experimental PDF

Ab initio structure determination is not possible from PDF data, although recently algorithm-based modelling has been able to determine the structure of C_{60} from a X-ray PDF (xPDF) data.[31] Instead, much of the information which is gained from a PDF is done so by coming up with a reasonable initial model and refining it using the experimental data to come up with a model which is compatible with what is found experimentally. Modelling the PDF can be done in real space or in reciprocal space.
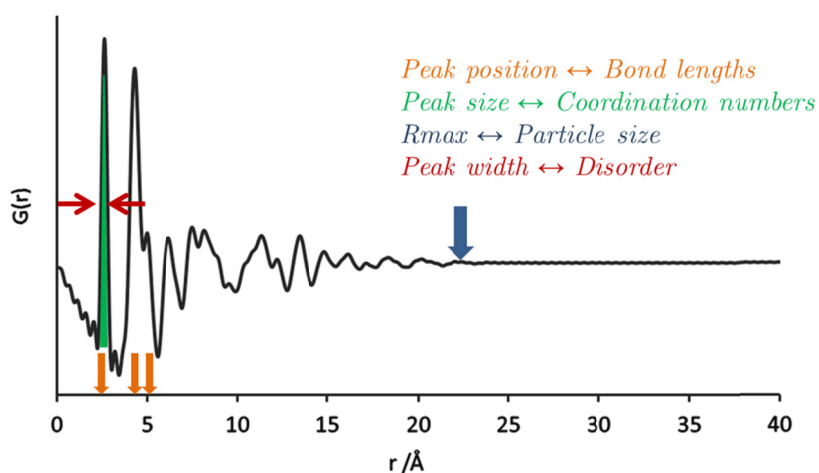

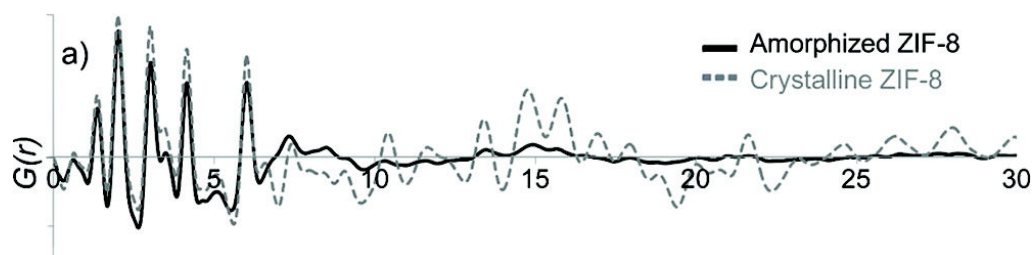**Figure 3-22: Illustration of the model-independent information available in the PDF.**

Figure 3-23: PDFs for crystalline and pressure-amorphised ZIF-8.[32]

In real space refinement, a calculated PDF from a structural model is compared to the experimentally determined PDF. This is generally done with a small number of atoms and gives information about the very local structure of the material. From a starting structural model a model PDF can be calculated using the close relation between the PDF and the radial distribution function (RDF), R(r), given in section 3.6.3. It is possible to calculate a model PDF with which to compare the data using the relation:

$$G_{calc}(r) = \frac{R_{calc}(r)}{r} - 4\pi r \rho_0 = \frac{1}{r} \sum_i \sum_j \left[\frac{f_i f_j}{\langle f \rangle^2} \delta(r - r_{ij}) \right] - 4\pi r \rho_0 \qquad (3.36)$$

This hypothetical PDF must be corrected for experimental features in a number of ways. Firstly, the relationship in equation 3.31 calculates the PDF for Q-values up to infinity. This cannot be the case experimentally where there is a maximum value of Q_{max}, determined by the wavelength of the radiation used. It can be described by multiplying the structure factor up to infinity with a step function cutting off at $Q = Q_{max}$ and it results in termination ripples. In PDFFit2, the hypothetical PDF is corrected for this by convoluting the G(r) function using a step function $S(r) = \sin(Q_{max}r)/r$. In addition to this, limited resolution of the experiment in Q-space is accounted for by the damping PDF function using the relationship, $\exp\left(-\frac{(Q_{damp}r)^2}{2}\right)$. The parameter Q_{damp} is a parameter dependent on the data collection, and is refined in the ambient temperature data set.

The calculated and experimental PDFs can be compared and the model refined using a full-profile fitting approach. The most commonly used program for this analysis is PDFFit2 with graphical user interface PDFGui.[33] This program uses a least-squares method and is analogous to the Rietveld method (section 3.5.4.1) but the fit is done in real-space as opposed to reciprocal space, and so is referred to in some literature as the 'Real-Space Rietveld' approach. Experiment-dependent parameters and structural parameters can be refined until a best-fit model is produced, with derived values for unit cell parameters, atomic positions in the unit cell expressed in fractional coordinates, anisotropic thermal ellipsoids for each atom and the average atomic occupancy of each site. These parameters can be compared with those derived from Rietveld to understand similarities and differences between the average and local structure.

The goodness of fit for a PDF refinement is calculated from the formula:

$$R_w = \left\{ \frac{\sum w_i (G_i^{exp} - G_i^{calc})^2}{\sum w_i (G_i^{exp})^2} \right\} \qquad (3.37)$$

where G^{exp} and G^{calc} are the experimental and calculated PDFs, respectively, and the w_is are weighting factors reflecting the statistical quality of individual data points.

R_w values from PDF refinements cannot be directly compared to values from Rietveld refinements for two reasons.[24] Firstly, Rietveld fits are optimised in reciprocal space, whereas R_w for PDF refinements are minimised in real space. Real space refinement is much more sensitive to local ordering in materials, which is ideal for considering local defects but means that R_w values greater than 15% are fairly common even in well-ordered materials. Secondly, the estimated standard deviations (esds) on individual data points are not correctly estimated by the integration software FIT2D when integrating the 2D output from area detectors during RAPDF. The points are highly correlated meaning the weighting of individual points for the calculation of R_w is not known. While R_w values cannot therefore be directly compared to those from Rietveld they remain a useful comparative for competing models – a lower value indicates a better model.

Similarly, uncertainties on refined parameters can also be calculated from the least-squares refinement, but for the same reason, these are inaccurate and are in many cases in the literature are not quoted.[34, 35] This problem, which effects only the *errors* on the parameter values, as refined parameters themselves are not affected by this bias and remain valid, is currently being addressed by the total-scattering community.

Reciprocal space modelling is done by calculating the scattering function, $S(Q)$, from a model. Much of this is done using a reverse Monte Carlo (RMC) type approach which involves many thousands of atoms in the model. This gives more information about the intermediate-range structure of the material. The reverse Monte Carlo algorithm is a global optimization algorithm. In this method, parameters of the system are allowed to vary in some random way. Following each iteration the diffraction data from the structure is calculated. If the fit to the experimental data has been improved then the move is accepted and if the fit is worsened then it is rejected, all according to an underlying probability distribution for bad moves.

3.6.6.3 Partial PDFs[15]

Partial PDFs are hypothetical PDFs which are calculated similarly to model PDFs used in refinements but using only using certain atoms or atom types. The calculation is done in the same way as that in equation 3.36 but summed only over i and j values corresponding to the chosen species. Partial PDFs allow the contribution of certain atom pairs to the total PDF to be analysed. These can be very useful in assessing changes occurring in structures in response to external stimuli.

3.7 Gas adsorption and release measurements[36-38]

Materials with pores or channels running through them have the potential for very large surface areas. When gas molecules enter the material, they can bind to sites on the internal surface of the material. This is adsorption. Adsorption is loosely divided into physical adsorption, or physisorption, and chemical adsorption, or chemisorption. Physisorption is generally weak, due to induced or permanent dipoles and is usually observed at low temperatures with reduced capacity at higher temperature. Chemisorption involves the exchange of electrons (formation of chemical bonds) between adsorbate and adsorbant and is a much stronger interaction. Whilst physisorption tends to be completely reversible on the decrease in partial pressure, species chemisorbed to a surface are likely to need an extra driving force such as heat for their removal.

Adsorption by a material is generally reported as an adsorption isotherm. Here, the weight, or volume of a gas taken up as a function of partial pressure of the adsorbate is recorded at constant temperature. This is plotted as the equivalent volume of gas at standard pressure and temperature *versus* partial pressure of the gas. Isotherms can be collected using volumetric or gravimetric analysis. Volumetric analysis doses a known pressure of a gas into a volume containing the sample, and the volume uptaken is calculated from the equilibrium pressure achieved. Gravimetric analysis measures the weight of gas taken up the by sample via the very accurate measurements of the sample weight. The shape of the isotherm and maximum adsorption values are unique to a material, and can imply the mechanism of gas adsorption. Isotherms are generally classified by their shape using six general isotherm types as defined Brunauer, and Sing *et al.*[39, 40] These are shown Figure 3-24.

Type I isotherms are characteristic of microporous materials. The initial steep section of the isotherm corresponds to monolayer deposition inside the micropores. Once the pores are filled, there is little extra room for adsorption and so the isotherm reaches a saturation value quickly. Condensation of the gas at high partial pressures results in an increase in uptake. Type I isotherms are characteristic of Langmuir theory (Section 3.7.1.1)

Type II and IV isotherms are found from non-porous materials or mesoporous structures. Type II characterises monolayer coverage at low pressures, a plateau when all energetically favourable sites have been covered, and multilayers at higher pressures. The hysteresis effect in type IV isotherms is due to the different energetics of condensation on the surface of the pore and evaporation away from the pore (the curvature of the surfaces is different in the forward and reverse direction).

When molecules in a gas have a stronger affinity for each other than for the surface of the adsorbant, type III and V isotherms are found. Type VI isotherms result from distinct monolayers being built up on a surface. For this it requires a material with a very uniform surface and no preferential adsorbant sites.

The adsorption isotherms of some materials deviate from these ideal isotherms. An example of this is a gate-opening isotherm. At low concentrations of the guest molecules, there is no appreciable uptake of the gas. Above a specific 'gate-opening' pressure, there is an abrupt increase in uptake by the material. This is generally associated with a structural transformation from a non-porous to a porous phase. At these pressures the material display isotherms similar to type I, where a plateau results from the pore surface being saturated. The gate-opening pressure is dependent on the properties of the gas adsorbed and how this interacts with the framework.[41]
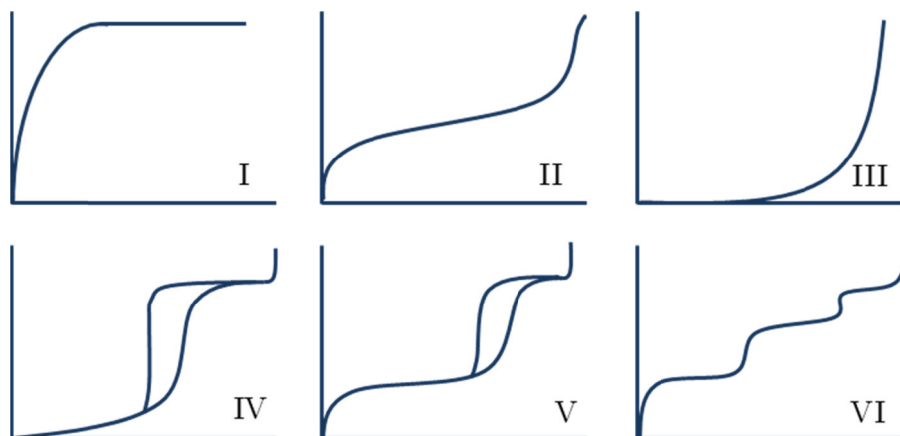
Figure 3-24: The six Brauener isotherms. X-axis shows pressure, y-axis shows amount of gas adsorbed.
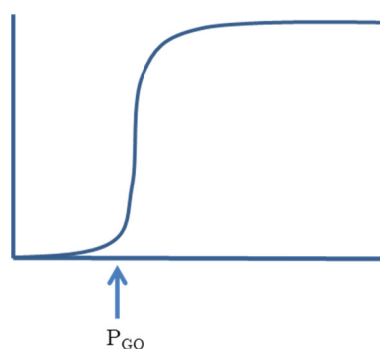
Figure 3-25: Gate-opening isotherm. X-axis shows pressure, y-axis shows amount of gas adsorbed. P_{GO} indicates the gate-opening pressure.

3.7.1 Surface area and porosity measurements

High surface areas are one of the key features of metal-organic frameworks. In the absence of additional gas storage-enhancing features such as CUS and extra-framework cations, surface area is a determinant of how much gas a material will store. The most common way of characterising surface area and pore volume is by nitrogen adsorption at liquid nitrogen temperature, 77 K. The two surface areas which are generally determined and quoted for any new material are the Langmuir and BET surface areas, and whilst these theories are not strictly applicable to microporous materials, they do provide a

100

useful indication of porosity and comparison between structures and can be considered as the equivalent surface area of a material if it had entirely planar surfaces.[42]

3.7.1.1   Langmuir theory[36, 37]

Langmuir theory assumes that all sites on the surface are energetically equivalent and considers only the interactions between gas and surface (assuming that the interaction between gas molecules is negligible). The theory also assumes that during adsorption the collision of the gas with the surface is inelastic – there is a time delay between the molecule hitting the surface and moving away from it, and this is the adsorption process. Assuming that the gas forms only a monolayer on the surface gives V_a, volume adsorbed at a certain pressure, P:

$$V_a = \frac{V_m bP}{1 + bP}$$

(3.38)

where V_m is the quantity of gas that covers the whole surface in a monolayer and b is an empirical constant. Manipulation of this equation gives:

$$\frac{P}{V_a} = \frac{1}{V_m b} + \frac{P}{V_m}$$

(3.39)

A plot of $\frac{P}{V_a}$ vs P should give a straight line in situations where the Langmuir equation applies, with a gradient equal to $\frac{1}{V_m}$ and a y-intercept of $\frac{1}{V_m b}$. The surface area of the adsorbant can be calculated by using the calculated value of V_m in the equation:

$$s = \frac{V_m \sigma N_A}{m V_0}$$

(3.40)

where σ is the area of the surface covered by a single gas molecule, m is the mass of the adsorbing sample, N_A is the Avagadro constant and and V_0 is the molar volume of the gas. Where nitrogen is used, the surface area covered by a molecule is 16.2 Å^2 so the expression becomes:

$$s \left(\frac{m^2}{g} \right) = \frac{4.35 V_m (cm^3 @STP)}{m(g)}$$

(3.41)

3.7.1.2 BET Theory

BET (Brunauer, Emmett and Teller) theory advances Langmuir theory by incorporating the effect of multilayer gas adsorption. It assumes that the force behind the binding of gas to a surface is the same as those forces accounting for condensation for gases. The BET method equates the rate of condensation of gas onto a monolayer with the evaporation of gas away from the monolayer and then sums this effect over an infinite number of layers to give the BET equation:

$$Va = \frac{V_m C P}{(P_0 - P)\left[1 + (C-1)\frac{P}{P_0}\right]} \tag{3.42}$$

where C is a constant and P_0 is the saturation pressure of the gas. C relates to the heat of adsorption of the first layer, q_1, and the heat of liquification, q_L, by the relationship:

$$C \propto exp\frac{q_1 - q_L}{RT} \tag{3.43}$$

where R is the gas constant and T is the absolute temperature of the measurement.

Equation 3.43 can be written in the linear form:

$$\frac{P}{V_a(P_0 - P)} = \frac{1}{V_m C} + \frac{C-1}{V_m C}\left(\frac{P}{P_0}\right) \tag{3.44}$$

A plot of $\frac{P}{V_a(P_0-P)}$ vs. $\left(\frac{P}{P_0}\right)$ can determine V_m and C from the intercept and slope of a regression line. The surface area can be calculated from the volume of the monolayer, by assuming that gas molecules at the surface are close packed and by using the formula:

$$\sigma = (4)(0.866)\left[\frac{M}{4(2N_A\rho)^{1/2}}\right]^{2/3} \tag{3.45}$$

where σ is the mean area per molecule, M is the molecular weight, N_A is Avagadro's number and ρ is the density of the liquid absorbate. Pore volume per unit mass can be assessed from the maximum uptake by assuming that the nitrogen which is adsorbing on the surface at 77K will have the same density as liquid nitrogen.

3.7.2 Equipment used for gas adsorption measurements

All physisorption measurements were performed on a Micromeritics ASAP 2020 surface area and porosity analyser. Approximately 150 mg of material is used for analysis and placed in a glass bulb which is sealed with a rubber seal frit to prevent exposure to the atmosphere. The material is activated to remove all solvent from the pores by heating at 150 °C under vacuum for 1000 minutes and then moved to the analysis port where the gas is dosed incrementally onto the sample. The volume of gas taken up by the sample as a function of partial gas pressure is recorded. For nitrogen, measurements were carried out at 77 K using a bath of liquid nitrogen around the sample. For carbon monoxide isotherms, the temperature was kept constant using a water bath around the sample. Langmuir and BET surface areas are calculated by the ASAP2020 software.

3.8 References

1.   S. Feng and L. Guanghua, in *Modern Inorganic Synthetic Chemistry, eds.* X. Ruren, P. Wenqin, Q. Huo, R. Xu and H. Qisheng, Elsevier, Amsterdam, 2011, pp. 63-95.

2.   C. Giacovazzo, *Fundamentals of crystallography,* International Union of Crystallography ; Oxford University Press, Chester, England, 1992.

3.   W. Clegg, *Crystal structure analysis : principles and practice,* Oxford University Press, Oxford ; New York, 2009.

4.   W. Clegg, *Crystal structure determination,* Oxford University Press, Oxford; New York, 1998.

5.   T. Hahn, U. Shmueli, A. J. C. Wilson and International Union of Crystallography., *International tables for crystallography,* D. Reidel Pub. Co.;Sold and distributed in the U.S.A. and Canada by Kluwer Academic Publishers Group, Dordrecht, Holland ; Boston, MA, 1984.

6.   C. Hammond, *The basics of crystallography and diffraction,* Oxford University Press, Oxford ; New York, 2001.

7.   A. Guinier, *X-ray diffraction in crystals, imperfect crystals, and amorphous bodies,* W.H. Freeman, San Francisco, 1963.

8.   *X-ray Data Booklet,* Centre for X-ray Optics and Advanced Light Source, 2009.

9.   W. Clegg, in *X-ray Structure Analysis, BCA/CCG Intensive Teaching School,* 2009, ch. 8.

10.   P. Main, in *X-ray Structure Analysis - BCA/CCG Intensive Teaching School*, 2009, ch. 9.

11.   G. M. Sheldrick, University of Göttingen, Germany, 1997.

12.   J. D. Dunitz, E. F. Maverick and K. N. Trueblood, *Angew. Chem., Int. Ed.*, 1988, **27**, 880-895.

13.   http://www.ccdc.cam.ac.uk/products/csd/, Accessed 13/01/12

14.   http://cds.dl.ac.uk/cds/datasets/crys/icsd/llicsd.html, Accessed 13/01/12.

15.   R. E. Dinnebier and S. J. L. Billinge, *Powder diffraction : theory and practice,* Royal Society of Chemistry, Cambridge, 2008.

16.   V. K. Pecharsky and P. Y. Zavalij, *Fundamentals of powder diffraction and structural characterization of materials*, Springer, New York, 2009.

17.   H. Rietveld, *Acta Crystallographica*, 1967, **22**, 151-152.

18.   F. O. Rouquerol, J. Rouquerol and K. S. W. Sing, *Adsorption by powders and porous solids : principles, methodology and applications,* Academic Press, San Diego, Calif. ; London, 1999.

19.   S. P. Thompson, J. E. Parker, J. Potter, T. P. Hill, A. Birt, T. M. Cobb, F. Yuan and C. C. Tang, *Rev. Sci. Instrum.*, 2009, **80**.

20.   B. H. Toby, *J. Appl. Crystallogr.*, 2001, **34**, 210-213.

21.   A. C. Larson, R. B. Von Dreele, *General Structure Analysis System (GSAS)*, Los Alamos National Laboratory, Los Alamos National Laboratory, 2000.

22.   S. J. L. Billinge, *Z. Kristallogr.*, 2007, 17-26.

23.   S. J. L. Billinge, *Z. Kristallogr.*, 2004, **219**, 117-121.

24.   S. J. L. Billinge, *Local Structure from Diffraction*, 1998, 137-156.

25.   S. J. L. Billinge and I. Levin, *Science*, 2007, **316**, 561-565.

26.   P. J. Chupas, X. Y. Qiu, J. C. Hanson, P. L. Lee, C. P. Grey and S. J. L. Billinge, *J. Appl. Crystallogr.*, 2003, **36**, 1342-1347.

27.   T. Egami and S. J. L. Billinge, *Underneath the Bragg peaks : structural analysis of complex materials*, Pergamon, Kiddington, Oxford, UK ; Boston, 2003.

28.   T. R. Welberry and T. Proffen, *J. Appl. Crystallogr.*, 1998, **31**, 309-317.

29.   X. Qiu, J. W. Thompson and S. J. L. Billinge, *J Appl Crystallogr*, 2004, **37**, 678.

30.   A. P. Hammersley, S. O. Svensson, M. Hanfland, A. N. Fitch and D. Hausermann, *High Pressure Research*, 1996, **14**, 235-248.

31.   P. Juhás, D. M. Cherba, P. M. Duxbury, W. F. Punch and S. J. L. Billinge, *Nature*, 2006, **440**, 655-658.

32.   K. W. Chapman, D. F. Sava, G. J. Halder, P. J. Chupas and T. M. Nenoff, *J. Am. Chem. Soc.*, 2011, **133**, 18583-18585.

33.   C. L. Farrow, P. Juhas, J. W. Liu, D. Bryndin, E. S. Bozin, J. Bloch, T. Proffen and S. J. L. Billinge, *J. Phys.: Condens. Matter.*, 2007, **19**.

34.   V. A. Burnell, J. E. Readman, C. C. Tang, J. E. Parker, S. P. Thompson and J. A. Hriljac, *J. Solid State Chem.*, 2010, **183**, 2196-2204.

35.   B. H. Toby and S. J. L. Billinge, *Acta Crystallogr., Sect. A: Found. Crystallogr.*, 2004, **60**, 315-317.

36.   P. A. Wright, *Microporous framework solids*, RSC Publishing, Cambridge, U.K., 2008.

37.   J. U. Keller and R. Staudt, *Gas adsorption equilibria : experimental methods and adsorptive isotherms*, Springer, New York, 2005.

38.   P. Webb and C. Orr, *Analytical methods in fine particle technology*, Micromeritics Instrument Corporation, Norcross, Ga., 1997.

39.   S. Brunauer, *The adsorption of gases and vapors*, Princeton University Press; H. Milford, Princeton, London, 1943.

40.   K. S. W. Sing, D. H. Everett, R. A. W. Haul, L. Moscou, R. A. Pierotti, J. Rouquerol and T. Siemieniewska, *Pure. Appl. Chem.*, 1985, **57**, 603-619.

41.   S. Horike, S. Shimomura and S. Kitagawa, *Nat. Chem.*, 2009, **1**, 695-704.

42.   R. E. Morris and P. S. Wheatley, *Angew. Chem., Int. Ed.*, 2008, **47**, 4966-4981.

4 Development of an environmental gas cell for single-crystal studies

4.1 Declaration

Gas loading experiments reported in this chapter were carried out in collaboration with Catherine Renouf, a PhD student with Professor Russell Morris. Both authors have contributed equally to the work, and the results will appear both in this thesis and in that of Miss Renouf in 2013.

4.2 Introduction

Metal-organic frameworks have been suggested as potential gas storage materials due to the high porosity and storage-enhancing features that many frameworks possess. In order to use materials for an application or to design improved materials, it is essential to understand the gas adsorption properties of the material; how much gas can be stored and released; how quickly the adsorption and release takes place; and the reversibility of any gas storage. As part of this, the structural properties of the material must be understood: where are the potential gas binding sites, how does the gas bind to the structure, and how does the structure change on dehydration and gas adsorption? Ideally, adsorption and structural analysis can be linked, enabling the determination of the relationship between gas adsorption and structure by studying the structure under the gaseous environments in question.

In the past, gas-loading powder X-ray diffraction experiments, both *ex situ* (where the gas is loaded onto the material before the diffraction data are collected) and *in situ* (where the gas is loaded onto the material whilst data are collected using specialised equipment such as gas flow cells) have been used to understand gas binding in materials.[1] This method of relating the gas adsorption properties of a material to its structural features is becoming increasingly common in the literature.

Single-crystal X-ray diffraction experiments can provide more detailed structural information about gas-framework adducts. Single-crystal structures for zeolite gas-

adducts are present in the literature as far back as 1974; the group of Karl Seff reported the binding of many small molecule gases (H_2S, CO, NO, C_2H_4, CH_4) to metal-exchanged zeolites through loading single crystals in capillaries, followed by dehydration and gas loading.[2-11] More recently, a similar method has been applied to single crystals of metal-organic frameworks to examine the role of channel-grafted amines in the adsorption of CO_2.[12] Whilst this method gives excellent information about the interactions between gas and framework, a better method still is to combine the two techniques through single crystals studied *in situ*. This gives in-depth information about how the structure of a single crystal changes through the full dehydration/activation and gas loading/unloading process. Environmental gas cells simulate 'real-life' situations relating to gas adsorption. A prototype environmental gas cell has recently been reported[13] and initial development work relating to the gas-loading (CO_2 and SO_2) onto metal-organic frameworks using a gas cell has been reported in the PhD thesis of Dr Anna Warren.[14] Initial experiments on nitric oxide loading onto Co-CPO-27 using an environmental gas cell in flow configuration at Station 9.8 at Daresbury Laboratory were reported in the PhD thesis of Dr Peter Byrne.[15]

4.2.1 Beamline 11.3.1 and the environmental gas cell

Beamline 11.3.1 at the Advanced Light Source, Lawrence Berkeley National Laboratory, is a specialised single-crystal beamline. As part of the equipment on the station, a prototype environmental gas cell has been developed. This equipment allows a crystal to be mounted and isolated in a cell. The crystal can then be exposed to dynamic vacuum as well as to gaseous stimuli. Use of a cryostream device which delivers a stream of dry nitrogen to heat or cool the sample allows simultaneous temperature control.

The environmental gas cell (Figure 4-1) consists of a standard goniometer head with additions to the top of the head to allow isolation of the crystal inside a glass chamber. Unlike many powder environment cells, the single-crystal gas cell has to be able to move with the diffractometer whilst it is rotating to ensure that sufficient points travel through the Ewald sphere for good data completeness. To achieve this, the cell has relatively slim modifications to the standard goniometer head.

The crystal is mounted on a MiTiGen MicroMount and this is glued into a bored hole in the gas cell so that the crystal remains stationary during data collection. The crystal is isolated by placing a glass head over the top of the sample, fixed in place by a

108

threaded loop. The top of the cell is made of glass to enable easy centring of the crystal on the diffractometer using the goniometer hear XYZ adjusters and the standard alignment camera.

Initially glass of 0.5 mm (NMR tube) was used. This meant that the cell was sturdy but also that the I/σ ratio of diffraction data in the region of 1.5 to 1.1 Å was severely diminished by the background scattering of the glass, and for data frames of greater than 20 seconds the background in this region could overload the detector. Subsequently, glass of 60 micron thickness was used. This was strong enough to allow the application of a dynamic vacuum but gave very little background scattering, allowing very reasonable data to be collected in all regions.

The glass head is soldered into a metal base, which is placed on top of the gas cell base and secured by means of a metal screw loop. Any small leaks can be sealed using vacuum grease or glue. To ensure a good seal of the system, an O-ring is placed at the interface of the glass head and the cell base. The gaseous environment of the cell is controlled via a hole in the gas cell base leading to a metal tube which leaves the gas cell at the base of the modified head. The metal tube is directed away from the glass head and is attached via a Swagelok adapter to a 1/16 inch Teflon tube connecting the cell to the gas rig. This flexible tube allows the cell to move freely with the diffractometer during data collections.

The temperature of the crystal environment can be controlled using the Oxford Cryostream 700 Plus device. The working temperature range of the cell is from 283 K to 500 K. Lower temperature data collections would be desirable in order to decrease uncertainty in atomic positions and this is particularly important in the case of adsorbed gas molecules, which show a high degree of movement and disorder. However, temperatures lower than 283 K were shown to distort the O-ring and break the vacuum seal in the system and so are not currently available. Vacuum can be pulled on the cell using a pump outside of the hutch. The pressure of the unit is monitored by a vacustat placed between the gas cell and the vacuum pump.

The gas cell is a static cell, meaning that gas flow in and out of the cell is via the same pathway. Gas flow is controlled via a gas rig outside of the hutch. This allows evacuation of the cell using a vacuum pump and introduction of a required pressure of gas into the cell. The external computerised control of the gas mixing rig, previously

unreported, allows the collection of data throughout the dehydration, gas adsorption and desorption process at precise gas pressures without entering the hutch.
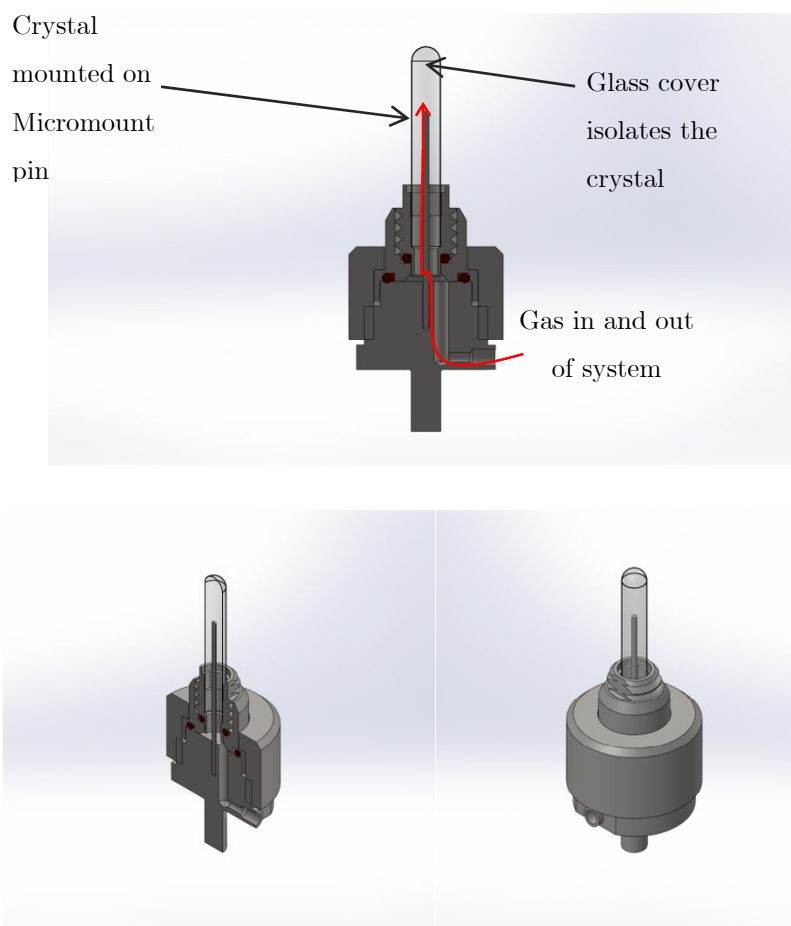

Figure 4-1: The environmental gas cell at beamline 11.3.1 (pictures courtesy of Simon Teat and Jamie Nasiatk).

Using the cell in combination with a synchrotron source is beneficial as the higher flux allows the use of smaller crystals which are more easily penetrable by gases. Additionally, collection times are much reduced (each data collection taking between 1.5 to 4 hours) meaning that the crystal can be studied under a variety of conditions with experimental times of the order of days as opposed to weeks on a standard laboratory diffractometer, a length of time for which many samples are unlikely to remain crystalline, especially under gaseous environments.
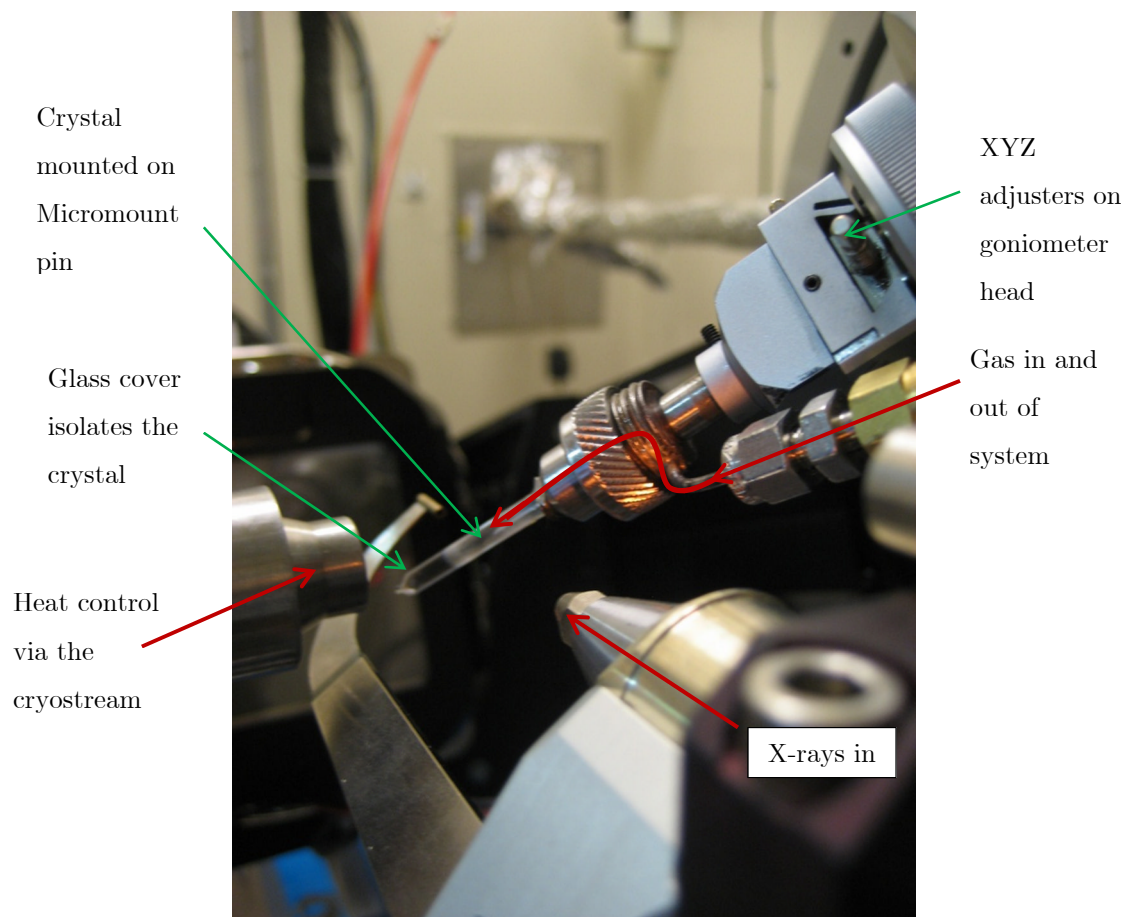
Crystal mounted on Micromount pin

XYZ adjusters on goniometer head

Glass cover isolates the crystal

Gas in and out of system

Heat control via the cryostream

X-rays in

Figure 4-2: Environmental gas cell mounted on the diffractometer at 11.3.1.

4.2.2 Co-CPO-27

The Co-CPO-27 framework is a cobalt-based metal-organic framework, with formula $[Co_2(C_8H_2O_6)(H_2O)_2]\cdot 8H_2O$. The first report of this framework was in 2005 by Dietzel *et al.*, shortly after the report of the isostructural zinc material, named MOF-74(Zn), was reported by the group of Yaghi.[16,17] These structures form part of a family of frameworks that share the same topology but with different metals making up the nodes in the structure. To date the same ($[M_2(C_8H_2O_6)(solvent)_2]\cdot solvent$) topology has been reported for M = Co,[16] Ni,[18] Zn,[17,19] Mg,[20] Mn[21] and Fe[22,23]. Within the literature this topology is sometimes referred to as MOF-74(M), M_2(dhtp) or M_2(dobdc), but in this thesis all frameworks are named M-CPO-27 for clarity.

The Co-CPO-27 framework was chosen for single-crystal studies. The structure is made up of chains of cobalt octahedra linked by *cis*-oriented edges into a helical chain

which runs parallel to the *c*-axis. Chains are linked by 2,5-dihydroxyterephthalic acid linkers forming a honeycomb framework with channels of approximately 11 Å running parallel to the *c*-axis. Figure 4-3 shows the Co-chains (top left), linker molecule (bottom left) and a unit cell of the framework with hexagonal channels viewed down the *c*-axis (right). Coordination of the linker molecule accounts for 5 out of 6 of the metal coordination sites: 3 carboxylate oxygens and 2 hydroxyl oxygens. The sixth is accounted for by a coordinated water molecule, which points into the channel of the material. This site is the most important for this work because the coordinated water molecule can be removed, leaving co-ordinatively unsaturated sites (CUS) on the metal ions. These sites are generally high energy and gas molecules adsorbed into the structure are known to interact strongly with them. The adsorption of a variety of gases, including nitric oxide, carbon dioxide, methane, hydrogen and carbon dioxide via interaction with the CUS, has been quantified in the literature. This interaction has been characterised by a variety of methods including powder X-ray diffraction, IR, EXAFS and neutron diffraction (Table 1).

While the isostructural nickel material has been used for many PXRD studies, Co-CPO-27 crystallises well with single crystals of up to 100 microns available. The dehydration of Co-CPO-27 is well understood and it has been shown that it is possible to dehydrate this material in single-crystal form.[16] The structure of Co-CPO-27 is highly crystalline and was shown by Dietzel *et al.* to have permanent porosity; the structure shows good crystallinity even after the removal of all solvent molecules within the structure. The ability to change the molecule on the open metal site is dependent upon the interaction energy between gas and framework. Coupled with the good crystallinity of the material, this makes Co-CPO-27 an ideal material for studying the structural details behind gas adsorption properties.
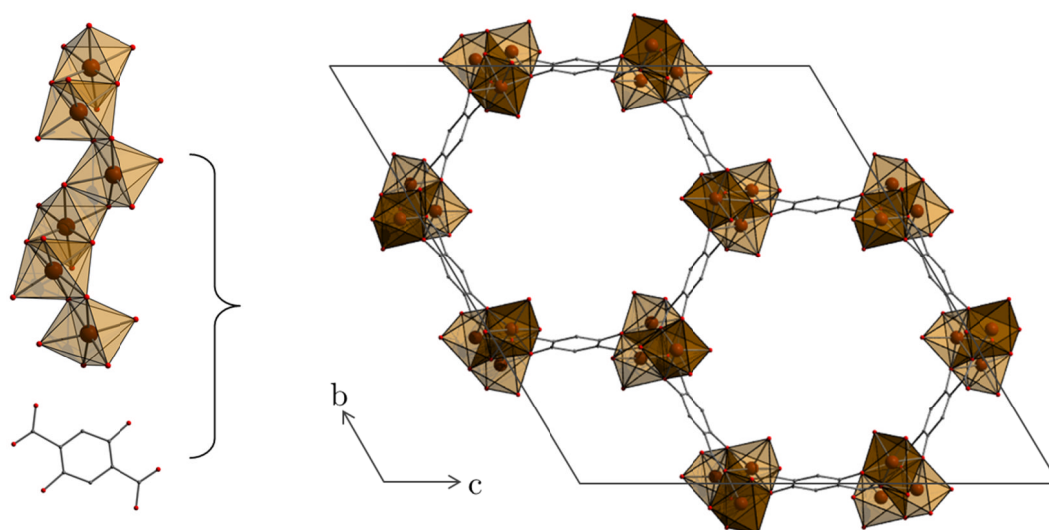
Figure 4-3: Schematic of the Co-CPO-27 framework. Cobalt = orange, carbon = grey, oxygen = red. This colour scheme is used in all subsequent figures, with nitrogen = blue.

Table 1: Summary of reported framework-gas interactions for the M-CPO-27 series.

Metal	Gas	Analysis method	M-X distance/$\mathring{A}$	Binding mode
Co	NO	PXRD,[24, 25]	Co-N 2.196(16) (293 K)	Coordination to metal site through N; M-N-O = 140.4°
Mg	CH_4	Neutron[26]	Mg-C 3.04 Å	Coordination to metal site
Zn,[27] Mg	H_2/D_2	Neutron[28], INS	Zn-H 2.6 Å (4K)	Interaction with metal site (geometry not reported)
Ni	CO_2	PXRD[29]	Ni-O 2.29(2) Å , Ni–C 3.04(2) Å (100 K)	Coordination to metal site through O, end-on; M-O-C = 117(2)°
	CO	IR[30]	-	Coordination to metal site through C; Linear
Fe	O_2	Neutron diffraction[22]	Fe-O 2.09(2) and 2.10(1) Å (4 K)	Symmetric side-on coordination mode to metal site
	N_2	Neutron diffraction[22]	Fe-N 2.30(1) Å (80 K)	End on coordination to metal site, Fe–N–N angle of 179(1)°
Ni, Fe, Co	C_2H_2	IR[31]	-	Side on π-coordination to interaction with metal site.

4.2.1 Nitric oxide

Nitric oxide is an important biological signalling molecule (section 1.1). Previous work has shown that nitric oxide released from MOFs can have a targeted biological effect (section 1.8.1.2). In addition to the biological interest, the properties of nitric oxide mean that it is ideal as a probe gas for MOF systems; although toxic in large amounts, it is relatively easy to handle and has low liquefaction temperatures and pressures. Additionally, it is a radical molecule that is known to readily form stable compounds with transition metals at the working temperature of the gas cell.

Previous work indicates a strong interaction between NO and the framework; Q_{st} for NO with Ni-CPO-27 has been estimated by IR studies as $90-92$ kJ/mol^{-1} indicating a chemisorption interaction.[25, 32] This strong interaction means that it is likely that the NO-adduct will be sufficiently ordered at the temperatures accessible to the gas cell to determine a structure.

The interaction of nitric oxide with this material has been studied in the past. Adsorption and release isotherms report that a significant amount of nitric oxide can be stored in the dehydrated material, and the isotherms show significant hysteresis, indicating that the gas is chemisorbed. The nitric oxide can be released on exposure to water which displaces the nitric oxide on the metal site, reforming the hydrated metal-coordination.[25]

The work of Seff and coworkers indicates that NO binds via the nitrogen to the Co-centre in Co-exchanged LTA, with a Co-N-O bond angle of 141(3)°.[3] PXRD data reported by McKinlay *et al.* indicates that nitric oxide binds to the Co-centre in Co-CPO-27 in a bent, end-on manner through the nitrogen, with Co-N and N-O bond lengths of 2.196(16) and 1.43(3) respectively and a Co-N-O angle of 140.4(16)°.[25] This end-on binding mode is similar to that of nitrogen, which was recently reported to bind in a linear fashion in Fe-CPO-27, and is significantly different to the O_2 molecule which binds through symmetric side-on coordination.[22] PXRD data has further been used to study the NO-binding to isostructural materials, Ni-CPO-27, Zn-CPO-27 and Mg-CPO-27 which show a similar bent configuration.[24]

The model for the nitric oxide adsorbed on the cobalt site was improved by studies on single crystals performed by Dr Peter Byrne using an environmental gas cell in flow

configuration. Nitrogen flow was used in combination with heat to partially dehydrate the material before the nitrogen flow was replaced by a low flow of nitric oxide. Nitric oxide was found to coordinate to the Co-centre in a bent confirmation. Two sites for the oxygen atom of nitric oxide were located, suggesting a degree of delocalisation. The high level of hydration in all data sets leads to ambiguity about the relative abundances of species on the metal centre, and a high level of restraint was needed to model the nitric oxide.

4.3 Aims

Experiments in Chapter 4 have two main aims. The first is to develop and use an environmental gas cell for the study of gas adsorption using single-crystal X-ray diffraction techniques. The experiments seek to determine potential problems with the set up in order to change and improve the performance of the gas cell set up. The material Co-CPO-27 is chosen as a test material for the gas adsorption experiments.

Secondly, this study aims to correlate structural details through the full dehydration/adsorption/release cycle with the reported nitric oxide isotherms on the material. To do this, the previous work on nitric oxide in the MOF Co-CPO-27 will be extended by using a new prototype static cell, as opposed to a the flow configuration previously reported, and will additionally demonstrate the first use of a computerised gas rig for gas loading at precise pressures. Through this study it is hoped to confirm and improve the previously suggested models of nitric oxide on Co-CPO-27 by achieving and maintaining a high level of dehydration of Co-CPO-27 in the gas cell throughout the data collection. Nitric oxide gas loaded onto the material aims to determine unambiguously the nature of the gas-loaded adduct of Co-CPO-27. Finally, an understanding of how the nitric oxide gas can be removed from the Co-CPO-27 material will be studied using vacuum, heat and moisture as stimuli to remove the nitric oxide.

4.4 Synthesis of Co-CPO-27

The synthesis of Co-CPO-27 was done using literature methods.[16] A 2:1 ligand:metal ratio was used in the synthesis of good quality crystals; 149 mg (0.75 mmol) of 2,5-dihydroxlteraphtahlic acid (dhtp) was dissolved in THF (10ml) and added to a

solution of 187 mg (0.75 mmol) of $Co(OAc)_2 \cdot 4H_2O$ in 10ml water. The resulting solution was heated in a 50ml Tefon-lined autoclave at 383 K for 5 days. Crystals were filtered and dried in air overnight. An orange crystalline solid was obtained and the product confirmed by PXRD as $[Co_2(dhtp)(H_2O)_2] \cdot 8H_2O$.

4.5 General experimental procedures

Details of activation and gas loading processes are given in the relevant experimental sections, but the general processes are as follows.

4.5.1 Activation and data collection

A well-formed single crystal was chosen and glued with a minimal amount of glue to a Micromount 25-10-x pin. The crystal was glued such that the least amount of the crystal's surface was in contact with the glue and mount to ensure that the water in the material could be removed easily. The mount was glued into the gas cell unit and isolated using the glass cell head. The gas cell was placed under vacuum, and checks were carried out to ensure that the cell held vacuum when not exposed to the dynamic vacuum.

After the mounting of a new sample, either a full data set, or several diffraction images were taken (depending on time restrictions) to determine crystal quality. All data were collected using a Bruker AXS ApexII diffractometer and were reduced using the corresponding Bruker ApexII software. The data were collected using omega-scans, through an angle range carefully defined to prevent the gas cell colliding with collimator whilst still allowing good completeness of the data. The gas cell collection strategy is shown in Table 2. Collection times depended on crystal size and quality but were generally between 1 and 5 seconds. The data were corrected for absorption effects using the program SADABS.

Table 2: Gas cell collection strategy.

Operation	Distance (mm)	2theta (deg)	Omega (deg)	Phi (deg)	Chi (deg)	Time (sec)	Width (deg)	Sweep (deg)	Direction
Omega Scan	50	-36	-36	200	54.71	1	0.3	180	negative
Omega Scan	50	-36	-36	100	54.71	1	0.3	180	negative
Omega Scan	50	-36	-36	0	54.71	1	0.3	180	negative
Position	50	-36	-36	90	54.71				

The gas cell was placed on the diffractometer and aligned using the XYZ adjusters of the goniometer head. The cell was aligned so that the sample was as close to the Crysostream as possible to ensure maximal heat transfer. The Cryostream was used to heat the cell and the temperature quoted in data is that of the Cryostream gas temperature. This may be slightly higher than the temperature inside the cell due to incomplete heat transfer. The crystal was heated for a number of hours to remove the water in the pores and also that coordinated to the metal sites. Data sets were taken throughout the heating process to monitor the dehydration. A data set was also taken to determine whether the material was sufficiently activated. The cell was then cooled under vacuum to the experiment temperature.

In early dehydration experiments it was found that while the material appeared to be dehydrated when under vacuum, reversal of the flow direction through introduction of gas to the cell also introduced water, and this coordinated to the open metal site preferentially over the nitric oxide. It was thought that some water accumulated in the tube connecting the gas rig and the cell during the dehydration process, which was reintroduced into the cell when the gas flow was reversed. This tubing is of narrow diameter and is not heated, so it is unsurprising that the vacuum is not very strong in the tube and that water condenses quite quickly before it is pulled into the pump.

Another method attempted to remove this water was to heat under alternating atmospheres of vacuum and low-pressure nitrogen. Nitrogen was added to the cell and the cell was heated before the nitrogen was removed and the cell heated under dynamic vacuum for 30 mins. The process was then repeated. However, it was found that the small amount of water present in the nitrogen and in the tubing of the setup was detrimental to the dehydration process so this method was not used routinely.

More success was achieved by heating the gas lines using a heat gun on a low heat several times throughout the activation process in order to remove the water in the tubing. Heating commenced close to the cell and worked towards the gas rig end of the lines. In a typical run, the lines were heated a) when the cell reached temperature, b) before the cell was cooled to room temperature and c) directly before any gas was introduced into the system. During long activation procedures the lines were heated occasionally throughout the activation. Not all the lines are accessible for heating in this manner, so the solution is not ideal, but it did lead to a considerable improvement in the degree of dehydration maintained.

4.5.2   Gas loading experiments

Prior to gas loading experiments a 'leak test' was done on the cell to make sure that there would not be significant gas release from the cell over the experiment. The cell was closed off to the vacuum and the pressure gauge was monitored for 5 minutes. A pressure rise of 2 Torr in this time was considered acceptable. If the cell passed the leak test then we proceeded with gas loading experiments. If it failed then the source of the leak was located and the sample was reactivated by the procedure above.

Gas loading in early experiments was done using a prototype gas loading setup. In this setup, gas was introduced from the gas cylinder into the lines up to the gas cell valve, and then added in segments up to a pressure of 1 atmosphere. For later experiments a computerised gas control rig was used, and this allowed the introduction of an accurate pressure of gas through the use of mass flow controllers. The gas was first introduced into a 'mixing chamber' where the partial pressure of one or more gases could be stored and mixed. The gas was then flowed into the gas cell area by opening a valve. A general procedure was to introduce just less than 1 atmosphere of gas into the mixing chamber before allowing gas into the cell. The pressure was then 'topped up' to slightly above 1 atmosphere to ensure that any gas leaks would result in a gas flow out of the cell, rather than air flow into the cell.

Once loaded, a period of 5 minutes was left for equilibration before the data collection was started. During data collection, if the pressure of gas in the cell fell to below atmospheric pressure then a small amount of gas was introduced into the cell to 'top up' the pressure. This procedure prevented water entering the cell from the

atmosphere. Subsequent to data collection, the gas was removed by pulling dynamic vacuum on the sample for at least 10 minutes until the pressure was at a minimum.

In situations where we experienced constant crystal rehydration on exposure to gas, gas loading was performed with the cell at elevated temperature. This was to expose the crystal to nitric oxide at a temperature where the water in the cell had not had a chance to coordinate to the metal centre. Once nitric oxide was in the cell the system was cooled and data collection was begun.

4.6 Dehydration studies

4.6.1 Previous studies of dehydration

The hydrated and dehydrated crystal structures of this material have been reported by Dietzel *et al.*[16, 19] There are 4 crystallographically independent bulk water sites in the structure, and a water molecule coordinated to the metal centre (O1c) (Figure 4-4). O1w sits approximately 2.934(12) Å from O1c forming a hydrogen bonding interaction to this atom, and also sits 3.038(12) Å from the ligand, and O1w is likely to be stabilised by interactions with both the framework and O1c. Both types of solvent molecules - those that sit in the pores and those that are coordinated to the metal centre - are removed by heating the material to 100 °C in a dry argon gas stream.
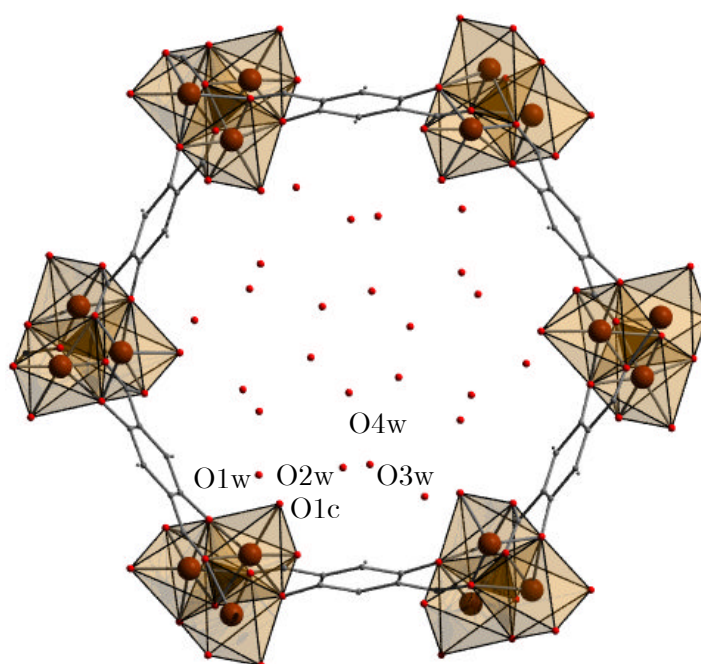

Figure 4-4: Hydrated Co-CPO-27 with water molecules labelled.

A variable temperature PXRD study performed in air showed that the water molecules closest to the centre of the channels (O3w and O4w) are removed very quickly on commencement of heating.[19] The remaining bulk water (O1w and O2w) is removed between 90 and 120 °C. The coordinated solvent molecule, O1s, is mostly removed between 108 and 140 °C and is completely removed by 180 °C.

4.6.2 Dehydration within the gas cell

In order to determine whether the single-crystal sample could be dehydrated in the gas cell, a sample was placed in the gas cell under vacuum, heated from 300 K to 400 K at a heating rate of 30 K/hr and held at this temperature for 8 hours. The temperature was increased continually throughout the data collections but the temperature quoted in the data is the median Cryostream temperature over the time taken for the three runs of data to be collected, and is approximated to be the crystal temperature. Data were collected by using continuous omega-scans of 5 second collection time whilst heating the crystal. The omega-scans were then integrated in groups of three, with each run being integrated in three different groups; for example runs 123, 234, 345 were all integrated separately to minimise the temperature interval for the data. The data were corrected for absorption effects using the program SADABS. The structures were solved using the program SIR-97 and refined on F^2 using full-matrix least squares using the program SHELXL-97 within the WinGX suite of programs. Non-hydrogen framework atoms were refined anisotropically, and the hydrogen atom present on the organic linker was placed geometrically using the HFIX command and refined with the value of U_{iso} set to be 1.5 times greater than the carrier atom. The coordinated water molecule, O1s, was found in the original solution from SIR97 in all data sets. Additional bulk water molecules were placed according to the residual electron density maxima (Q-peaks) found in the Fourier map of the low temperature data set, and placed in all subsequent data sets, until their occupancy was found to be zero. At this point they were removed from the model. No further significant Q-peaks (height greater than 0.5 electrons $Å^{-3}$) were found in the channel of the dehydrated material, indicating that the water was removed from the material and had not just moved within the channel.

For O1s, the coordinated solvent molecule, both the ADPs and occupancy were refined freely in all data sets. For each data set, after the main framework atoms (including the coordinated solvent molecule O1s) were placed and refined anisotropically.

The remaining electron density present in the pores of the materials was assessed using the program PLATON SQUEEZE.[33, 34] PLATON SQUEEZE is an algorithm used to determine the electron density present outside of the ordered part of the structure. The electron density within a solvent accessible void (defined as a region where a sphere of 1.2 Å can be accommodated without intersecting with any of the van der Waals radii of any of the atoms in the structure) is calculated and assigned as a contribution from disordered guests. SQUEEZE produces a new reflection file with these contributions removed that can be refined against the original model, and additionally gives a value estimating the number of electrons per cell which are assigned to disordered guests. Therefore SQUEEZE can be used to give an estimate of the disordered guests (e.g. physisorbed gas molecules) present in the pores of a framework.

The occupancy and anisotropic displacement parameters of the oxygens atoms of the water molecules were carefully refined. Thermal parameters and occupancy factors are linked;[35] for instance, when a site is partially occupied the thermal parameter may be unusually large as the refinement attempts to place enough electron density for the occupancy to be unity. For the case of disordered solvent molecules, the thermal parameters are likely to increase with temperature as the disorder of the solvent increases due to the flexible bonding environment. A value was chosen for the thermal parameter of bulk solvent molecules of 0.05 Å^2, which was approximately twice that of framework atoms, to account for the increased movement that non-bonded atoms are likely to have, particularly at higher temperatures. The occupancy of oxygens of the bulk water was then refined freely. To determine whether this method was suitable, a Fourier map (F_o - F_c) was calculated in the plane of Cu-O1s-O1w with the partial occupancy and thermal parameter set for the Run 7 data set. No negative electron density can be seen around the solvent sites, indicating that the model is not placing electron density from the channel in the water positions. When the occupancy was set to unity and the Fourier synthesis was repeated, negative electron density can be clearly seen, indicating that the occupancy of the water molecules is set too high.

Results are shown in Figure 4-5 and Table 3. The non-coordinated solvent molecules in the middle of the channel are removed quickly when the sample is placed under vacuum. O1w can be removed by mild heating under vacuum. Approximately 35% of O1c can be removed by placing the sample under vacuum. More can be removed after prolonged heating at 400K; in the final data set, the O1c occupancy was determined

to be 0.053(19). A further data set was taken after the sample had been activated for 8 hours. No significant Q-peaks were found in the channel of the material, indicating that dehydration was complete.

These results indicate that it is possible to dehydrate Co-CPO-27 in the environmental gas cell on beamline 11.3.1. The experimental conditions required for dehydration are heating to 400 K overnight under vacuum. The vacuum from the pump appears to be strong enough to remove the water from the pores, indicating that this activation process leads to a material suitable for gas-loading experiments. Good data were collected for all data sets. The R_{int} and R_1 values initially improve with temperature to a value of around 6% for R_{int} as a result of the removal of disordered solvent molecules in the initial data sets.

Table 3: Selected data for the dehydration of Co-CPO-27 in the gas cell.

| Dataset	Run	T /K	Vacuum	Squeeze	R_1	R_{int}
dehydinitial	1	300	No	466	9.84	9.05
dehyd123	2	336	Yes	338	8.29	9.83
dehyd234	3	354	Yes	218	6.38	7.97
dehyd345	4	372	Yes	211	6.1	7.04
dehyd456	5	390	Yes	222	5.88	6.29
dehyd567	6	400	Yes	229	5.90	6.04
dehyd678	7	400	Yes	197	5.83	6.03
dehyd789	8	400	Yes	200	5.86	6.07
dehyd8910	9	400	Yes	197	5.91	5.99
dehyd91011	10	400	Yes	201	6.08	6.38
dehyd101112	11	400	Yes	200	6.08	6.18
dehyd111213	12	400	Yes	200	5.99	6.11
dehyd121314	13	400	Yes	192	5.82	6.08
dehyd131415	14	400	Yes	190	6.61	6.08
dehyd141516	15	400	Yes	198	5.99	6.46
dehyd151617	16	400	Yes	200	5.94	6.26
dehydfinal	17	400	Yes	219	5.95	6.07
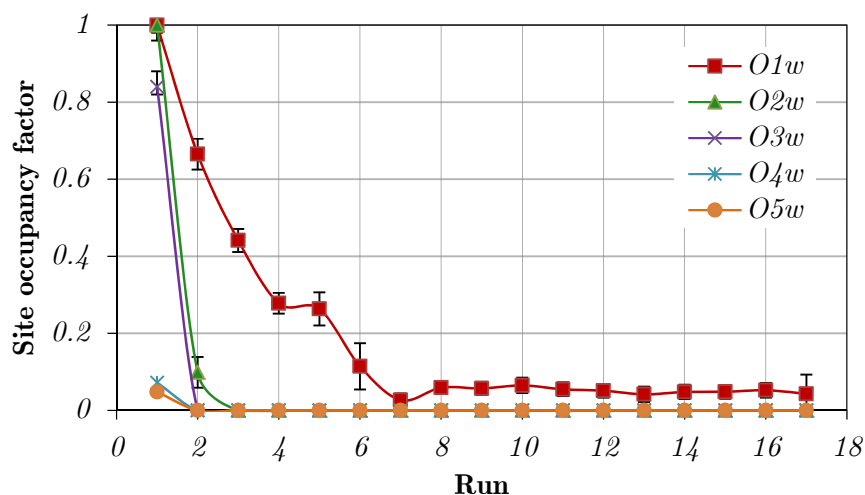
Figure 4-5: Water occupancy in Co-CPO-27 as a function of temperature. Error bars are estimated standard deviations (esds) determined from the least-squares SHELXL refinement.

4.7 Gas-loading studies

4.7.1 Experimental details

The cell was placed under vacuum on the diffractometer and a data set (CPOhyd) was taken at room temperature. The cell was then heated at a rate of 30 K/hr to a temperature of 500 K and held at this temperature for approximately 8 hours. A data set (CPOdehyd) was taken and showed that the water occupancy on the metal site was 0.050 (17). This extent of dehydration was deemed acceptable for further gas loading experiments.

The cell was cooled to 300 K. The pipes connecting the gas cell to the gas rig were heated using a heat gun for a period of 10 minutes before the gas was introduced to remove any water that had condensed in the tubes so that it was not reintroduced into the cell when the direction of flow was reversed. Gas was introduced into the cell in short bursts up to a pressure of 800 Torr. The cell was allowed to equilibrate for 10 minutes before starting a data collection (CPOno). After data collection the excess NO was removed from the system using dynamic vacuum for 1 hour before the gas cell was opened to the air.

Structures were solved using the program SIR-92 and refined on F^2 using full-matrix least squares using the program SHELXL-97. Non-hydrogen atoms were refined

anisotropically, and the hydrogen atom present on the organic linker was placed geometrically using the HFIX command, and refined with the value of U_{iso} set to be 1.5 times greater than the carrier atom on which the HFIX command was centred. Water molecules present in the sample were identified using a Fourier difference map. Where partial occupancy of water molecules was evident, the U_{iso} value of the atom was set to a sensible value (taking into account the temperature of the data collection and the U_{iso} values for other atoms in the structure) and the occupancy allowed to refine freely. Data sets were refined until convergence was achieved and no further significant Q-peaks were identified in the Fourier difference map. Selected data for the structural refinements are shown in Table 4. Data collected in the gas cell are of high quality; the internal error on the data is relatively low, and refinements show convergence to low r-values.

Table 4: Refinement details for hydrated, dehydrated and NO-loaded Co-CPO-27.

	Hydrated	**Dehydrated**	**NO-loaded**
T/K	300	500	300
R_{int}/R_σ	0.091/0.073	0.061/0.037	0.068/0.044
formula	$CoHC_4O_7$	$CoHC_4O_{3.05}$	$CoHC_4O_4N$
FW/g mol^{-1}	219.98	155.98	185.99
crystal system	trigonal	trigonal	trigonal
space group	R-3	R-3	R-3
a/Å	26.106 (5)	25.950 (5)	25.911 (5)
c/Å	6.714 (5)	6.819 (5)	6.794 (5)
V/Å^3	3963 (3)	3977 (3)	3950 (3)
Z	18	18	18
ρcalc/Mg m^{-3}	1.946	1.573	2.643
μ/mm^{-1}	3.73	2.51	5.01
data/restraints/ parameters	2836/100/0	1267/77/0	1638/106/0
R(F) (I > 2σ(I))/%	0.0786	0.0595	0.0690
R(F) (all)/%	0.1048	0.0703	0.0854
$R_w(F^2)$ (I > 2σ(I))/%	0.2756	0.2622	0.2607
$R_w(F^2)$ (all)/%	0.2830	0.2643	0.265
GoF	1.81	2.09	1.97

4.7.2 Comparison of the hydrated, dehydrated and NO-loaded crystal structures

The hydrated (Figure 4-7, top) and dehydrated (Figure 4-7, middle) crystal structures of the material are identical to those reported by Dietzel *et al.*[16] A summary of data collection details is shown in Table 4. Full refinement details can be found in CPOhyd.cif and CPOdehyd.cif in Appendix B. In the hydrated material, five of the coordination sites of the cobalt atom are coordinated by ligand groups and the sixth coordinated by a water molecule from the synthesis. Bond lengths for the Co-coordination sphere are given in Table 5, and bond angles are shown in Table 6. Four Co-O bonds are fairly short, in the range of 2.043(4) to 2.059(4) Å. The Co-O1w bond length is longer at 2.139(6) Å and the bond length trans to this is also elongated at 2.190(4) Å.

The unbound water molecules in the channel and O1w are removed from the material and are present at 5% occupancy at 500 K. Bond lengths for the cobalt coordination sphere are found in Table 5. The removal of the coordinated water molecule results in a change of coordination of the Co-atom from octahedral to square-pyramidal geometry. Additionally, there is a slight reduction in all Co-O bond lengths, which can be associated with the decreased electron count on the metal-centre. The Co-O1(trans) bond length shows particular contraction, from 2.190(4) to 2.072(6) Å. Bond angles show relatively little change (Table 6 versus Table 7).

The structure for dehydrated Co-CPO-27 was used as a starting model for the nitric oxide-loaded structure. Positions of the framework atoms were refined anisotropically, and the hydrogen atoms on the ligand molecules were placed geometrically. The highest Q-peak of height 6.61 electrons $Å^{-3}$ was found at a position analogous to the positions of the water molecule in the hydrated structure. This was assigned as a nitrogen atom with unity occupancy, and the positions and thermal parameters were refined. The ADP for the nitrogen was slightly larger than that found for other framework atoms, but similar to that of the coordinated water molecule in the hydrated structure of the material. A Fourier search highlighted three significant peaks around the nitrogen atom of heights 1.90, 1.76 and 1.33 electrons $Å^{-3}$. These were assigned as oxygen atoms of the nitric oxide. The occupancies of these peaks were fixed to 0.17 and the thermal parameter for each atom refined freely. Thermal parameters

were quite large, indicating a high degree of disorder or lower occupancy of the sites than was assigned. Three further peaks were located in a Fourier difference map and assigned asoxygens When the thermal parameters were fixed at a value of 0.05 Å^2 and the occupancies refined freely, the total occupancy of the site summed to 87.190%. No further peaks appeared in this area in the Fourier map. The final refinement converged to a value of 6.87%.

The nitric oxide structure (CPOno.cif, Appendix B) can be described in the same space group as the other structures. Nitric oxide coordinates through the nitrogen to the metal-centre in a bent coordination. For an unrestrained refinement, the Co-N bond length is 1.94(3) Å - shorter than the Co-O(w) bond length in the hydrated structure. This is also considerably shorter than the Co-N bond length determined from powder diffraction (2.19(2)Å).[25] The oxygen atom is disordered over several sites. Six sites were located from the Fourier map, though in reality the nitric oxide is probably either spinning or delocalised over a circle of positions around the nitrogen.

Significantly, nitric oxide coordinates in a bent manner to the metal centre; the Co-N-O bond angles are in the range of 120(2)° to 135(5)° with a mean value of 128.2 ° (Standard error on the mean, SEM = 2.05). This indicates that the nitric oxide acts as a 1-electron donor to the metal centre, and, as such, is sp^2 hybridised, with the lone pair residing in the sp^2 orbital coordinating to the metal centre. 1-electron donation is common in the later transition metals as these centres are often electron-rich. The mean N-O bond length of the structure is 1.082 Å (SEM = 0.035). For 1-electron donation (NO$^-$), the N-O bond order is reduced to 2, meaning that this bond length is expected to be longer (approximately 1.14 Å). This is likely to be artificially short because of the high level of disorder in the material resulting from the nitric oxide spinning on the metal site. More electrons are likely to be found in the area of the nitrogen-oxygen bond than at each oxygen site (each of which only contains 1/6 of an oxygen at most) meaning that the model places oxygen atoms falsely close to the nitrogen atom.

SADI commands were used to restrain the O_{NO} atoms to a regular hexagon, with identical Co-O_{NO} and N-O_{NO} bond lengths for all oxygen atoms. This led to a Co-N bond length of 1.95(1) Å and an average N-O_{NO} bond length of 1.07(4) Å. R_1 converged to 7.09% (CPOnoPartialRestraint.cif).

The refinement was further restrained using DFIX and SADI commands to fix the Co-N and N-O bond lengths. The Co-N bond was restrained to a length of 2.23(5) Å (the value determined by Cruz *et al.*[3]) and the N-O bonds were restrained to be identical and of length 1.14 (6) Å which is the average double N-O bond length found in the Cambridge Structural Database. Addition of these restraints led to an increase in R_1 to 8.15%, and the thermal parameters of the O_{NO} atoms increased considerably. A Co-N bond length of 2.141 (8) Å and an average N-O_{NO} bond length of 1.136 (SEM = 0.002) Å were determined. This data can be found in CPOnoRestrained.cif.

The occupancy of the nitrogen species coordinated to the Co-atom is unity. The total occupancy of the O_{NO} is 87(2)%. The 13% discrepancy in occupancy indicates that either some O_{NO} occupancy is not accounted for in the model, or that there is duel occupancy of the water and nitric oxide on the site. To model the duel occupancy the nitrogen site occupancy factor was fixed as 0.872 and an oxygen atom was placed close to this site with a site occupancy factor of 0.128. The refinement converged to a value of 6.95% with a Co-N_{NO} distance of 1.95(1) Å and a Co-O_w bond length of 2.00(6) Å. This is shown in Figure 4-8.
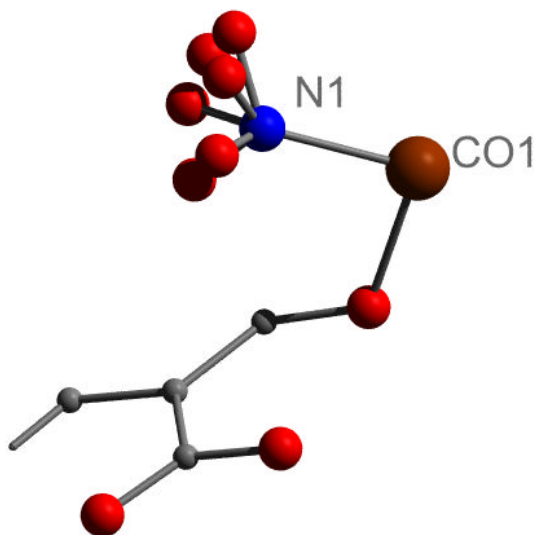

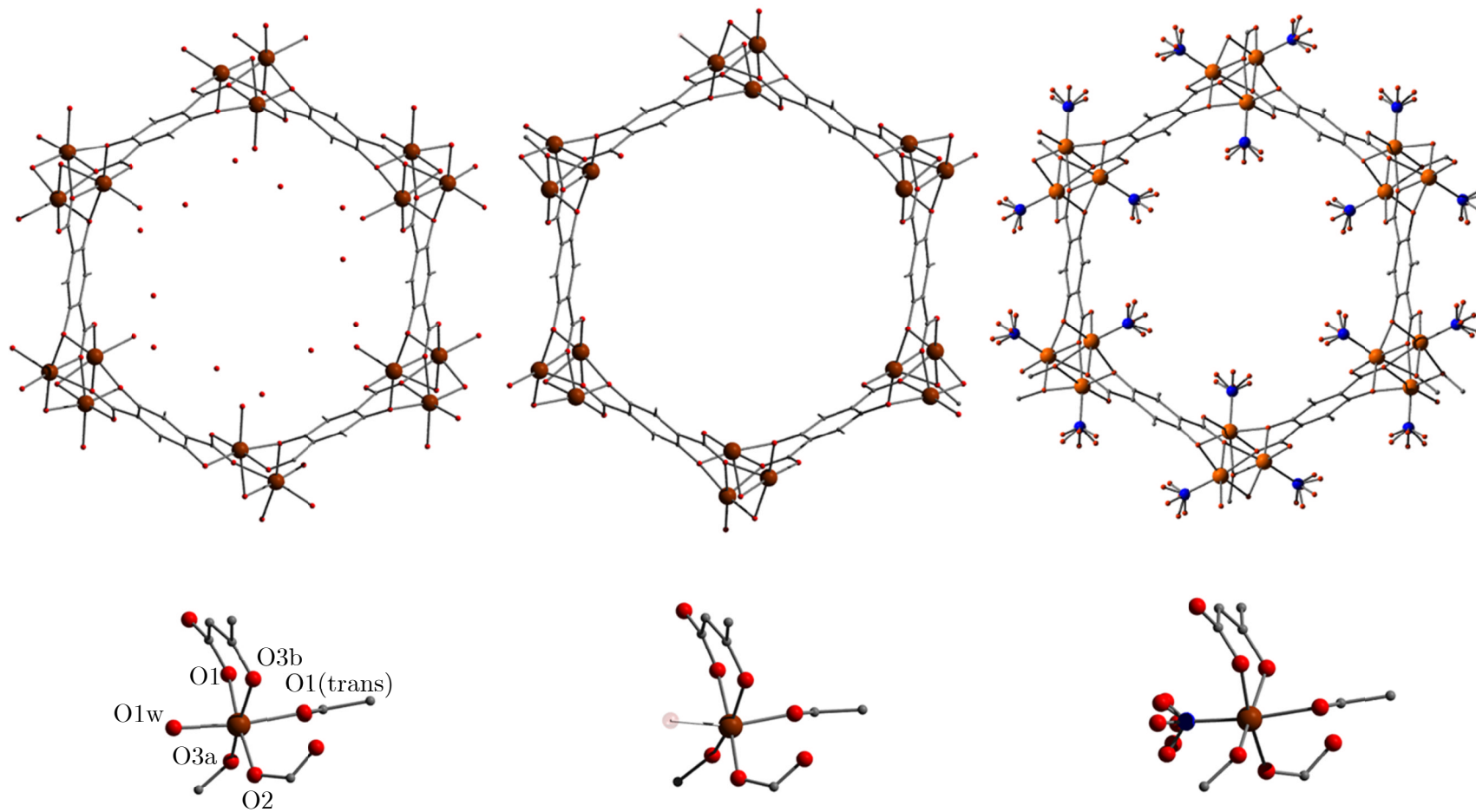**Figure 4-6: Asymmetric unit of the nitric oxide adduct of Co-CPO-27**

Figure 4-7: Hydrated (left), dehydrated (middle) and nitric oxide-loaded (right) Co-CPO-27 structures. Top pictures show the pore of the material and bottom pictures show the Co-coordination sphere in the three structures. Co = orange, O = red, N = blue, C = grey, H = light grey.

Table 5: Bond lengths for the cobalt atom in Co-CPO-27 for the hydrated, dehydrated and nitric oxide-loaded crystal structures. Labels for the atoms can be found in Figure 4-7.

	Hydrated	Dehydrated	NO-loaded
Co-O1c (water/NO)	2.139 (6)	2.016 (2)	1.95 (1)
Co-O1(trans)	2.190 (4)	2.072 (6)	2.161 (6)
Co-O1	2.058 (4)	2.084 (7)	2.081 (6)
Co-O2	2.045 (4)	2.008 (6)	2.017 (6)
Co-O3a	2.048 (4)	1.999 (6)	2.007 (6)
Co-O3b	2.042 (4)	2.031 (6)	2.010 (6)

Table 6: Bond angles for the Co-centre in the hydrated structure (Atom1-Co-Atom2). Table shows atom1 in the left hand column and atom2 on the bottom row. Labels for the atoms can be found in Figure 4-7.

	O1c	O1(trans)	O1	O2	O3a
O1(trans)	171.3 (2)	-			
O1	93.0 (2)	79.6 (5)	-		
O2	92.4 (2)	94.9 (2)	174.6 (2)	-	
O3a	95.2 (2)	88.8 (2)	84.9 (2)	95.0 (2)	-
O3b	93.0 (2)	81.7 (2)	84.4 (2)	95.0 (2)	166.8 (2)

Table 7: Bond angles for the Co-centre in the dehydrated structure (Atom1-Co-Atom2). Table shows atom1 in the left hand column and atom2 on the bottom row.

	O1c	O1(trans)	O1	O2	O3a
O1(trans)	162.8 (4)	-			
O1	88.4 (4)	87.0(3)	-		
O2	86.8 (4)	101.0 (3)	175.2 (3)	-	
O3a	96.6 (4)	81.4 (3)	96.9 (3)	99.9 (3)	-
O3b	82.9 (4)	81.6 (2)	81.0 (3)	97.0 (3)	163.0(3)

Table 8: Bond angles for the Co-centre in the nitric oxide-loaded structure (Atom1-Co-Atom2). Table shows atom1 in the left hand column and atom2 on the bottom row. Labels for the atoms can be found in Figure 4-7.

	O1c	O1(trans)	O1	O2	O3a
O1(trans)	173.1 (4)	-			
O1	80.0 (1)	80.0 (1)	-		
O2	93.1 (2)	93.1 (2)	173.2 (2)	-	
O3a	90.6 (2)	90.7 (2)	82.1 (2)	98.0 (2)	-
O3b	80.1 (2)	80.1 (2)	82.8 (2)	96.1 (2)	163.5 (2)

Table 9: N-O bond lengths and Co-N-O angles for the nitric oxide-loaded structure.

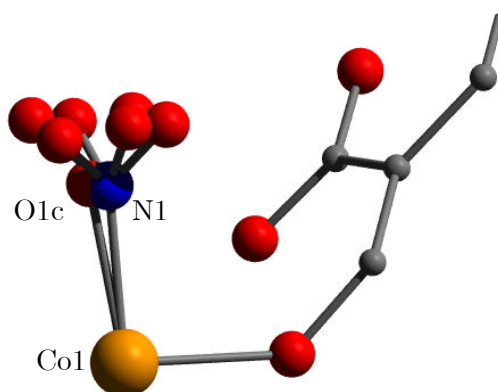| Atom	Bond distance (N-atom) /Å	Bond angle (Co-N-atom) /Å
O1no	1.16(6)	121 (2)
O2no	1.13(9)	126 (4)
O3no	1.09(8)	131 (6)
O4no	0.94 (8)	135 (5)
O5no	1.00 (1)	130 (6)
O6no	1.15(6)	126 (3)
Mean	1.08 (SEM = 0.04)	128.3(SEM = 2.1)

Figure 4-8: Co-coordination environment for the duel-occupancy model of the nitric oxide-adduct.

4.7.3 NO release from the material using water/vacuum/heat

Co-CPO-27 is known to release all of the nitric oxide it adsorbs.[25] An experiment was undertaken to determine how the nitric oxide could be removed from the single crystal. The results are summarised in Table 10. The Co-CPO-27 sample was heated at a rate of 100 K/hr from 300 K to 500 K and held there for 4 hours. A data set was recorded at 500 K (CPO2-500.cif). The cell was cooled to 355 K and a data collection was taken. (CPO2-355.cif).

NO was introduced to the gas cell to a pressure of 793 Torr at 355 K and was left for 10 minutes to equilibrate before a data set was collected (CPO2-NO355.cif). The cell was cooled to 283 K (CPO2-NO283.cif) and another data set was taken. The pressure in the cell was reduced by applying vacuum to the cell and a data set collected at 283 K (CPO2-vac283.cif). The cell was heated under vacuum at 360 K/hr to 373 K and 500K and data sets recorded at each temperature (CPO2-vac373.cif, CPO2-vac500.cif). The cell was cooled to room temperature by removing the cryostream, and exposed to moisture by opening the end of the Teflon tube up using a Swagelok attachment. It was left for 15 minutes before a data set was recorded (CPO2-moisture.cif).

Refinements were performed with the site occupancy factors of the water oxygen O1c and nitric oxide nitrogen N1 as free variables with U_{iso} set to 0.04 Å^2. The occupancies of oxygen atoms from the nitric oxide were determined by fixing the thermal parameters to 0.05 Å^2 and refining the site occupancies freely. Results are summarised in Table 10. The data set taken at 500 K indicates that the material is dehydrated. The Q-peak of height 0.70 electrons Å^{-3} located at the O1w site occupancy factor was unstable to free refinement, indicating that there was no significant occupancy by water at this temperature. When cooled to 355 K, the occupancy on this site was 0.130(5), indicating that partial rehydration takes place on cooling. Therefore, when nitric oxide is introduced into the cell, the occupancy of the metal site will be shared between the water and nitric oxide. Several different estimates of the nitric oxide occupancy can be made. Presuming that the lines were dry, and no further water was introduced to the cell when the nitric oxide was added, the occupancy can be calculated by subtracting 12.7% of an oxygen occupancy off the site occupancy. Alternatively, summation of the O_{NO} electron density could give an indication of the amount of nitric oxide on the site, and the remaining electron density could be assigned as water.

In the nitric oxide-loaded data set taken at 355 K, six Q-peaks around the nitrogen on the metal sites were assigned as oxygens. The thermal parameters were fixed to be 0.05 Å² and the occupancy of the sites was refined freely. The total occupancy of the oxygens around the nitrogen was found to be 0.64 and no further significant Q-peaks were found in the area. When refined to be nitrogen, the total occupancy of the atom on the open metal site is 0.82. Assuming the occupancy of the nitrogen will be identical to the total oxygen occupancy, this calculates an occupancy of nitrogen of 0.64 and left over occupancy of 0.16. This is close to the occupancy which is expected based on 12.7% of water known to be on the site before gas was introduced, suggesting that slightly more water is introduced on gas addition to the cell. The occupancy of the nitrogen was fixed to be 0.64 and an oxygen atom was placed close to the nitrogen atom on the site. The site occupancy factor for this atom was freely refined and the occupancy of the oxygen was found to be 0.22(1) by this method.

When cooled to 283 K the structure is very similar, although it is now possible to locate O1w with site occupancy factor 0.138(9). The coordination site on the metal is fully occupied at this temperature. By using the same procedure, the O_{NO} occupancy was estimated as 0.78(9), leaving 0.22 assigned to the water on the metal site. Duel occupancy was modelled by fixing the nitrogen occupancy as 0.78 and placing a water molecule close to the nitrogen on the open metal site; a free refinement determined the site occupancy to be 0.26(1).

When vacuum is pulled on the cell the metal site is still fully occupied, although the total O_{NO} occupancy has declined to 0.52(5), indicating that some nitric oxide may have been displaced by water or removed under vacuum and then the site taken up by water. The quality of the data for this run was lower than any other run, indicating that the structure of the crystal may be changing throughout the experiment. Heating the cell decreased the amount of NO in the structure; the data sets taken at 355 K and 500 K indicate a NO occupancy of 0.47(4) and 0.18(5) respectively. The water occupancy drops to 0.13 (4) and close to zero during these runs, indicating that the water is more easily removed from the open metal site upon heating than the NO, and that NO cannot be completely removed from the structure by heating the material. Once exposed to moisture, the crystal structure confirmed that all nitric oxide had been removed from the metal site and had been replaced with water.

Table 10: Summary of nitric oxide desorption experiment.

Conditions	R (%)	Metal site occupancy (%)	Total O_{NO} occupancy (%)	Derived $N_{NO}:O_w$ ratio	Occupancy of O1w (%)	Derived $N_{NO}:O_w$ based on duel occupancy models
Dehydration at 500 K (CPO2-500.cif)	4.01	0	-	-	0	-
Cooled to 355 K (CPO2-355.cif)	5.15	0.127(5)	-	-	0	-
800 Torr NO at 355K (CPO2-NO355.cif)	5.15	0.82(6)	0.64(6)	0.64(6):0.16(6)	0	0.6366:0.21(1)
800 Torr NO at 283K (CPO2-NO283.cif)	5.07	1.0	0.78(9)	0.78(9):0.22(9)	0.14(9)	0.26(1)
Vacuum at 283K (CPO2-vac284.cif)	6.12	1.00 (2)	0.51 (5)	0.51(5):0.49(5)	0.32(1)	0.51:0.44(2)
Vacuum at 373K (CPO2-vac373.cif)	5.44	0.60(1)	0.47(4)	0.47(4):0.13(4)	0	-
Vacuum at 500K (CPO2-vac500.cif)	4.51	0.19(9)	0.18 (5)	0.19(5):0.008(5)[1]	0	-
Atmospheric moisture at RT (CPO2-moistureRT.cif)	6.00	1.00(1)	0	-	0.90(2)	-

[1] The large error on this value (see previous page) means that there may in fact be no water left present on the open metal site

4.8 Discussion

From the single-crystal structures of the hydrated, dehydrated and NO-loaded materials, it is possible to understand how Co-CPO-27 stores gas by comparison with the reported nitric oxide desorption isotherms (Figure 4-9).[25] At 800 Torr of nitric oxide (CPOgasNO), we see approximately 1 molecule of nitric oxide associating with each cobalt ion. This equates to an uptake of 6.4 mmol g^{-1} at this pressure, which is comparable to the 7 mmol g^{-1} reported in the adsorption isotherm. The extra amount of nitric oxide is likely to be physisorbed and therefore disordered in the pore and not located in the single-crystal structure.

On reduction of pressure the isotherm only dips very slightly to an amount of 5 mmol g^{-1} indicating that the vast majority of the nitric oxide remains in the structure. The single-crystal structure confirms that under reduced pressure the majority of the nitric oxide stays on the open metal site; the O_{NO} occupancy at 283 K under an NO atmosphere is 0.52(5), reducing only slightly to 0.47(4) under vacuum. Heating the material is sufficient to remove most of the chemisorbed water and some of the chemisorbed nitric oxide. Exposure to moisture rehydrates the structure with no nitric oxide remaining on the open metal site. The hydrated material is reformed with some loss of crystallinity after the prolonged exposure to vacuum, heat and moisture.
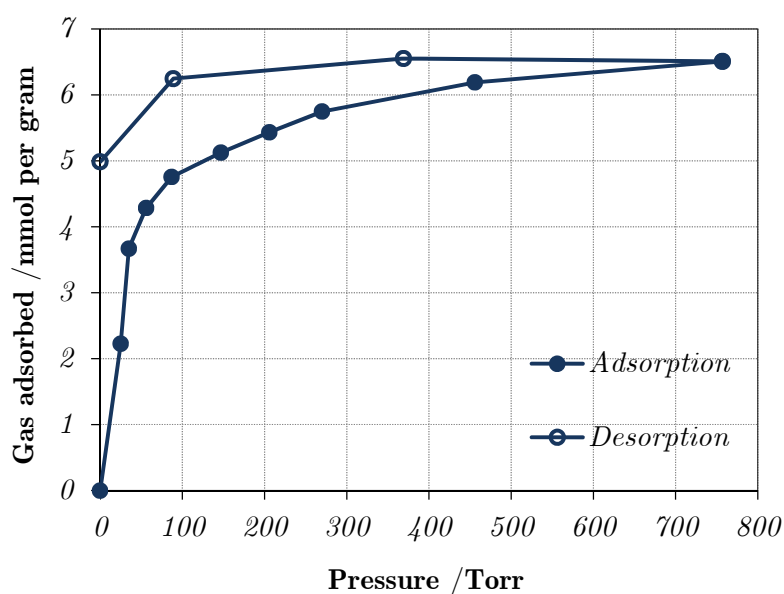

Figure 4-9: Nitric oxide adsorption/desorption isotherm for Co-CPO-27.[25]

4.9 Conclusions and Further Work

This work has demonstrated that the 11.3.1 environmental gas cell is able to collect high quality data, suitable for detailed crystallographic analysis, throughout the activation, gas-loading and gas-release processes for the Co-CPO-27 framework. Problems with dehydration were addressed by heating the lines and, where this is not sufficient to remove water from the system, adsorbing the gas onto the crystal at elevated temperatures can decrease the amount of water found on the metal site.

This work has shown that it is possible to locate chemisorbed gas molecules in the Co-CPO-27 structure using *in situ* single-crystal X-ray diffraction using the environmental gas cell at 11.3.1 at the ALS. The gas cell on 11.3.1 has allowed a much higher degree of dehydration than previously possible; $>95\%$ of the water present on the open metal site can be removed. This has allowed the confirmation and improvement of the model for the nitric oxide adduct of Co-CPO-27 suggested by McKinlay *et al.* and Byrne; nitric oxide was observed to coordinate through the nitrogen in a bent fashion, indicating 1-electron donation from the NO to the metal. The nitrogen atom is localised on the open metal site, whilst the oxygen atoms are disordered in a ring which sits approximately 0.67 Å from the nitrogen, perpendicular to the Co-N bond. In comparison to the model proposed by Byrne which suggests delocalisation of the oxygen over two sites, this work suggests that nitric oxide is delocalised over more sites in the structure. These additional sites are most likely to be a consequence of the increased occupancy of nitric oxide on the open metal site due to the higher level of dehydration which was achieved.

The nitric oxide occupancy was monitored throughout the desorption process and it was found that the nitric oxide could not be fully removed by heating the material under vacuum. However, after exposing the crystal to atmospheric moisture, all the nitric oxide was removed and the crystal was fully hydrated.

These results have extended previous work by using a prototype static cell with computerised gas rig allowing control of static gas-loading from outside of the experimental hutch. This cell has been able to dehydrate the crystal to a higher degree than previously attained. Use of a static cell means that the environment around the crystal must be evacuated before the conditions of the environment can be altered, in

contrast with a flow cell where the environment can be changed continuously. While this increases experiment times, it limits the amount of gas which is in contact with the crystal and, where the gas may be slightly wet and the sample very hydroscopic, this can improve the data quality. In addition, this setup uses the minimal amount of gas which is an important consideration if the gas is toxic, as is the case with nitric oxide, or very expensive.

There is great potential for further work in this area. This work has concentrated on the adsorption of one gas on one framework, but there are many variations of gases and frameworks which could be used. An exciting possibility would be studying the gas-adduct crystal structures for isostructural frameworks containing different metal ions, or different framework architectures, in order to assess the structure/property relationship for gas adsorption. Similarly, comparison of the different gases within one framework could give a lot of information about the way in which gases bind.

While problems with activation were partially overcome by heating the lines, a better solution still could be to use a flow cell, as this would mean that the water from the dehydration should not reside in the same tubing as the incoming gas. This, in combination with a flow of hot dry nitrogen to dehydrate the crystal, could lead to a great improvement in the efficiency and quality of data collection.

Further work could also concentrate on developing low-temperature data collection strategies for the equipment. Nitric oxide, as a radical, has a high affinity for metal sites and so is localised on metal sites at room temperature. However, for gases where the primary interaction is physisorption, the degree of localisation at room temperature is unlikely to be enough to locate the gas molecules crystallographically. A low-temperature collection method would make the cell applicable to a wide range of structural studies.

4.10 Key to data sets given in Appendix B

Data Set (.cif file)	Experiment
dehydinitial	Co-CPO-27 in gas cell, not under vacuum
dehyd123	Co-CPO-27 in gas cell, under vacuum, heated
dehyd234	Co-CPO-27 in gas cell, under vacuum, heated
dehyd345	Co-CPO-27 in gas cell, under vacuum, heated
dehyd456	Co-CPO-27 in gas cell, under vacuum, heated
dehyd567	Co-CPO-27 in gas cell, under vacuum, heated
dehyd678	Co-CPO-27 in gas cell, under vacuum, heated
dehyd789	Co-CPO-27 in gas cell, under vacuum, heated
dehyd8910	Co-CPO-27 in gas cell, under vacuum, heated
dehyd91011	Co-CPO-27 in gas cell, under vacuum, heated
dehyd101112	Co-CPO-27 in gas cell, under vacuum, heated
dehyd111213	Co-CPO-27 in gas cell, under vacuum, heated
dehyd121314	Co-CPO-27 in gas cell, under vacuum, heated
dehyd131415	Co-CPO-27 in gas cell, under vacuum, heated
dehyd141516	Co-CPO-27 in gas cell, under vacuum, heated
dehyd151617	Co-CPO-27 in gas cell, under vacuum, heated
dehydfinal	Co-CPO-27 in gas cell, under vacuum, at 400 K.
CPOhyd	Co-CPO-27 in gas cell at RT
CPOdehy	Co-CPO-27 in gas cell at 500K
CPOno	Co-CPO-27 in gas cell with NO gas at 293K
CPOno-Partialrestraint	Co-CPO-27 in gas cell with no at 293 K with SADI restraints
CPOno-Restrained	Co-CPO-27 in the gas cell with NO at 293 K with restraints
CPO2-500	Dehydration at 500 K
CPO2-355	Cooled to 355 K
CPO2-NO355	800 Torr NO at 355K
CPO2-NO283	800 Torr No at 283K
CPO2-vac283	Vacuum at 283K
CPO2-vac373	Vacuum at 373K
CPO2-vac500	Vacuum at 500K
CPO2-moistureRT	Atmospheric moisture at RT

4.11 References

1. P. J. Chupas, K. W. Chapman, C. Kurtz, J. C. Hanson, P. L. Lee and C. P. Grey, *J. Appl. Crystallogr.*, 2008, **41**, 822-824.

2. P. E. Riley and K. Seff, *Inorg. Chem.*, 1974, **13**, 1355-1360.

3. W. V. Cruz, P. C. W. Leung and K. Seff, *Inorg. Chem.*, 1979, **18**, 1692-1696.

4. Y. Kim, S. H. Song and K. Seff, *Bull. Korean Chem. Soc.*, 1989, **10**, 230-234.

5. Y. H. Yeom, Y. Kim, Y. W. Han and K. Seff, *Zeolites*, 1996, **17**, 495-500.

6. Y. H. Yeom, Y. Kim and K. Seff, *J. Phys. Chem.*, 1996, **100**, 8373-8377.

7. S. B. Jang, M. S. Jeong, Y. Kim, Y. W. Young and K. Seff, *Microporous Mesoporous Mat.*, 1998, **23**, 33-44.

8. N. H. Heo, C. W. Chun, J. S. Park, W. T. Lim, M. Park, S.-L. Li, L.-P. Zhou and K. Seff, *J. Phys. Chem. B*, 2002, **106**, 4578-4587.

9. M. N. Bae, M. K. Song, Y. Kim and K. Seff, *Microporous Mesoporous Mat.*, 2003, **63**, 21-31.

10. Y. M. Lee, Y. Kim and K. Seff, *J. Phys. Chem. B.,* 2005, **109**, 4900-4908.

11. G. H. Jeong, Y. Kim and K. Seff, *Microporous Mesoporous Mat.*, 2006, **93**, 12-22.

12. R. Vaidhyanathan, S. S. Iremonger, G. K. H. Shimizu, P. G. Boyd, S. Alavi and T. K. Woo, *Science*, 2010, **330**, 650-653.

13. J. E. Warren, R. G. Pritchard, D. Abram, H. M. Davies, T. L. Savarese, R. J. Cash, P. R. Raithby, R. Morris, R. H. Jones and S. J. Teat, *J. Appl. Crystallogr.*, 2009, **42**, 457-460.

14. A. J. Warren, PhD Thesis, *University of Bath*, 2011.

15. P. J. Byrne, PhD Thesis, *University of St Andrews*, 2009.

16. P. D. C. Dietzel, Y. Morita, R. Blom and H. Fjellvag, *Angew. Chem., Int. Ed.,* 2005, **44**, 6354-6358.

17. N. L. Rosi, J. Kim, M. Eddaoudi, B. Chen, M. O'Keeffe and O. M. Yaghi, *J. Am. Chem. Soc.*, 2005, **127**, 1504-1518.

18. P. D. C. Dietzel, B. Panella, M. Hirscher, R. Blom and H. Fjellvag, *Chem. Comm.*, 2006, 959-961.

19. P. D. C. Dietzel, R. E. Johnsen, R. Blom and H. Fjellvag, *Chem. A. Eur. J.*, 2008, **14**, 2389-2397.

20.   S. R. Caskey, A. G. Wong-Foy and A. J. Matzger, *J. Am. Chem. Soc.*, 2008, **130**, 10870-10871.

21.   W. Zhou, H. Wu and T. Yildirim, *J. Am. Chem. Soc.*, **130**, 15268-15269.

22.   E. D. Bloch, L. J. Murray, W. L. Queen, S. Chavan, S. N. Maximoff, J. P. Bigi, R. Krishna, V. K. Peterson, F. Grandjean, G. J. Long, B. Smit, S. Bordiga, C. M. Brown and J. R. Long, *J. Am. Chem. Soc.*, 2011, **133**, 14814-14822.

23.   M. Märcz, R. E. Johnsen, P. D. C. Dietzel and H. Fjellvåg, *Microporous Mesoporous Mat.*, 2012*, In Press,* DOI: 10.1016/j.micromeso.2011.12.035

24.   A. C. McKinlay, PhD Thesis, *University of St Andrews*, 2010.

25.   A. C. McKinlay, B. Xiao, D. S. Wragg, P. S. Wheatley, I. L. Megson and R. E. Morris, *J. Am. Chem. Soc.*, 2008, **130**, 10440-10444.

26.   H. Wu, W. Zhou and T. Yildirim, *J. Am. Chem. Soc.*, 2009, **131**, 4995-5000.

27.   Y. Liu, H. Kabbour, C. M. Brown, D. A. Neumann and C. C. Ahn, *Langmuir*, 2008, **24**, 4772-4777.

28.   K. Sumida, C. M. Brown, Z. R. Herm, S. Chavan, S. Bordiga and J. R. Long, *Chem. Commun.*, 2011, **47**, 1157-1159.

29.   P. D. C. Dietzel, R. E. Johnsen, H. Fjellvag, S. Bordiga, E. Groppo, S. Chavan and R. Blom, *Chem. Commun.*, 2008, 5125-5127.

30.   S. Chavan, J. G. Vitillo, E. Groppo, F. Bonino, C. Lamberti, P. D. C. Dietzel and S. Bordiga, *J. Phys. Chem. C*, 2009, **113**, 3292-3299.

31.   S. M. Chavan, G. C. Shearer, E. Bloch and S. Bordiga, *ChemPhysChem*, 2012, **13**, 445-448.

32.   F. Bonino, S. Chavan, J. G. Vitillo, E. Groppo, G. Agostini, C. Lamberti, P. D. C. Dietzel, C. Prestipino and S. Bordiga, *Chem. Mater.*, 2008, **20**, 4957-4968.

33.   A. Spek, *J. Appl. Crystallogr.*, 2003, **36**, 7-13.

34.   A. L. Spek, *Acta Crystallogr., Sect. D: Biol. Crystallogr., 2009, **65**, 148-155.*

35.   P. Müller, *Crystal structure refinement: a crystallographers guide to SHELXL*, Oxford University Press, Oxford ; New York, 2006.

5 *In situ* single-crystal diffraction studies on copper-sulfoisophthalate

5.1 Introduction and aims

Over the last decade a large volume of work has been published relating to gas adsorption in MOFs due to their potential as solutions to a number of technological problems, as outlined in section 1.7. Increasingly, focus has shifted towards more exotic frameworks, which have incorporated framework features that can enhance gas adsorption by interacting with guest molecules in a specific manner. These features can improve adsorption amounts, adsorption strength, or the selectivity for one gas over another.

Crystallographic studies of these materials can be very helpful to determine the structural reasons behind properties. In particular, the advent of single-crystal environmental gas cells[1] such as the one at 11.3.1 at the ALS, introduced in Chapter 4, allow the isolation of crystal samples under vacuum, or exposure to gaseous environments with controlled pressure of gas. Much of the work reported here was done using the early-stage gas cell and gas-dosing rig using manual control of gas pressure.

A flexible copper sulfoisophthalate framework, henceforth called Cu-SIP-3, was first reported by Xiao *et al.* in 2009.[2] This framework undergoes a structural transformation upon exposure to heat involving the breaking of several bonds in the low temperature structure and the removal of the water molecules in the framework. The dehydrated framework shows ultra-selective gas adsorption of nitric oxide over a number of other small molecule gases of similar size and shape. The reasons behind this selectivity are unknown, but are likely to be linked to the structural changes on exposure to different gaseous stimuli. Hence the material poses an interesting system to correlate how the structural features relate to the gas adsorption properties.

This work therefore aims to understand the link between structure and gas adsorption in the Cu-SIP-3 material through single-crystal studies. The structural transition of the material will be studied by variable temperature diffraction studies in

order to determine the structural changes associated with temperature. These structural parameters will be observed with increasing temperature to determine atomic movements. The interaction of the material with nitric oxide gas will be investigated using *in situ* single crystal gas loading studies.

5.2 Structure of copper sulfoisophthalate (Cu-SIP-3)

5.2.1 Hydrated structure of Cu-SIP-3

$Cu_2(OH)(C_8H_3O_7S)(H_2O) \cdot 2H_2O$, Cu-SIP-3, ($M_w$ = 440.0 gmol^{-1}) is a three-dimensional metal-organic framework constructed from copper building units and the 5-sulfoisophthalate (SIP) ligand (Figure 5-1). The hydrated form of the structure crystallises in the space group P2$_1$/c with the asymmetric unit formula $Cu_2O_{11}C_8S$, shown in Figure 5-2. There are 8 formula units per unit cell. The structure is formed of copper-based secondary building units (Figure 5-3), comprising of a tetramer of copper-ions linked by two three-coordinated hydroxyl ion bridges, identical to the building unit reported in other metal-organic frameworks.[3] Coordination of the carboxylate oxygens and one sulfonate oxygen to the metal centre links the tetramer SBUs into layers. These layers are further connected into a three dimensional structure via the coordination of a second sulfonate oxygen to a tetramer in another layer (Figure 5-4). The copper tetramers between layers are slightly offset when viewed down the *a*-axis (Figure 5-4) and there is a separation of 7.333 (1) Å between equivalent copper atoms in different layers.

There are two copper environments in the asymmetric unit, and an inversion centre at the centre of the tetramer generates the other two copper ions of the tetramer. Both copper ions are in the +2 oxidation state. Cu1 is five-coordinate and takes slightly distorted square-pyramidal geometry, the base of which is made up of the coordination of four oxygen ligands; two from two separate SIP ligands which lie trans to one other, one from the bridging hydroxyl group and one from the coordinated water molecule, O9w. The apex of the pyramid is formed by the coordination of a sulfonate oxygen, O8, from a third SIP ligand. This bond length is significantly longer than the four planar Cu−O bonds at 2.3703(4) Å. This is not unexpected as the sulfonate binding is likely to be significantly weaker than the carboxylate binding.

Cu2 also takes square-pyramidal geometry. Here, carboxylate oxygens from two ligands lie *cis* on the base of the pyramid, and the base is also coordinated to oxygens from the two bridging hydroxyl atoms. The apex of the pyramid is made up by coordination of O7, a sulfonate-group oxygen. Again, this bond length is significantly longer than the base Cu−O bonds at 2.280(4) Å. The sulfonate ligand bridges between the apexes of the two copper square pyramids (Figure 5-5).

In the hydrated form of the structure, all carboxylate oxygens are coordinated to the metal centres. Only two out of the three possible bonding interactions between sulfonate oxygens and copper ions take place; two sulfonate oxygens bind to the metal centres and the third is uncoordinated, pointing into the channels defined by the framework (Figure 5-5). There are three water molecules in the asymmetric unit; two sit uncoordinated in the channels of the structure and hydrogen bond to the framework atoms (O10w and O11w) and one is coordinated to Cu2 at the end of the Cu-tetramer (O9w).

Sulfonate coordinates more weakly to the metal centre

Carboxylate groups coordinate strongly to metal centres
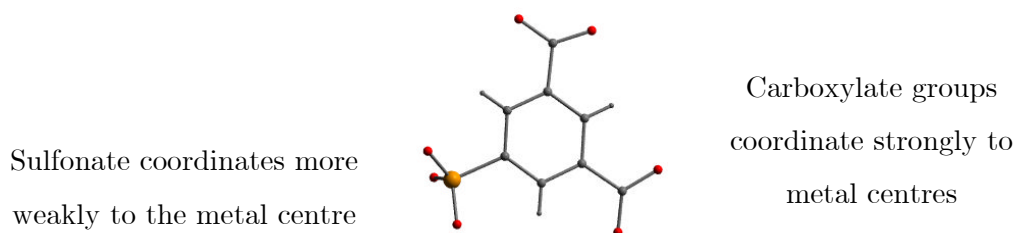
Figure 5-1: The 5-sulfoisophthalte (SIP) ligand used in Cu-SIP-3. Oxygen = red, sulfur = orange, carbon = dark grey, hydrogen = light grey.
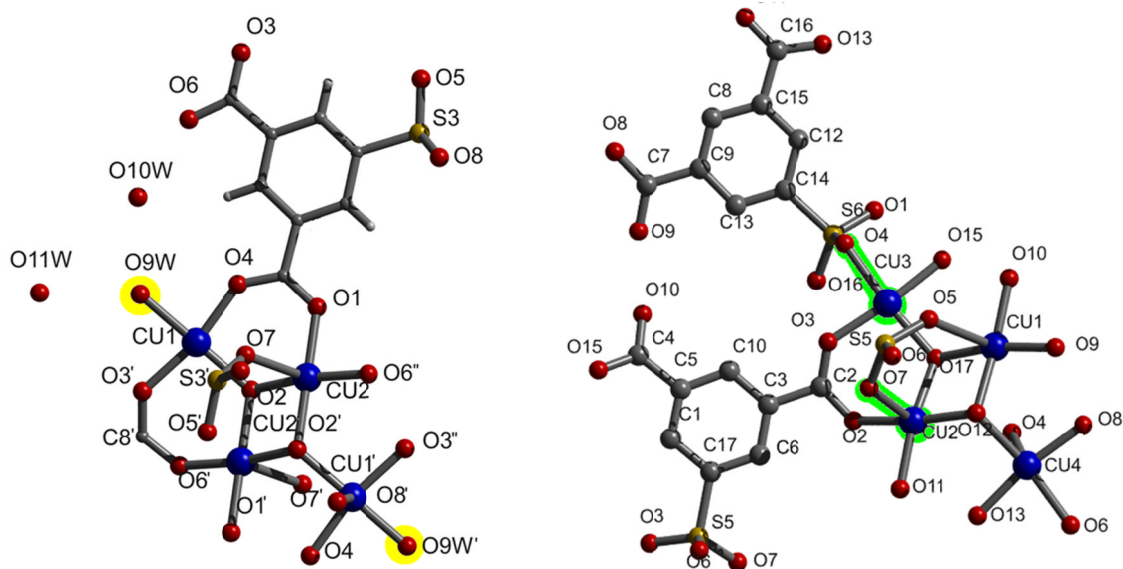
Figure 5-2 Asymmetric unit of Cu-SIP-3: hydrated (left) and dehydrated (right). Copper = blue, Sulfur = yellow, oxygen = red, carbon = dark grey, hydrogen = light grey. All subsequent pictures in the chapter use identical colour scheme. Highlighted are the main coordination changes in the structural transition: Left (yellow): O9w is removed in the structural transition. Right (green): extra sulfonate linkages in Cu-centre.
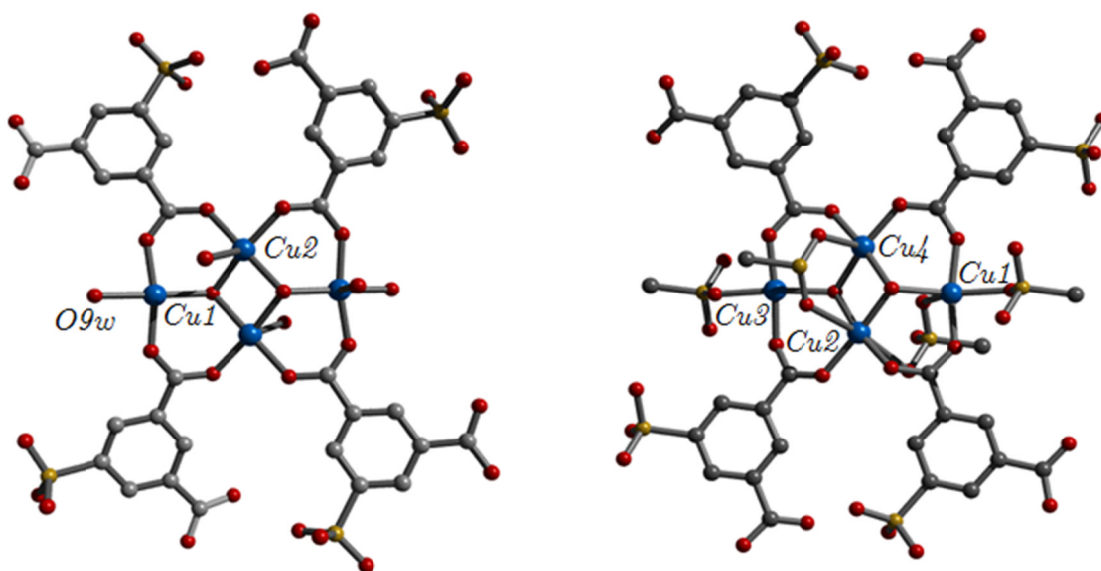

Figure 5-3 Copper-tetramer secondary building unit of Cu-SIP-3.

144
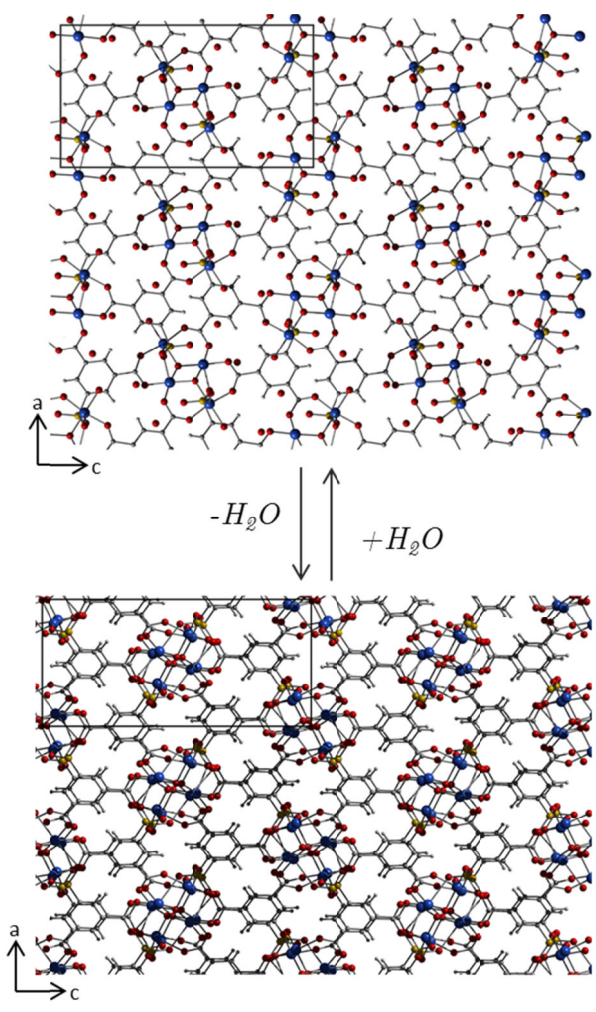
Figure 5-4 Three-dimensional structure of Cu-SIP-3 viewed along the *a*-axis for the hydrated (top) and dehydrated (bottom) structures.
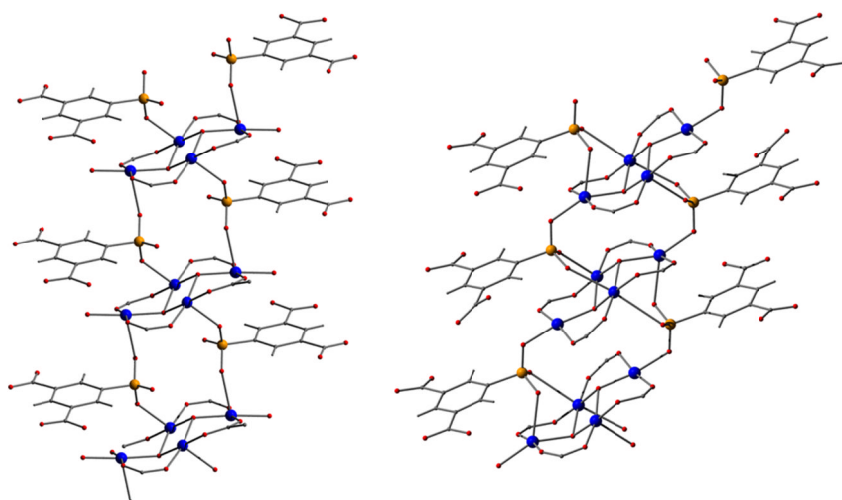
Figure 5-5 Tetrameter chains linked by sulfonate groups: hydrated (left) and dehydrated (right).

5.2.1.1 Dehydrated structure of Cu-SIP-3

Upon heating, the Cu-SIP-3 framework undergoes a structural transformation to give the dehydrated structure which significantly differs in its coordination from the hydrated form. Dehydration removes the uncoordinated water molecules O10w and O11w from the material, and the coordinated water molecule, O9w, is also removed from the structure. Several other coordination changes also take place during the transition so no vacant Cu-coordination sites are left within the material. The third sulfonate oxygen, which is uncoordinated in the hydrated form of the structure, coordinates during the transition to the copper tetramer. The uncoordinated sulfonate molecule does not coordinate into the same geometrical position that the water leaves; instead, one of the already coordinated sulfonate oxygens twists to take the place of the water at the copper centre and the uncoordinated sulfonate forms an additional interaction with the Cu atom at the acute vertex of the tetramer. The difference in coordination environments is highlighted in Figure 5-2. Yellow highlights O9w which is removed in the structural transition. Green highlights the extra sulfonate linkages to the Cu-centre in the dehydrated structure.

The structural formula of dehydrated Cu-SIP-3 is $Cu_4(OH)_2(C_8H_3O_7S)_2$ ($M_w = 772.5$ gmol^{-1}). The size of the asymmetric unit is approximately doubled (but with the removal of the water molecules). The volume of the unit cell is also increased, but is less than doubled as the structure is more densely packed after the removal of the water molecules and of the distortion of the layers.

The inversion symmetry of the copper-tetramer is also removed, and four distinct copper environments, one four-coordinate, two five-coordinate and one six-coordinate, remain. The coordination spheres of the copper ions differ from the hydrated structure. Cu1, equivalent to Cu2 in the hydrated structure, expands its coordination sphere to become octahedral in geometry. In equatorial positions are the carboxylate oxygens from two ligands lying *cis* to each other, with the other two coordination sites being taken up by the bridging hydroxyl ions. The two axial positions are sulfonate oxygens, although the bond length between O16 and Cu1 is very long at 2.837 (9) Å so can be considered only as a very weak interaction. The other atom equivalent to Cu2 in the hydrated structure remains in square-pyramidal geometry with very little change in its coordination sphere when compared with the hydrated structure.

Cu3, equivalent to Cu1 in the hydrated structure, takes distorted square planar geometry with O-Cu-O distances within the plane in the range of 84.98(3)° to 97.60(3)°. The additional sulfonate coordination necessitates the layers of the material pulling closer together, allowing the coordination to take place. When viewed along the *a*-axis, the layers now lie almost directly on top of each other (Figure 5-4). The Cu-Cu distance between tetramers is reduced to between 5.802(4) Å and 6.285(2) Å. The coordination site previously occupied by the oxygen from the water molecule, O9w, is now filled by the sulfonate oxygen, O1. The reduced coordination number of the copper increases the strength of the Cu-O(S) interaction and so decreases the Cu-O(S) bond length from 2.2487(5) Å to 1.997(6) Å. Cu4, the remaining copper atom, also equivalent to Cu1 in the hydrated structure, has five-coordinate geometry, but with significant distortion from square pyramidal geometry to allow interaction with the sulfonate oxygen, O4.

Table 1: Copper coordination spheres in the hydrated (150 K) and dehydrated structures (500 K). Cu-O(C) represents a bond with a carboxylate oxygen, Cu-O(S) a sulfonate oxygen, Cu-(OH) a Cu-O bond with a bridging hydroxyl, and Cu-O(w) a Cu-O bond with a water molecule.

Hydrated			Dehydrated					
Cu1			**Cu1**			**Cu2**		
Bond type	Atom	Length /Å	Bond type	Atom	Length /Å	Bond type	Atom	Length /Å
Cu-O(C)	O4	1.911 (4)	Cu-O(C)	O9	1.899 (5)	Cu-O(C)	O11	1.917 (6)
Cu-O(C)	O3	1.936 (4)	Cu-O(C)	O10	1.935 (5)	Cu-O(C)	O2	1.922 (5)
Cu-(OH)	O2	1.947 (3)	Cu-(OH)	O12	1.994 (6)	Cu-(OH)	O17	1.980 (5)
Cu-O(w)	O9W	1.976 (4)	Cu-(OH)	O17	1.987 (5)	Cu-(OH)	O12	1.996 (5)
Cu-O(S)	O8	2.361 (5)	Cu-O(S)	O3	2.542 (6)	Cu-O(S)	O7	2.275 (6)
			Cu-O(S)	O16	2.837 (7)			
Cu2			**Cu3**			**Cu4**		
Bond type	Atom	Length /Å	Bond type	Atom	Length /Å	Bond type	Atom	Length /Å
Cu-O(C)	O6	1.911 (4)	Cu-O(C)	O5	1.905 (5)	Cu-O(C)	O8	1.901 (5)
Cu-O(C)	O1	1.934 (4)	Cu-O(C)	O15	1.917 (6)	Cu-O(C)	O13	1.900 (6)
Cu-(OH)	O2	1.971 (3)	Cu-(OH)	O17	1.959 (5)	Cu-(OH)	O12	2.000 (5)
Cu-(OH)	O2'	1.979 (3)	Cu-O(S)	O1	1.999 (5)	Cu-O(S)	O6	2.031 (6)
Cu-O(S)	O7	2.280 (4)				Cu-O(S)	O4	2.410 (7)

148

5.2.2 Gas adsorption properties of the Cu-SIP-3 framework

Xiao *et al.* reported that Cu-SIP-3 showed ultra-selective gas adsorption properties for nitric oxide.[2] The adsorption properties for many small molecule gases were tested; N_2, H_2, CO, CO_2, N_2O and CH_4 all showed no appreciable adsorption up to pressures of 10 bar. At low pressures of nitric oxide the same behaviour was observed, but above a gate-opening pressure of 275 mbar there was significant uptake of nitric oxide. The isotherm featured a linear portion with continued uptake up to 1 bar where the isotherm had not reached saturation. The total uptake of 1.1 mmol/g of material equates to 0.88 NO molecules per formula unit of the dehydrated material. On the reduction of pressure the material retains nitric oxide leading to significant hysteresis, but the nitric oxide can be released in gaseous form and the original hydrated coordination reinstated when the material is exposed to moisture.

Xiao *et al.* reported that PXRD data on the nitric oxide-loaded sample featured peaks which were too broad for structural determination, but postulated that the high adsorption capacities for nitric oxide lay in a strong interaction between nitric oxide and the Cu^{2+} sites as seen for other Cu^{2+}-based MOFs[4, 5] as well as other framework materials.[6-8]

5.3 Experimental details

5.3.1 Synthesis of Cu-SIP-3

Crystals of Cu-SIP-3 were synthesised according to the literature procedure outlined by Xiao *et al.*[2] The procedure is given in detail in Appendix A.

5.3.2 Variable temperature single-crystal studies

Variable temperature single-crystal data was collected at beamline 11.3.1 of the Advanced Light Source, Lawrence Berkeley National Laboratory. The wavelength used was 0.77490 Å.

Regularly shaped single crystals were selected for the variable temperature data sets; those chosen were blue blocks without sharp corners or edges but which extinguished light when rotated under plane polarised light. The chosen crystal was glued to the end of a glass fibre using the minimum quantity of glue in order to allow maximum manoeuvrability of the crystal during the variable temperature experiment.

The glass fibre was mounted on a magnetic pin head and attached to a standard goniometer head. Data were collected using a Bruker AXS ApexII diffractometer and collected and reduced using the corresponding Bruker ApexII SAINT software.

Data were collected by via continuous omega-scans with one second frame collection times over a 12 hour period whilst heating the crystal. Variation in the crystal temperature was achieved using an Oxford Cryosystems cryostream device. An initial ramp rate of 15 K hr^{-1} was used. The temperature was ramped continually throughout the data collections but the temperature quoted in data is the median cryostream temperature over the time taken for the three runs of data to be collected, and is approximated to be the crystal temperature. The omega-scans were then integrated in groups of three, with each run therefore being integrated within three different groups; for example runs 123, 234, 345 were all integrated separately to maximise the number of temperatures which could be extracted from the data. The data were corrected for adsorption effects using the program SADABS.

Structures were solved using the program SIR-97 and refined on F^2 using full-matrix least squares using the program SHELXL-97 within the WinGX suite of programs. Non-hydrogen atoms were refined anisotropically, and the hydrogen atoms present on the organic linker were placed geometrically using the HFIX command, and refined with the value of U_{iso} set to be 1.5 times greater than the carrier atom on which the HFIX command was centred. The data sets were refined until convergence was achieved and there were no significant Q-peaks left in the Fourier difference map. The occupancy of the water molecules was refined freely to monitor the dehydration process.

5.3.3 *In situ* single-crystal gas loading experiments

In situ gas loading onto single crystals was performed using the environmental gas cell on beamline 11.3.1. The main features of this gas cell are outlined in Chapter 4. Single crystals were mounted using glue on a glass fibre and secured into the gas cell by gluing the fibre to the goniometer head. The crystal was isolated using the glass head of the gas cell and the sample was heated at a rate of 30 K hr^{-1} to 450 K and heated overnight under vacuum to dehydrate the material and anneal the crystal in the high temperature regime. The crystal was cooled rapidly to room temperature and a data set was collected at this temperature to ensure that the crystal was still dehydrated. Due to the amorphous scattering from the glass head of the gas cell, and some loss in

crystallinity throughout the heating process, longer collection times of typically 3 seconds per frame were used for this data collection compared to 1 second per frame used with crystals from the same sample analysed outside the gas cell. The gas was introduced to the crystal environment slowly to prevent the crystal from blowing off the glass fibre and to prevent degradation of the crystal.

Nitric oxide was introduced from the bottle into the system and the bottle immediately closed again in order to allow the flow of gas into the cell to be more carefully controlled. A small burst of nitric oxide was introduced into the cell by opening the valve to the cell for a short time. The pressure was monitored using a pressure gauge located inside the hutch next to the cell. After each addition, the system was allowed to equilibrate before any data were taken to allow time for the gas to diffuse into the crystal. Enough data were then collected using 20 second frames to allow a unit cell to be indexed.

5.4 Variable temperature single-crystal studies

5.4.1 Change in diffraction pattern with temperature

X-ray diffraction data were collected over the temperature range of 150 K to 500 K. Between 150 K and 365 K, diffraction from the sample was good and data sets have low R_{int} values, which rises at higher temperatures (Table 2). Refinements against data collected in the temperature range of 150 K to 365 K gave the hydrated crystal structure discussed in section 5.2.1. Crystal structures were determined for all data measured between 150 K and 365 K. CIFs for these structures can be found in Appendix C.

Above 365 K, Bragg scattering became increasingly sparse and the diffraction peaks distorted significantly. This meant that their maxima could not be determined accurately, and therefore a unit cell and structure could not be determined. In the temperature range between 370 K and 405 K diffraction frames showed very little Bragg diffraction (Figure 5-6), indicating that the long-range order of the material had been lost.

At temperatures above 405 K, Bragg diffraction began to return in discrete diffraction spots. Above 430 K this Bragg diffraction was strong and indicative of a highly crystalline material. Enough data were collected to index a unit cell and solve the crystal structure at 435 K and 450 K. Data collected at these temperatures also had low

internal error. Refinement of data above 430K gave the dehydrated structure described in section 5.2.1.1. Crystal data and selected refinement details for the hydrated structure obtained at 150 K and the dehydrated data set obtained at 500 K are shown in Table 3. Crystallographic data files for all models refined from variable temperature data sets can be found in Appendix C.

Table 2: Variation of the structure obtained at various temperatures along with the R_{int} for the data set and R_1 after final refinement.

Temperature /K	Structure	R_{int}	$R[F^2 > 2\sigma(F^2)]$
150	Hydrated	0.052	0.037
165	Hydrated	0.053	0.040
180	Hydrated	0.039	0.051
195	Hydrated	0.048	0.049
210	Hydrated	0.046	0.043
225	Hydrated	0.048	0.046
240	Hydrated	0.048	0.045
255	Hydrated	0.053	0.050
270	Hydrated	0.055	0.044
285	Hydrated	0.066	0.057
300	Hydrated	0.053	0.051
310	Hydrated	0.041	0.050
315	Hydrated	0.041	0.051
320	Hydrated	0.061	0.060
325	Hydrated	0.064	0.062
330	Hydrated	0.053	0.052
335	Hydrated	0.070	0.063
340	Hydrated	0.070	0.124
345	Hydrated	0.074	0.064
350	Hydrated	0.053	0.055
355	Hydrated	0.059	0.053
360	Hydrated	0.075	0.063
365 - 420	No structure	-	-
435	Dehydrated	0.044	0.049
450	Dehydrated	0.043	0.048

Table 3: Selected crystal data and refinement details for the hydrated (150 K), dehydrated (500 K) and rehydrated (293 K) Cu-SIP-3 structures.

T/K	150	500		293 (rehydrated)
formula	$Cu_2O_{11}C_8S$	$Cu_4O_{16}C_{16}S_2$		$Cu_2O_{11}C_8S$
FW/g mol^{-1}	435.26	766.4		435.26
crystal system	monoclinic	monoclinic	monoclinic	monoclinic
space group	P2$_1$/n	P2$_1$/c	P2$_1$/n	P2$_1$/n
a/Å	7.2949 (4)	12.909(2)	13.796(2)	7.3333 (14)
b/Å	18.2726 (10)	19.430 (4)	19.430(4)	18.153 (3)
c/Å	10.1245 (6)	9.164 (2)	12.057(2)	10.1729 (19)
β/°	94.8910 (10)	100.169 (4)	139.172(4)	94.379 (4)
V/Å³	1344.65 (13)	2254.9 (8)	2112.9(16)	1350.3 (4)
Z	8	8	8	8
ρcalc/Mg m^{-3}	1.624	1.928	2.428	1.617
μ/mm^{-1}	1.81	2.88	8.92	1.80
data/restraints/parameters	4033/6/202	6899/6/363	3412/6/343	3925/6/192
R(F) (I > 2σ(I))/%	0.04	0.0545	0.0478	0.0769
R(F) (all)/%	0.038	0.0856	0.0769	0.144
R$_w$(F2) (I > 2σ(I))/%	0.1309	0.1431	0.1223	0.2048
Rw(F2) (all)/%	0.1281	0.1431	0.1486	0.1875
GoF	1.03	1.04	0.873	1.23

Diffraction frames for the data collected at 300 K, 405 K and 435 K are shown in Figure 5-6. These diffraction frames have the same ω, ɸ, θ values and show the change in diffraction pattern from highly crystalline (300 K) to having very little Bragg diffraction (405 K, middle) then recovering crystallinity at higher temperatures (435 K, bottom). An animation of diffraction frames for the full temperature range can be found in Appendix C.

There is no presence of rings of diffracted intensity expected from a polycrystalline powder in any diffraction data set. This indicates that at no temperature does the crystal break apart into a powder and that there is single crystal behaviour throughout the visible data. It is believed, therefore, that the structural change represents a single-crystal to single-crystal transformation of the material. The highly crystalline nature of the single crystal at high temperatures indicates that the crystal remains intact throughout the transition, rather than breaking apart and recrystallizing

in the new structure. The similarity of the orientation matrices (Table 4) supports this claim.

The single crystal data are consistent with the powder data published by Xiao *et al.* which shows that dehydration between T = 368 K and T = 408 K in an atmosphere of dry nitrogen is accompanied by significant weakening of diffracted intensity and heavy broadening of powder-diffraction peaks.[2] The small difference in the temperature range during which we see the loss of Bragg diffraction data can be attributed to differences in experiential methods such as the use of a ground powder rather than a single crystal.

Table 4: Orientation matrices of the crystal at 300 K and 435 K.

	300K			435K		
ORT1	-0.12121	2.489174	0.005421	-0.1287	-0.02036	0.040504
ORT2	0.057494	0.048005	-0.01983	0.069521	0.046776	-0.00097
ORT3	-0.03052	-0.00842	-0.09698	0.083711	0.007545	-0.103277
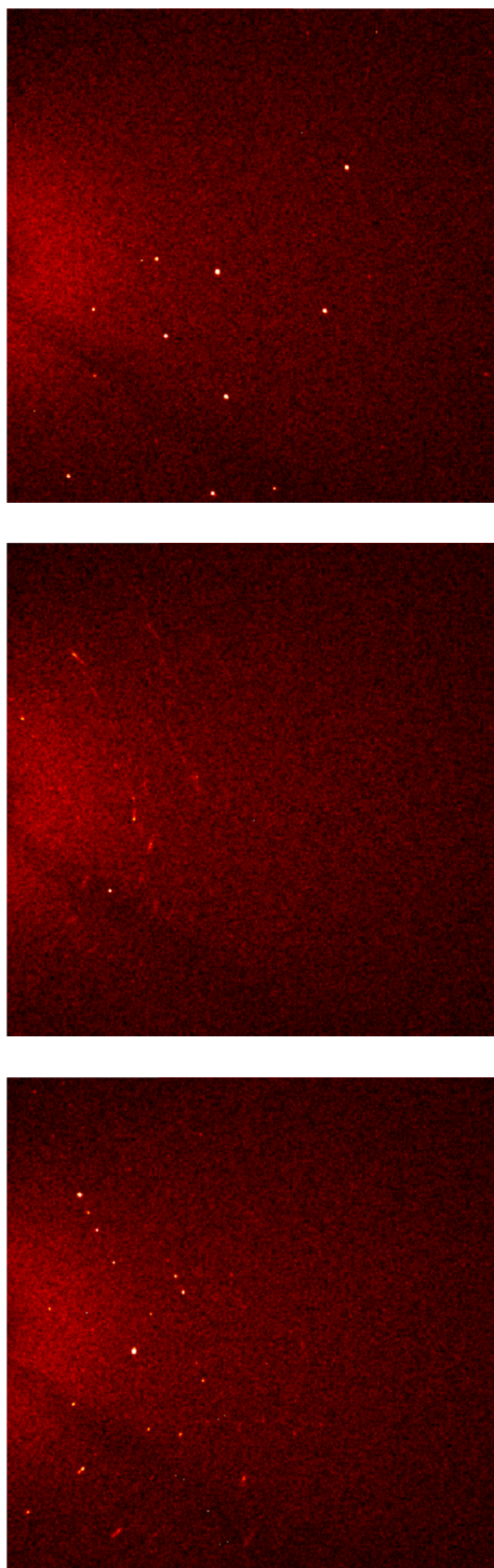
Figure 5-6: Diffraction frames with the same φ, ω, Θ for Cu-SIP-3 at 300 K, 405 K and 435 K.

5.4.2 The effect of moisture on the reverse transition

Xiao *et al.* report that the transformation can be reversed on exposure to water vapour, reinstating the original copper-coordination. A single crystal of Cu-SIP-3 was heated to 500K. A data set was taken to confirm that dehydration had taken place. The crystal was then cooled to 300 K at 30 K/hr in the dry nitrogen stream with shells of data with one second frames being taken throughout. All collected data were strong and the crystal remained in the dehydrated regime down to room temperature. Data collected during the cooling of the crystal were integrated in groups of three. *a*- and *c*-axes showed a linear decrease on reduction of temperature, and the *b*-axis showed no change within error. The β-angle showed a linear decrease with the reduction in temperature. This data is shown in Appendix C.

The same crystal was kept on the diffractometer at 300K but the dry nitrogen stream was removed, exposing the crystal to air. Shells of data were collected for three hours. Diffraction peaks quickly became weaker and less well-defined. The structure could not be indexed for the first 2.5 hours of the experiment. However, data collected subsequent to this were indexed to the low-temperature structure and refined to a R_w value of 7.69%. The change in copper-coordination in the dehydration structural transition was fully reversed and all three water molecules found in the hydrated form of Cu-SIP-3 were in full occupancy in the rehydrated form of the material. This data are available in 293Krehydration.cif in Appendix C.

These data indicate that the Cu-SIP-3 structural transformation can be controlled via the gaseous environment moisture content and that the water is the key to reversing the structural transformation. The loss of some diffracted intensity shows that the crystallinity of the material is disturbed by the subsequent rehydration. It is possible that this crystallinity could be better preserved with a carefully controlled release of moisture into the system, for example if the moisture was re-introduced at the same rate as it was removed using careful vapour pressure control.

5.4.3 Change in unit cell parameters with temperature

Data for the change in unit cell parameters are shown in Figure 5-7. The *a*-axis and *b*-axis show reductions in length at higher temperature, whilst the *c*-axis shows expansion. The unit cell volume (Figure 5-8) shows very little variation below the temperature at which diffraction data is lost, and the material can therefore be described

approximately as a zero-expansion material. At higher temperatures the data is less reliable, visible as larger standard uncertainty values, due to the significant movement of the crystal when it nears the phase transition as well as the increased error associated with higher temperature data collection. The unit cell parameters start to show significant change above 320 K, indicating that the material is starting to change. Single-crystal diffraction data are generally considered less reliable in the calculation of unit cell parameters than powder-diffraction data but the consistency of unit cell data obtained indicate satisfactory accuracy in this case.[2]
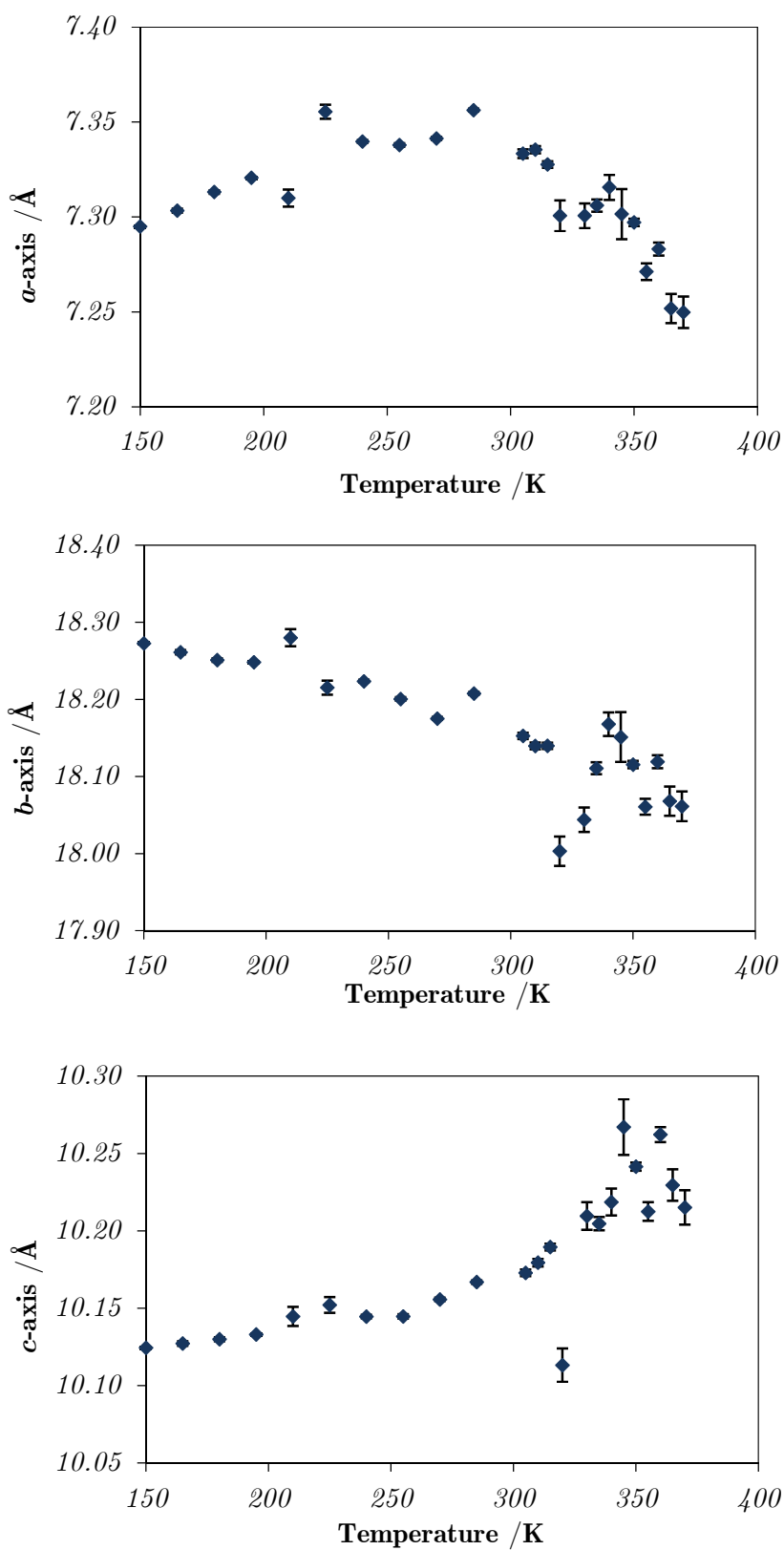
Figure 5-7: Change in unit cell parameters with temperature. Error bars are shown on all data points (some have small magnitude and therefore are not visible).
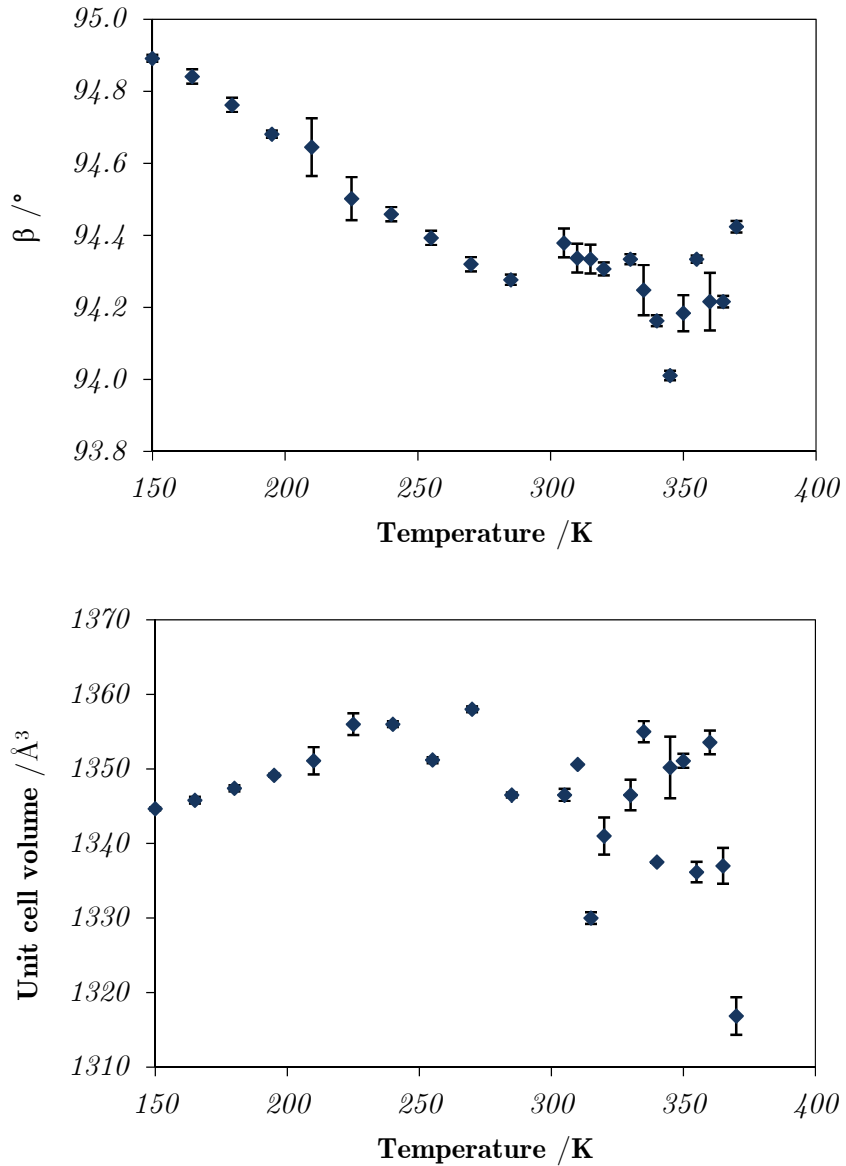
Figure 5-8: Variation in monoclinic angle, β (top), and unit cell volume (bottom) with temperature. Error bars are shown on all data points (some have small magnitude and therefore are not visible).

5.4.4 Change in site occupancy factors with temperature

In the absence of disorder, site occupancy factors (SOF) are often fixed to be one, meaning that the atom occupies the site in every unit cell.[9] In the case of partial dehydration, the water molecule may not be present in every unit cell, and therefore the overall average site occupancy factor is less than one. For the structure determined at

150 K, the coordinated water molecule, O9w, and those sitting in the channels of the material, O10w and O11w, were present in 100% occupancy. The site occupancy factor for the water molecules was allowed to refine freely in variable temperature refinements. As the temperature increased, the site occupancy of the two water molecules sitting in the channels of the material, O10w and O11w, decreased. This is shown in Figure 5-9. The occupancy of O11W began to decrease in data sets with temperatures greater than 270 K, and in the highest solvable data set of this structure with T = 360 K, the occupancy of O11w was reduced to 0.497(6). O10w is removed at higher temperatures and is removed more slowly than O11w. The site occupancy factor is 1.0 at data sets collected at temperatures lower than 300 K, and decreases to a minimum value of 0.7874(6) at 365 K.
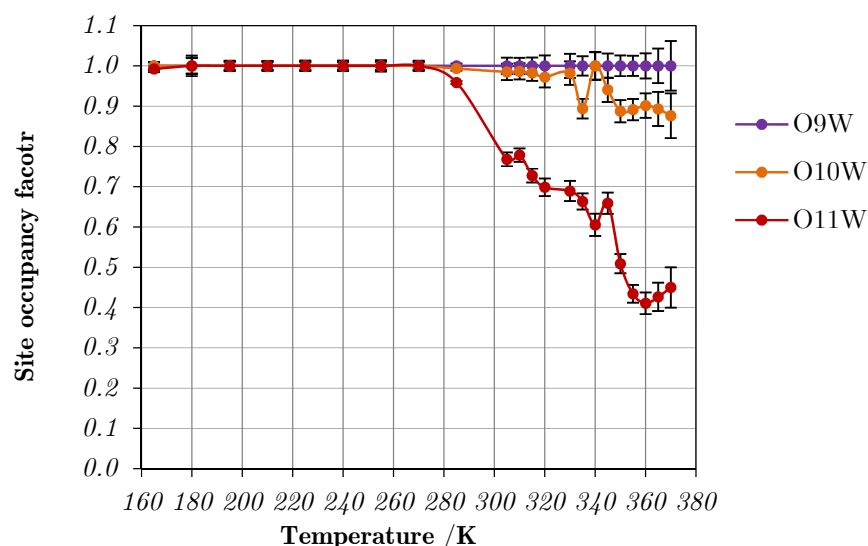
Figure 5-9: Variation in site occupancy factor for water molecules O9w (coordinated to the metal centre), O10w and O11w (residing in the channels) with temperature.

The removal of O10w and O11w at elevated temperatures is not unexpected; dehydration has been followed in other metal-organic frameworks by single-crystal diffraction.[10]   There is an apparent rise in the occupancy of O10w at temperatures between 350 K and 365 K. This is unlikely to actually be the case, but rather to be the effect of co-dependence of site occupancy factors and displacement parameters.[9] Additionally, at higher temperatures where some long-range order begins to be lost,

Bragg peaks distort significantly and it becomes difficult to accurately determine the position of peak maxima. There is a reduction in the quality of the refinement in this region as detailed by the rising residuals (Table 2) and this leads to more difficulty in separating displacement parameters and site occupancy factors. However, there is good correspondence between weight loss calculated from single crystal data and the thermal gravimetric analysis performed on the sample (Ref 2, supplementary information).

Site occupancy factors and displacement parameters are not independent; a symptom of partial occupancy is often very large displacement parameters. However, it is difficult to tell in cases such as partially occupied solvent molecules whether a site is actually partially occupied or whether the molecule is just very mobile. Negative electron density in the region around a nuclear position is an indicator that the position is partially occupied.[9] For the refinement at 360 K, Fourier difference maps (F_o - F_c) were calculated in the plane of Cu1, O10w and O11w with the site occupancy factors of all water molecules fixed as 1.0 (Figure 5-10). It is possible to observe negative electron density (red dashed lines) around O10w and O11w resulting from the refinement pulling electron density from the surrounding areas for assignment as electron density for the fully occupied water molecule. This effect is more pronounced for molecule O11w, indicating that the occupancy for this water molecule is significantly lower than 1. The site occupancy factors of 0.901(30) and 0.410(31) for O10W and O11W respectively, as obtained from the structural refinement, agree with this observation. No negative electron density is located around atom O9w, indicating that the atom is in full occupancy. In fact, it is possible to begin to locate the hydrogen atoms on the water molecule, O9w; peaks of positive electron density are found at a distance 0.87 and 1.0 Å, from O9w, close to the expected O-H bond length in water (0.96 Å).[11]
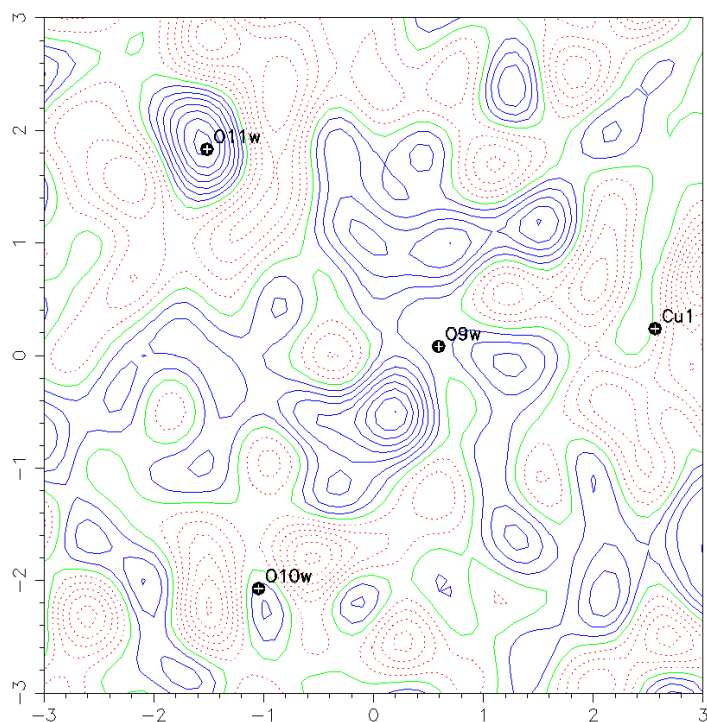
Figure 5-10: Fourier difference map defined in the plane of Cu1 O10w and O11w for the data collected at 360K, with the site occupancy of all water molecules fixed as 1.0. Blue contours indicate areas of positive electron density; green lines show the zero contour, and red-dotted line show negative contours.

O10w and O11w are removed from the structure at different temperatures. O10w shows very little reduction in occupancy until around 340 K, whereas the occupancy of O11w has already fallen to less than 60% by this temperature. Neither atom is coordinated to a metal centre in the structure, but both have hydrogen-bonding frameworks which hold them in place. A possible hydrogen-bonding network for the two molecules was determined by first considering the shortest $O(w) \cdots O$ distances as calculated for the structure collected at 150 K. (Table 5).

When a Fourier difference map (F_{obs} - F_{calc}) in the slant plane defined by Cu1, O9w, O10w and O11w was calculated for the structure at 150 K, areas of electron density were located in the area around O9w, O10w and O11w, which could correspond to hydrogen positions on the water molecules (Figure 5-11). These were assigned as hydrogen atoms on the water molecules, and the DFIX command was used to fix the distance as 0.96 Å. The hydrogen bonding network defined by this placement of hydrogen atoms is shown in Figure 5-12. In this framework, the lone pairs on both O10w

162

and O11w hydrogen bond to the hydrogen atoms on O9w. This is the shortest distance for both uncoordinated solvent molecules (2.7571(29) Å for O10w and 2.8211(28) Å for O11w), indicating that this interaction is strongest. O10w also hydrogen bonds to O6 and is likely to hydrogen bond to another oxygen atom, most likely O8. The placed hydrogen atoms on O11w are of correct orientation and distance for interaction with oxygen atoms O5 and O1.

Table 5: Shortest O $\cdots$ O distances for O10w and O11w with other oxygen atoms possible for hydrogen bonding. (w) signifies that the oxygen is a water molecule, (S) signifies a sulfonate oxygen and (C) signifies a carboxylate oxygen.

O10w	O$\cdots$O distance /Å	O11w	O$\cdots$O distance /Å
O10w$\cdots$O9(w)	2.7571(29)	O11w$\cdots$O9(w)	2.8211(28)
O10w$\cdots$O8(S)	2.9646(26)	O11w$\cdots$O5(S)	2.9591(31)
O10w$\cdots$O6(C)	2.9796(27)	O11w$\cdots$O1(C)	3.2017(25)
O10w$\cdots$O7(S)	3.4605(29)	O11w$\cdots$O6(C)	3.2934(26)
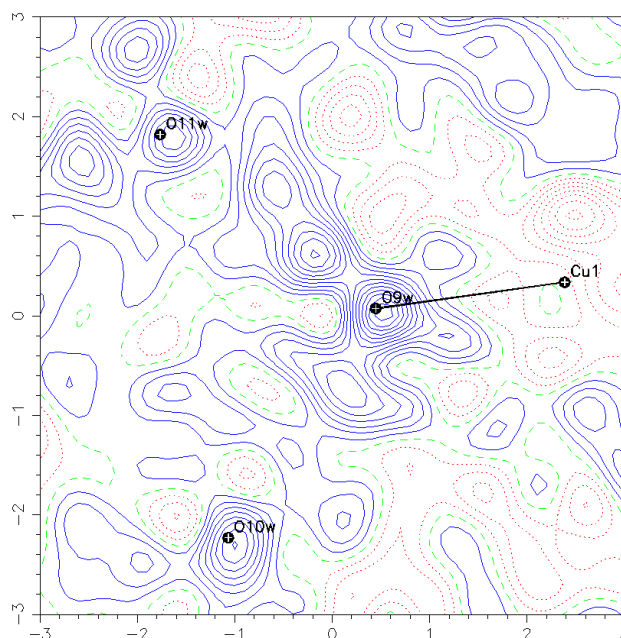
Figure 5-11: Fourier difference map for the data collected at 150K defined in the plane of Cu1, O10w and O11w. Blue contours indicate areas of positive electron density, green lines show the zero contour, and red dotted lines show negative contours.
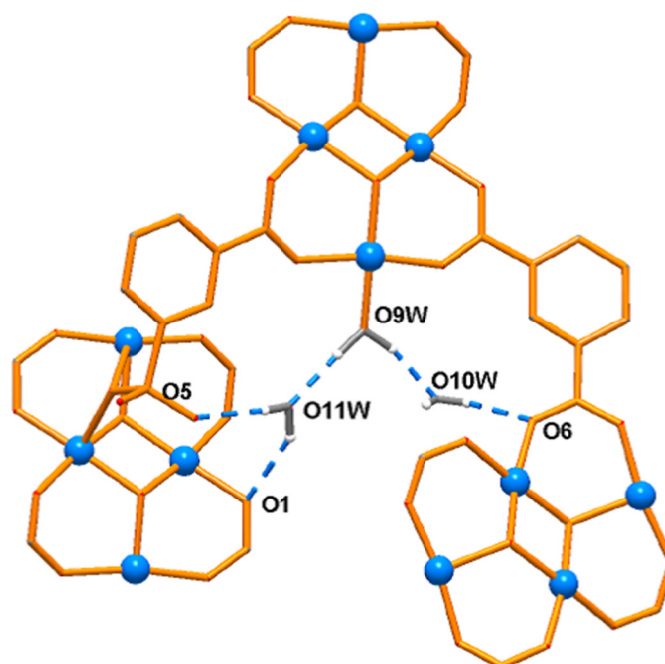
Figure 5-12: Possible hydrogen bonding framework defined by the placement of hydrogen atoms at areas of positive electron density in the Fourier difference map for the data collected at 150 K. Turquoise atoms represent copper, white represent placed hydrogen atoms. All other atoms are shown skeletally for clarity. Dotted lines indicate hydrogen bonds.

The average of the four shortest $O(w) \cdots O$ distances is very similar; 3.040 Å for O10w and 3.067 Å for O11w. The difference is greater for the first three bond distances, 2.900 Å for O10w and 2.994 Å for O11w. As hydrogen bond strength decreases exponentially with distance, this hydrogen bonding is likely to be stronger for O10w than for O11w and therefore a higher temperature is needed to remove the molecule from the pores. However, the difference in temperature required for removal of the water molecule is quite significant and unlikely to be accounted for entirely by the difference in hydrogen bonding distances.

A fuller explanation can be found by also considering the nature of the atoms to which the water molecules hydrogen bond. Both O10w and O11w are within hydrogen bonding distance from O9w. O10w is also within hydrogen bonding distance of O8 and O6. O8 is from the sulfonate group and O6 is a carboxylate oxygen, both of which are used in framework bonding and have displacement parameters that show very little susceptibility to temperature (see section 5.4.5). Therefore, the hydrogen bonding environment of O10 is likely to be quite stable, even at elevated temperatures. O11w is

within hydrogen bonding distance of O5 and O1. O1 is a carboxylate oxygen that shows very little movement at elevated temperature. O5 is the uncoordinated sulfonate oxygen. This atom shows particular susceptibility to temperature (see section 5.4.5, Figure 5-14) and its increased movement at elevated temperatures means it is unable to provide a stable hydrogen bonding environment. The hydrogen bonding network of O11w is disrupted at moderately low temperatures, and therefore O11w is removed earlier in the dehydration process.

The site occupancy of O9w, the coordinated water molecule, was also freely refined but was found in full occupancy throughout all solvable data sets. For the structural transition to complete O9w must be removed from the structure, but the variable temperature single-crystal data indicate that this process does not take place whilst the material has long range order, and therefore must take place in the region where Bragg data is unavailable. This suggests that as soon as the O9w begins to be lost from the structure, atomic rearrangement takes place. This further suggests a correlation between the removal of O9w and the subsequent movement of the sulfonate group, with the loss of long-range order from the material.

In temperatures leading up to the transition, the Cu-O9w bond length increases from 1.955(2) Å at 270 K up to a maximum value of 1.987(8) Å at 360 K (Figure 5-13). This indicates that the Cu-O9w bond weakens with increasing temperature so the removal of the atom from the structure may be imminent.
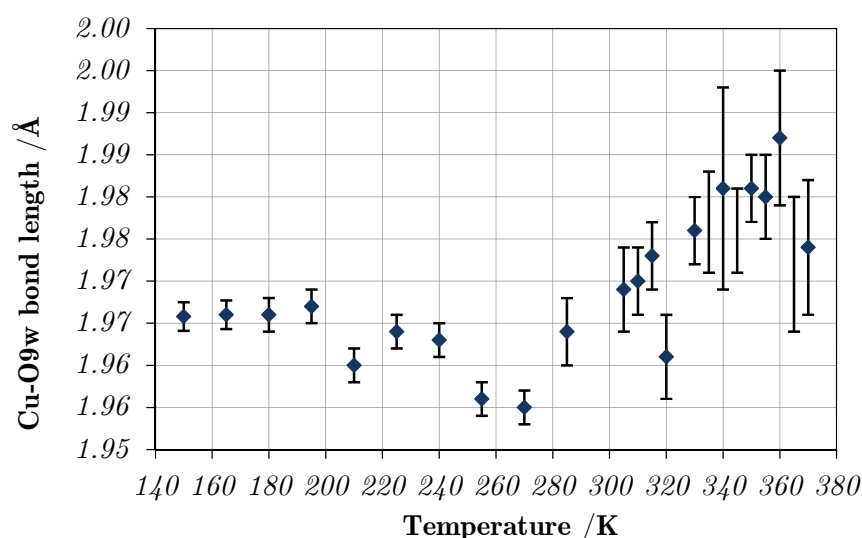
Figure 5-13: Variation in Cu-O9w bond length with temperature

5.4.5 Change in Atomic Displacement Parameters (ADPs) with temperature

Refinements of the Cu-SIP-3 model using variable temperature data sets were completed with all atoms defined anisotropically. Values for anisotropic displacement parameters (ADPs), U_1 and U_{eq}, were taken from the SHELX *.lst* file and are plotted in Figure 5-14. U_{eq} is the radius of a sphere which has the same volume as the ellipsoid defined by the three axes U_1, U_2 and U_3, and gives information about the amount of uncertainty in the position of an atom (and therefore how much an atom could be moving around) but no direction information. U_1 is the largest magnitude of the principal mean square displacements (from the diagonalised anisotropic displacement parameter tensor), equating to the longest axis of an atom's thermal ellipsoid. This value gives information about the largest axis of vibration and therefore information about whether an atom could be moving in a certain direction.

For the dataset obtained at 150 K, all atomic displacement parameters are low. U_{eq} are all below 0.04 $Å^3$ with maximum values of 0.0369(8) and 0.0357(8) for O10w and O11w, and U_1 values are below 0.06 $Å^3$. For most atoms the values for U_{eq} and U_1 are similar, meaning that the thermal ellipsoid is close to spherical. As the temperature rises there is an expected rise in the values of the ADPs – atoms with more energy are likely to move around more leading to greater uncertainty in their positions. The increase in both U_{eq} and U_1 values accelerates for all atoms between 255 K and 270 K. This coincides with the loss of water from the framework; O11w starts to lose occupancy at this temperature.

There appears to be relatively little movement within the tetramer and in the Cu-carboxylate framework; the oxygens which are involved in the framework structure all show a consistent and relatively small increase in ADPs even at high temperatures near the phase transition. This is consistent with the observation that the carboxylate binding of the tetramer in unchanged throughout the phase transition, and only small changes in bond lengths are evident despite the large atomic movements which are involved. The stability of the main carboxylate framework could well account for the material being able to undergo the large coordination changes necessary for the transition without the material breaking up.

The movement of the sulfonate group with temperature is more complicated. O6 and O8, which are used in framework bonding at all temperatures, show ADPs consistent

with those of the carboxylate framework; these are slightly larger than the carboxylate oxygens and on a par with thermal parameter of O9w. O5, which in the hydrated regime of the material is uncoordinated, shows particular susceptibility to temperature. The values for U_{eq} rise significantly above room temperature to a value of 0.103(3) Å^3 in the 365 K data set, which is similar to the values obtained for the partially occupied solvent molecules. In the case of U_1 the difference is even more striking. The maximum value for U_1 for O5 is 0.2238 Å, which is higher than any other atom in the structure including the partially occupied solvent molecules. This means that the movement of the O5 uncoordinated sulfonate atom is very large in one direction. This direction is perpendicular to the plane of the Cu-tetramers (Figure 5-15). The heightened movement for this atom is likely to arise from several factors. Firstly, O5 only shows one formal bond and as such is able to move around much more freely than the atoms in the framework which are held by three or four strong bonds. Another possible factor which could lead to the large ADP is the presence of defects within the structure (Figure 5-16). Whilst the structure is heating up, it is possible that there are a very small number of unit cells which are dehydrated. If in these minority cases the sulfonate oxygen, O5, has coordinated to the metal-centre, then the long range structure will still be the hydrated form, but there will be some unit cells which have the new sulfonate coordination and these will also contribute to the average crystal structure determined by SCXRD. Most O5 positions will be that of the original hydrated form, but some might be in the dehydrated position. The average will see a large uncertainty in the position, and therefore a large ADP parameter.
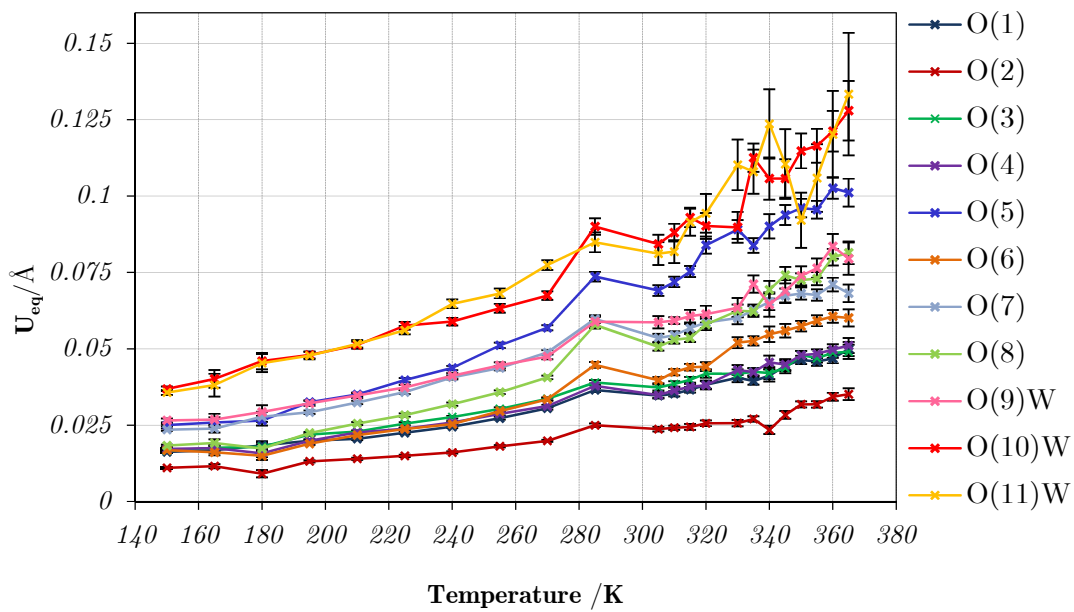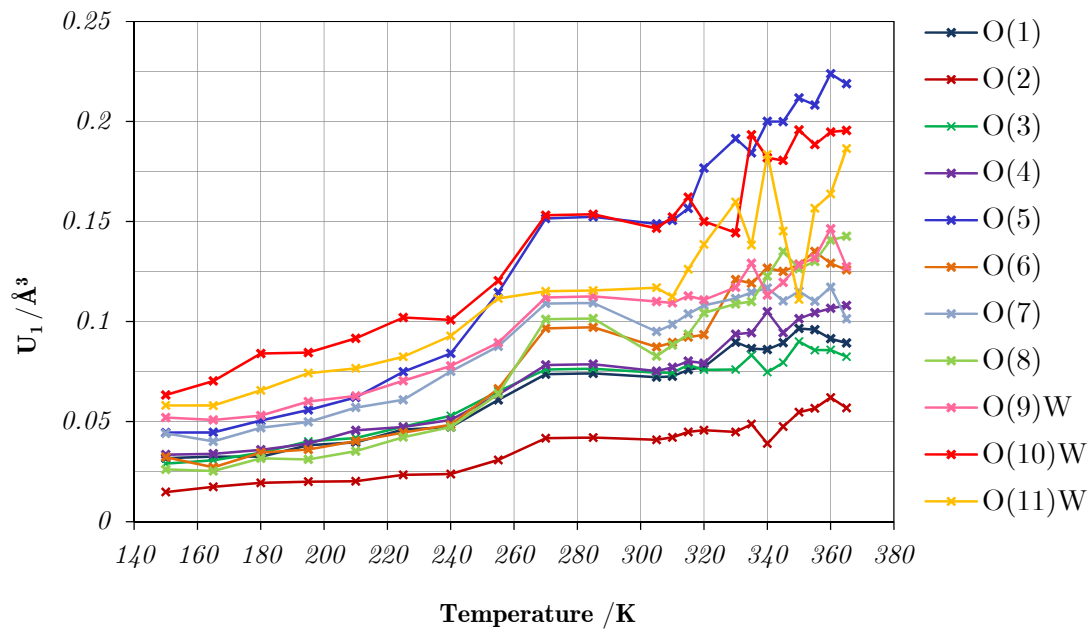
Figure 5-14: Variation in atomic displacement parameters with temperature, U_1 (top) and U_{eq} (bottom).
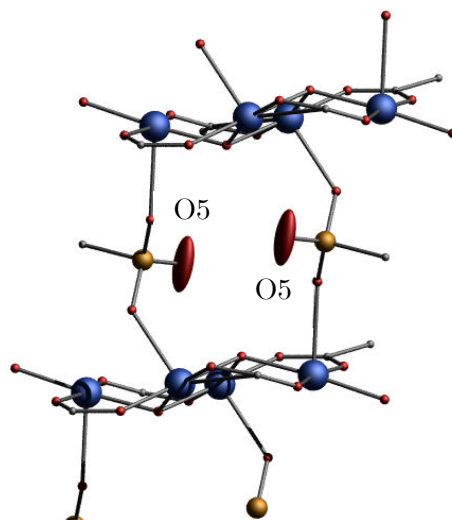
168

Figure 5-15: Part of the structure of Cu-SIP-3 showing the uncoordinated sulfonate molecule in ellipsoid form (all other atoms are shown as spheres for simplicity).
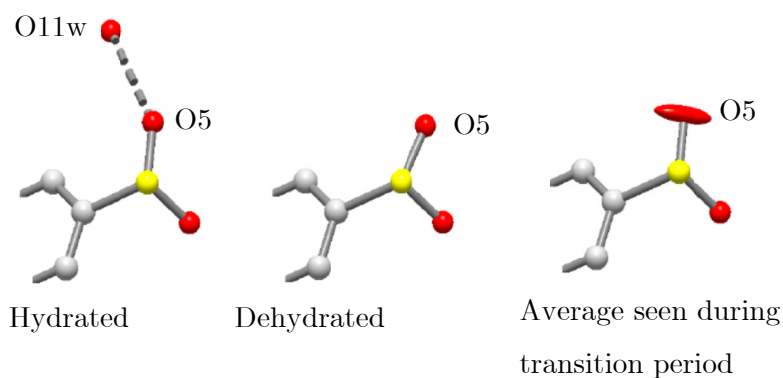

Hydrated   Dehydrated   Average seen during

transition period

Figure 5-16: Cartoon of a defect model which could result in large ADPs for O5 in temperatures leading up to the structural transition.

5.5 Where does the Bragg diffraction go?

The loss of single-crystal Bragg diffraction in the temperature range between 370 K and 405 K can be attributed to the loss of long-range order in the sample between these temperatures. This loss of long-range order means that the conditions for Bragg diffraction are broken and the diffracted intensity is redistributed in reciprocal space as

diffuse scattering. Diffuse scattering is more delocalised over reciprocal space and is, therefore, of much weaker intensity at any given point than the discrete Bragg peaks.

Unit cells with coordinated water still present are significantly different from those without the coordinated water. Initially, when very few coordinated water molecules are lost this is probably equivalent to having a small number of "defects" in the structure, and long-range order is retained on average. As a larger proportion of the water molecules are removed, the concentration of these "defects" increases until there is necessarily a loss of long-range order in the structure. The order, and therefore Bragg diffraction, only reappears when the majority of the coordinated water has been lost and the material can be regarded as having predominantly the high temperature, dehydrated structure, with "defects" of the hydrated crystal structure. The loss of particular water molecules from the crystal induces significant structural change in parts of the crystal which destroys the long-range order, and this is unsurprising given the large atomic movements necessary to fill the residual vacant coordination site.

5.6 Nitric oxide adsorption in Cu-SIP-3

5.6.1 Single-crystal X-ray diffraction studies using the environmental gas cell

The interesting gas adsorption properties of the Cu-SIP-3 framework were outlined in section 5.2.2. The gas adsorption properties of a single crystal were investigated using an *in situ* environmental gas cell.

The crystal was isolated in the gas cell and dehydrated by heating to 500 K under dynamic vacuum and then cooled to room temperature. A data collection at 500 K confirmed that the structure had been annealed in the dehydrated regime. Nitric oxide was added in small bursts and the crystal was allowed to equilibrate before a unit cell was determined. Diffraction frames showed some loss in crystallinity on the addition of nitric oxide, so longer data collection times were required to obtain enough high angle data. Five separate bursts of nitric oxide were added to the gas cell to increase the pressure of nitric oxide. The results are summarised in Table 6.

At nitric oxide pressures up to 270 mbar there was no change in diffraction data quality (Figure 5-17) and indexed as the dehydrated material showing that the nitric

oxide had no effect on the structure. This is consistent with adsorption isotherm data which shows there is no appreciable adsorption at low pressures.[2] Above 270 mbar (data taken at 340 mbar) there was an immediate loss of Bragg scattering from the crystal, and only diffuse scattering remained. No unit cell could be indexed for the data in this region. The setup was left at this pressure of nitric oxide for 1 hour, but Bragg diffraction did not return.

The change in diffraction data above the gate-opening pressure clearly indicate the gas storage in Cu-SIP-3 is driven by a structural change. However, the structure which results from the addition of nitric oxide does not appear to have long-range order, as evidenced by the lack of Bragg scattering.

The nitric oxide adsorption isotherm of Cu-SIP-3 is not saturated at 1 atmosphere pressure of nitric oxide. The 1.1 mmolg^{-1} uptake at 1 atmosphere is equivalent to 0.88 molecules of nitric oxide per dehydrated formula unit, i.e. per 4 copper atoms. If the nitric oxide is coordinating to the axial copper sites analogous to the water binding, 2 molecules of nitric oxide per formula unit would be expected for chemisorption saturation. Due to the toxic nature of the gas it has not been possible to perform a high pressure isotherm on the material, but at 1 atmosphere it is evident that the material is still taking up significant amounts of gas. If this uptake is associated with a structural transition in the material, then it is possible that this structural transition is still incomplete at an atmosphere pressure of nitric oxide.

As evidenced from the difference between the hydrated and dehydrated structures, when the structural transition is only partially complete, unit cells in the structure show significant differences and there is no long-range order present. If this is the case for nitric oxide, then we would not expect to see long-range order in the material for an incomplete transition at 1 bar of nitric oxide in ambient temperature conditions. Possibly, at high enough pressures Bragg diffraction would return, but current set ups do not allow this experiment to be performed.

Table 6: Details of variable pressure nitric oxide addition to the Cu-SIP-3 framework and the structure index through the collection of an orientation matrix.

Addition	Pressure of nitric oxide /mbar	Structure indexed
1	203	Dehydrated structure
2	237	Dehydrated structure
3	270	Dehydrated structure
4	338	No indexing possible
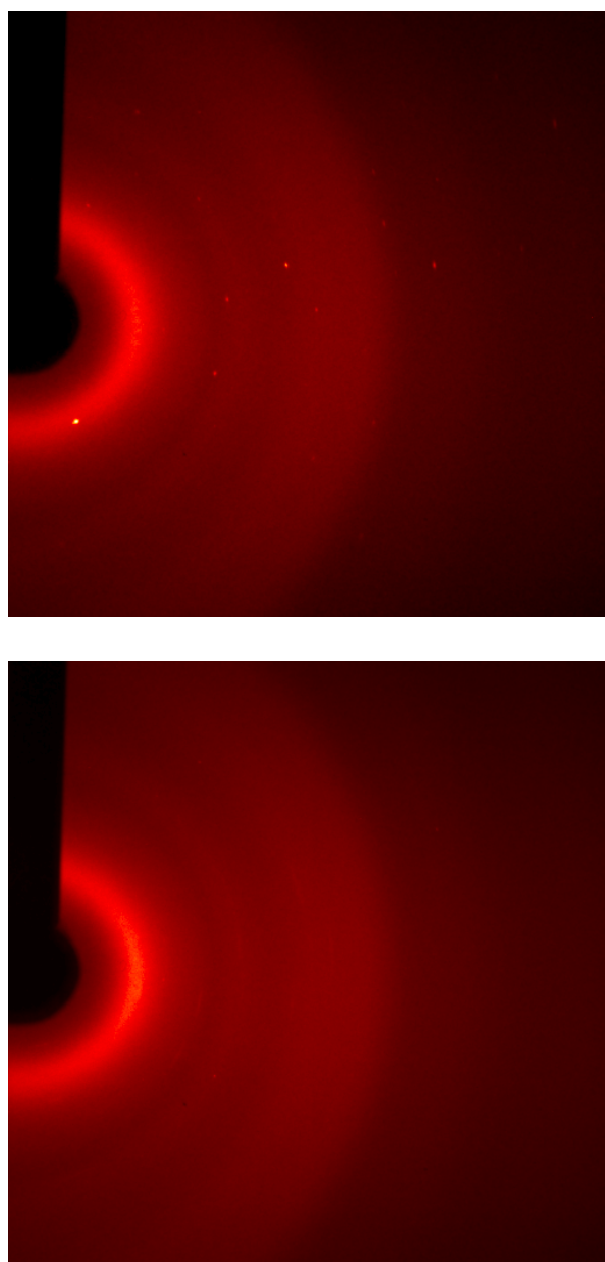
Figure 5-17: Diffraction data frames with the same ω and θ value after the addition of 270 mbar (top) and 338 mbar (bottom) of nitric oxide.

5.7 Conclusions and further work

In situ single crystal studies on the Cu-SIP-3 framework have been performed. Cu-SIP-3 has been shown to be versatile towards a single-crystal to single-crystal transition on exposure to heat, which can be reversed by the exposure to moisture with the retention of crystallinity in the hydrated sample.

Consideration of the variation in structural parameters gives clues towards a mechanism of transformation; the low ADPs for carboxylate framework oxygens at all temperatures indicates that the backbone of the framework is stable even at elevated temperatures and is likely to stay intact throughout the transition, allowing other coordination changes to take place without breakup of the structure. It is clear that significant structural movement in this material commences around 270 K when water loss from the framework is accompanied by a stark increase in movement of all atoms, though most particularly of the uncoordinated sulfonate oxygen atom, O5. The movement of O5 and the removal of solvent molecules O10w and O11w appear to be correlated. However, it cannot be determined from the data whether the increased vibration of O5 leads to the removal of O11w from the structure, or whether the removal of O11w from the structure destabilises O5 and leads to its increased vibration.

Long range order is lost from the material during the transition and it is not possible to follow the removal of O9w, indicating that the loss of this atom triggers the large structural movements which destroy Bragg scattering from the material.

Nitric oxide storage in Cu-SIP-3 is derived from a distinct structural change which, at low pressures of nitric oxide, results in a structure with no long range order, possibly due to an incomplete structural change in the material.

This work opens up several avenues for further research. The temperature region where the transition takes place cannot be studied by Bragg methods, but could be studied using other, total scattering methods (Chapter 6). The structure of the nitric oxide-adduct of the material has also not been solved. The use of a carrier gas or thermal cycling of the nitric oxide loaded material could be attempted to regain long-range order. These experiments would require preliminary work to discover the optimal conditions for the regain of long-range order.

5.8 References

1. J. E. Warren, R. G. Pritchard, D. Abram, H. M. Davies, T. L. Savarese, R. J. Cash, P. R. Raithby, R. Morris, R. H. Jones and S. J. Teat, *J. Appl. Crystallogr.*, 2009, **42**, 457-460.

2. B. Xiao, P. J. Byrne, P. S. Wheatley, D. S. Wragg, X. Zhao, A. J. Fletcher, K. M. Thomas, L. Peters, S. O. EvansJohn, J. E. Warren, W. Zhou and R. E. Morris, *Nat. Chem.*, 2009, **1**, 289-294.

3. Q. Y. Liu, D. Q. Yuan and L. Xu, *Cryst. Growth Des.*, 2007, **7**, 1832-1843.

4. S. Bordiga, L. Regli, F. Bonino, E. Groppo, C. Lamberti, B. Xiao, P. S. Wheatley, R. E. Morris and A. Zecchina, *Phys. Chem. Chem. Phys.*, 2007, **9**, 2676-2685.

5. B. Xiao, P. S. Wheatley, X. B. Zhao, A. J. Fletcher, S. Fox, A. G. Rossi, I. L. Megson, S. Bordiga, L. Regli, K. M. Thomas and R. E. Morris, *J. Am. Chem. Soc.*, 2007, **129**, 1203-1209.

6. M. I. H. Mohideen, B. Xiao, P. S. Wheatley, A. C. McKinlay, Y. Li, A. M. Z. Slawin, D. W. Aldous, N. F. Cessford, T. Duren, X. B. Zhao, R. Gill, K. M. Thomas, J. M. Griffin, S. E. Ashbrook and R. E. Morris, *Nat. Chem.*, 2011, **3**, 304-310.

7. A. C. McKinlay, B. Xiao, D. S. Wragg, P. S. Wheatley, I. L. Megson and R. E. Morris, *J. Am. Chem. Soc.*, 2008, **130**, 10440-10444.

8. P. S. Wheatley, A. R. Butler, M. S. Crane, S. Fox, B. Xiao, A. G. Rossi, I. L. Megson and R. E. Morris, *J. Am. Chem. Soc.*, 2006, **128**, 502-509.

9. P. Müller, *Crystal structure refinement: a crystallographers guide to SHELXL*, Oxford University Press, Oxford; New York, 2006.

10. P. D. C. Dietzel, Y. Morita, R. Blom and H. Fjellvag, *Angew. Chem., Int. Ed.*, 2005, **44**, 6354-6358.

11. *CRC handbook of chemistry and physics*, Chapman and Hall/CRCnetBASE, Boca Raton, FL, 1999, pp. CD-ROMs.

6 Pair distribution function analysis of copper-sulfoisophthalate

6.1 Motivation

The single-crystal data outlined in Chapter 5 indicated that the Cu-SIP-3 material underwent a single-crystal to single-crystal transition. The crystallinity of both the hydrated structure and the dehydrated structure was excellent and thus good-quality single-crystal structures were obtained. During the dehydration process, however, Bragg scattering from the material appears to be extinguished making it impossible to determine the structure of the material using single-crystal diffraction. Similarly, PXRD is unable to assign a structure to the material, as the Bragg peaks decrease in intensity and broaden making structure solution impossible. Using Bragg diffraction alone in this area therefore seemed unviable.

The pair distribution function (PDF) technique is described in section 3.7. This technique uses the total scattering from a material in order to produce the PDF, $G(r)$, which represents a weighted histogram of atomic separations in the material. The advantage of using the total scattering is that while Bragg scattering is taken into account during analysis, it also takes into account the diffuse scattering with *equal weighting*. This means that the PDF is obtainable even for those materials which show very little Bragg scattering. PDF is therefore a useful technique for materials which show disorder or amorphous behaviour which precludes Bragg scattering.

For the Cu-SIP-3 material, the middle region of the dehydration shows very little Bragg diffraction (Figure 5.6). However, the crystal is still being irradiated with X-rays during this period, so there is scattering intensity from the material but this scattering intensity does not interfere constructively to produce Bragg peaks. Instead, it is redistributed throughout reciprocal space as diffuse scattering. Using a total scattering method, we can therefore analyse the scattering without the need for long-range order.

6.2 Aims

This chapter aims to apply pair distribution function analysis to the structural transitions of Cu-SIP-3, particularly in the area which cannot be analysed using Bragg diffraction. Total scattering data will be collected for the material in a range of temperatures and PDFs extracted for each temperature. The PDFs will be analysed using 'Real space Rietveld' refinements and through differential and partial PDF calculation with comparison to model PDFs determined from the single-crystal structures. This will allow the analysis of the change in local structure over the period of the structural transition to be analysed.

Furthermore, total scattering data will be collected for *in situ* nitric oxide-loading experiments for the material to characterise the change in structure on addition of gas to the system. Finally, the information from PDF analysis will be compared and linked with information gained from single-crystal and powder X-ray diffraction methods to propose a mechanism of transformation for the material, and help to explain the behaviour of the single crystal detailed in Chapter 5.

6.3 Experimental details

6.3.1 Variable temperature PDF data collection

PDF data were collected at beamline 11-ID-B at the Advanced Photon Source, Argonne National Laboratory, IL, USA. The wavelength used was 0.21280 Å. A Perkin Elmer amorphous silicon area detector was placed perpendicular to the X-ray beam at a distance allowing high angle diffraction data to be collected.[1] Variable temperature data were collected using a flow gas cell.[2] A sample of Cu-SIP-3 was carefully ground to prevent large crystallites forming Bragg diffraction spots in diffraction frames, which could lead to inaccurate intensity determination, and to prevent any preferential orientation. Approximately 50 mg of the ground sample was placed in the middle of a 7 cm long polyimide capillary. Glass wool was placed either side of the sample to ensure that the sample did not blow out of the capillary when gas-flow was introduced. The capillary was loaded into the flow gas cell. The flow gas cell setup is shown in Figure 6-1. This allows the simultaneous control of the temperature and gaseous environment of the sample. The cell was attached to a goniometer head and mounted on the machine and was centred by moving the goniometer head on the machine. Gas lines can be

attached to the cell to allow the flow of gas through the sample capillary and out through the outlet line. A multi-valve line before the gas cell inlet allows the flow of different gases at different times in the experiment; the flow rate was controlled by the use of gas bubblers. For variable temperature studies, dry nitrogen gas flow was passed over the sample in order to remove the water from the sample and maintain a dry environment. The temperature is controlled via an Oxford Cryosystems cryostream device placed perpendicular to both the X-ray beam and the capillary containing the sample. The temperature of the sample is monitored via a thermocouple device which is placed along the sample within the capillary.

The sample-to-detector distance for the experiment was determined by collecting scattering data from a sample of CeO_2. Prior to the experiment, an empty Kapton capillary was irradiated with the same sample-to-detector distance and frame collection times as the experiment. This was to allow the background scattering from the polyimide material and from the air between the sample and detector to be measured explicitly. This frame was integrated using the same parameters as for data collection frames and the produced background intensity file was used to subtract the background scattering from experimental intensity data during the production of $S(Q)$ in PDFGetX2.[3]

Variable temperature PDF data were collected in the temperature range 300 K to 500 K. A heating rate of 60 K/hr was chosen and data were collected using frames of 120 seconds and obtained at approximately 2 K intervals. The temperature at which data frames were collected was monitored by the thermocouple and recorded from the instrument readout for the frame.

6.3.2 Gas-loading PDF experiments

A ground sample of the material was placed in a Kapton capillary in the flow gas cell and placed under a flow of dry nitrogen. The material was dehydrated by heating the material to 500 K under nitrogen flow. The sample was kept at 500 K for 3 hours before cooling to room temperature. A three way valve allowed the nitrogen flow to be swapped for a nitric oxide flow. Immediately after the gas was changed the hutch was closed and secured and data was collected as soon as was safely possible. 120 second data frames were collected for a period of two hours.
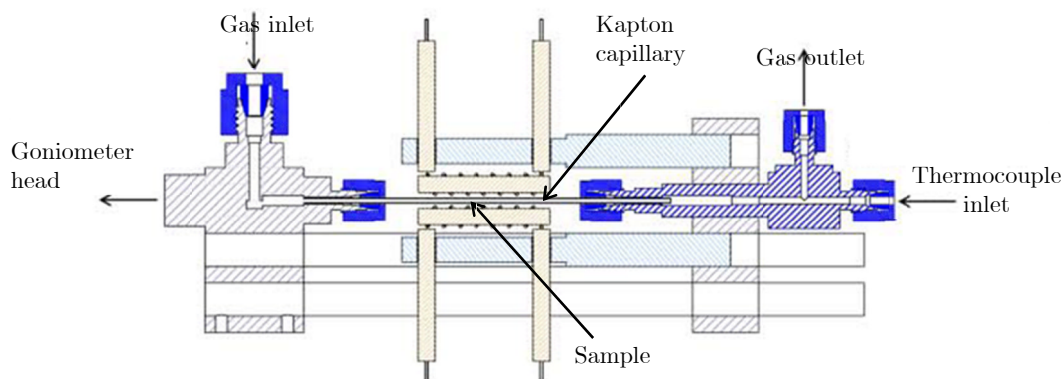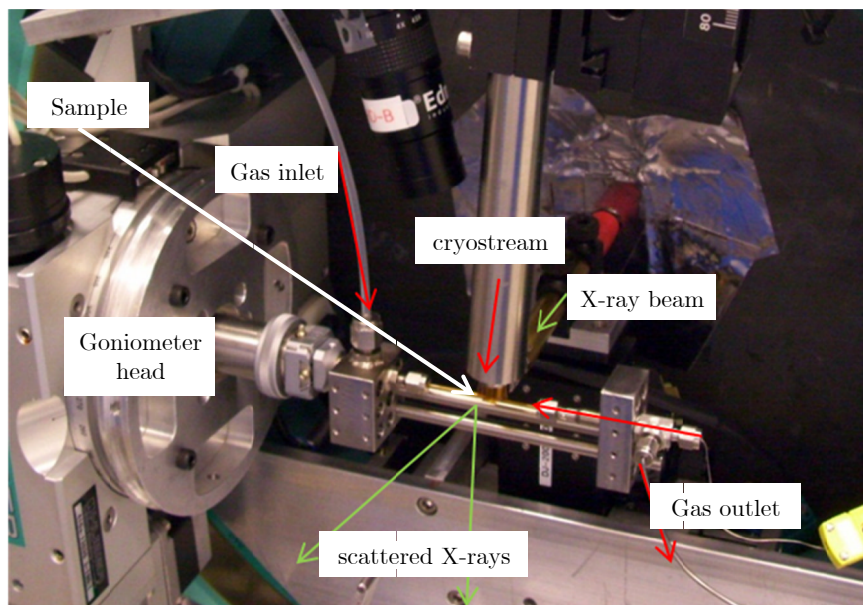
Figure 6-1: Top: Flow gas cell set up on station 11-ID-B (top). Bottom: Schematic of the flow gas cell taken from Chupas _et al._[2]

6.3.3   Data processing

Data frames were integrated using the program FIT2D.[4] The resulting _.chi_ files were converted to $I(Q)$ files in PDFGetX2. The known sample composition for the hydrated Cu-SIP-3 structure was entered in order to normalise $I(Q)$ with respect to the atomic form factor. Corrections for adsorption, multiple scattering, polarization and background were applied to the data in PDFGetX2 to produce $S(Q)$ and $F(Q)$. These corrections were optimised for the data set collected at 300 K and applied to all other data sets. Q_{max} for the Fourier Transform was determined as 22 Å⁻¹ by examination of the $F(Q)$ function to determine the maximum distance to which it was possible to see features in the data. $S(Q)$ was optimised by convergence to 1.0 in the range of 12 to 40

Å. The sample thickness was estimated to be 2.0mm. For the data set at 300 K the background function was multiplied by a 1.05 to obtain the best analysis. The corrected and normalised scattering data were Fourier transformed to produce $G(r)$ in the range of 0.01 to 40 Å.

For the data frames collected at other temperatures, an identical correction and Q-values for the Fourier transform were used (this is important if the data is to be directly compared) and the same background multiplication factor was used in all data sets. The change in scattering power of the sample was addressed through the use of r - averaging over any normalisation ripples later in the analysis (section 6.4.2.1, page 194)

For the positions in the PDFs to be accurately quoted, a Gaussian was fit to the peak of interest using the program Fityk.[5] The positions are quoted to two decimal places.

6.3.4 Structural refinement using PDFs

Refinements were performed in PDFGui.[6] Refinement of the data was performed for the distance range 1.0 Å to 40 Å. A starting value of Q_{damp} of 0.08 was chosen. Short-range correlated motion of the atoms was accounted for in the refinement using the parameters S_{ratio} and r_{cut}. Short-range correlated motion will make peaks in the low-r region narrower because the movement of one atom will induce the same movement in another, correlated atom. S_{ratio}, which is defined as the PDF peak ratio between the low-r and high-r regions where correlated motion is and isn't present respectively, was set to a starting value of 0.5, with a cut-off distance, r_{cut}, of 3.6 Å. 3.6 Å was chosen for the value of r_{cut} because peaks below this distance are considerably more intense, whereas after this value the peaks in the PDF fluctuate around approximately the same maximum and minimum values. This value is the approximate Cu-Cu distance in the sample, which indicates that the short range correlation in the material extends only over the Cu-O-Cu distances in the sample and no further. The scale factor for the model structure was set to 1.0 as a starting value. The scale factor for the experimental data was not refined because this would have the same effect as refinement of the model scale factor.

The atomic displacement parameters were set to be isotropic, with $U_{11} = U_{22} = U_{33} = 0.05$ Å^2 with $U_{12} = U_{23} = U_{31} = 0$. These were not refined independently as to not over-parameterise the refinement. Instead, they were refined as atom types; all copper

diagonal terms were constrained to refine as one parameter. U_{11}, U_{22} and U_{33} for all carbons were refined as one value, sulfur atoms as another. U_{11}, U_{22} and U_{33} for oxygens were refined in batches depending on their chemical environment; the bridging hydroxyl oxygens were considered as one environment, the carboxylate carbons and coordinated sulfonate oxygens which are all used in framework bonding were considered another bonding environment. U_{11}, U_{22} and U_{33} for the uncoordinated sulfonate oxygen were refined independently. For the hydrated structure, U_{11}, U_{22} and U_{33} for the uncoordinated water molecules, which were expected to have much higher displacement parameters than the other oxygen molecules were refined independently.

6.4 Results

6.4.1 PDF for Cu-SIP-3 at 300 K

The PDF for the Cu-SIP-3 structure at 300 K was calculated out to 40 Å and is shown in Figure 6-2. This PDF can be compared to the single-crystal structure at this temperature and peak assignments can be made from this reference using partial PDFs calculated from the single-crystal structure at 300 K shown in Figure 6-3. Partial PDFs calculate the PDF contribution from a particular set of atom pairs in the material, and weigh it according to the total number of atoms of that species in the sample (section 1.7.6.3).
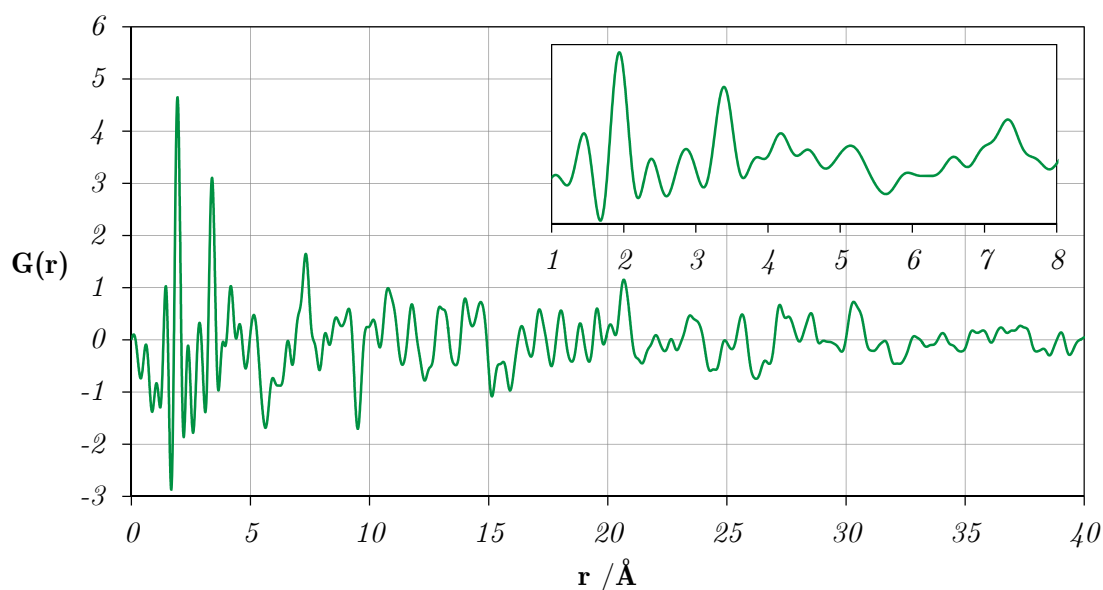

Figure 6-2: The PDF for Cu-SIP-3 at 300 K. Inset shows the region of 1 Å < r < 8 Å

Peaks below 1 Å do not have physical meaning because this is closer than two atoms can approach each other. They are the result of experimental errors and Fourier termination errors (section 3.7.5). Peaks between 1.2 and 2.5 Å are due to the bonding interactions in the structure. The first chemically meaningful peak is found at 1.44 Å. This peak is due to the S-O, C-C and C-O nearest neighbour distances in the sulfoisophthalate linker (bond length range of 1.266(3) to 1.495(3) Å from the single-crystal model).

The most intense peak of the PDF is found at 1.96 Å. Peak intensity in the PDF decreases with distance due to the Debye-Waller factor and instrument damping. However, PDF peaks are also weighted by multiplicity and abundance of species, and by atomic scattering factor (in the case of X-rays, atomic number) meaning that strong peaks appear at distances where copper-atom correlations occur. The peak at around 1.96 Å can be assigned to Cu-O bonds in the framework. The high intensity of this peak in comparison to those peaks at close distances to it can be attributed to several factors. Firstly, the atomic scattering power of copper is high. Secondly, there are a large number (total of 20) Cu-O bonds within one unit cell which will form a strong peak. Finally, this peak is quite sharp, indicating that the range of bond lengths for this species is narrow. From the single-crystal model at 300 K (300K.cif in Appendix C) we can see this is the case, with the Cu-O(carboxylate) bond length range being 1.975(3) – 1.913(3) Å and the Cu-O(sulfonate) bonds being slightly longer at 2.374(3) and 2.248(3) Å. Having many bonds in a narrow distance range will lead to a narrow intense peak in the PDF.

The peak at 2.39 Å is has contributions from Cu-O(sulfonate) bonding, Cu-S, carbon-oxygen and carbon-carbon cross ring distances in the sulfoisophthalate linker. Distances greater than 2.5 Å are longer than nearest neighbour bond distances in the material. Peaks at higher distances are due to atom-atom correlations which are not formal covalent bonds. The peak at 2.34 Å is due to carbon-carbon cross ring distances in the sulfoisophthalate linker.

Two intense peaks are found with maxima at 2.87 Å and 3.39 Å. These are due to the copper-copper distances in the material. The Cu-tetramer has three distinct sets of Cu-Cu distances: one between adjacent copper ions in the rhombus, one between the two copper atoms at the acute vertex of the rhombus and one between the two copper

ions at the obtuse vertex of the rhombus. From the single-crystal model at 300 K these fall at 3.3053(5) and 3.4098(5) Å, 6.0367(5) Å and 2.9432(4) Å, respectively. These distances make up the bulk of the peak found at 2.87 Å and 3.39 Å.

At longer distances peaks generally cannot be assigned to a single inter-atomic distances, because of multiple overlapping contributions for correlations of similar distances. However, because the contribution of heavy atoms is so significant, it is possible to assign the large peak at around 7.3 Å to the Cu-Cu distance between tetramers in different layers of the material.
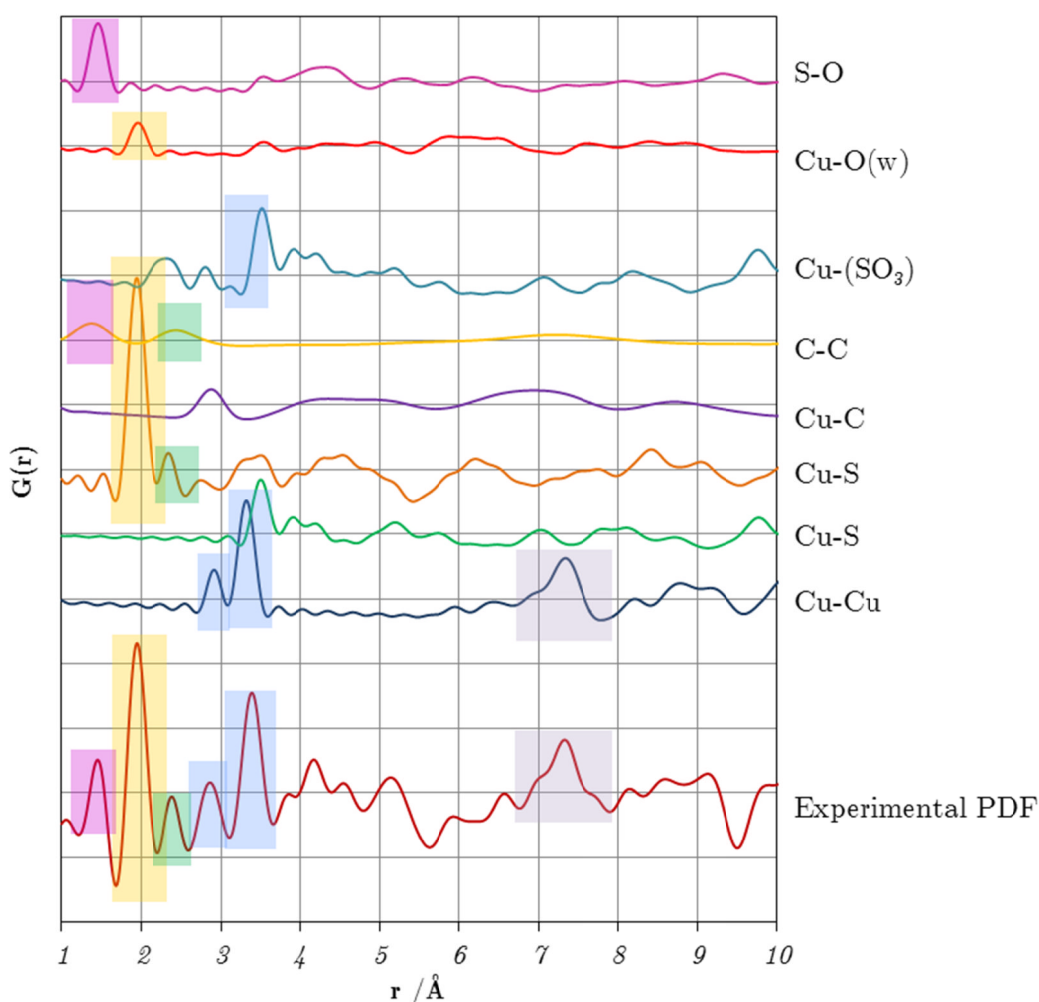
Figure 6-3: Comparison of experimental PDF (bottom) with partial PDFs for specific atom type pairs. Peaks at low-r can be assigned to specific atomic correlations. Colour panels represent specific atom pairs assigned to peaks in the experimental PDF.

6.4.1.1   Refinement of the Cu-SIP-3 structure at 300 K using PDF data

Inspection of the PDF can identify likely atom-atom species responsible for certain peaks in the PDF. But, because of the increasing number of atom-atom distances which contribute to peaks at higher r-values, and the decreasing intensity due to the Debye-Waller factor, it is difficult to gain more information about the peaks at higher distances by visual inspection alone. Therefore, a refinement of the PDF data obtained at 300 K against the model from single-crystal data at the same temperature was performed in PDFGui.

The initial refinement run refined only the scale factor, Q_{damp} and s_{ratio}. Once these were stable and unchanged by further refinement cycles, the unit cell parameters of the structure were refined. These showed very little change from the single-crystal model (Table 1). When no further improvement to residual factors could be achieved by more refinement cycles, the atomic displacement parameters were added to the refinement for all atoms. The symmetry-constrained[1] positions of the Cu-atoms were also refined, improving the fit despite showing very little movement from the positions determined by single-crystal X-ray diffraction. Addition of framework oxygens to the refinement resulted in significant distortion of bond lengths and framework geometry, so these were not included as parameters in the refinement.

The final refinement is shown in Figure 6-4. CIF and results files[2] for the structure are available in Appendix C. The refinement gave $R_w = 27.25$ %, and the model showed a good fit at all distances; the differential PDF shows no discrete features representative of aspects of the structure which hadn't been accounted for in the model structure. The good fit of the refinement indicates that the local structure of the structure at 300 K is very similar to the long-range structure determined from the Bragg methods.

Comparison of the structural parameters determined by PDF refinement with those determined from the single crystal are shown in Table 1. Unit cell parameters are very similar between the two models and the monoclinic angle of the cell agrees within

---

[1] PDFGui expands the space group from the model structure and performs the refinement in P1 to allow local distortions to be modelled. However, it is possible to constrain positions and ADP values to the original space group during the refinement.

[2] PDFGui-generated *.cif* files do not contain errors on refined parameters. Errors are contained in the *.res* file which is produced, although errors produced from RAPDF measurements are not strictly accurate for reasons outlined in Section 3.7.6.

0.2°. Anisotropic displacement parameters are small for all atoms with the exception of the carbon atoms. The Cu-O bond lengths do change (Table 2), but all remain within expected range for Cu-O bonds. Furthermore, the ability to discriminate between sulfonate and carboxylate linkages by Cu-O bond lengths remains.
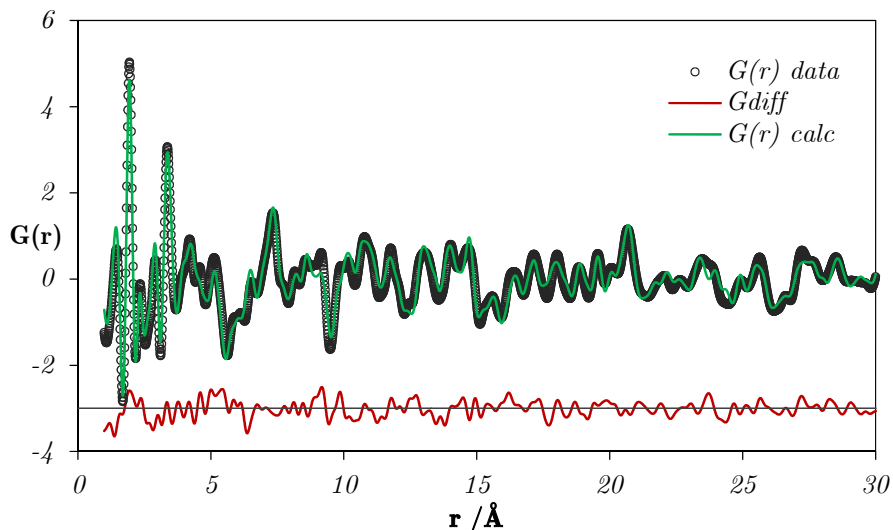

Figure 6-4: Refinement of the Cu-SIP-3 structure against PDF data at 300 K. The black markers show the experimental data, the green line shows the simulated PDF from the refined model structure. The differential, defined as $G(r)_{exp} - G(r)_{calc}$ shown in red and offset by -3.

Table 1: Comparison of the unit cell parameters for Cu-SIP-3 obtained from single-crystal and PDF refinements. The esds on the numbers from the PDF analysis are undetermined as esds on the individual data points are unknown.

Parameter	SCXRD	PDF analysis
a /Å	7.3333(14)	7.3446
b /Å	18.1527(32)	18.1180
c /Å	10.1729(19)	10.0645
β /°	94.379(4)	94.204

Table 2: Cu-O bond length for the single-crystal and PDF refinement of Cu-SIP-3 at 300 K. The esds on the numbers from the PDF analysis are undetermined as esds on the individual data points are unknown.

Atom 1	Atom 2	Bond length /Å		Atom 1	Atom 2	Bond length /Å	
		SCXRD	*PDF*			*SCXRD*	*PDF*
Cu1	O4	1.911(4)	1.8912	Cu2	O6	1.911(4)	1.97
	O3	1.936(4)	1.9345		O1	1.934(4)	1.8651
	O2	1.947(3)	1.9637		O2	1.971(3)	1.9935
	O9W	1.976(4)	2.0199		O2	1.979(3)	1.9353
	O8	2.361(5)	2.4127		O7	2.280(4)	2.2251

Table 3: Anisotropic displacement parameters for 300 K structure of Cu-SIP-3 after PDF data refinement. The esds on the numbers from the PDF analysis are undetermined as esds on the individual data points are unknown. O(s) = sulfonate group oxygen; O(c) = carboxylate group oxygen; O(w) = water oxygen.

Atom	ADP /Å^3
Cu	0.012
S	0.011
O(s)	0.024
O(c)	0.024
C	0.194
O(w)	0.014

6.4.1 PDF for Cu-SIP-3 at 500 K

The PDF extracted for Cu-SIP-3 at 500 K is shown in Figure 6-5. This was also compared to the single-crystal model determined at 500 K. Overall, peaks were broader at this temperature. This is expected as increased thermal movement of the atoms leads to greater uncertainty in their positions, and so a greater possible range of atom-atom distances for each atom pair.

The refinement of the 500 K model from single-crystal X-ray diffraction was set up with the same initial parameters as the 300 K refinement detailed above and parameters refined in the same order until the R-factor could not be improved by further refinement cycles. The final fit of the data was less good than the data set at 300 K, but

again this is to be expected because of the higher atomic position uncertainties associated with the higher temperature. The final R_w was 29.98%. A comparison of structural parameters determined by PDF refinement with those determined from single crystal is shown in Table 1. The values for unit cell parameters determined by the two methods are very similar (Table 1) and there is very little difference between atomic positions determined by the two methods, thus little change in Cu-O bond length (Table 5). This indicates that the local structure of the material is very similar to the long-range structure at this temperature.
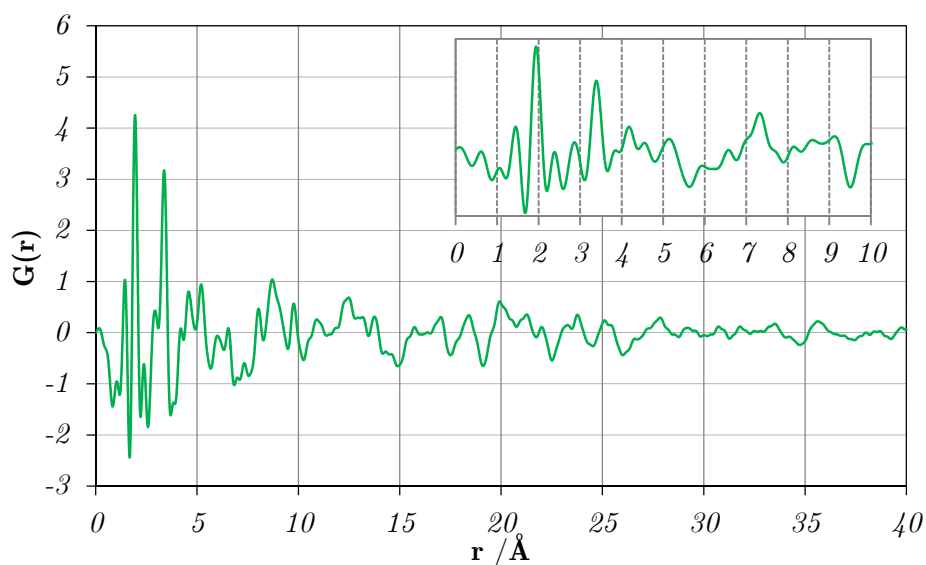
Figure 6-5: The PDF for Cu-SIP-3 at 300 K. Inset shows the region of 1 Å < r < 8 Å
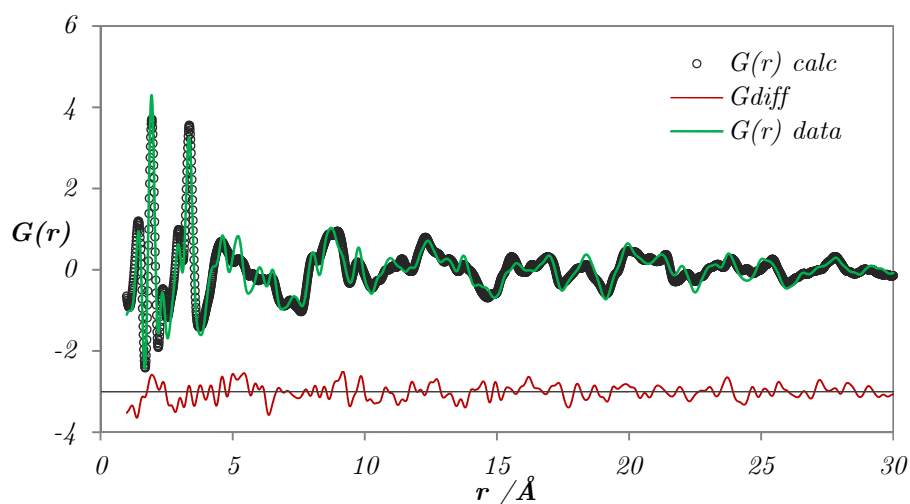
Figure 6-6: Refinement of the structure of dehydrated Cu-SIP-3 against data collected 500 K.

186

Table 4: Comparison of the Cu-SIP-3 structure obtained from single-crystal and PDF refinements. The esds on the values from the PDF analysis are undetermined as esds on the individual data points are unknown.

Parameter	SCXRD	PDF analysis
a /Å	13.796(2)	13.7465
b /Å	19.430(4)	19.4734
c /Å	12.057(3)	12.1856
β /°	139.172(10)	139.74

Table 5: Cu-O bond lengths for the single-crystal and PDF refinement of Cu-SIP-3 at 500K (Atom numbers relate to figure 5.2). The esds on the numbers from the PDF analysis are undetermined as esds on the individual data points are unknown.

Atom 1	Atom 2	Length /Å	
		SCXRD	PDF
Cu1	O2	1.905 (6)	1.895
	O16	1.915 (7)	1.9274
	O14	1.959 (6)	1.9431
	O1	1.998 (6)	1.9994
Cu2	O15	1.900 (6)	1.9274
	O3	1.901 (6)	1.8355
	O12	2.000 (6)	1.9662
	O6	2.030 (6)	2.0509
	O11	2.408 (7)	2.421
Cu3	O8	1.917 (6)	1.8355
	O9	1.923 (6)	1.9561
	O14	1.981 (6)	1.9594
	O12	1.997 (6)	2.0437
	O7	2.276 (7)	2.2247
Cu4	O4	1.899 (6)	1.9541
	O10	1.935 (6)	1.9137
	O12	1.988 (5)	1.9834
	O14	1.992 (6)	1.9239

Table 6: Anisotropic displacement parameters for 500 K structure of Cu-SIP-3 after PDF data refinement.

Atom	ADP /$\mathring{A}^2$
Cu	0.012
S	0.004
O	0.0026
C	0.0079

6.4.2   Variable temperature PDFs

PDFs for the Cu-SIP-3 structure were determined for temperatures between 300 K and 500 K. Data sets were taken approximately every 2 K. Figure 6-8 shows the variable temperature PDFs for the full temperature range of 300 K to 500 K with data sets shown every 10 K. PDFs can be extracted from the data at all temperatures, including temperatures where Bragg methods are unable to analyse the data (365 K to 420 K).

6.4.2.1   Change of r_{max} with temperature

The distance range to which distinct features can be seen in the PDF, r_{max}, reduced with temperature (Figure 6-7). At 300 K, PDFs can be extracted to 70 Å and there is information visible in the PDF to distances of greater than 60 Å. With increasing temperature, the distance to which information can be seen in the PDF is reduced. The reduction indicates that the crystallinity of the material is reduced.[7] At 400 K r_{max} is reduced to around 50 Å. Whilst the single crystal shows regain of crystallinity at higher temperatures, there is no increase in the distance to which the PDF holds information at higher temperatures - at 500 K r_{max} is very similar to that at 400 K. This indicates that each individual crystallite retains good crystallinity throughout the transition, but does not regain perfect crystallinity once the structural transition is complete.

6.4.2.2   Change in PDF peaks with temperature

The peaks for the PDF of Cu-SIP-3 show substantial change with temperature meaning that significant changes in atom-atom distances take place. The data set at 300 K corresponds to the hydrated structure and that at 500 K corresponds to the dehydrated material. Therefore, the changes in the PDF between these temperatures must correspond to the structural transition of the material taking place. There are few changes to the PDF at temperatures below 360 K. Similarly, above 450 K, there are few

further changes to the PDF indicating a temperature range of transition of 360 K to 450 K. This range is similar to the range displaced by the single crystal (370 K – 405 K) and previous powder data (368 K – 405 K).
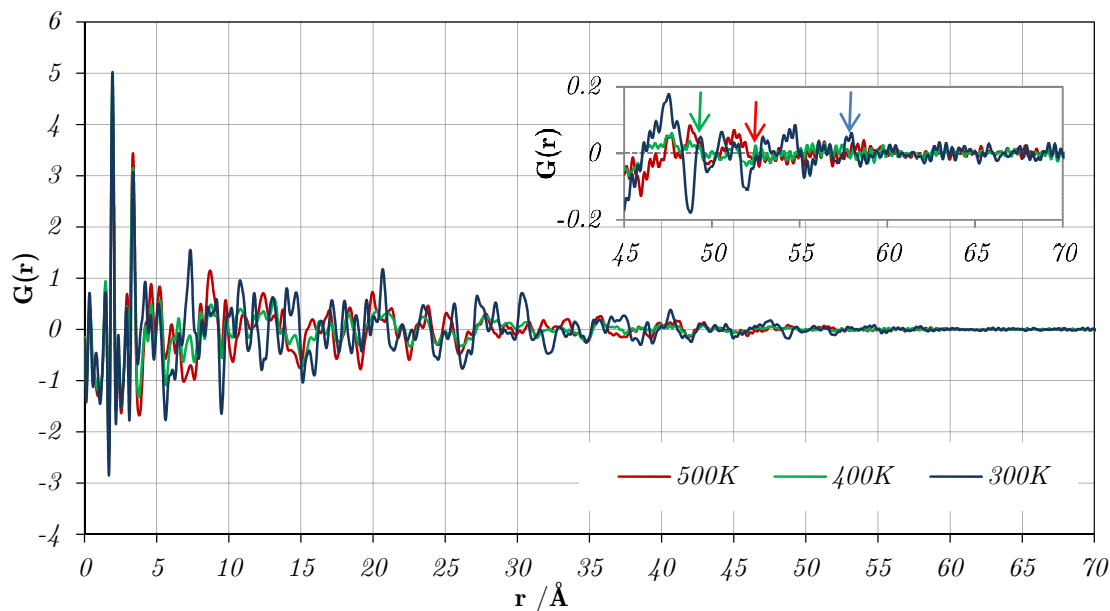

Figure 6-7: PDFs for Cu-SIP-3 extracted to 70 Å. Blue = 300K, Green = 400 K, Red = 500 K. Inset shows zoom in high-r region. Arrows show estimated r_{max} for the three data sets.
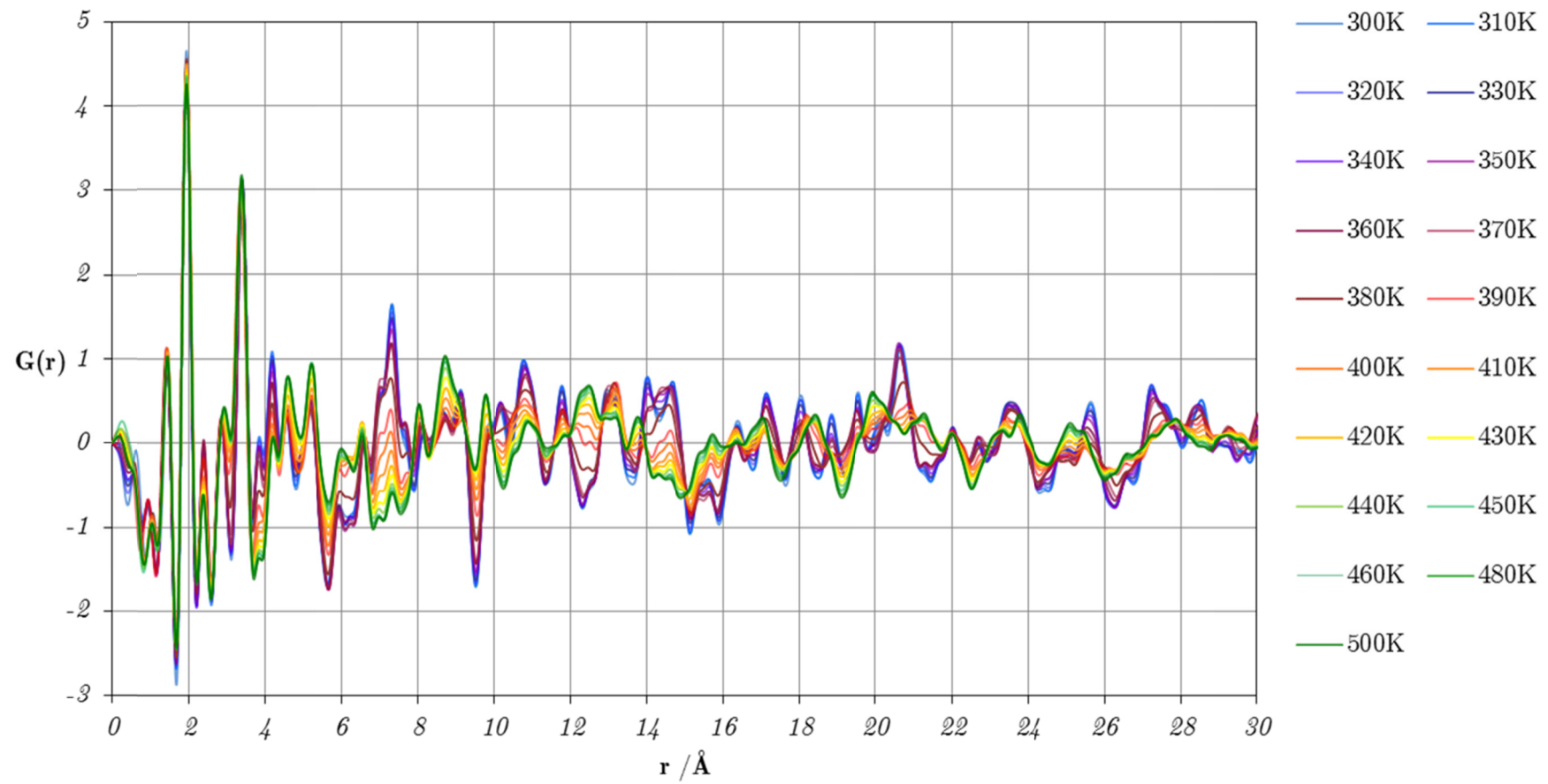
Figure 6-8: Variable temperature PDF results for Cu-SIP-3 between 300 K and 500 K.

6.4.3 Two phase refinement of the Cu-SIP-3 structure

Data sets taken every 10 K were analysed using a two phase model. The best fit structure at 300 K was used as a model for the hydrated phase, and that from the best fit at 500 K used as the model for the dehydrated phase. A two phase refinement was set up in PDFGui. The phase scale factors of the two phases were allowed to vary, with scale factor of the dehydrated structure constrained to be $1 - SF_{Hyd}$ where SF_{Hyd} is the scale factor of the hydrated structure. This allowed determination of the relative amounts of the two phases of the material. The results of the analysis are shown in Figure 6-9.

The two phase refinement allows the phase fraction to be monitored. The phase fraction of the hydrated structure reduced with temperature as the materials transforms. In both end data sets where the material is assumed to be fully hydrated (300 K) or dehydrated (500 K), the two phase analysis assigns a small proportion of the material to the alternative phase. It is possible that not all of the material has dehydrated at 500 K, but this could also be the product of errors in the refinement.

Figure 6-9 (left) shows the residual factor, R_w for each of the refinements between 310 K and 500 K. The R_w values for the refinements at the intermediate temperatures increase sharply, peaking at 42.2% for the data set at 390 K. The poorer fit of the two phase model in this area indicates that there is something more subtle associated with the structural change of this material than a transition between two phases. The data indicate that there could be a third phase associated with the partially dehydrated material which causes the two-phase model to be a poorer fit at intermediate temperatures. This is further suggested by differential PDF analysis (see section 6.4.2).

6.4.1 Analysis of peak variation with temperature

Several features of the variable temperature data indicate that the transition undergone by this material is more complex than a conversion between two phases. Firstly, some areas of the variable temperature PDFs (Figure 6-8) do not show clear isosbestic points. Isosbestic points are specific points in the data which the function passes through at all temperatures. The presence of isosbestic points generally indicates that the system is two phase with conversion of one phase to another and with intermediate temperatures being made up of a phase fraction of the two phases.[8, 9] In addition to this, peaks of the PDF show different temperature dependence; the peaks

change at different rates with variation in temperature. This point is illustrated in Figure 6-10 where the peaks which show early movement, late movement and gradual movement are highlighted. The variable peak change indicates that different atom-atom distances change at different times during the structural transition, meaning that the movement of different parts of the structure is not concurrent and bodies in the structure move independently.
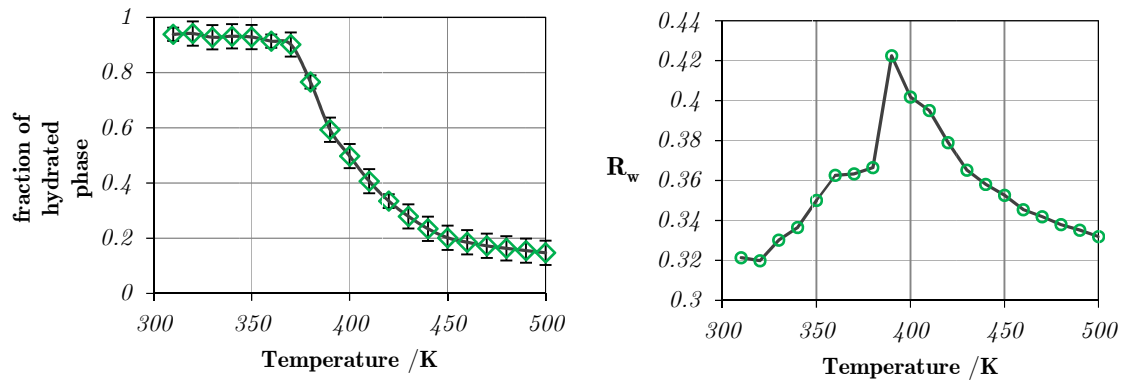

Figure 6-9: Two phase refinement of the Cu-SIP-3 system. Left: variation in phase fraction of the hydrated phase in the material with temperature. Right: R_w values determined for each of the two-phase PDF refinements.
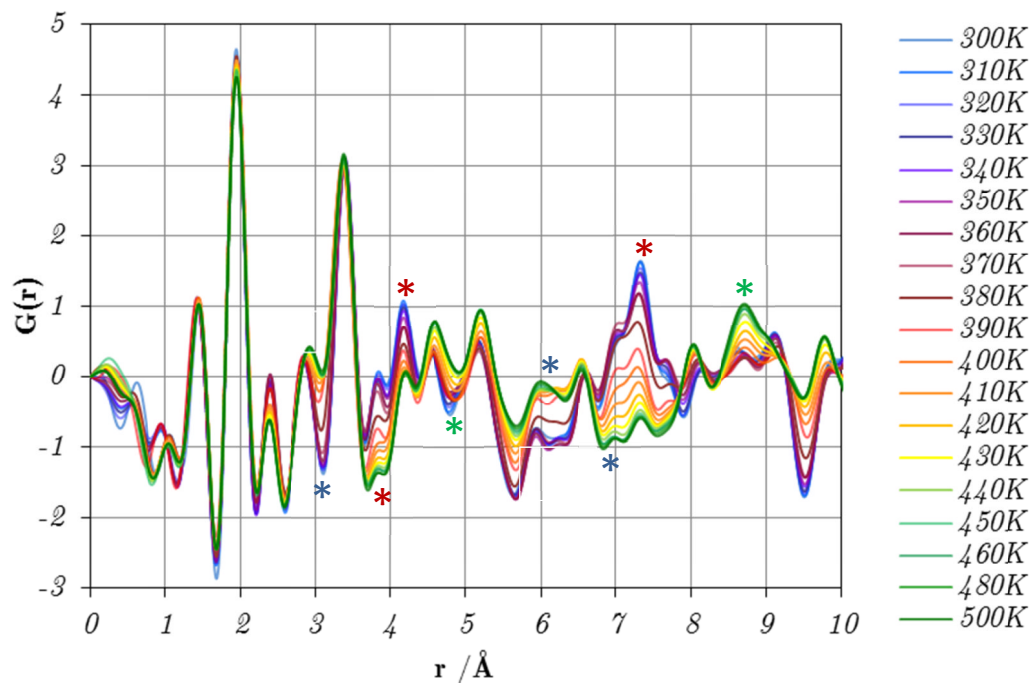
Figure 6-10: Variable temperature PDFs for the distance range 0 Å < r < 10 Å. Peaks which change within a very narrow temperature range are marked as blue ＊. Peaks which change

Figure 6-10 illustrates that there are few changes in the PDF at distances less than 3 Å. This indicates that the nearest neighbour distances in the structure remain unchanged. The unchanged peak at 1.44 Å indicates that the sulfoisophthalate linker remains intact at all temperatures. This is unsurprising considering the high bond energies of these covalent bonds compared to other linkages in the structure. The peak at 1.96 Å is also essentially unchanged at all temperatures indicating that Cu-O linkages are unchanged and so the carboxylate framework remains intact throughout the transition.

The constancy of the peak at 1.96 Å is also significant because it is known from the single-crystal structures that a change in Cu-O coordination takes place during the transition; the water molecule is removed from the metal-centre and the sulfonate oxygen coordinates into the vacant coordination site. Experimental data does not observe a change in the peak at 1.96 Å indicating that the change in metal coordination is too quick to measure using PDF and that the population of co-ordinately unsaturated sites in the material during the transition is minimal. This is unsurprising – coordinately unsaturated sites are likely to be unstable and highly reactive, meaning that the coordination of the sulfonate oxygen is likely to happen the instant that the water leaves the site.

6.4.2 Variable temperature differential PDFs

Differential PDFs allow visual examination of the way in which the PDF of a material changes between data sets on exposure to a synthesis. In this case, the external stimulus is heat inducing the dehydration of the material. Differential PDFs are calculated by subtracting the initial PDF from subsequent PDFs in the experiment. Differential PDFs were initially calculated for the full temperature range, but as the bulk of the phase transition happens at temperatures above 360 K, for detailed analysis the differential PDFs were calculated by subtracting the data set obtained at 360 K from all subsequent PDFs. The result is a function which describes how the PDF at a subsequent temperature, T, is different to the PDF at 360 K. A positive peak in the differential PDF at a temperature represents an atom-atom separation in the structure which is

present in the sample at temperature, T but not at 360 K. Correspondingly, a negative peak in the differential PDF for temperature, T, represents atom-atom distance in the material at 360 K which is no longer present at temperature, T.

6.4.2.1 *R*-averaging differential PDFs over the period of normalisation ripples

Differential PDFs were calculated for Cu-SIP-3 in the temperature range 300 K to 500 K (Figure 6-11). It is possible to observe normalisation ripples in the differentials at low *r*-values. These occur because of the reduction in scattering power of the sample with temperature, meaning that the overall intensity of each PDF also decreases with temperature. The presence of normalisation ripples in the data can result in the over-interpretation of small features in the differentials and assignment of some peaks which are nothing more than experimental noise, to changes in atom-atom distances. The period of the normalisation ripples is constant with distance, and the reduction in scattering intensity affects all of the scattering data, so the intensity of the normalisation ripple can be reduced by *r*-averaging the data over the period of the normalisation ripples. Whilst there will still be some contribution to the differential PDF from the reduction in scattering intensity, the contribution is likely to be small so the main features of the differential are due to the change in atom-atom distances. The period of the normalisation ripples was determined as 0.34 Å by analysis of the period of the peaks occurring below 1.3 Å. The normalised differential PDFs for Cu-SIP-3 in the temperature range 360 K to 420 K are shown in Figure 6-12. There are still some peaks visible in the differential PDFs in the low-*r* region where no chemically meaningful peaks appear. These are due to residual errors in the data. Because of the presence of these peaks, small peaks in the differential which show intensity smaller than these low-*r* peaks are not included in the analysis because to avoid over-interpretation of data noise.
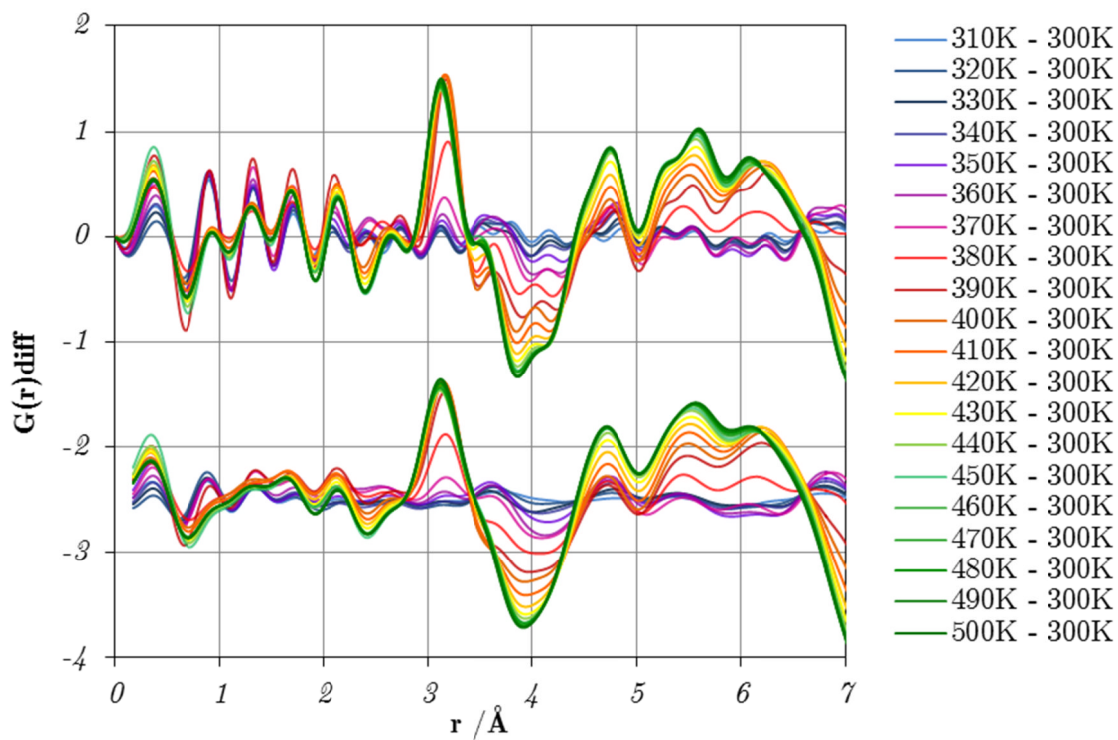
Figure 6-11: Differentials for Cu-SIP-3 in the distance range of 0 − 5 Å for 300 K < T < 500 K. Top: Raw differentials Bottom: Normalised differentials after r-averaging with period of 0.34 Å.
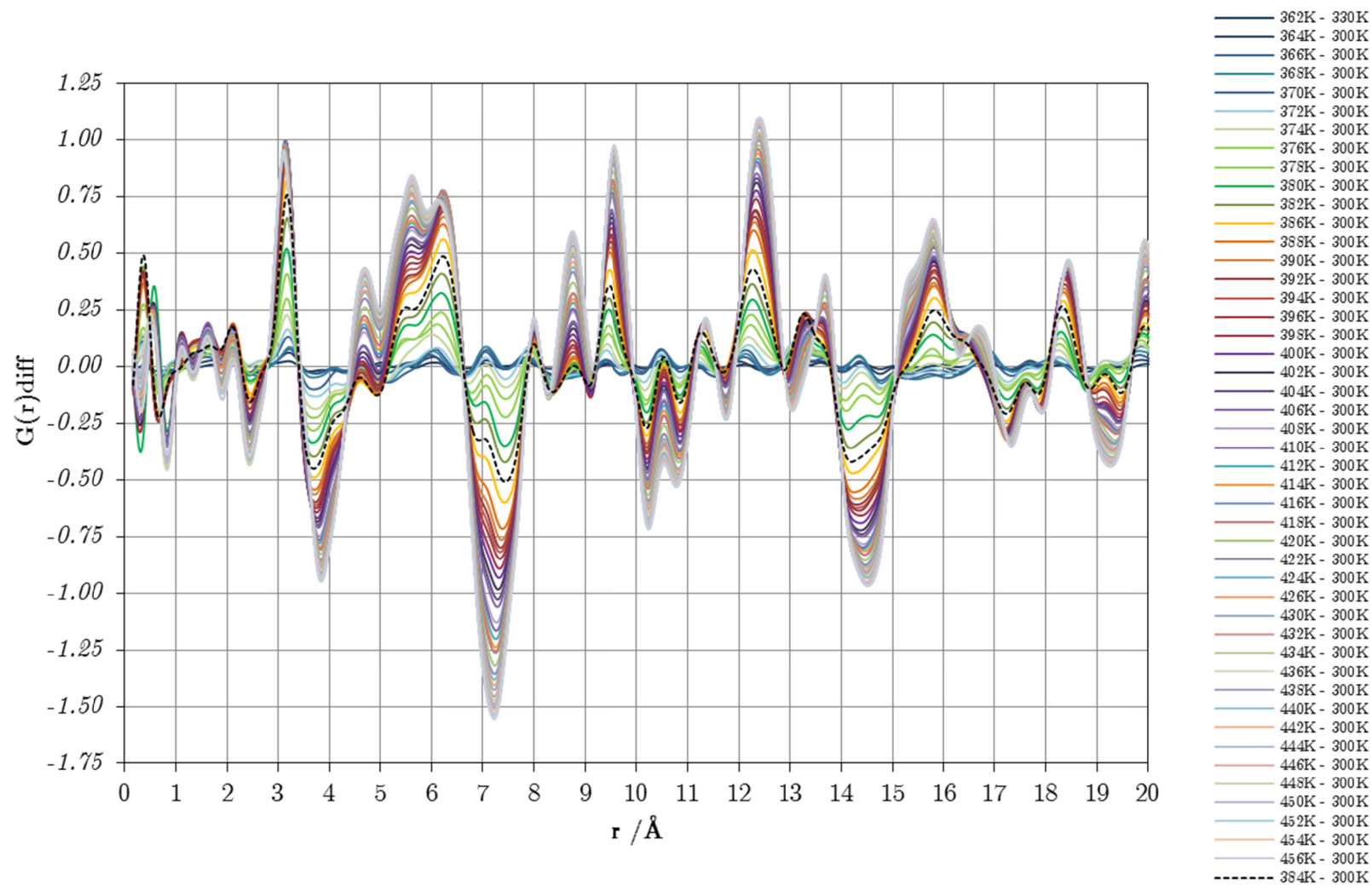
Figure 6-12: Normalised differential PDFs for Cu-SIP-3 for the temperature range 360 K < T < 420 K. The black dashed line represents the differential at 384K where the transition is approximately half complete, for easy visual comparison of peak completion.

6.4.2.2 Change in differential peaks with temperature

Peaks in the differential PDF for Cu-SIP-3 show non-uniform temperature dependence. Some peaks in the differential, for example those present at 3.12 Å and 5.59 Å, change very quickly within the temperature range 360 to 400 K and show little further change above 400 K. Others, like the large peak found at 7.33 Å show gradual change which is sustained over a much larger temperature period and only complete at 450 K. Other changes appear to happen much later on in the transition, such as the peaks at 8.72 Å.

These differences indicate that the structural transition does not happen by the combination of two phases where each unit cell or crystallite is either hydrated or dehydrated. If this was the case then the PDF for intermediate temperatures would be a simple combination of the PDFs for the relative phase fractions of the phase pure hydrated and dehydrated material. In this case, all the peaks in the differential PDF are expected to change at the same rate. A model differential PDF for dehydration transition was calculated using the models for the 300 K and 500 K. Model PDFs for the intermediate structures made up of phase fractions of the hydrated and dehydrated structures were calculated by the addition of the relative percentages of the model PDFs determined from the two phase refinement outlined earlier. For example, the calculated phase fraction at 400 K is 49.8% hydrated and 50.2% dehydrated. The model PDF for this temperature was calculated at each distance point using the relation: $G(r)_{300} = 0.498 + (1 - 0.498)G(r)_{500}$. Differential PDFs for these calculated PDFs were calculated by subtracting the PDF for the 300 K structure from each subsequent temperature shown in Figure 6-13. The calculated two-phase differential PDFs have peaks which all change at the same rate. This is not found in the experimental PDF (shown in Figure 6-13) for comparison.
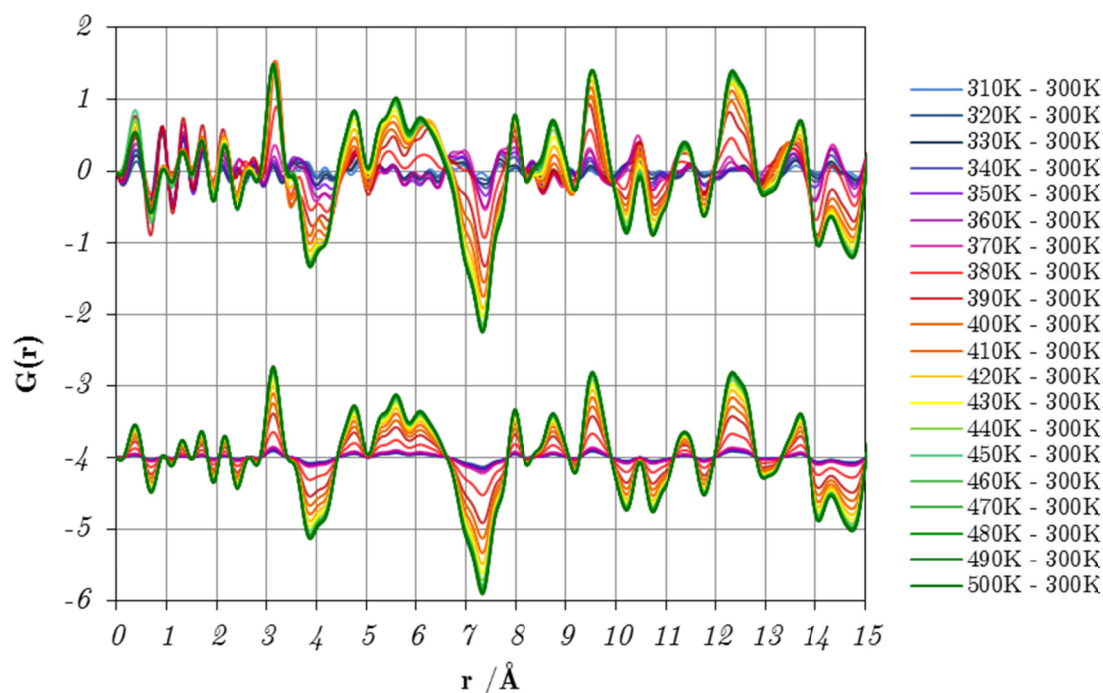
Figure 6-13: Experimental differential PDF (top) with model differential PDF from a two phase refinement (bottom).

6.4.2.3 Integration of differential PDF peaks

In order to quantify the rate at which peaks changed the heights and areas of peaks in the differential PDF were determined by peak integration. The differential PDFs were calculated for the temperature region 360 K to 460 K, the region where the bulk of the changes to the PDF take place, using temperature intervals of 2 K. Three peaks at ~3.12 Å, ~7.33 Å and ~8.72 Å were chosen for peak analysis. These were chosen because visual inspection of the differential PDF indicates that these peaks change at different rates. Furthermore, through partial PDF analysis (below), it is possible assign these peaks to particular groups of atoms in the structure, making it possible to understand which parts of the structure may be moving first.

Analysis was performed using the peak analysis feature in the program Origin (OriginLab, Northampton, MA). The baseline level from which the integral was performed was set to be a constant (0.015) for the peak at ~7.33 Å and zero for the peak at ~3.12 Å. For the peak at ~8.72 Å, the minima of the peak varied with temperature, so the background was set to be the minimum value in the plot of the peak. Peak

integration gave the position of the peak maximum, the peak height at the maximum and the area of the peak defined by the curved and the linear minima. The maximum change in the peak height and area was determined and all values plotted as a percentage of the maximum change. Results are shown graphically in Figure 6-14 and tabulated values are outlined in Appendix C.

There is little difference between plotting peak height and peak area because the lines for the two variables sit almost on top of each other on the graph. More importantly, Figure 6-14 also shows that the rate of change of the three peaks is substantially different. The peak at ~3.12 Å shows fast changes between 370 K and 400 K which accounts for over 90% of the total change in peak height and area. The peak height and area is fairly constant at all temperatures above 400 K indicating that there is little further movement in the structure above 400 K. The peak centre moves at temperatures above 400 K from 3.14 Å to 3.11 Å indicating a contracting of some bond lengths. Peak area continues to increase after the peak height stops increasing, which indicates that there is a broadening of the peak at higher temperatures. This is unsurprising considering the increased thermal motion associated with higher temperatures.

The peak at ~7.33 Å shows much more gradual movement than that at ~3.12 Å. The temperature dependence of this peak is more complex; one can see a change in slope at about 393 K. First it shows rapid change in the same temperature region as the peak at ~3.2 Å with a similar gradient, but this change accounts for only about 50% of the total peak height and area change. There is then a more gradual increase in height and area up to 450 K, indicating the atomic movements at this bond length continue at higher temperatures.

The peak at ~8.7 Å shows much slower movement than the other two highlighted peaks. Below 376 K it is difficult to define a peak for the differential, which is why there are not data points for this region. The peak does not show the fast change region that both the peaks at 3.2 Å and 7.3 Å show. Instead, the change in this region is relatively slow, with only 25% of the peak growth complete by 400 K. Most of the peak intensity appears between 390 K and 430 K, much later than the other two peaks.

The differences in height and area change for peaks in the PDF show that different atom-atom correlations change at different rates. This indicates that different parts of the structure change at different temperatures. If this is the case, then the transition of the material cannot take place by a linear combination of two phases, where we would expect all peaks to change at a constant rate.
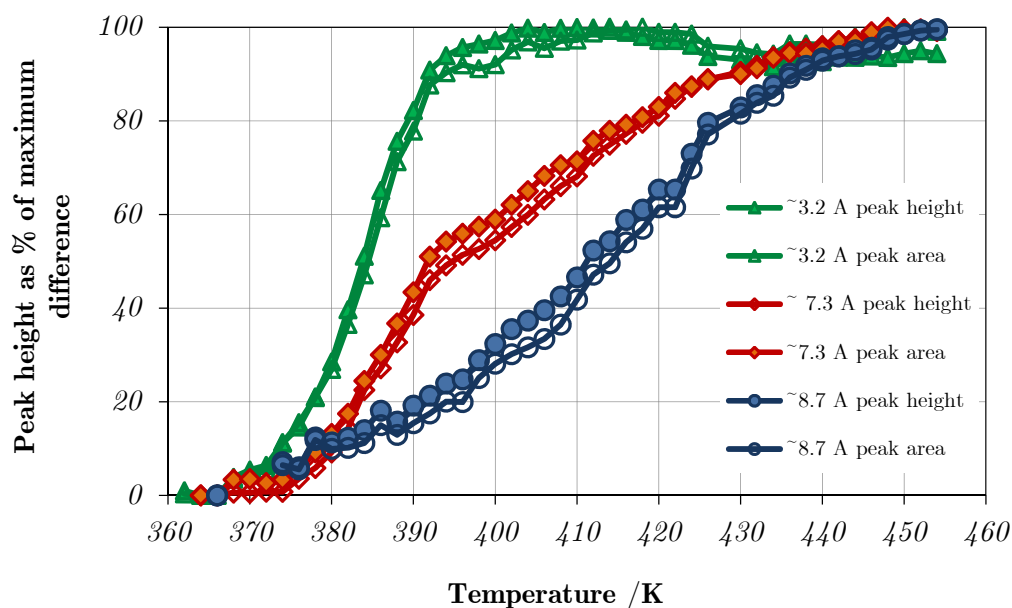

Figure 6-14: Variation in the peak height and area with temperature for three peaks in the normalised differential PDF.

6.4.3   Simulated partial PDFs

For the assignment of atom-atom correlations responsible for differential PDF peaks, partial PDFs were calculated for comparison with the known single-crystals for the hydrated and dehydrated structures. Partial PDFs were calculated using the PDF-refined models at 300 K and 500 K in the distance range 0 to 20 Å using PDFGui. Partial PDFs were calculated for Cu-Cu, Cu-O(carboxylate), Cu-water, Cu-S, Cu-C, C-C, S-O(sulfonate) and C-O pairs. In addition to this, partials were calculated for Cu-sulfonate bond lengths (Cu-(SO$_3$)). Figure 6-15 shows the calculated partial PDFs with the experimental differential PDFs for comparison.

Comparison of the calculated partial PDFs with the experimental differential PDF can, in theory, assign peaks in the differential PDF to the movement of particular atoms. In fact, the majority of the time, it is difficult to assign particular peaks to a single atom-atom pairing because of the large number of atoms associated with the MOF structure which results in a large number of possible correlations. This makes assignment of the differential peaks very tricky. However, there are two peaks in the differential PDF where the bulk of the peak can be assigned to a particular atom-atom correlation relatively unambiguously.

The peak in the differential PDF at ~3.2 Å is positive, indicating that there is a bond length at higher temperatures which is not present at lower temperatures. Partial PDFs indicate this peak has a large contribution from the change in Cu-sulfonate bond lengths as the previously uncoordinated sulfonate oxygen coordinates to the copper-centre. The peak between at 3.5 and 5 Å due to Cu-S lengths changes to peaks between 2.8 and 3.8 Å as the sulfonate oxygen coordinates, producing the positive peak in the differential PDF at 3.2 Å. This peak changes very quickly, (Figure 6-14) indicating that this movement is very quick, and happens at relatively low temperatures.

The increase of the peak at ~3.2 Å should be accompanied by a decrease in peak intensity for the peak at the distance corresponding to the Cu-sulfonate distance in the low temperature structure. These distances fall between 3.5 and 5 Å. In this region there are negative peaks in the PDF corresponding to bond lengths which has changed and is not present at higher temperatures. However, because of the presence of other atom-atom correlations in the sample at this distance it is impossible to attribute the peaks to specific atom-atom movements.

The peak at ~7.3 Å is largely associated with Cu-Cu bond lengths. In the low temperature structure the Cu-Cu lengths between layers of tetramers lie between 6.7919(7) Å and 7.5071(9) Å. In the denser, high temperature structure the tetrameters pull closer and the distances reduce to between 5.165(3) and 7.997(2) Å. This movement would lead to a decrease in peak intensity at 6 and 7 Å, and an increase in intensity between 5 and 6 Å where new atom-atom distances are formed. The peak at ~7.3 Å can be largely associated with this change. This peak, by contrast with the peak at ~3.2 Å, moves very gradually, with much of the movement requiring higher temperatures. This indicates that the movement of the layers on top of each other is a slower relaxation into

the high temperature structure. Perhaps this movement requires more energy and therefore a higher temperature.

The complex thermal dependence of the peak at 7.3 Å indicates that there are two distinct movements. While the majority of change is due to the Cu-Cu changes, as can be seen from the partial PDFs, there are very minor contributions from other atom-atom pairs including small changes due to changes in Cu-S(O$_3$) and Cu-C distances. The slightly increased rate of change with temperature in the intensity of this peak at low temperatures is probably due to these contributions. Support for this hypothesis comes from the fact that the change in slope of the 7.3 Å peak occurs at about the same temperature as the Cu-S(O$_3$) changes cease.

Whilst there is clear reduction in the peak at 7.3 Å, there is no clear peak in the differential which can be clearly associated with the reduced tetramer-tetramer distances. This is because peaks in the region where these would be expected have contributions from other atom-pair species such as Cu-sulfonate and Cu-(O)carboxylate. This makes it impossible to determine what proportion of the change in the differential PDF can be attributed to the Cu-Cu bond lengths and which is due to other species.
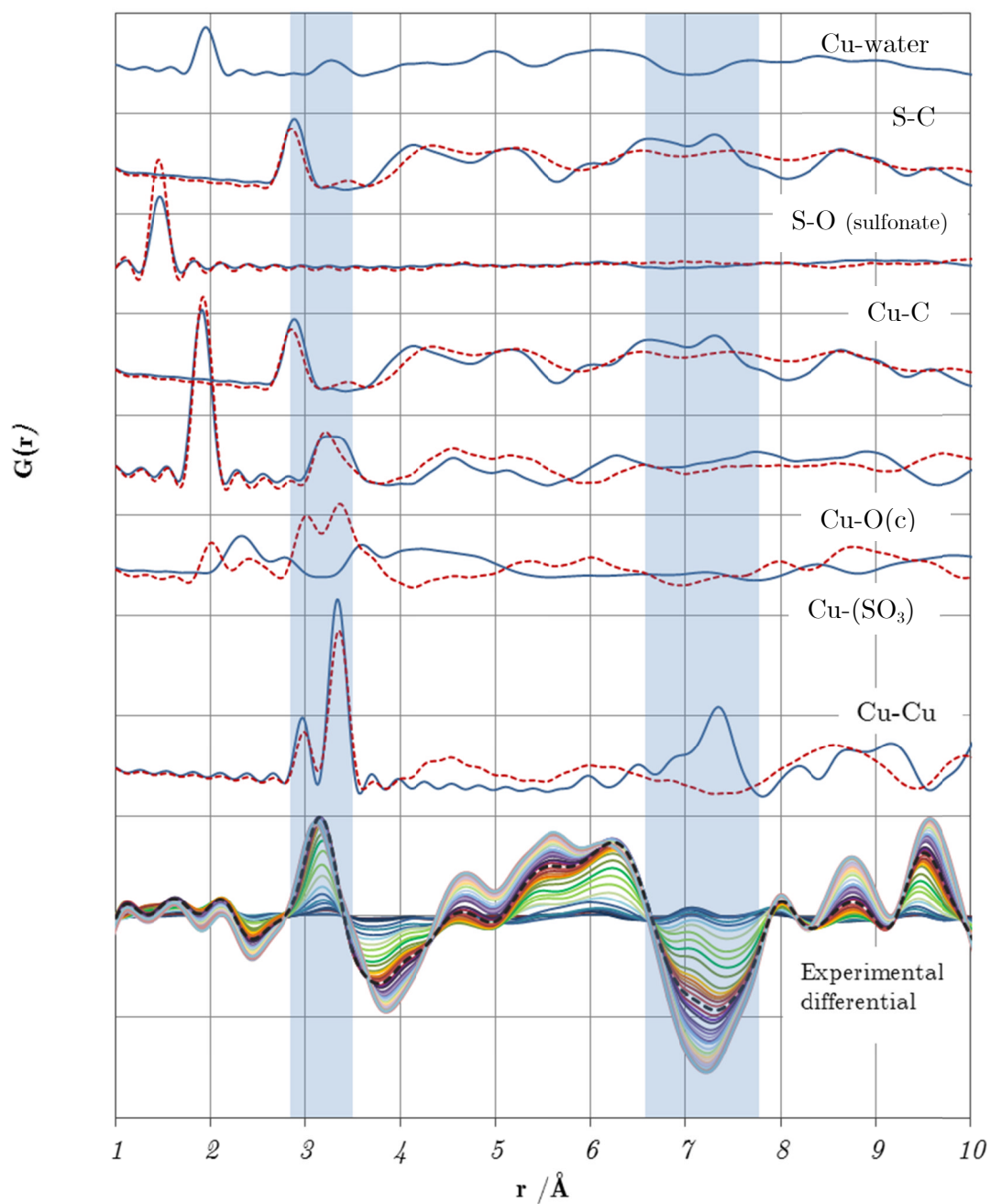
Figure 6-15: Calculated partial PDFs and experimental differential PDFs. Differential PDFs are shown for the temperature range 360 K < T < 450 K where the bulk of the transition takes place. Blue lines indicate partial PDFs for the 300 K structure, red lines indicate partial PDFs for calculated the 500 K structure. O(c) = carboxylate oxygens.

6.5   Gas-loading experiments

As detailed in section 5.6, the loss of diffraction from the single crystal on exposure to greater than 230 mbar of nitric oxide, indicates that there is a structural change associated with the uptake of nitric oxide, but that this structural change results in a material which has no long-range order or crystallinity. Broadening of Bragg peaks in PXRD data collected from NO-loaded Cu-SIP-3 supports this hypothesis.

The PDFs for the nitric oxide-loaded material are shown in Figure 6-16. Exposure of the dehydrated material results in an immediate change in the PDF which continues to progress for approximately 30 minutes after nitric oxide exposure. No further changes are evident after this time. The resulting PDF (Figure 6-17) corresponds to neither the hydrated or dehydrated PDFs but something which resembles the PDF obtained at 400 K. The 400 K PDF is also shown in Figure 6-17, along with the differential $(G(r)_{400K} - G(r)_{NO})$. This shows several non-zero features, which indicates that the nitric oxide-adduct of the material is similar, but not identical to the structure of the partially dehydrated material. This is to be expected, as extra O_{NO}-framework interactions are expected in the material.

Differential PDF for the nitric oxide exposure $(G(r)_{NO(xmins)} - G(r)_{dehyd})$ are shown in Figure 6-18. Unfortunately, the nature of the experimental set up (the gas flow must be started and checked, the detector moved in, hutch locked and data collection started before any data is collected) results in a time delay of approximately 5-10 minutes between the exposure of the material to gas and the first data set. Therefore, the detail of the changes in this period are lost and the majority of the change is complete before the first data set was complete. This means that a similar mechanistic analysis is not possible for the nitric oxide loading of the material, but this is something to be considered for further work.
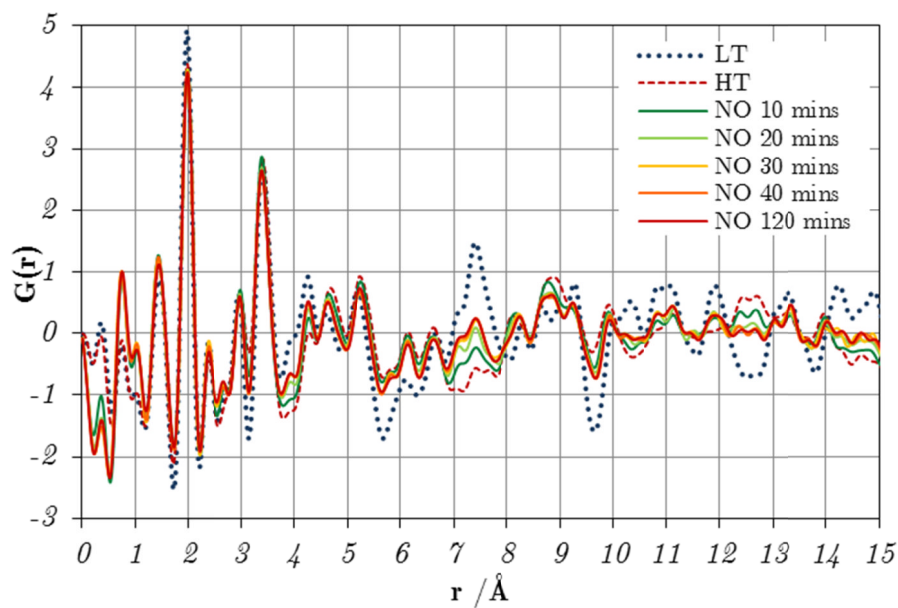
Figure 6-16: Nitric oxide-loaded PDFs for Cu-SIP-3 in the distance range 0 -15 Å. Dashed lines represent the LT (hydrated) and HT (dehydrated) PDFs determined for the first and final run of the dehydration done prior to gas loading. Solid lines represent the PDFs determined after gas loading.
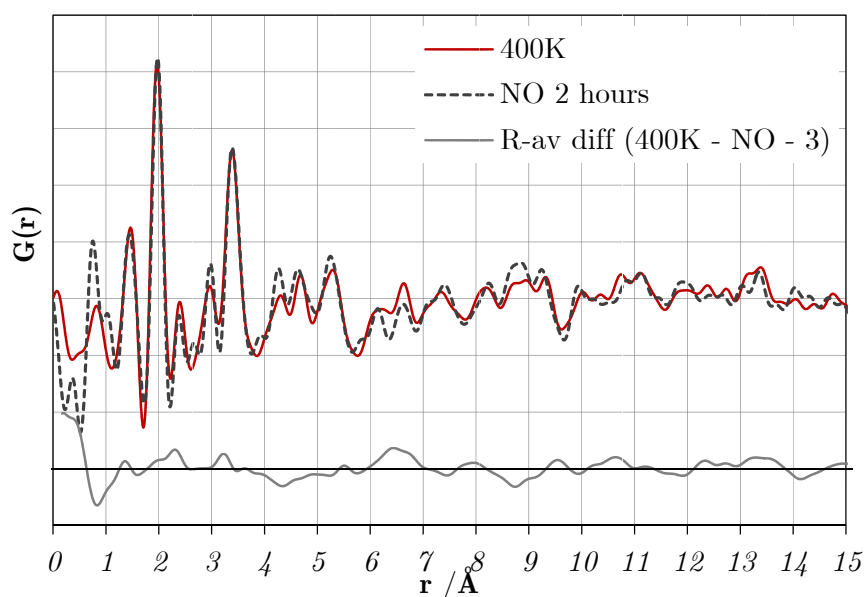

Figure 6-17: Comparison of the final nitric oxide-loaded PDF with the PDF obtained at 400 K. The differential PDF $G(r)_{400K} - G(r)_{NO}$ is shown at the bottom.
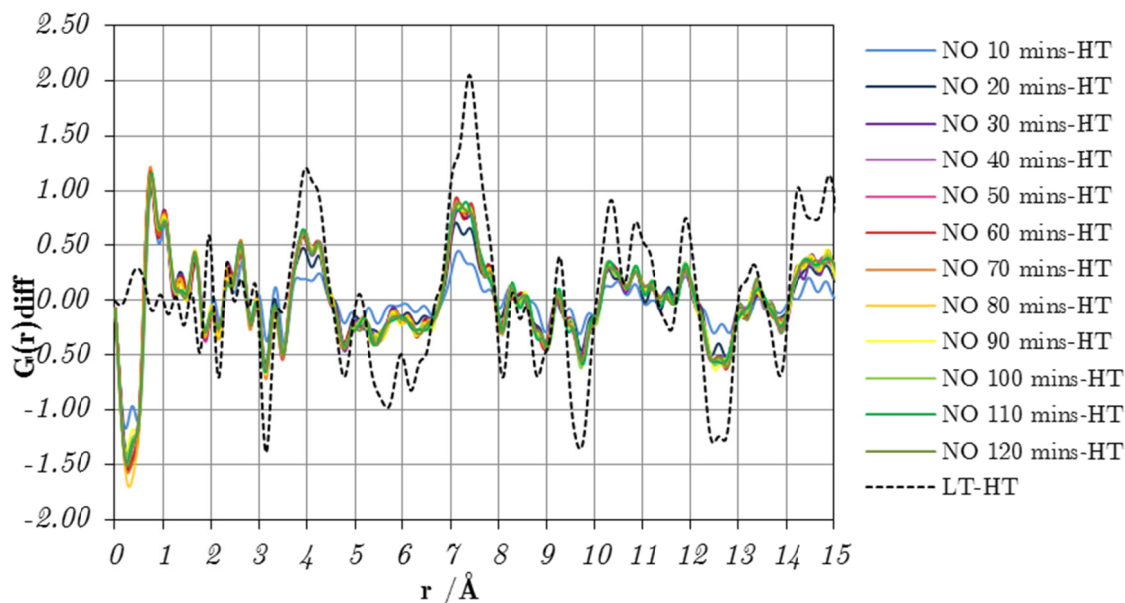
Figure 6-18: Differential PDF for the nitric oxide-loaded material.

6.6 Discussion

The PDF analysis reported here can be correlated with the analysis of single-crystal data from the previous chapter and the previously reported Rietveld analysis to understand the behaviour of the Cu-SIP-3 material on exposure to thermal and gaseous stimuli.

Both single-crystal and PDF analysis indicate that the behaviour of the material is due, in a large part, to the hemi-labile behaviour of the sulfoisophthalate ligand; in the low temperature structure only two out of three sulfonate oxygens are coordinated but the final sulfonate oxygen coordinates to stabilise the metal centre on the removal of the water molecule, O9w.

The two phase refinement of Bragg scattering and total scattering data from the sample allow determination of the approximate amount of the two phases in the powder sample at different temperatures. However, the poor fit of the two phase refinement of PDF data at intermediate temperatures along with the non-uniform temperature dependence of the peaks in the differential PDFs indicate that the material dehydrates through a complex structural transformation. The loss of Bragg diffraction from the

single crystal, and the increased width of peaks in the PXRD are therefore unsurprising, as long range order is almost certainly lost during this transition.

Single-crystal analysis results in the structure of the LT (hydrated) and HT (dehydrated) phases and highlights several atomic movements which are necessary for the structural transition to be complete. Firstly, the water molecules which are coordinated to the Cu-centre are removed. Secondly, the sulfonate oxygen which point into the pore, uncoordinated to the framework structure, must coordinate to the Cu-centre and, as a consequence of these changes, the coordination of the Cu-tetramers must also change. Thirdly, the layers of the material must move with respect to each other to form the dense phase HT structure. However, because of the reduced Bragg diffraction from the material, SCXRD gives no indication of whether these changes are concurrent or whether there are discrete stages associated with the changes.

PDFs can be extracted at all temperatures throughout the transition. The rate of change of peaks indicates at which temperature certain atom-atom correlations change, and comparison of peaks in the differential PDF with simulated partial PDFs for the hydrated and dehydrated material allows us to assign particular changes and temperature ranges to different atomic movements, and subsequently to propose a mechanism of transformation for the material. This mechanism is shown in Figure 6-19. The partial PDFs indicate that the sulfonate group moves early on, to coordinate to the copper site, concurrent to the removal of water from this site. There is no evidence from the PDF that the Cu-coordination number changes at any point, which precludes the formation of open metal sites on the Cu-centres. The increased movement of the sulfonate group and the lengthening of the Cu-O9w bond towards the temperature of the transition, indicate that the two movements may occur concurrently, or even that in some unit cells in the single crystal it has already taken place.

At approximately 400 K, enough of the sulfonate groups (approximately 98 % by peak height at 3.2 Å) in the structure have moved to allow the layers of the material to relax into the dehydrated regime. Where each crystallite finds itself incompletely transformed, there will be a range of unit cells in different conformations and subsequently no long range order in the crystallite. In the single-crystal sample, which is notionally a very large 'crystallite', the period where the dehydration has taken place breaks the conditions for Bragg diffraction, and this Bragg diffraction only returns when

the material has almost completely transformed to the dehydrated structure and long-range order is regained.

Presumably, the carboxylate framework, which is characterised by low ADP parameters in the single crystal at all temperatures, and whose PDF peaks at low-r show negligible change with temperature, represents a strong framework which allows the significant atomic movements associated with the structural transition to take place without the material breaking up or even really losing much crystallinity in the single-crystal sample.

The proposed mechanism of transformation can be related to the observed experimental diffraction (Figure 6-20). At low temperatures all crystallites and all unit cells in the single crystal are hydrated, the material has long-range order giving good Bragg diffraction in the single crystal and powder diffraction experiments. At higher temperatures, some of the unit cells and eventually crystallites dehydrate, whilst others are partially dehydrated when the sulfonate has moved but the layers have not relaxed on top of each other. This breaks up the long range order, first distorting the Bragg peaks and diminishing them altogether in the single crystal. Here, there is an increase in the diffuse scattering coming from the material. Once enough of the sulfonates have moved to allow relaxation of the layers in the dehydrated regime, long range order begins to return with narrower PXRD peaks and sharp Bragg peaks in the single-crystal diffraction.

The loss of Bragg diffraction from the single crystal on exposure to nitric oxide pressures greater than the gate-opening pressure reported by Xiao *et al.*[10] indicates that a structural change is responsible for the gas uptake. The change of the PDF on exposure to nitric oxide also indicates a structural change, and the stagnation of the change to form a PDF analogous to the partially dehydrated structure which we know to show disorder, indicates that the nitric oxide adduct of the structure is not an ordered structure. This analogous structure indicates that the nitric oxide is stored on the Cu-site of the material as with water in the hydrated structure, and this binding to the metal centre helps to explain why only nitric oxide and water are able to be stored in the material, and not any of the other small molecule gases which were attempted; none of these other gases are likely to bind as strongly to the metal sites to allow the structural transition to be reversed.

The nitric oxide isotherm is not saturated at 1 atmosphere of pressure. Therefore, it is likely that the material is still adsorbing gas at this pressure and if this uptake is correlated with a structural change, then the structural change is unlikely to be complete. In the single crystal, this results in a structure which is partially transformed and therefore shows no long range order and no Bragg diffraction. In the PDF this results in a PDF which is analogous to the partially dehydrated PDF which we known to show disorder. It is possible that the NO-adduct of the structure exists in a state where perhaps the nitric oxide has coordinated to the metal centre but the material does not have enough energy to form an analogue of the fully hydrated structure.
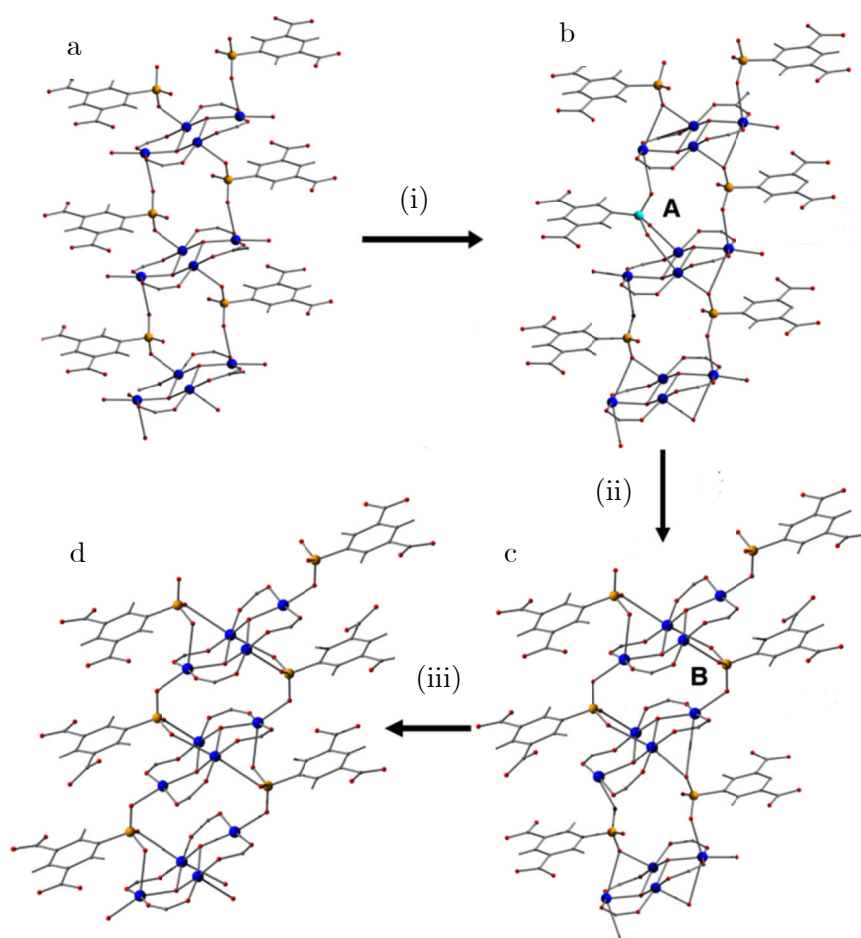

Figure 6-19: Schematic diagram of the PDF-derived mechanism of transformation of Cu-SIP-3. Each panel shows chains of tetramers linked by the sulfonate groups of the sulfoisophthalate ligand. Panel **a** shows the low temperature (LT) structure of the material. Panel **b** shows the first step in the transformation; the concurrent loss of a coordinated water molecule and a reorientation of one sulfonate group (marked by the letter **A**). At this point the Cu-Cu distances in the structure remain unchanged. Panel **c** illustrates the reorientation of the other sulfonate joining the two tetramers, marked by the letter **B**, and the resultant reduction in Cu-Cu distance as the structure then relaxes. The process then repeats until all the sulfonates have reoriented and all the Cu-Cu distances have relaxed to form the HT structure (panel **d**).

Temperature	300K	350K	400K	420K	440K

Powder composition
(Blue = LT domain, red = HT domain, green = intermediate/disordered domain)

PXRD pattern
(blue = LT peak, ref = HT peak, green = diffuse scattering)

Bragg Diffraction
→ Sharp peaks in PXRD
→ Little diffuse scattering

Distortion of Bragg Diffraction
→ Peaks broaden

Movement and strain disrupts long range order
→ Wide peaks in PXRD
→ Lots of diffuse scattering

Long range order returns
→Sharp Bragg peaks
→ Diffuse scattering decreases

Single crystal
(Blue = LT unit cell red = HT unit cell, green = intermediate unit cell)

Single crystal diffraction pattern

Bragg Diffraction
→ Single crystal structure

Distortion of Bragg Diffraction
→ Single crystal structure
→ Large ADP values for O5

Movement and strain disrupts long range order
→ No diffraction

Long range order returns
→Bragg Diffraction

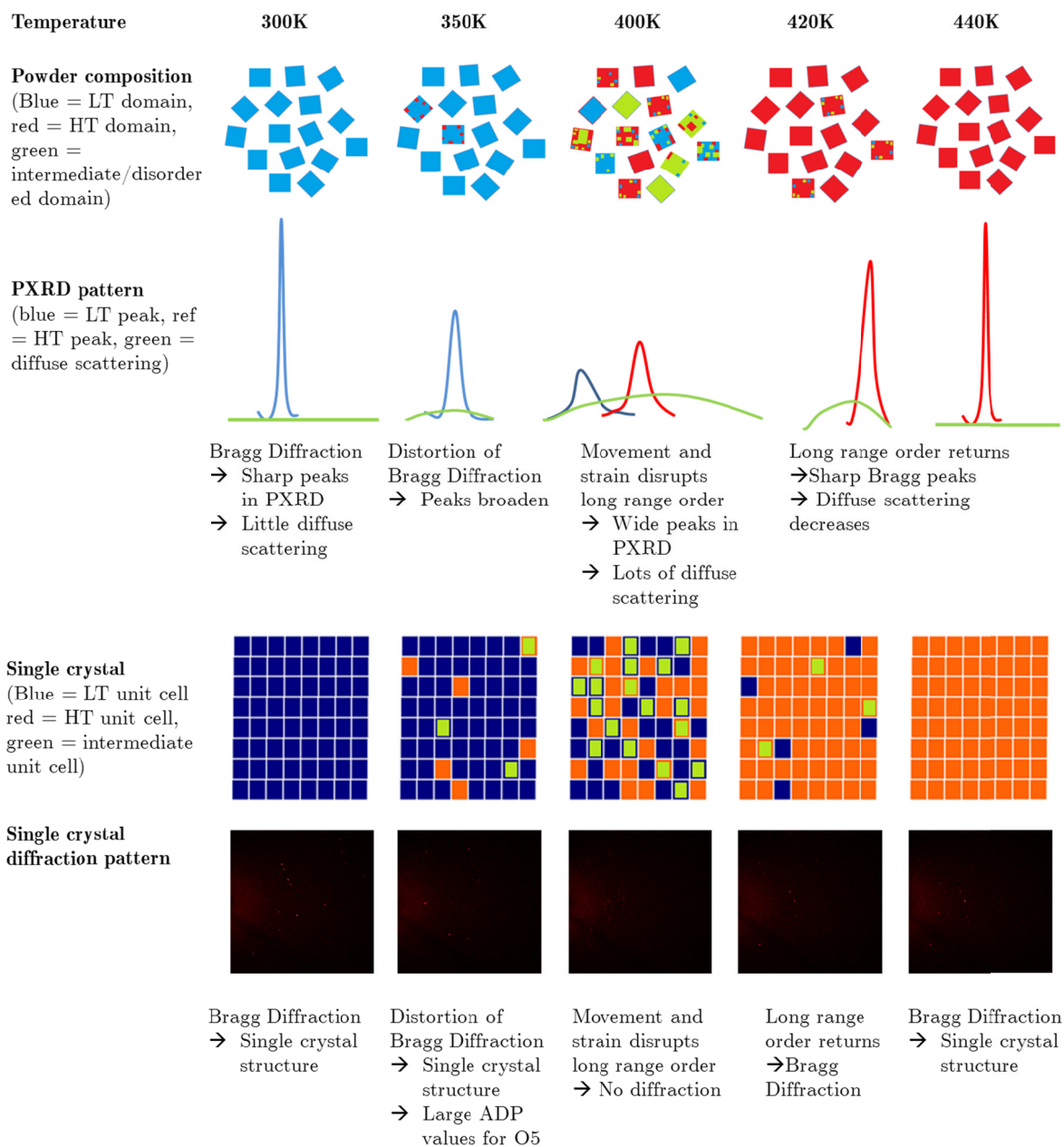Bragg Diffraction
→ Single crystal structure

Figure 6-20: Schematic of how the mechanism of transformation of Cu-SIP-3 relates to the change in experimental diffraction data for a single-crystal and PXRD sample.

6.7 Conclusions and Further Work

Chapter 6 has discussed the application of the pair distribution function method to the structural transition of the metal-organic framework Cu-SIP-3. It was found that the PDFs could be extracted for the material at all temperatures, even in areas where Bragg methods were not able to provide a structure, indicating the strength of PDF analysis in gaining subtle information in regions of disorder.

A two phase refinement of data showed poor fits at intermediate temperatures, indicating that the transition involved more subtle structural movements. The comparison of experimentally derived differential PDFs with modelled partial PDFs highlighted a possible order for these atomic movements in the material, which, along with information from single crystal (Chapter 5) and PXRD (Xiao *et al.*), allowed a mechanism of transformation for the material to be postulated.

In situ nitric oxide-loading experiments were also performed; these indicated that the nitric oxide adduct of the material resembles the disordered, partially dehydrated structure of the material.

This work has highlighted the use of PDF analysis for metal-organic frameworks. There are many opportunities for further work, both using the Cu-SIP-3 compound, as well as other flexible frameworks. Comparison of the diffuse scattering from a single crystal with this analysis could lead to interesting information about the difference in mechanism in a large particle compared to a powder.

Chapter 5 and Chapter 6 have used two diffraction techniques to gain complementary information about the structural transition of Cu-SIP-3. This has demonstrated the use of Bragg and total scattering techniques to obtain information to propose an overall mechanism of transformation which would not be elucidated without the duel-approach. Single-crystal studies gave the single-crystal structure of the hydrated and dehydrated material and allowed elucidation of the subtle structural effects such as site occupancy factors and anisotropic displacement parameters as temperature varied, which would not be obtainable from PDF alone. PDF analysis allowed structural information to be obtained in a disordered region where single-crystal diffraction was not able to probe.

To unambiguously determine the structure of the partially dehydrated structure, modelling of the structure using the PDF data is required. The application of RMC modelling which fits the medium range structure of the material would be an interesting further direction to take this work.

In order to further characterise the nitric oxide-loaded material, closer inspection of the changes to the material on immediate exposure to nitric oxide could allow a detailed differential PDF study on this structural transition in order to analyse atomic movements associated with the structure. Similarly, a study of the rehydration of the material could give clues as to why the hydration of the material proceeds to completion whilst the nitric oxide transition does not.

If it is the case that the structure does not have the energy to fully transform on exposure to nitric oxide, thermal cycling of the powder sample or single crystal could help force this to completion and therefore regain long range order in the material. Linking analyses to other characterisation techniques could also be helpful. For example, a setup which allows concurrent IR and PDF measurements to be taken is currently being developed at 11-ID-B. This could give extremely useful information about the nature of nitric oxide loading as the IR stretch of NO is very characteristic of bonding environment. Nitric oxide isotherms performed to higher pressures or at different temperatures would give indication of whether the isotherm ever reaches saturation and therefore whether the return of long-range order is likely.

6.8 References

1. P. J. Chupas, K. W. Chapman and P. L. Lee, *J. Appl. Crystallogr.*, 2007, **40**, 463-470.

2. P. J. Chupas, K. W. Chapman, C. Kurtz, J. C. Hanson, P. L. Lee and C. P. Grey, *J. Appl. Crystallogr.*, 2008, **41**, 822-824.

3. X. Qiu, J. W. Thompson and S. J. L. Billinge, *J. Appl. Crystallogr.*, 2004, **37**, 678.

4. A. P. Hammersley, S. O. Svensson, M. Hanfland, A. N. Fitch and D. Hausermann, *High Pressure Research,* 1996, **14**, 235-248.

5. M. Wojdyr, *J. Appl. Crystallogr.*, 2010, **43**, 1126-1128.

6. C. L. Farrow, P. Juhas, J. W. Liu, D. Bryndin, E. S. Bozin, J. Bloch, T. Proffen and S. J. L. Billinge, *J. Phys.: Condens. Matter.*, 2007, **19**, 335219.

7. R. E. Dinnebier and S. J. L. Billinge, *Powder diffraction : theory and practice,* Royal Society of Chemistry, Cambridge, 2008.

8. C. J. Benmore, J. K. R. Weber, M. C. Wilding, J. Du and J. B. Parise, *Phys. Rev. B.*, 2010, **82**, 224202.

9. J. S. Tse, D. D. Klug, M. Guthrie, C. A. Tulk, C. J. Benmore and J. Urquidi, *Phys. Rev. B.*, 2005, **71**, 214107.

10. B. Xiao, P. J. Byrne, P. S. Wheatley, D. S. Wragg, X. Zhao, A. J. Fletcher, K. M. Thomas, L. Peters, J. S. O. Evans, J. E. Warren, W. Zhou and R. E. Morris, *Nat. Chem.*, 2009, **1**, 289-294.

7 Application of pair distribution function analysis to metal-organic frameworks for gas storage

7.1 Introduction

7.1.1 Motivation

Many metal-organic frameworks are crystalline and their the structure can be determined by single-crystal (if large enough crystals can be synthesised) or powder diffraction methods. However, as the search for new frameworks continues, more materials that are 'crystallographically challenged' (amorphous, or with particle sizes too small to be characterised by these standard methods) are being synthesised, and therefore new methods of characterising their structure must be sought. Gas-loading onto materials can complicate matters further, and characterising the nature of the gas-loaded adducts using Bragg diffraction methods is not always possible.

Total scattering methods have been used since the early twentieth century to study the structure of liquids. However, their use for solid materials was limited by the small Q-ranges that were accessible through conventional X-ray sources. Recent advances in synchrotron radiation and the invention of large area detectors means that it is now possible to collect total scattering data to large scattering angles, making the PDF much less susceptible to experimental noise. For this reason, PDF analysis has been applied to a number of solid-state materials and more recently to framework materials, including zeolites,[1-5] Prussian blues[6] and metal-organic frameworks[4, 7-13].

7.1.2 Previous reports of PDF analysis on porous materials

Section 3.7.6.1 outlined the ways that information can be extracted from the PDF. *Ab initio* structure solution is rare and there have been no reports of this for MOFs. 'Real-space Rietveld' refinement of structures from PDF data is complicated by several factors. Firstly, the very large number of atoms in the material, and consequently the huge number of potential atom-atom pairs that can contribute to the

PDF make it extremely computationally intensive. The unquantifiable degree of solvation in the material means that the atomic density of the material is unknown, and often makes it impossible to fit the very lowest r-region of the PDF since this is likely to contain a well-structured contribution from the included solvent, for example, the O-H distance if the solvent were H_2O.[14] In addition, there is currently no simple way to model rigid bodies for items such as organic linkers in materials. In a rare report of an attempt to refine a MOF structure from PDF data Mulfort *et al.* report that none of their refinements converged to completion.[15]

In place of this, various other methods are used to extract structural information from PDF data. Direct comparison of PDFs can give some information about the difference between two structures. By this method, Melfort *et al.* identify the change in structure of a zinc-based framework on dehydration and adsorption of carbon dioxide as rotation of the linker group. They postulate that this rotation represents a dynamic structural change from an interwoven to an interpenetrated framework with appreciable change in surface area, explaining the hysteric gas adsorption properties of the material.[15]

A more elegant approach is to use differential PDFs, and this can give an indication of the differences in atom-atom bond pairs between two different structures. Model PDFs can be calculated from known structures for either an entire structure or for specific atom pairs (partial PDFs). Particular success has been noted when these two items are combined and the changes in the structure related back to particular atom-atom bond lengths. Readman *et al.* reported the mechanism of amorphisation of zeolite-A under pressure and determined from the comparison of differential PDFs that the deformation of the zeolite was via the distortion and breakdown of the double 4-ring units of the zeolite.

The nature of host-guest interactions have been elucidated using differential PDF methods and, more recently, incremental differential PDFs which are calculated from subtracting the PDF immediately before the one of interest, allowing a real-time analysis of how the peaks are changing. Incremental differential PDFs showed that the iodine-loading process in ZIF-8 takes place with two discrete structural changes.[4] Iodine can be captured in the framework by pressure-induced amorphisation of the framework, which closes the pores of the material.[7]

Hydrogen adsorption in MOF-5 has been studied using neutron PDF work via *in situ* loading of deuterium onto the framework.[16] Integration of the entirely new peak assigned to the H-H interatomic distance shows that all gas molecules are adsorbed as molecular deuterium. The adsorption sites for the gas were determined by reverse Monte Carlo (RMC, section 3.7.6) modelling of the scattering data, referencing first principles molecular dynamic calculations. RMC modelling studies have also been used to relate PDF data to the mechanisms of amorphisation of several materials.[8-10, 12, 13]

The formation of silver nanoparticles in a zeolite has been monitored using differential PDFs, to determine the mechanism responsible for the growth of the small particles at low temperatures, and small particles growing into large particles on the side of the zeolite support at high temperatures.[5]

7.2 Aims

This chapter aims to collect and process total scattering data for known and novel metal-organic frameworks which have the potential for gas storage, and demonstrate a number of ways, using both modelling and model-independent methods, in which this can be interpreted and analysed.

Firstly, the structure of hydrated and dehydrated Ni-CPO-27 will be refined using both Rietveld methods and PDF methods and the results compared to determine to what extent the long-range and short-range correlations are similar. Secondly, PDF analysis will be used as a method of fingerprinting to determine which pore of the framework STAM-1 certain gases enter. Lastly, PDF analysis will be used to determine the nature of a secondary building block in an unknown nanoparticular MOF structure and subsequently, in combination with other structural techniques, used to validate the structural solution.

7.3 Experimental methods

7.3.1 Powder X-ray diffraction data collection for Rietveld refinement

Ground powder samples of Ni-CPO-27 were loaded into 0.5 mm borosilicate capillaries. The hydrated data set was collected on the as-synthesised sample. The dehydrated data were collected after the capillary was heated to 150 °C under dynamic vacuum overnight to dehydrate the sample, cooled to room temperature, placed under an

argon atmosphere and flame sealed. High resolution powder X-ray diffraction data were collected on beamline I11 at Diamond Light Source, Harwell, UK. Data were collected at room temperature using a monochromated X-ray beam of wavelength 0.827439(1) Å. Thirty minute data sets were collected for the angle range of 1-50° and binned to produce data with a step size of 0.001°.

7.3.2 Sample preparation for guest-loaded PDF data collection

A ground sample of STAM-1 was placed in a 1 inch Kapton® polyimide capillary which was sealed with 3M Scotch-Weld epoxy adhesive at one end. The sample was heated to 150 °C overnight in a Schlenk to dehydrate it before being exposed to methanol vapour by placing a small amount of methanol in the bottom of the Schenk tube and leaving for 3 days. The sample was sealed with quick seal adhesive. For the ethylene-loaded sample, the dehydrated capillary was exposed to an atmosphere of ethylene for a period of one hour before being sealed with glue.

7.3.3 Total scattering data collection

Total scattering data were collected at beamline 11-ID-B at the Advanced Photon Source, Argonne National Laboratory, IL, USA. A wavelength of 0.21280 Å was used for all experiments. *Ex situ* experiments were ran using a sample changer with a frame exposure time of 5 minutes.

For the *in situ* dehydration of Ni-CPO-27 the sample was held in the capillary by placing glass wool either side of the sample to prevent the sample being blown out by the airflow. The capillary was placed in the flow gas cell outlined in section 6.3.2. The sample was placed under helium flow and heated using an Oxford Cryosystems Cryostream device from room temperature to 500 K at a rate of 60 K/hr and held at this temperature for 6 hours. Data were collected with a frame time of 1 minute. The dehydrated data set is taken as the final data set which was collected in the variable temperature experiment having allowed maximum time for the water to be removed from the framework.

All data were recorded using a Perkin Elmer amorphous silicon area detector which was placed perpendicular to the X-ray beam at a distance allowing high angle diffraction data to be collected.[17] This sample-to-detector distance was determined as 151.338 mm by the use of a CeO_2 powder standard. The program FIT2D was used to integrate the data from two dimensional image format into a one-dimensional numerical

format *.chi* file.[18] An empty Kapton capillary was run for the same counting time and subjected to the same integration process in order to explicitly measure the air and Kapton contributions to the total scattering. These contributions were removed in data processing in PDFgetX2. Other standard corrections were applied to the total scattering data, and G(r) was obtained by the Fourier Transform of the corrected total scattering data using the program PDFGetX2.[19]

Gaussian functions are fitted to peaks of interest in the PDF produced using the program Fityk,[20] and these peak positions are quoted in subsequent analysis results.

7.3.4 General refinement procedure

Refinements were performed in PDFGui.[21] The exact refinement approach depended on the material and how good the initial fit was. Starting parameters for each of the refinements is given in the relevant sections. In order to avoid repetition, a detailed general procedure of refinement is given below.

A starting value for Q_{damp} of 0.08 was chosen for all refinements. In the case of variable temperature data sets, Q_{damp} was refined in the room temperature data set and then fixed for higher temperature data sets. In most refinements S_{ratio} was set to a starting value of 0.5, with a cut-off distance, r_{cut}, of 3.6 Å.   This value is the approximate M-M distance in the sample and allows the correlated movement of the secondary building blocks in the frameworks to be modelled.

The inclusion of solvent molecules means that the atomic density, ρ_0, is not accurately known for MOF compounds and so all refinements are done whilst refining the overall scale parameter. A starting value for the scale factor for the model was set by observational comparison of the two biggest peaks in the model and experimental PDFs. The scale factor for the experimental data was not refined because this would have the same effect as refinement of the model scale factor and therefore would be redundant.

Atoms are refined isotropically; U_{11}, U_{22} and U_{33} are set to an initial 0.005 Å^3 and constrained to be identical.   Cross diagonal terms are set to zero and were not included in the refinement. To avoid over parameterisation, thermal parameter environments are defined by atom type and environment. For example, U_{11}, U_{22} and U_{33} of all copper atoms are set as one variable. Those for carboxylate oxygen atoms which are used in framework bonding are defined as another single variable, and those which are not used

in framework bonding as a separate variable. Where atom positions were added to refinements, they were constrained by space group symmetry.

Addition of parameters to the refinement generally proceeded as follows: (1) Phase scale factor, Q_{damp} (2) S_{ratio} (3) Unit cell parameters (4) Thermal parameters (5) Metal atom positions and framework oxygen positions. Each stage of the refinement was allowed to converge until no improvement in the residual values was obtained through further refinement cycles.

7.3.5 Calculation of partial PDFs

Partial PDFs were calculated using PDFGui from the models from single crystal data. U_{11}, U_{22} and U_{33} were set to 0.005 $Å^2$ and cross diagonal terms were set to zero. A value for Q_{damp} was estimated using any data refinement which had been done, otherwise set to 0.08. The value for Q_{max} was taken from the data set being considered, otherwise set to 22 $Å^{-1}$.

7.4 Pair distribution function analysis of Ni-CPO-27

7.4.1 Rietveld refinement of Ni-CPO-27

Rietveld refinements of the hydrated and dehydrated data sets were performed using the GSAS suite of programs.[22, 23] The refinement of the hydrated data set was based on the hydrated form of Ni-CPO-27 found in the CSD database (structure reference code LECQEQ). The model structure showed good fit to the data, converging to residual values of $R_w = 0.098$ and $R_{wp} = 0.125$. The elevated values for the R-factors can be explained by the data collection temperature and the presence of disordered physisorbed water molecules in the channels of the material which cannot be located in the refinement. A Rietveld refinement of the dehydrated structure was based on the dehydrated structure of Co-CPO-27 which had been determined experimentally using single-crystal X-ray diffraction (Chapter 4). A Fourier difference map performed after the main framework had been refined could find no significant residual electron density peaks which could be assigned to water molecules occupying the channels, indicating that material was fully dehydrated. Final refinement parameters are shown in Table 1 and atomic positions are shown in Table 4. The structure is isostructural to the dehydrated Co-CPO-27 described in section 4.6 with a coordinatively unsaturated metal site on the

square-pyramidal Ni-ion where the water molecule has been removed by heating (Figure 7-1).   Plots of the final Rietveld refinements for both data sets are shown in Figure 7-2.

Table 1: Details of the Rietveld refinement of hydrated Ni-CPO−27 against synchrotron X-ray data ($\lambda = 0.827439(1)$Å)

	Hydrated	**Dehydrated**
a /Å	25.95881 (4)	25.76086 (8)
c /Å	6.685398 (16)	6.76316 (2)
V /Å³	3901.46 (1)	3886.88 (2)
T /K	295	295
Space group	R-3	R-3
R_w	0.098	0.095
R_{wp}	0.125	0.119
R_{exp}	0.053	0.056
2θ range	5.01-70	5.01-70
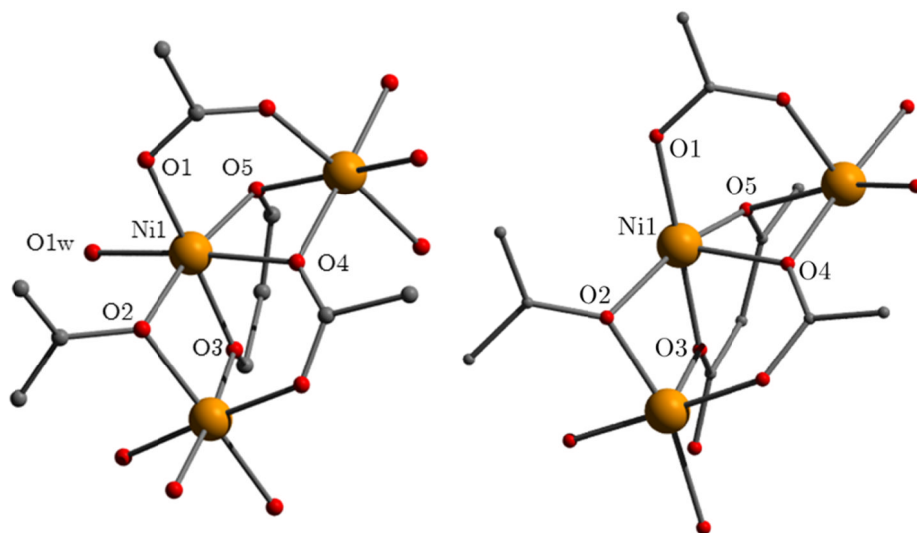
Figure 7-1: Coordination environment of the nickel atom in hydrated (left) and dehydrated (right) Ni-CPO-27 structure from Rietveld refinement of synchrotron X-ray data.
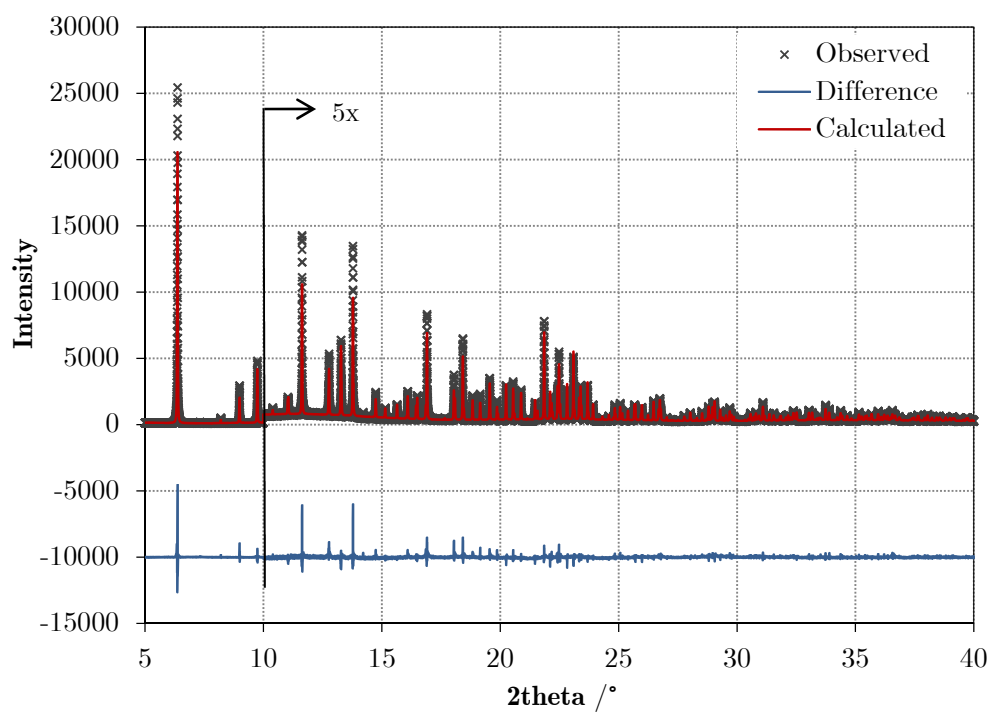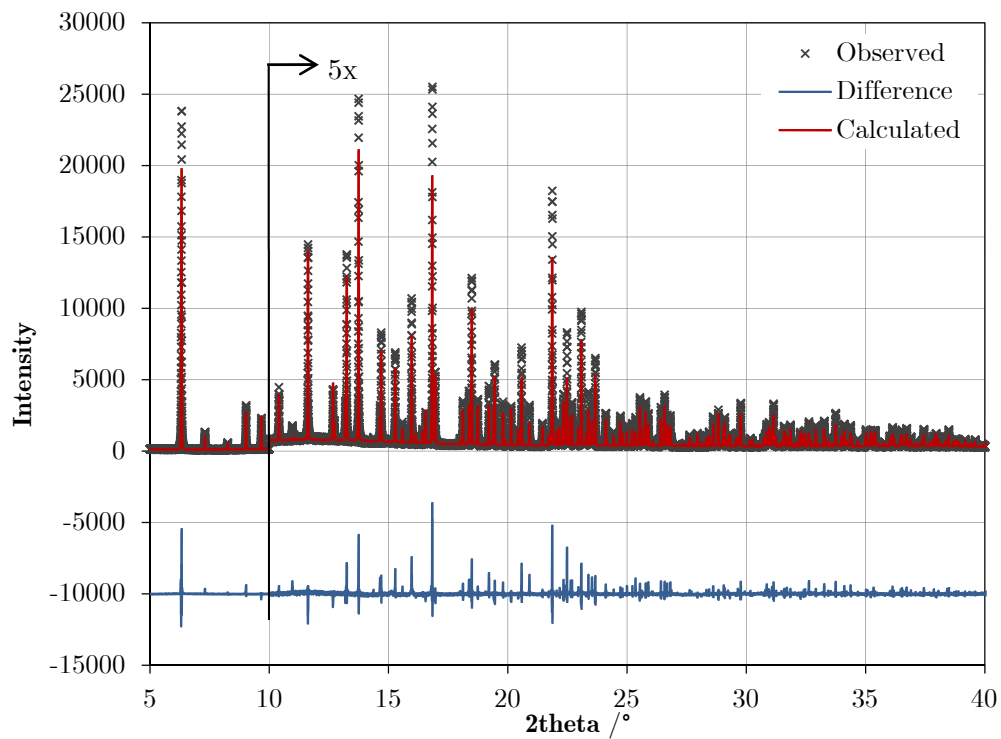
Figure 7-2: Rietveld plots for hydrated (top) and dehydrated (bottom) Ni-CPO-27 in the range of 5 − 40° from synchrotron powder X-ray diffraction data, measured at 293 K, showing measured data (black crosses), fitted data (red), and the difference plot (blue). Data and difference curves for >10° are magnified by a factor of 5.

7.4.2 Extraction of PDFs for Ni-CPO-27

The experimental PDFs for hydrated Ni-CPO-27 and dehydrated Ni-CPO-27 are shown in Figure 7-5 and Figure 7-4 respectively. Each PDF features sharp peaks indicating good crystallinity. Peaks in the PDFs are observed out to a distance of 60 Å. Peaks below 1.0 Å have no physical meaning as they are below the distance where bond distances in a material can fall; they are the result of Fourier truncation errors and systematic errors in the data.[24] These are minimised by careful subtraction of the background and doing the Fourier transform out to a maximum value of Q where the data has a meaningful data-noise ratio (generally, the undulation of $S(Q)$ at higher Q values is still visible over the noise of the data). The data below 1.0 Å is included in plots to give an idea of the data quality. In the PDF for Ni-CPO-27, peaks below 1.0 Å are relatively small, indicating that the data is of good quality.
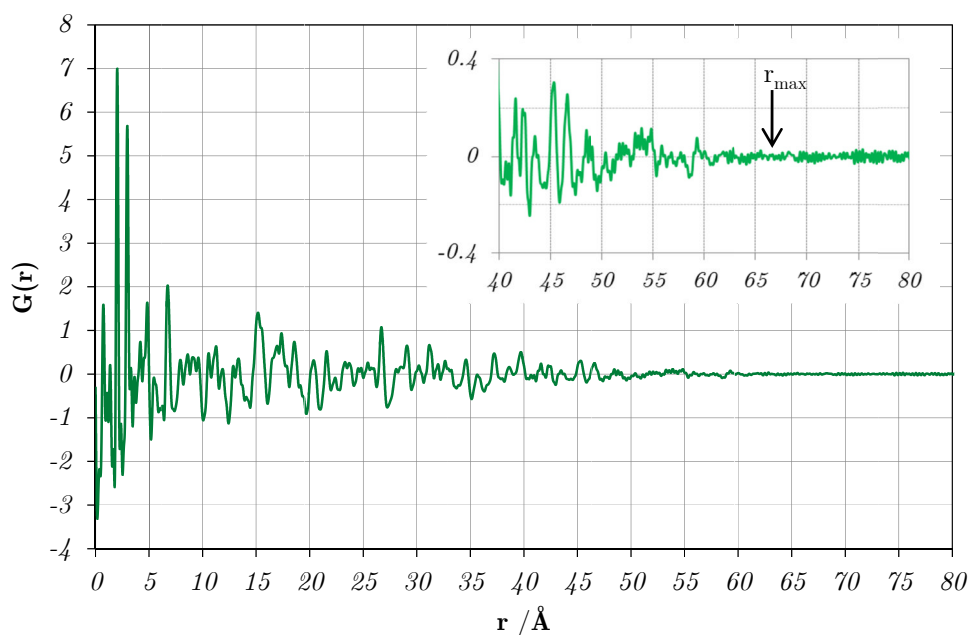
Figure 7-3: PDF for hydrated Ni-CPO-27 extracted to a distance of 80 Å. Inset shows the distance range 40 to 80 Å. R_{max} is approximately 60 Å (marked by arrow on inset).
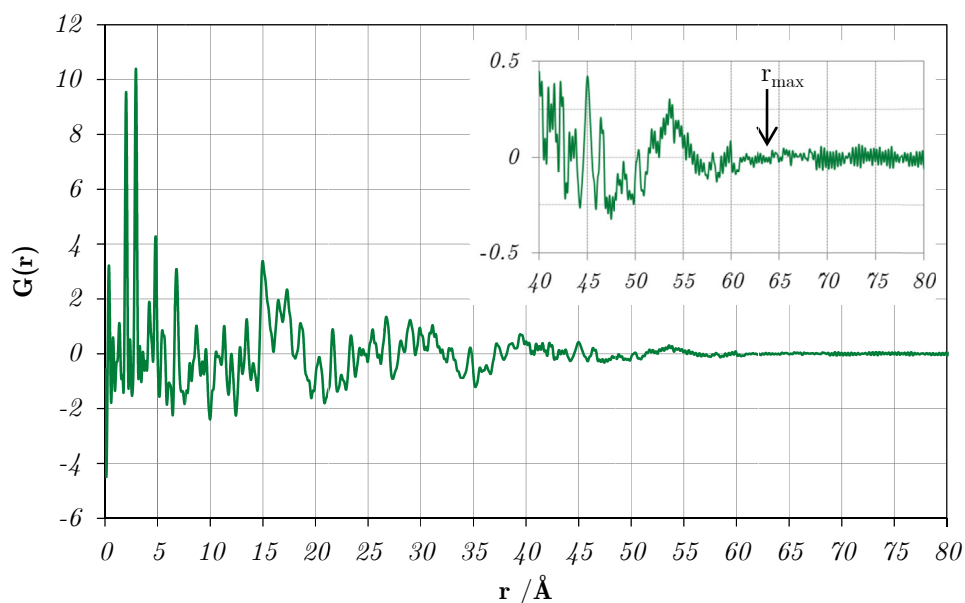
Figure 7-4: PDF for hydrated Ni-CPO-27 extracted to a distance of 80 Å. Inset shows the distance range 40 to 80 Å. R_{max} is approximately 60 Å (marked by arrow on inset).

Peaks at low-r can be assigned to specific atom-atom correlations by reference to a calculated partial PDF. The partial PDFs for Ni-Ni, Ni-O, Ni-C, C-C, C-O and O-O calculated from the Ni-CPO-27 model from section 7.4.1 are shown in Figure 7-5. Peaks below 2 Å (1.33 Å and 1.62 Å) are the result of C-C and C-O distances within the linker molecule. The main contributions to the peak at 2.03 Å are Ni-O distances characterising the ligand coordination interactions which link the material together. C-C and C-O cross-aromatic ring distances contribute to the peak at 2.95 Å. Even at short distances, the PDF is not straightforward: for example, the peak at 3.00 Å has two large contributions, from Ni-Ni distances within the Ni-chains and distances between the linker carbons and their nearest nickel ions.

At higher distances it is not possible to assign peaks to specific atom correlations as the large number of possible correlations for each distance is very large, resulting in increased peak widths in both the partial PDFs and experimental PDF.

7.4.3   PDF refinement of dehydrated and hydrated Ni-CPO-27

The dehydrated structure was initially chosen for refinement. The dehydration process should have removed the water from the pores, meaning that there should be fewer complications at low-r due to solvent-framework interactions.[25] Using a CIF generated

224

from the crystal structure from the ISCD (reference LEJRIC) a model PDF was generated using the program PDFGui, using equation 3.38, where the contributions of each atom pair in the structure are summed and weighted according to atomic weight.
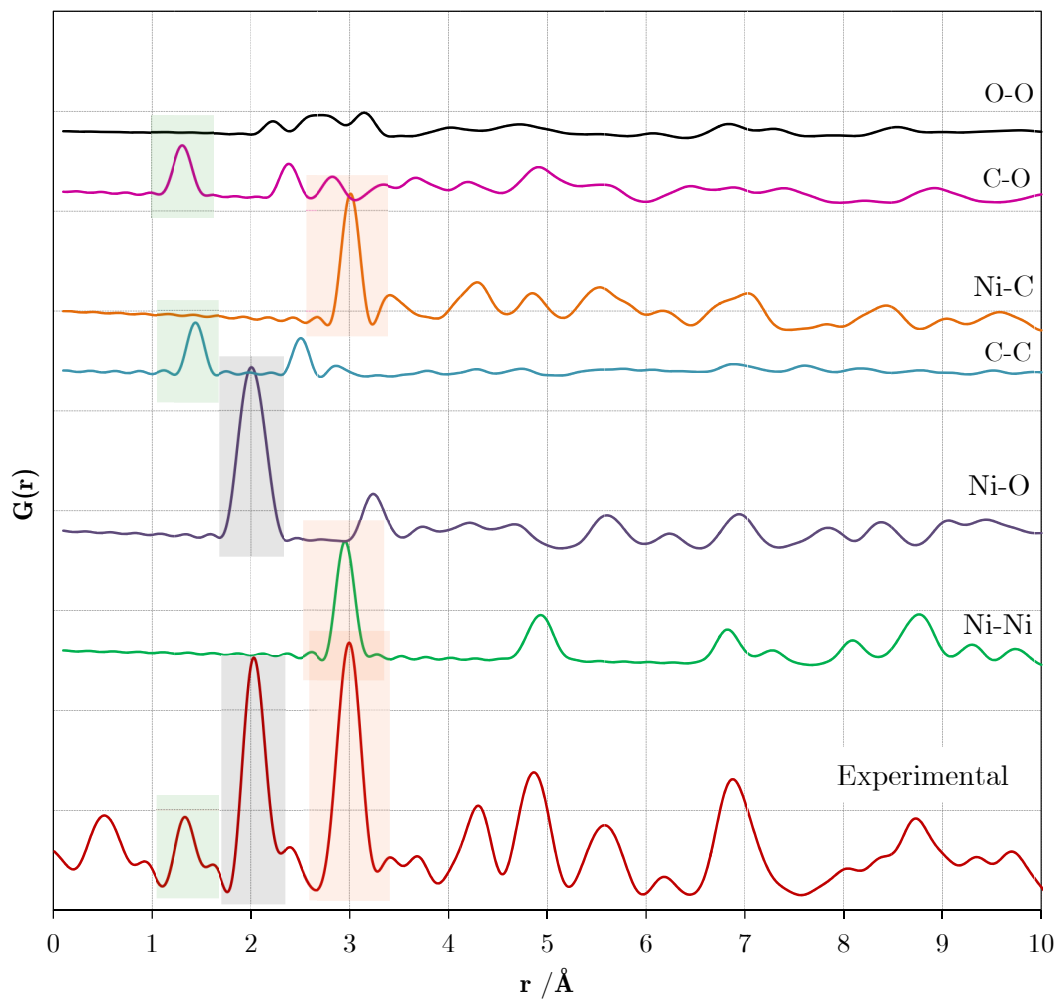

Figure 7-5: Experimental PDF for Ni-CPO-27 with partial PDFs. Coloured blocks highlight peaks in the experimental PDF which can be assigned to particular atom correlations from partial PDFs.

This model was refined against the experimental PDF in the distance range 1 – 40 Å. Table 2 shows the R-factors for the free variables used. Initial refinement of the scale factor and instrument damping factor alone produced an R-factor of 54.5 %. The worst fit was achieved at low-r, where the peaks were substantially sharper and more

intense than calculated from the crystal structure. This indicated that there was significant correlated motion in the crystal.[26] Refinement of the correlated motion parameter, S_{ratio}, with a cut off distance, r_{cut} of 3.6 Å, the approximate distance to which sharp intense peaks were observed, improved the fit substantially to give an R-factor of 47.1%. Unit cell parameters were refined and thermal parameters were assigned to particular atom types to avoid over parameterisation. All nickel atoms were assigned as @101, oxygen as @102 and carbon as @103. These were allowed to refine from their original set values of 0.005 Å^2. The refinement of the thermal parameters improved the peak width fit of all peaks, and so improved the fit considerably (R_w= 35.6%). Refinement of the space group-symmetry constrained nickel and oxygen atomic positions further improved fit, resulting in a final residual of R_w = 20.6%.

A plot of the final refinement is shown in Figure 7-6. Overall, the agreement of the experimental PDF with the model PDF is good. The good agreement out to 40 Å indicates that the local structure of the material to the distance of 40 Å is the same as the average structure. The fit of data at distances greater than 5 Å is significantly better than at low-r values. Refinement of the structure using only the data in the range of 5 – 40 Å led to decreased residual values in all refinement cycles (Table 2). The poorer fit at low-r indicates that there is some aspect of the very local structure which is not accounted for in the average structure. The most likely source of this is residual solvent in the structure which is not included in the dehydrated structural model.

Refinement of the symmetry-constrained carbon positions improved the fit with a final R_w of 16.15%. However, a free refinement of the carbon positions did lead to loss of shape and geometry of the benzene ring. Whilst the main shape of the ring remained, the ring was not planar and some of the carbon-carbon distances were longer than expected for a normal double bond distance. Symmetry restraints are necessary for the refinement of ligand-atom rigid body groups within metal-organic frameworks with PDF data but these cannot be applied in current software.

Table 2: Details for the refinement of Ni-CPO-27 using PDF data

Distance range /Å	Refined parameters	Hydrated Ni-CPO-27	Dehydrated Ni-CPO-27
		R-factor /%	
0-40	Q_{damp}	54.5	50.4
	+ Scale factor, S_{ratio}	47.1	46.2
	+ Unit cell	43.6	36.3
	+ Thermal parameters	35.6	31.2
	+ Ni, O(C) positions	31.5	20.6
	+ O(w) positions	25.6	-
	+ C positions	21.4	16.1
5-40	Q_{damp} Scale factor	62.6	54.1
	+ Unit cell	48.3	34.0
	+ Thermal parameters	32.8	28.0
	+ Ni, O(C) positions	28.1	21.5
	+ O(w) positions	23.0	-
	+ C positions	21.7	13.4
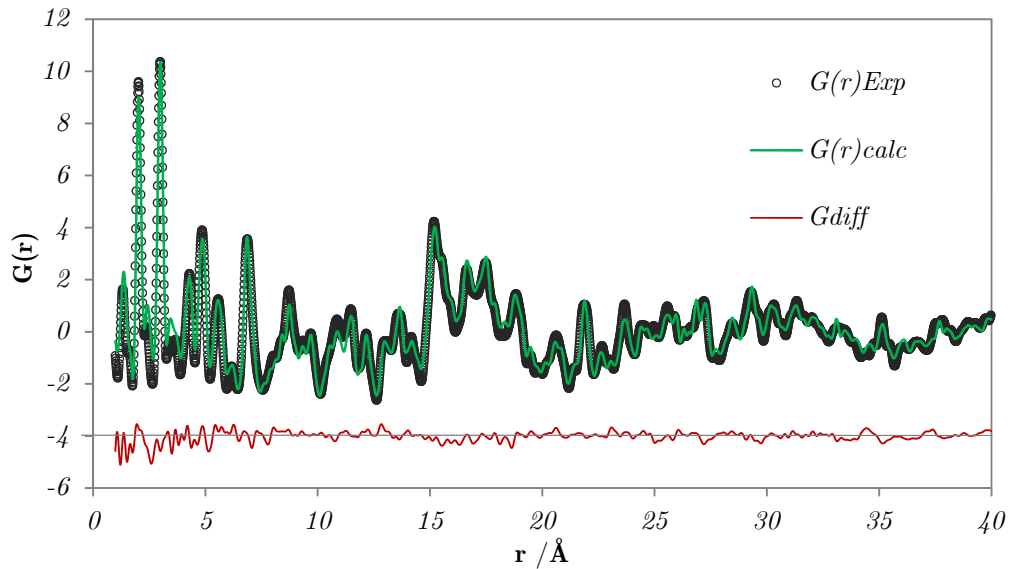
Figure 7-6: Final PDF refinement for dehydrated Ni-CPO-27 after refinement of experimental parameters, unit cell parameters, anisotropic displacement parameters and Ni- and O-positions. The black markers show the experiential data, the green line shows the simulated PDF from the refined model structure. The differential, defined as $G(r)_{exp} - G(r)_{calc}$ is shown by the red line offset by -4, with the grey horizontal line representing zero difference between the two functions.

Table 3: Comparison of the model for dehydrated Ni-CPO-27 from PXRD and PDF data.

Parameter	From PXRD model	From PDF model
a /A	25.76081 (8)	25.964 (21)
c /A	6.76319 (2)	6.831 (8)

Table 4: Fractional atomic positions for dehydrated Ni-CPO-27 determined from Rietveld and PDF analysis. Rietveld analysis is shown in normal font and PDF numbers are shown in italics for comparison. The esds on the numbers from the PDF analysis are undetermined as esds on the individual data points are unknown.

	x	y	z	Uiso*/Ueq
Ni1	0.36257 (5)	0.04722 (5)	0.02131 (15)	0.03228 (16)*
	0.359509	*0.046944*	*0.022012*	*0.00672**
O2	0.30644 (18)	0.0552 (2)	−0.1698 (7)	0.0266 (16)*
	0.30791	*0.061647*	*-0.164232*	*0.009054**
O3	0.3618 (2)	0.1038 (2)	−0.7703 (8)	0.0332 (18)*
	0.358198	*0.104395*	*-0.764913*	*0.009054**
O4	0.33564 (18)	0.0333 (2)	−0.5282 (7)	0.0336 (19)*
	0.333094	*0.030339*	*-0.53745*	*0.009054**
C5	0.3403 (3)	0.1264 (4)	−0.4495 (11)	0.010 (3)*
	0.34032	*0.1264*	*-0.44950*	*0.009141**
C6	0.3477 (3)	0.1777 (4)	−0.5339 (10)	0.019 (3)*
	0.34767	*0.1777*	*-0.53390*	*0.009141**
C8	0.3196 (4)	0.1117 (4)	−0.2507 (13)	0.032 (3)*
	0.3196	*0.1117*	*-0.2507*	*0.009141**
C9	0.3437 (5)	0.0815 (5)	−0.5958 (13)	0.070 (4)*
	0.3437	*0.0815*	*-0.5958*	*0.009141**

Table 5: Selected bond lengths and angles in dehydrated Ni-CPO-27 determined from Rietveld and PDF analysis. Rietveld analysis is shown in normal font and PDF numbers are shown in italics for comparison. The esds on the numbers from the PDF analysis are undetermined as esds on the individual data points are unknown.

Atoms	Bond Length /Å		Atoms	Bond angle	
	Rietveld	*PDF*		*Rietveld*	*PDF*
Ni1—O2	2.025 (5)	*2.0705*	O2—Ni1—O2$^\text{i}$	167.6 (2)	*167.204*
Ni1—O2$^\text{i}$	1.941 (5)	*2.0167*	O2—Ni1—O3$^\text{ii}$	96.1 (2)	*93.153*
Ni1—O3$^\text{ii}$	2.035 (5)	*2.0957*	O2—Ni1—O4$^\text{iii}$	95.6 (2)	*97.764*
Ni1—O4$^\text{iii}$	2.010 (5)	*2.1552*	O2—Ni1—O4$^\text{i}$	80.79 (18)	*88.811*
Ni1—O4$^\text{i}$	1.956 (5)	*1.9776*	O2$^\text{i}$—Ni1—O3$^\text{ii}$	96.3 (2)	*99.751*
C6—C8$^\text{vii}$	1.391 (8)	*1.4023*	O2$^\text{i}$—Ni1—O4$^\text{iii}$	81.55 (16)	*79.219*
C6—C5	1.363 (8)	*1.3736*	O2$^\text{i}$—Ni1—O4$^\text{i}$	86.9 (2)	*82.939*
C5—C9	1.558 (9)	*1.5702*	O3$^\text{ii}$—Ni1—O4$^\text{iii}$	98.94 (18)	*93.286*
C5—C8	1.426 (8)	*1.4398*	O3$^\text{ii}$—Ni1—O4$^\text{i}$	175.4 (2)	*175.395*
C8—C2	1.428 (8)	*1.378*	O4$^\text{iii}$—Ni1—O4$^\text{i}$	84.78 (8)	*90.572*
C9—O3	1.294 (8)	*1.2207*			
C9—O4	1.238 (9)	*1.2689*			
<Ni-O>	1.9934(4)	*2.04314*			

In a similar manner, the hydrated structure of Ni-CPO-27 was refined against PDF data. The fit for this structure was expected to be lower due to the unknown amounts of solvent in the pore. Interactions between these solvent molecules are expected to change the fit, particularly at low-r. The refinement was done using the method described above, and it converged to a final value of R_w of 31.5% when the positions of the nickel atoms and carboxylate oxygen atoms were refined. When the positions of the water oxygens were also refined the fit improved to $R_w = 25.7\%$. The fit is shown in Figure 7-7. The fit is slightly poorer at low-r, indicating that there may be short-range correlations which are unaccounted for by the average structure. The most likely source of this deviation is the placement of guest water molecules in the pore. In the structure from PXRD water molecules are placed in the same position in each unit cell, but in reality many are likely to be disordered throughout the channel, and so atomic correlations will not be properly modelled by the long-range structure.

The structure of the framework holds together during the unrestrained PDF refinement. A comparison of cell parameters, Ni-O bond lengths and O-Ni-O bond angles obtained from Rietveld and PDF analysis is shown in Table 6. The most notable difference is that of the a-cell parameter which is 25.95881(4) from Rietveld and 25.786(2) from PDF refinement. This reduction is quite interesting as the dehydrated data set shows an opposite change (i.e. PDF refinement finds the unit cell parameters to be larger than Rietveld refinement) and the resultant cells are very similar. Unit cell parameters from Rietveld are more accurate because of the way in which is they are calculated, and wherever possible unit cell parameters should be calculated from a Rietveld refinement of data.

Ni-O bond lengths do show a slight reduction in comparison to those calculated from the Rietveld refinement, but all remain in the range expected for Ni-O bonds and the axial bonds of the framework still appear to be elongated, symptomatic of a Jahn-Teller distortion. Bond angles do vary between the two methods, but the nickel atom remains in distorted octahedral geometry.
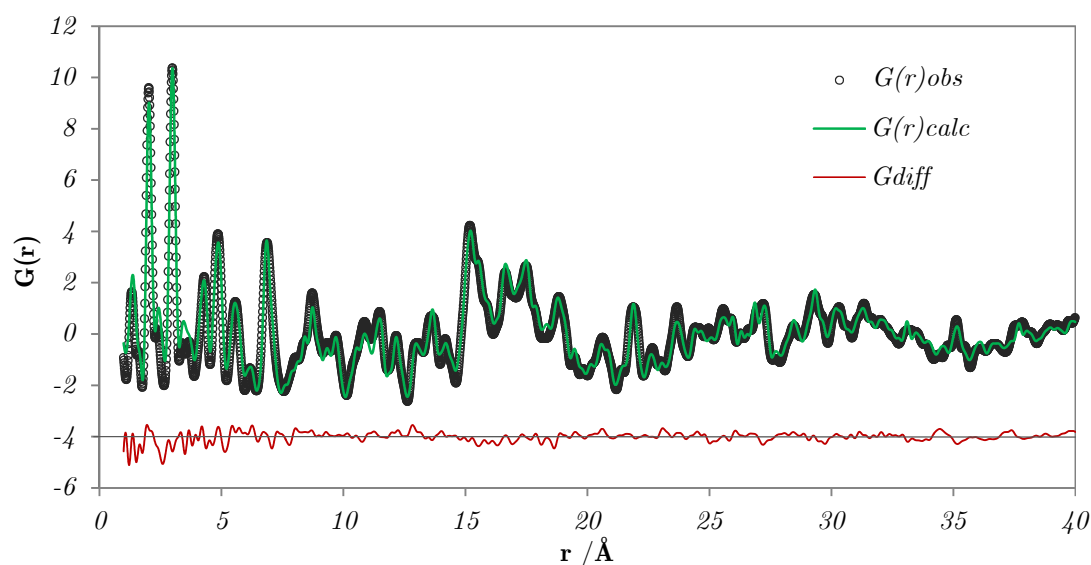
Figure 7-7: Final refinement of hydrated Ni-CPO-27 against PDF data. Black markers show the experimental data, the green line shows the simulated PDF from the refined model structure. The differential, defined as $G(r)_{exp} - G(r)_{calc}$ is shown by the red line offset by -3, with the grey horizontal line representing zero difference between the two functions.

Table 6: Comparison of cell parameters for hydrated Ni-CPO-27 determined from Rietveld and PDF analysis.

Parameter	PXRD	PDF
a /A	25.95881(4)	25.786 (24)
c /A	6.68539(2)	6.692 (8)

Table 7: Fractional atomic positions for hydrated Ni-CPO-27 determined from Rietveld and PDF analysis. Rietveld analysis is shown in normal font and PDF numbers are shown in italics for comparison. The esds on the numbers from the PDF analysis are undetermined as esds on the individual data points are unknown.

	x	y	z	Uiso*/Ueq
Ni1	0.65124 (4)	0.61658 (4)	0.65165 (14)	0.0209 (2)*
	0.651646	*0.61706*	*0.651811*	*0.007137*
C1	0.4019 (3)	0.4174 (3)	0.7379 (9)	0.031 (2)*
	0.3995	*0.4153*	*0.736*	*0.0616*
C2	0.4543 (3)	0.4589 (3)	0.8835 (9)	0.014 (2)*
	0.4516	*0.4569*	*0.889*	*0.0616*
C3	0.5445 (3)	0.5545 (3)	0.9161 (11)	0.035 (2)*
	0.5452	*0.5533*	*0.922*	*0.0616*
C4	0.4948 (3)	0.5111 (3)	0.7947 (9)	0.017 (2)*
	0.4935	*0.5108*	*0.812*	*0.0616*
O1	0.40424 (17)	0.43750 (18)	0.5571 (6)	0.0270 (14)*
	0.404678	*0.445317*	*0.551425*	*0.0134729*
O2	0.36194 (17)	0.37083 (17)	0.8005 (6)	0.0227 (14)*
	0.358285	*0.366217*	*0.802276*	*0.0134729*
O3	0.58252 (17)	0.60665 (16)	0.8210 (7)	0.0288 (14)*
	0.58065	*0.601339*	*0.853192*	*0.0134729*
O4 (1w)	0.65310 (18)	0.54638 (16)	0.7906 (5)	0.0331 (14)*
	0.655303	*0.547788*	*0.793011*	*0.0166489*
O5 (1s)	0.6963 (2)	0.55233 (18)	0.2005 (7)	0.0597 (16)*
	0.696097	*0.541867*	*0.0176022*	
O6(2s)	0.7554 (4)	0.5251 (5)	0.7782 (17)	0.110 (5)*
	0.724858	*0.487875*	*0.72287*	*0.0219593*
O7(3s)	0.8307 (14)	0.4336 (14)	1.035 (5)	0.033 (11)*
	0.74217	*0.373474*	*0.0890464*	
O8(4s)	0.5512 (4)	0.1563 (4)	0.4357 (16)	0.116 (4)*
	0.585206	*0.168657*	*0.476431*	*0.126955*

Table 8: Selected bond lengths and angles in hydrated Ni-CPO-27 determined from Rietveld and PDF analysis. Rietveld analysis is shown in normal font and PDF numbers are shown in italics for comparison. The esds on the numbers from the PDF analysis are undetermined as esds on the individual data points are unknown.

Atoms	Bond Length /Å		Atoms	Bond angle /°	
	Rietveld	PDF		Rietveld	PDF
Ni1—O3	2.017 (4)	*2.1425*	O2ix—Ni1—O3	85.55 (15)	*81.007*
Ni1—O3v	2.043 (4)	*2.0208*	O2ix—Ni1—O3v	87.43 (17)	*84.092*
Ni1—O1(w)	2.068 (4)	*2.0642*	O2ix—Ni1—O4	92.40 (15)	*92.19*
Ni1—O1ii	1.993 (4)	*1.9795*	O2ix—Ni1—O2x	80.86 (5)	*81.236*
Ni1—O2iii	2.046 (4)	*2.0079*	O2x—Ni1—O3	88.46 (16)	*95.418*
Ni1—O2iv	2.118 (4)	*2.052*	O2x—Ni1—O3v	83.06 (13)	*83.403*
C1—C2	1.579 (7)	*1.3649*	O2x—Ni1—O4	173.09 (15)	*172.384*
C2—C3i	1.388 (7)	*1.3029*	O3—Ni1—O3v	169.75 (13)	*165.053*
C2—C4	1.367 (7)	*1.3649*	O3—Ni1—O4	92.53 (17)	*87.29*
C3—C4	1.463 (7)	*1.435*	O1ii—Ni1—O2ix	175.28 (18)	*174.733*
C1—O1	1.306 (6)	*1.4281*	O1ii—Ni1—O2x	95.62 (15)	*100.022*
C1—O2	1.208 (7)	*1.2582*	O1ii—Ni1—O3	91.24 (17)	*93.766*
C3—O3	1.370 (7)	*1.2041*	O1ii—Ni1—O3v	95.30 (18)	*101.12*
Mean Ni-O	2.047(4)	*2.0445*	O1ii—Ni1—O4	91.20 (17)	*86.893*

Symmetry codes: (i) −x+1, −y+1, −z+2; (ii) −x+1, −y+1, −z+1; (iii) y−1/3, y−x−2/3, −z+1/3; (iv) x−y−2/3, x−1/3, −z+2/3; (v) −y+4/3, x−y+2/3, z−1/3; (vi) x−y−1/3, x−5/3, −z+1/3; (vii) y−5/3, y−x−1/3, −z+2/3; (viii) y−x+2/3, −x+4/3, z+1/3; (ix) y+2/3, y−x+1/3, −z+4/3; (x) x−y+1/3, x+2/3, −z+5/3.

PDF refinements are able to distinguish between the hydrated and dehydrated structure by comparison of the fit residuals; a refinement using a hydrated model converged to a final R-factor of 36.05% when the same free variables were refined. The fit at r < 6 Å is poor; the model overestimates the number of correlations in the range 1.8 to 2.2 Å, indicating that too many water-framework interactions are modelled in this case. Whilst the structural changes between hydrated and dehydrated Ni-CPO-27 are quite subtle and do not involve a change in the overall framework structure, PDF refinement is able to distinguish between the two. This indicates total scattering data has great potential for comparing potential structures.

7.5 PDF as a fingerprinting methods for gas adsorption

PDF analysis offers an easy visual comparison of compounds, and it is able to highlight the structural similarities and differences between materials. This 'fingerprinting' technique was recently reported in the thesis of T. Davis at Colombia University describing the fingerprinting analysis of non-crystalline pharmaceutical compounds using PDF analysis.[27] Here, amorphous pharmaceutical compounds were compared qualitatively and quantitatively to each other for structural identification or to highlight changes in the compound over time. Fingerprinting is very useful in situations where a full structural refinement is not possible and where the different states of a material have very different PDFs.

The MOF STAM-1 was recently reported to contain two types of 1-dimensional channel, one of which is lined by metal ions with coordinated water molecules and the other by organic ester groups.[28, 29] The hydrated and dehydrated structures of STAM-1 are significantly different (Figure 7-8). Computer modelling suggests that on dehydration the material twists, resulting in a change in atom-atom correlations. STAM-1 has pore-discriminating adsorption properties; the structural change on dehydration closes the hydrophobic pores and makes the hydrophilic pores accessible for adsorption. Some species which cannot reverse the structural transition (N_2, CO_2, O_2) are able to adsorb in only one pore, resulting in a structure analogous to the dehydrated structure, whilst other species which interact more strongly with the framework (H_2O, MeOH, NO) can reverse the structural transition and adsorb in both channels resulting in a structure analogous to the hydrated structure. This differential adsorption has been studied by the comparison of unit cell parameters through powder X-ray diffraction.

The PDFs of the materials look very different (Figure 7-9). At low-r, where C-C and Cu-O correlations dominate, the two PDFs are very similar suggesting that the immediate bonding environment of the materials is identical. At longer distances the PDFs are significantly different, as indicated by the residual curve in Figure 7-9, suggesting that the framework structure is different.

The methanol-loaded PDF is shown in Figure 7-10 (black dotted line). The PDF shows great similarity to the PDF of the hydrated material (navy line). This indicates that the pore structure of the material when exposed to methanol is very similar to that

of the hydrated material. In contrast, the PDF of the ethylene-loaded material (Figure 7-11) shows more similarity with the dehydrated PDF of STAM-1. This indicates that when exposed to ethylene, the material remains in the dehydrated structural form.

Whilst very preliminary in nature, this study highlights how PDF analysis can be used as a fingerprinting method to determine the nature of gas adsorption in frameworks which have more than one distinct structural state. A further study of a host of polar and non-polar guests could lead to a greater understanding of the adsorption properties of this material.
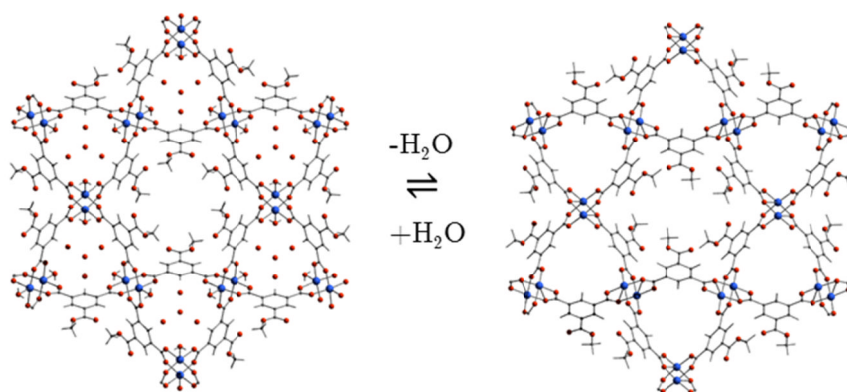
Figure 7-8: The as-synthesised (hydrated) structure of STAM-1 from single crystal analysis (left) and the dehydrated structure determined from computational studies (right).[28]
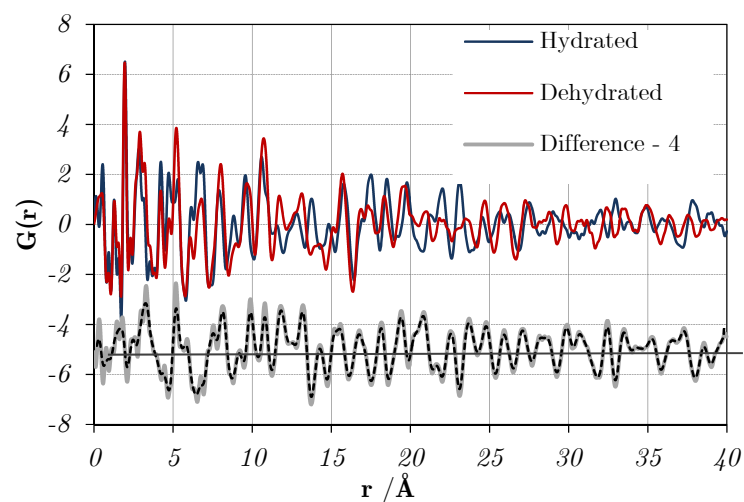
Figure 7-9: PDFs for hydrated and dehydrated STAM-1. The light grey line shows the experimental differential $(G(r)_{dehydrated} - G(r)_{hydrated})$. The black dotted line shows the r-averaged differential curve.
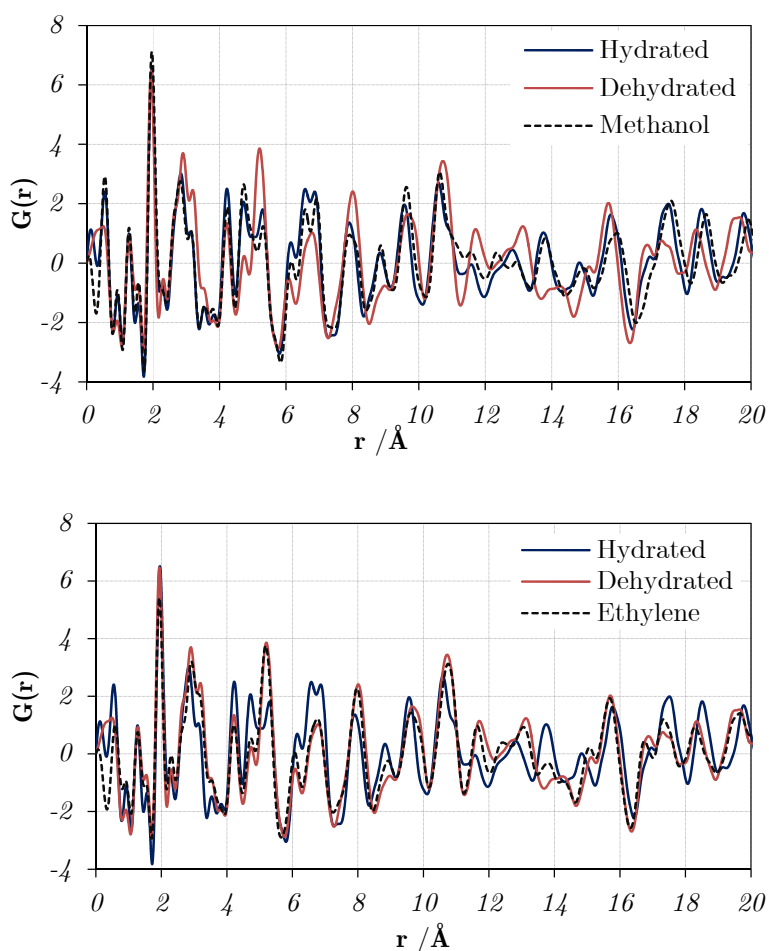
Figure 7-10: PDF for hydrated, dehydrated and methanol-loaded STAM-1 (top), and hydrated, dehydrated and ethylene-loaded STAM-1 (bottom).

7.6 Application of pair distribution function analysis to the novel framework STAM-2

7.6.1 Background

The width of Bragg peaks is dependent upon particle size as given by the Scherer equation (equation 3.27). As particle size decreases the width of the peaks increases, so when very small particles are considered, peak width becomes a serious obstacle for Bragg methods, and the overlap of peaks even at low angles in the PXRD make any interpretation of the data very difficult.[30] PDF uses the diffuse component of scattering so it is not reliant on interpretation of Bragg peak intensities alone.

7.6.2 Synthesis of STAM-2 and initial PXRD analysis

The novel material, STAM-2 is synthesised from a parent-framework, STAM-1, which has been recently reported.[28] The structure of STAM-1 has been described in section 7.5. The synthesis of STAM-2 and subsequent PXRD characterisation detailed in this section were performed by Professor Russell Morris and reported in the thesis of Dr M. I. Mohideen.[29] STAM-1 was dispersed in water and exposed to pulses of ultrasonic radiation over a few hours. A very fine powder solid was obtained from the synthesis, which was a slightly lighter blue colour than the parent material. The PXRDs for STAM-1 and STAM-2 (Figure 7-11) showed substantial differences, indicating that a structural transformation had taken place with a significant change in morphology. The PXRD of the new material had very wide Bragg-peaks, indicative that there had been a loss in crystallinity or a reduction in particle size accompanying the ultrasonic treatment.

Scanning electron microscopy of the new materials indicated a change in morphology; STAM-2 consists of nanorods of no more than 100 nm width and with a length of between 500 – 1000 nm, which is significantly different from the large crystalline blocks of the starting framework. Solid state NMR of STAM-2 indicated that the ester of the linker group formed *in situ* during the synthesis of STAM-1 remains intact in STAM-2.

The small particle size of STAM-2 made it impossible to use SCXRD methods, even through the application of synchrotron radiation. The PXRD data were also difficult to interpret, as there is significant overlap of Bragg peaks, even at low angles. High resolution PXRD data were collected at Diamond Light Source, UK. Initial

attempts to assign a unit cell from the PXRD resulted in relatively poor figures of merit. Once a suitable cell was found, structure validation and solution were attempted by a number of different software packages, but none of these approaches produced any models which were obviously correct.
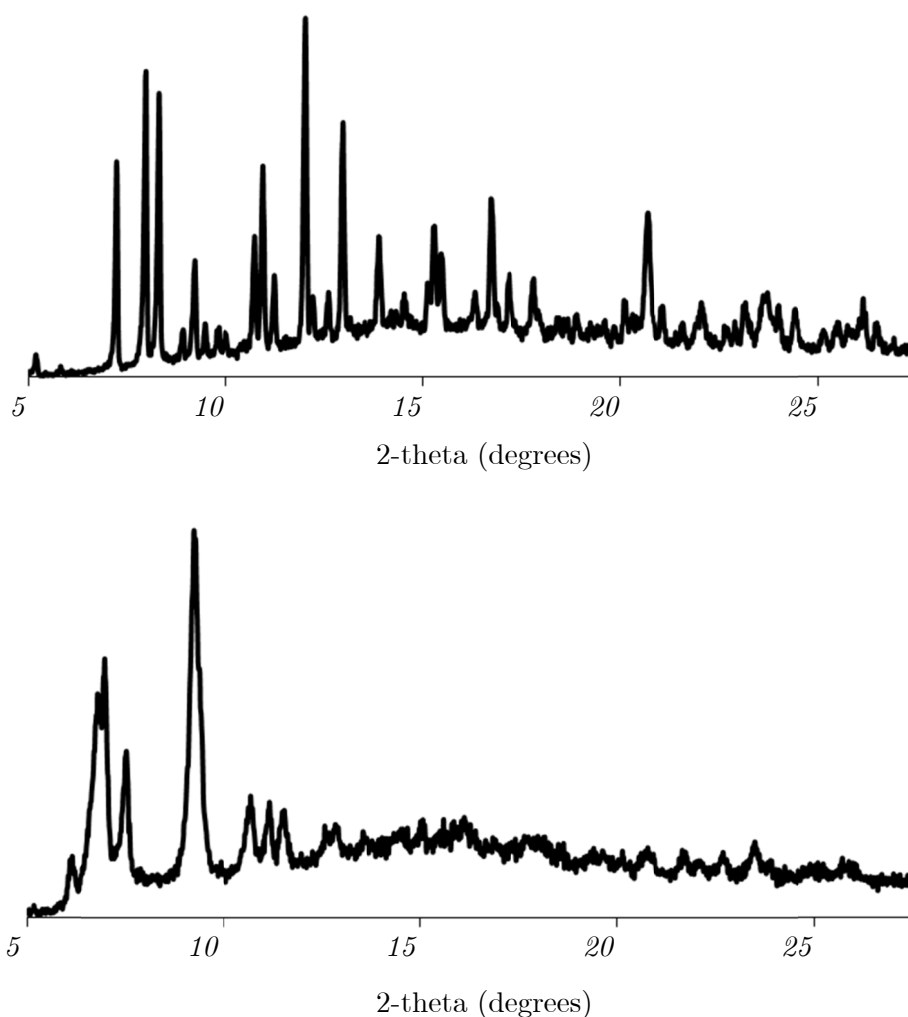

Figure 7-11: X-ray powder diffraction for starting material, STAM-1 (top) and product, STAM-2 (bottom)[31]

7.6.1 Determination of the secondary building block of STAM-2 using PDF analysis

The PDF, G(r) was determined for STAM-1 and STAM-2 (Figure 7-12). The G(r) for STAM-2 was extracted to 100 Å (Figure 7-13) and shows peaks to 40 Å. Consideration of low-r peaks confirms that the organic linker is present in the structure. The contribution of the linker to the PDF can be simulated using a partial PDF

calculated using only the atom positions for the linker (Figure 7-14). Like STAM-1, STAM-2 shows peaks at 1.28 Å and at 2.37 Å due to the C-C and C-O distances in the organic linker molecule. The peak at 1.28 Å corresponds to the aromatic C=C bonds in the linker. The longer distances at 2.37 Å are due, in part, to the C···C interactions across the benzene ring.

The intense peak at 1.96 Å is indicative of Cu-O bonding within the material. This peak has been observed in the PDFs of other MOF frameworks. The high peak intensity is due to the large number of atom-atom correlations of this type and the high scattering power of copper. STAM-1 has a Cu-O distance range of 1.960(4) – 1.964(4) Å, meaning that all the atom-atom distances within this narrow distance range give an intense, sharp peak. STAM-2 shows very similar peaks at this distance, indicating that the material is extended through the Cu-O(carboxylate) linkages, similar to STAM-1.

Above 2.5 Å the PDFs are significantly different giving an indication that the 3D framework structure of STAM-2 is different to STAM-1. Peaks from the M-M distances in the secondary building units (SBUs) of MOFs are usually visible between 2.5 Å and 4 Å and are quite intense because they involve heavy atoms with high scattering factors. Therefore, it is possible to identify the likely SBU in an unknown MOF by the identification of strong peaks around the correct distances for M-M distances. Simulated partial PDFs were calculated for known copper-based secondary building units using PDFGui. CIF files for the structures were taken from single crystal data[28, 32, 33] and the contributions from Cu-Cu interactions were summed in the distance range of 1 - 5 Å (Figure 7-15).

STAM-1 (Figure 7-8) is made up of Cu-Cu dimers characterised by short Cu-Cu distances of approximately 2.6 Å. The dimers do not have Cu-Cu bonding but are bridged by carboxylate ligands which account for the short M-M distance. In the PDF for STAM-1 there is an intense peak at 2.71 Å corresponding to the Cu-Cu distance in the dimer. This peak is not present in the PDF for STAM-2, indicating that the Cu-Cu dimers are not present in this material. STAM-2 features strong peaks at 3.00 Å and 3.43 Å which are likely to correspond to the Cu-Cu distances in the material. When compared to other known copper frameworks it was found that the hydroxide bridged Cu-tetramer from Cu-SIP-3 matches well for peak position, but not for relative peak intensity (Figure 7-15). This indicates that the SBU of STAM-2 is similar but not

identical to the tetramer in Cu-SIP-3. Figure 6.3 indicates that the peak at 3.43 Å in Cu-SIP-3 has a contribution from Cu-(SO_3) atom correlations, which increases the intensity of this second peak, partially accounting for the difference in relative intensity.
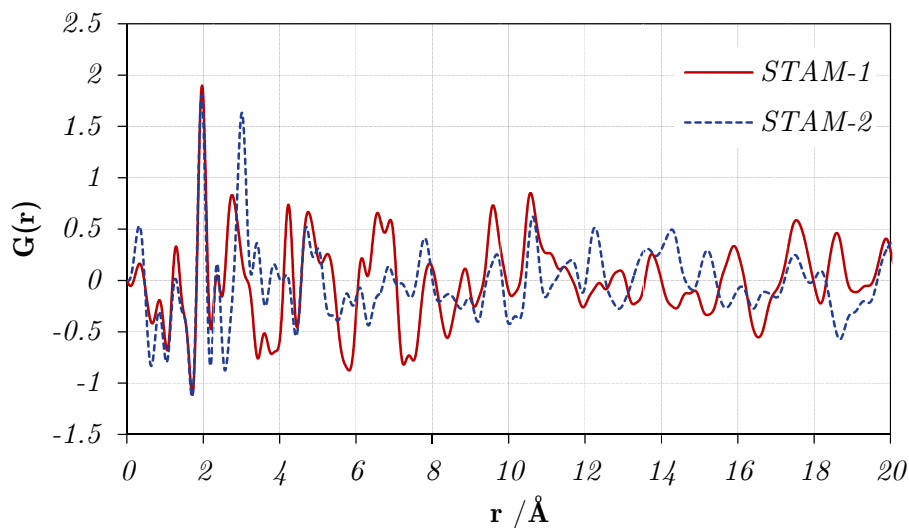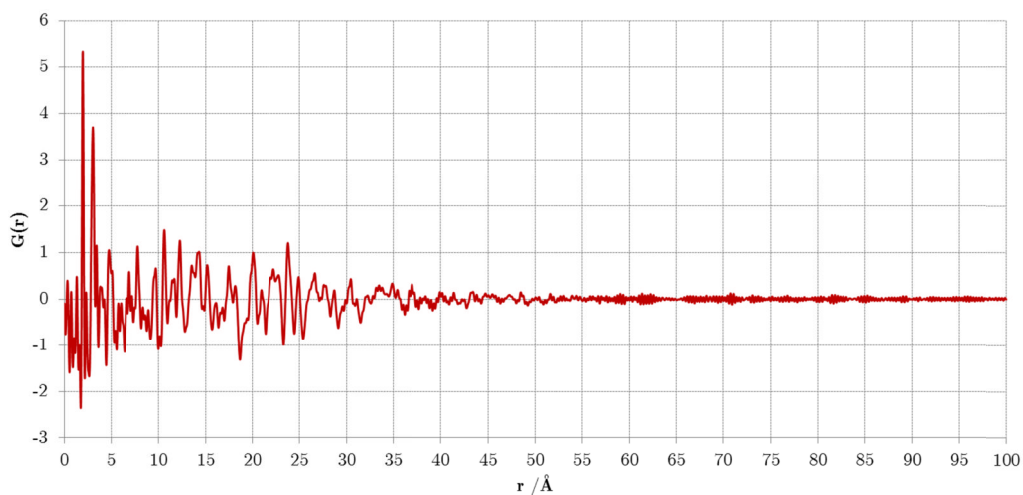

Figure 7-12: PDF for STAM-1 and STAM-2.
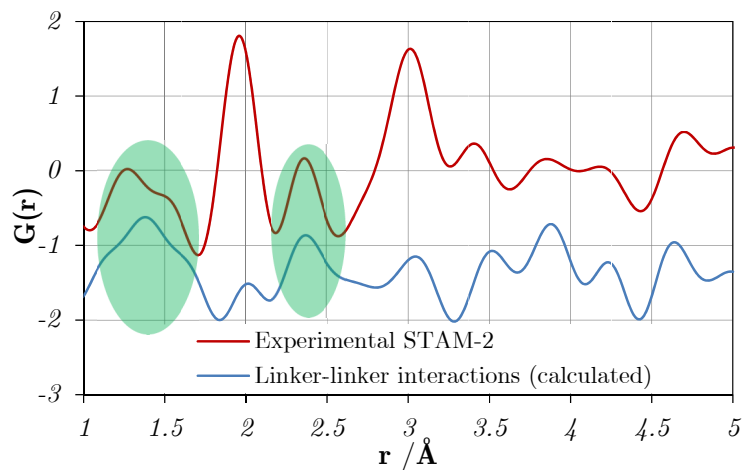

Figure 7-13: PDF for STAM-2 extracted to r = 100 Å.

Figure 7-14: Experimental PDF (top) with calculated linker-linker interactions (bottom). Green circles indicate the major contributions of the linker to the low-r PDF.
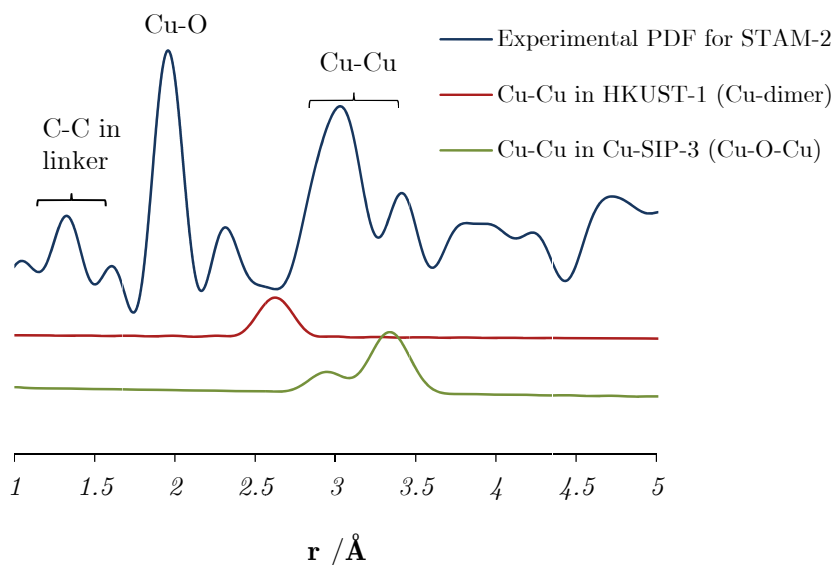

Figure 7-15: Experimental PDF for STAM-2 in the range of $1 - 5$ Å (top) compared to simulated partial Cu-Cu PDFs for two known Cu-SBUs, the paddle wheel dimer (middle) and tetramer (bottom). Vertical axis is G(r) shown in arbitrary units.

7.6.1 Restraint of the PXRD solution of STAM-2 using the PDF-derived SBU

The following PXRD analysis was performed by Professor Russell Morris using the additional information about the Cu-SBUs from the PDFs. Previous PXRD data

240

solutions were revisited but solutions were sought which had Cu-Cu interatomic distances of around 3.0 and 3.4 Å consistent with the Cu-tetramer distance. The solution from the charge-flipping algorithm in the program Superflip[34] gave suitable interatomic distances between peaks of electron density (numbered 1 and 5 by electron count). These positions were assigned as copper atoms. Closer inspection of the solution showed that there were potential positions of oxygen atoms at a distance of ~ 2.0 Å from the proposed Cu-atoms. This information was sufficient to begin building up the coordination around the copper atoms. This identified the SBU present in the material as a chain of vertex-shared copper tetramers (Figure 7-16). Each tetramer is similar to those found in the Cu-SIP-3 structure, but the extra interaction between tetramers through the shared vertices in the chain structure accounting for the difference in peak intensity when compared to Cu-SIP-3.

The remaining carbon and oxygen atoms in the structure were placed by calculating the position of the benzene ring. It was assumed that the ester group was coplanar with this ring on the carboxylate group that was not used as a bridging ligand. This model was used as a starting point and refined using Rietveld analysis. Strong restraints were required to retain a chemically sensible model, which is reflective of the particle size and poor crystallinity of the material. Selected structural details for the PXRD model are shown in Table 9. Errors on atomic positions are not shown due to the number of restraints required for the refinements to converge, making the esd values meaningless.

The structure solved from PXRD data is shown in Figure 7-17. STAM-2 crystallises in the P-1 space group. Chains of Cu_2O_{10} dimers (Figure 7-16) are linked with monomethyl benzene tricarboxylate linkers into a two-dimensional layered structure, where each ligand binds through carboxylate linkers to two chains and the ester group of the linker points into the vacant space between chains.
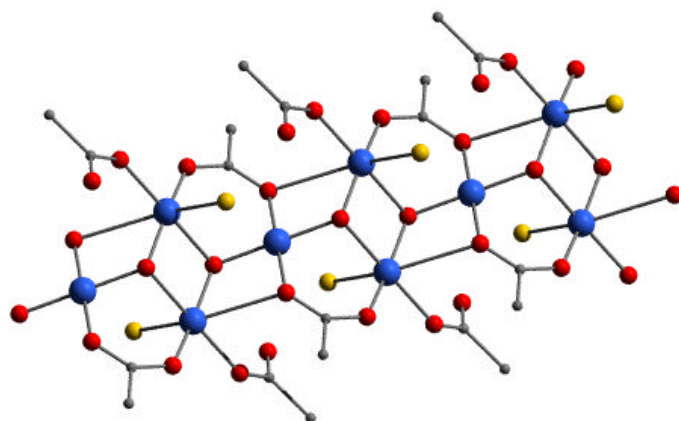
Figure 7-16: The chains of vertex-shared copper tetramers in STAM-2. Yellow atoms represent terminal water molecules attached to the copper atoms.
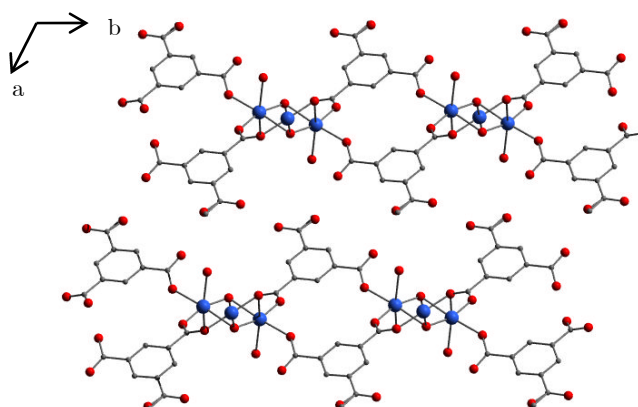

Figure 7-17: Structure of STAM-2 viewed down the *c*-axis.

Table 9: Structural details for the PXRD model of STAM-2.

a /Å	11.2527 (3)
b /Å	10.6146 (3)
c /Å	5.74709 (2)
α /°	86.572 (2)
β /°	97.710 (2)
γ /°	106.834 (2)
V /Å³	650.57 (2)
T /K	293
Space group	P-1

7.6.1 Refinement of the PXRD model against PDF data

The model from Rietveld refinement of PXRD data was refined against the PDF data set using the program PDFGui. Refinements were done in the r-range of 1.0 to 15.0 Å. The material was constrained to have P-1 symmetry as indicated by the PXRD data and the positions of all atoms were constrained by this symmetry. The thermal parameters were not constrained by the P-1 symmetry; instead, they were restrained by atom type in order to avoid over-parameterisation. Five distinct thermal parameter environments were defined: (1) copper atoms, (2) carboxylate oxygen atoms used in framework bonding to the Cu-atoms, (3) the oxygens of the ester group, (4) the ester group thermal carbon, (5) all other carbon atoms. All atoms were refined isotropically, with $U_{11} = U_{22} = U_{33}$ and set to a starting value of 0.005 Å^3 and the cross diagonal terms U_{12}, U_{23} and U_{13} set to zero.

7.6.1.1 Initial refinement runs

The initial model from PXRD showed poor fit to the experimental PDF data. Inspection of the experimental and theoretical PDFs suggested that the model from PXRD overestimated the Cu-Cu bond length and underestimated the Cu-O bond length in the material. The Cu-O(carboxylate) bond length for the material had a range of 1.8035 – 2.3313 Å, the lower limit of which is much shorter than the range of Cu-O(carboxylate) bond lengths found in HKUST-1, Cu-SIP-3 and STAM-1 (1.9130 - 2.3743 Å, 1.9513 – 2.1651 Å and 1.9130 - 2.3743 Å, respectively).[28, 32, 33] As a result, intense peaks in the model and experiment were mismatched and so refinement of scale factor R-values were reduced by drastically increasing Q_{damp} or decreasing the scale factor. This improved the overall R_w value for the refinement by decreasing the amount of mismatch in the peaks, but meant that refining the structure further by this method was impossible.

Instead of refining experimental parameters in the initial runs, these were fixed at values determined by visual inspection of the functions. The positions of the copper and oxygen atoms were allowed to refine freely (though constrained to P-1 symmetry) in these initial stages of the refinement, in effect refining the Cu-O and Cu-Cu bond lengths in the material. This improved the fit in the low-*r* regions dramatically.

Further refinement of the model had to be carefully controlled to ensure that a chemically sensible model was produced and not just the model with the lowest R-factor.

The refinement was very dependent on the order in which parameters were refined. Some models would stagnate at an R_w value of 0.42 whilst others would reach values of < 0.30 easily.

For the STAM-2 structure, the best fit was achieved by refining the copper-positions and the oxygen positions early in the refinement until there was no appreciable change in the value of R_w with further refinement cycles. Unit cell parameters were added to the refinement and the parameters refined until stable. Thermal parameters were added to the refinement, although some of these values became unreasonably large and so were fixed to 0.06 $\mathring{A}^3$. The scale factor and Q_{damp} were refined late on in the process and showed relatively little change or improvement to the refinement. The final R_w-value obtained was 31.2563%.

7.6.1.2 Refinement of the carbon positions via definition of a 'rigid body'

When the positions of the carbons atoms were allowed to refine in an unrestrained manner, the fit of the model to the data improved significantly. Unfortunately, the model which was produced by this process did not keep the carbon positions in a sensible regime; the free refinement led to significant distortion of the benzene ring, and in some cases carbon atoms would move large distances into the channels of the material. The reason for this is that peaks in the PDF are weighted with respect to atomic number. Carbon is very light compared to the copper atoms in the structure and so contributes relatively little to the PDF. Additionally, the shortest Cu-C distance is 2.76 $\mathring{A}$, meaning that the positions of the carbon atoms are, at low-r values, being refined solely on the C-C position in the structure. This is not ideal, as the relatively small contribution that these atoms make to the overall PDF makes it possible to move these atoms around without much restraint to improve the fit at low-r values and the refinement will not pick this up as incorrect.

There is no simple method for adding bond length restraints to a refinement. However, it is possible to relate the atomic positions of atoms to one another via the relation of free variables. Here, the positions of carbon atoms in the benzene ring were calculated relative to C3, the carboxylate group carbon atom between two ligating carboxylate oxygen atoms. The refinement parameters for the C3 x, y and z positions were set as @154, @155 and @156. The refinement parameters for the other carbon atoms of the benzene ring were set relative to this position, for example, C5 with an

atomic position relative to C3 of $(x + 0.0133)$, $(y + 0.1231)$, $(z + 0.8674)$ had positional refinement parameters set as (@154 + 0.0133), (@155 + 0.1231), (@156 + 0.8674), etc. This meant that the benzene ring was restrained to move effectively as a rigid body throughout the refinement of the carbon positions.

Refinement using this rigid body improved the fit with comparison to having the carbon position unrefined (Table 10). The final R_w value obtained by refinement with restrained carbon atoms was 28.3122%. The R-factor obtained was not as good as allowing the carbon positions to refine freely, but the model produced was chemically sensible and so the refinement is considered superior to the previous model. The resulting structure made more chemical sense; the SBU and Cu-O framework held together well. The benzene ring was flat, though showed some slight distortion. The carboxylate group *para-* to the carboxylate group which bridged between Cu-atoms, which was not restrained as part of the rigid body, was twisted out of the plane. Bond lengths and angles are shown in Table 11. The final fit of the PDF is shown in Figure 7-18.

The unit cell from the PDF refinement is significantly different to that using PXRD refinement. The errors on the cell angles are quite large which raises questions about the accuracy of the cell, especially because PXRD is generally a more accurate way of determining unit cell parameters than other diffraction techniques. However, the PDF refinement was attempted in several ways, refining the unit cell at various stages of the process (e.g. the unit cell was refined before the Cu-O bond lengths, at the same time as the Cu-O bond lengths, after the Cu-O bond lengths and also very late on in the refinement) and all refinements gave similar parameters.

Table 10: Refinement details for the refinement without carbon position refinement, free carbon position refinement and restrained carbon position refinement. The esds on the numbers from the PDF analysis are undetermined as esds on the individual data points are unknown.

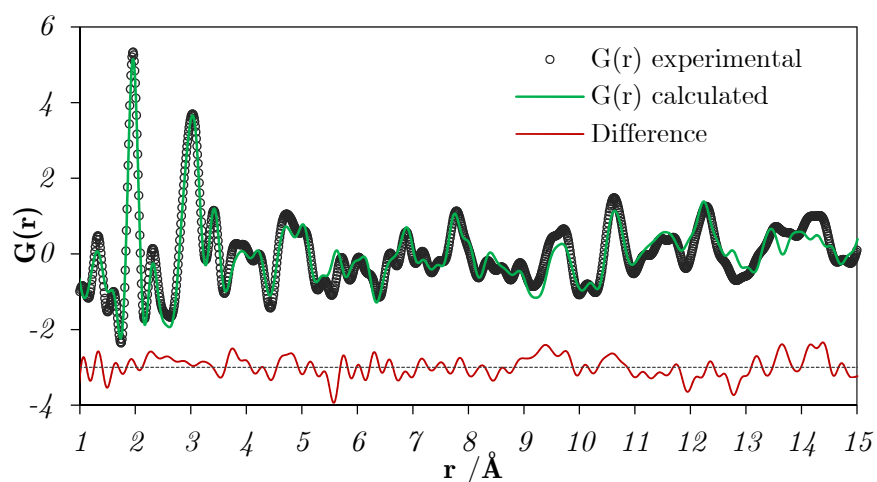|	Refinement with restrained carbon positions	Refinement with no carbon positions refined	Refinement with free refinement of carbon positions	Model from powder diffraction
a /Å	11.4332	11.425	11.456	11.2527 (3)
b /Å	10.5687	10.5839	10.5313	10.6146 (3)
c /Å	5.6184	5.6293	5.6321	5.74709 (2)
α /°	85.18	85.3075	85.3235	86.572 (2)
β /°	96.248	96.1454	96.4409	97.710 (2)
γ /°	109.0506	109.164	109.022	106.834 (2)
r_w	28.3122	31.2563	20.022	

Figure 7-18: Final PDFGui refinement for STAM-2. The black markers show the experimental data, and the green line shows the simulated PDF from the refined model structure. The differential, defined as $G(r)_{exp} - G(r)_{calc}$, is shown in red and offset by -3.

7.6.1 Comparison of the model from PXRD with that from PDF analysis

The asymmetric unit of STAM-2 after PDF refinement is shown in Figure 7-19. The overall structure is shown in Figure 7-20 and a CIF (and *.res* file) for the structure is given in Appendix D. The structure contains two copper-environments, Cu1 and Cu2/Cu3 (these are symmetry equivalent via a centre of inversion but the PDFGui program places all atoms in the unit cell and names in them in numerical order without considering symmetry equivalence).

Bond lengths and angles for the Cu-O framework of the material from PXRD and PDF refinements are shown in Table 11. There is an increase in the Cu-O bond length in the material; PXRD data gave a range of Cu-O bond lengths from 1.8035 – 2.3313 Å. After PDF refinement, the range of bond lengths is 1.9375 Å to 2.3498 Å, within the expected range for Cu-O bond lengths.

The Cu-coordination environment is shown in Figure 7-19. The bond angles around the copper atoms also show some changes (Table 11). The original PXRD model had Cu1 in a square planar geometry with angles within the plane of close to 90°. In the model refined by PDF the Cu-O plane is still maintained, but the O7-Cu1-O7 angles are squeezed from close to 90° to 76.17° and 103.83° which is a significant change but is not possible to constrain these angles in the PDF refinement. Cu2 is of pseudo-octahedral geometry from the PXRD model with O-Cu-O angles within the equatorial plane of between 83.97° and 99.72°. The final model from PDF refinement also shows this octahedral geometry, with O-Cu-O bond angles that are similar within a couple of degrees to the PXRD model.

Previous analysis using solid state NMR indicated that the linker group is still esterified from the original STAM-1 synthesis. Free refinement of the ester oxygen and carbon pointing into the space between layers resulted in imperfect ester geometry, but the carbon of the ester group held well to the benzene ring which indicates that the placement of the ester group is correct.
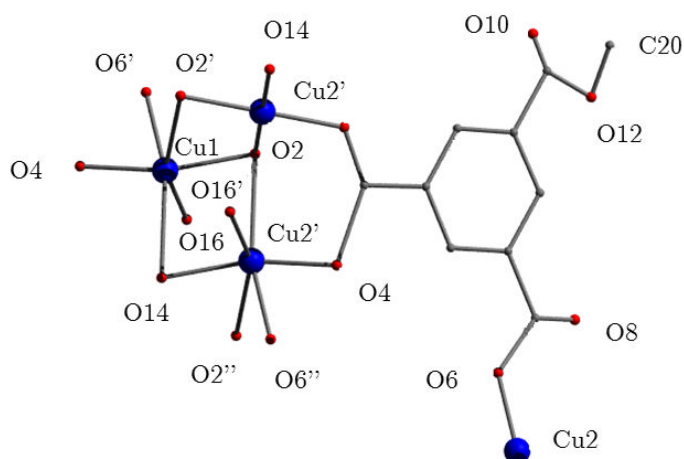
Figure 7-19: The structure of STAM-2 from refinement using PDF data. Only half the atoms are shown. Odd numbered atoms are related to those shown by a centre of inversion.
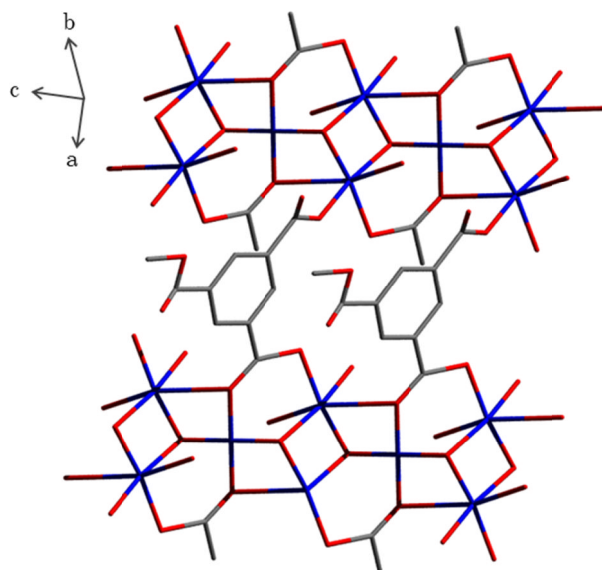

Figure 7-20: Structure of STAM-2 after refinement using PDF data. Blue = copper, red = oxygen, grey = carbon.

Table 11: Cu-O bond lengths and angles of the PDF refined structure of STAM-2. The esds on the numbers from the PDF analysis are undetermined as esds on the individual data points are unknown. Errors on PXRD values are not given due to the level of restraint required for the refinement to converge.

Atom 1	Atom 2	Distance from PXRD model /Å	Distance from PDF model /Å
Cu1	O2	1.8035	1.9493
	O1	1.8035	1.9493
	O13	1.9469	1.9836
	O14	1.9469	1.9836
Cu2	O6	2.2522	1.9375
	O3	1.8383	1.9592
	O13	1.8382	2.0701
	O15	2.3313	2.3498
Cu3	O5	2.2522	1.9375
	O4	1.8383	1.9592
	O14	1.8382	2.0701
	O16	2.3313	2.3498

Table 12: Atomic positions for the PDF model of STAM-2.

	x	y	z	U_{iso}*/U_{eq}
Cu1	0	0	0	0.02495*
Cu2	0.028 (2)	0.153 (1)	0.512 (3)	0.02214*
Cu3	0.972 (2)	0.847 (1)	0.480 (3)	0.02214*
O1	0.888 (3)	0.103 (3)	0.900 (4)	0.00143*
O2	0.112 (3)	0.897 (3)	0.101 (4)	0.00143*
O3	0.982 (3)	0.297 (3)	0.331 (5)	0.00143*
O4	0.017 (3)	0.703 (3)	0.669 (5)	0.00143*
O5	0.911 (3)	0.685 (3)	0.303 (5)	0.00197*
O6	0.088 (3)	0.315 (3)	0.697 (5)	0.00197*
O7	0.658 (3)	0.608 (3)	0.068 (5)	0.00197*
O8	0.342 (3)	0.392 (3)	0.932 (5)	0.00197*
O9	0.546 (3)	0.149 (3)	0.277 (5)	0.00197*

O10	0.454 (3)	0.851 (3)	0.723 (5)	0.00197*
O11	0.517 (2)	0.311 (3)	0.352 (7)	0.00197*
O12	0.483 (2)	0.689 (3)	0.648 (7)	0.00025*
O13	0.125 (2)	0.058 (4)	0.761 (5)	0.00025*
O14	0.875 (2)	0.943 (3)	0.239 (5)	0.00871*
O15	0.201 (3)	0.179 (6)	0.307 (7)	0.00871*
O16	0.799 (3)	0.821 (6)	0.693 (7)	0.00871*
O17	0.319 (3)	0.188 (4)	0.688 (7)	0.00600*
O18	0.681 (3)	0.812 (4)	0.312 (7)	0.00600*
C1	0.893 (3)	0.208 (3)	0.039 (6)	0.06529*
C2	0.107 (3)	0.792 (3)	0.961 (6)	0.06529*
C3	0.817 (3)	0.280 (3)	0.923 (6)	0.02990*
C4	0.183 (3)	0.720 (3)	0.077 (6)	0.02990*
C5	0.830 (3)	0.403 (3)	0.055 (6)	0.02990*
C6	0.170 (3)	0.597 (3)	0.945 (6)	0.02990*
C7	0.757 (3)	0.471 (3)	0.956 (6)	0.02990*
C8	0.243 (3)	0.529 (3)	0.044 (6)	0.02990*
C9	0.672 (3)	0.416 (3)	0.722 (6)	0.02990*
C10	0.328 (3)	0.584 (3)	0.278 (6)	0.02990*
C11	0.663 (3)	0.293 (3)	0.594 (6)	0.02990*
C12	0.337 (3)	0.707 (3)	0.407 (6)	0.02990*
C13	0.734 (3)	0.225 (3)	0.690 (6)	0.02990*
C14	0.266 (3)	0.775 (3)	0.310 (6)	0.02990*
C15	0.772 (3)	0.606 (3)	0.099 (6)	0.01335*
C16	0.228 (3)	0.394 (3)	0.901 (6)	0.01335*
C17	0.570 (3)	0.233 (3)	0.350 (6)	0.03130*
C18	0.430 (3)	0.768 (3)	0.650 (6)	0.03130*
C19	0.506 (3)	0.287 (3)	0.132 (6)	0.06747*
C20	0.494 (3)	0.713 (3)	0.868 (6)	0.06747*

7.7 Conclusions and Further Work

Total scattering data have been collected for a number of metal-organic framework materials. PDFs have been extracted for these materials and a number of methods to analyse data have been presented.

Three applications for PDF data have been demonstrated. PDF can be used for comparison with and verification of other diffraction techniques. The structure of hydrated and dehydrated Ni-CPO-27 has been refined using both a Rietveld analysis and a total scattering (so called 'Real-Space Rietveld') refinement. The PDF fit of the model from Rietveld is good at longer lengths but shows worse agreement at low-r, indicating that there may be local deviations from this average model. This effect is less pronounced in the dehydrated data set, indicating that modelling of the solvent in the pores may be the reason behind the worse fit. Certainly in single-crystal studies lower residuals are often found when the structure is dehydrated, indicating again that the modelling of solvent through an average structure is not ideal. Models from the PDF and Rietveld refinement show similar bond lengths and bond angles for the Ni-coordination environment, but cell parameters differ considerably between the two models and this may indicate that PDF is not suitable for unit cell determination.

PDF has been shown to be a potential fingerprinting method for metal-organic frameworks using both model-independent and model-dependent methods. Comparison of residual factors from PDF refinements indicates strongly whether the structure of Ni-CPO-27 is hydrated or dehydrated. Because real-space refinements are more sensitive to distance fluctuations, the difference between models is reflected more clearly in residuals allowing different models to be easily compared. Where a structure such as STAM-1 exists in two different forms with different atomic correlations, the PDFs of the material can be used to fingerprint which results from a defined change in experimental conditions, even if the exact structure of the material is unknown.

In the case where Bragg diffraction is insufficient for full structural determination, PDF can be the primary source of information about a structure. Here, the secondary building block of STAM-2 was determined by comparison of intense peaks in the PDF whose likely derivation were Cu-Cu correlations in the material. This information allowed the restraint of PXRD data to find a likely solution. The PDF

refinement converged more easily and with minimal restraint compared to the highly-restrained Rietveld refinement of PXRD data, due to the inclusion of diffuse scattering data. This refinement allowed validation of the determined solution.

Refinement of a structure with a large number of atoms in the unit cell, particularly those which contain large assemblies of lighter atoms such as organic linkers, is not going to give as accurate answer as SCXRD or PXRD and input of chemical knowledge into a refinement is difficult. In the case of STAM-2, the final PDF-refined structure is not ideal; the linker molecule is not entirely planar and some of the bond angles deviate from those expected from Cu-complexes. However, the fact that the structure from PXRD can be refined against the PDF data with the linker and carboxylate framework staying mostly intact gives weight to the PXRD analysis being correct. Some aspects of the structure are improved by the PDF analysis, for example the refined value for the Cu-O bonds is much closer to other reported values for the copper MOFs.

This work has indicated that MOF PDF refinements may be improved by the definition of rigid bodies. The definition of a rigid body through the calculation of atomic positions relative to one particular atom is possible for structures with low symmetry (P1 or P-1). However, in practical terms, this approach is not ideal for higher symmetry frameworks as it involves a large number of calculations followed by the removal of errors in the model, both of which are time-consuming. Further work in this area could concentrate on making the definition of rigid bodies automated in a program such as PDFGui, in order for framework materials to be dealt with more easily.

7.8   References

1.   J. E. Readman, P. M. Forster, K. W. Chapman, P. J. Chupas, J. B. Parise and J. A. Hriljac, *Chem. Commun.*, 2009, 3383-3385.

2.   M. M. Martínez-Iñesta, I. Peral, T. Proffen and R. F. Lobo, *Microporous Mesoporous Mat.*, 2005, **77**, 55-66.

3.   K. W. Chapman, P. J. Chupas and T. M. Nenoff, *J. Am. Chem. Soc.*, 2010, **133**, 12398–12401.

4.   D. F. Sava, M. A. Rodriguez, K. W. Chapman, P. J. Chupas, J. A. Greathouse, P. S. Crozier and T. M. Nenoff, *J. Am. Chem. Soc.*, 2011, **133**, 12398–12401.

5.   H. Zhao, T. M. Nenoff, G. Jennings, P. J. Chupas and K. W. Chapman, *J. Phys. Chem. Lett.*, 2011, **2**, 2742-2746.

6.   K. W. Chapman, P. J. Chupas and C. J. Kepert, *J. Am. Chem. Soc.*, 2005, **127**, 11232-11233.

7.   K. W. Chapman, D. F. Sava, G. J. Halder, P. J. Chupas and T. M. Nenoff, *J. Am. Chem. Soc.*, 2011, **133**, 18583-18585.

8.   T. D. Bennett, S. Cao, J. C. Tan, D. A. Keen, E. G. Bithell, P. J. Beldon, T. Friscic and A. K. Cheetham, *J. Am. Chem. Soc.*, 2011, **133**, 14546-14549.

9.   T. D. Bennett, A. L. Goodwin, M. T. Dove, D. A. Keen, M. G. Tucker, E. R. Barney, A. K. Soper, E. G. Bithell, J. C. Tan and A. K. Cheetham, *Phys. Rev. Lett.*, 2010, **104**, 115503.

10.   T. D. Bennett, D. A. Keen, J. C. Tan, E. R. Barney, A. L. Goodwin and A. K. Cheetham, *Angew. Chem., Int. Ed.*, 2011, **50**, 3067-3071.

11.   T. D. Bennett, P. Simoncic, S. A. Moggach, F. Gozzo, P. Macchi, D. A. Keen, J. C. Tan and A. K. Cheetham, *Chem. Commun.*, 2011, **47**, 7983-7985.

12.   T. D. Bennett, J. C. Tan, S. A. Moggach, R. Galvelis, C. Mellot-Draznieks, B. A. Reisner, A. Thirumurugan, D. R. Allan and A. K. Cheetham, *Chem.--Eur. J.*, 2010, **16**, 10684-10690.

13.   A. K. Cheetham, T. B. Bennett, T. D., D. A. Keen, J. C. Tan, E. R. Barney and A. L. Goodwin, *Angew. Chem., Int. Ed.*, 2011, **50**, 3067-3071.

14.   I. E. Collings, Tucker, M.G., Keen, D. A., Goodwin, A. L., *Z. Krist.*, 2012, *In Press*.

15.   K. L. Mulfort, O. K. Farha, C. D. Malliakas, M. G. Kanatzidis and J. T. Hupp, *Chem.--Eur. J.*, 2010, **16**, 276-281.

16.   I. Kanoya, T. Furuta, R. Sakamoto, M. Hosoe, M. Ichikawa, K. Itoh and T. Fukunaga, *J. Appl. Phys.*, 2010, **108**.

17. P. J. Chupas, K. W. Chapman and P. L. Lee, *J .Appl. Crystallogr.*, 2007, **40**, 463-470.

18. A. P. Hammersley, S. O. Svensson, M. Hanfland, A. N. Fitch and D. Hausermann, *High Press. Res.*, 1996, **14**, 235-248.

19. X. Qiu, J. W. Thompson and S. J. L. Billinge, *J. Appl. Crystallogr.,* 2004, **37**, 678.

20. M. Wojdyr, *J .Appl. Crystallogr.*, 2010, **43**, 1126-1128.

21. C. L. Farrow, P. Juhas, J. W. Liu, D. Bryndin, E. S. Bozin, J. Bloch, T. Proffen and S. J. L. Billinge, *J. Phys.-Condens. Matter.*, 2007, **19**, 335219.

22. B. H. Toby, *J. Appl. Crystallogr.*, 2001, **34**, 210-213.

23. A. C. Larson, Von Dreele, R.B., *General Structure Analysis System (GSAS)*, Los Alamos National Laboratory, Los Alamos National Laboratory, 2000.

24. T. Egami and S. J. L. Billinge, *Underneath the Bragg peaks : structural analysis of complex materials*, Pergamon, Kiddington, Oxford, UK ; Boston, 2003.

25. P. D. C. Dietzel, R. E. Johnsen, R. Blom and H. Fjellvag, *Chem.--Eur. J.*, 2008, **14**, 2389-2397.

26. I. K. Jeong, T. Proffen, F. Mohiuddin-Jacobs and S. J. L. Billinge, *J. Phys. Chem. A*, 1999, **103**, 921-924.

27. T. D. Davis, PhD Thesis, *Columbia University*, 2011.

28. M. I. H. Mohideen, B. Xiao, P. S. Wheatley, A. C. McKinlay, Y. Li, A. M. Z. Slawin, D. W. Aldous, N. F. Cessford, T. Duren, X. B. Zhao, R. Gill, K. M. Thomas, J. M. Griffin, S. E. Ashbrook and R. E. Morris, *Nat. Chem.*, 2011, **3**, 304-310.

29. M. I. Mohideen, PhD Thesis, *University of St Andrews*, 2011.

30. M. I. Mohideen, P. K. Allan, D. Aldous, K. W. Chapman, J. A. Hriljac, E. Iglesia, S. I. Zones and R. E. Morris, *Manuscript in preparation.*

32. S. S. Y. Chui, S. M. F. Lo, J. P. H. Charmant, A. G. Orpen and I. D. Williams, *Science*, 1999, **283**, 1148-1150.

33. B. Xiao, P. J. Byrne, P. S. Wheatley, D. S. Wragg, X. Zhao, A. J. Fletcher, K. M. Thomas, L. Peters, J. S. O. Evans, J. E. Warren, W. Zhou and R. E. Morris, *Nat. Chem.*, 2009, **1**, 289-294.

34. L. Palatinus and G. Chapuis, *J. Appl. Crystallogr.*, 2007, **40**, 786-790.

8 Towards the use of MOFs for storage and release of hydrogen sulfide and carbon monoxide: the isostructural series M-CPO-27

8.1 Motivation

Carbon monoxide and hydrogen sulfide have been identified as signalling molecules in the body, and as such have vast therapeutic potential (see section 1.1). In order to harness this potential, it is necessary to have a method of dosing the gases. Dosing an appropriate amount of the gas is a challenge; too little is likely to be ineffective whilst too much of the gas can be toxic. With this in mind, dosing gases from a gas cylinder is not ideal. There are chemical methods of producing the gases after exposure to a stimulus, often contact with water, but the side products of these reactions frequently have their own biological effects which aren't necessarily beneficial. There are additional challenges relating to release rate as with many therapeutics; it is often the case that a slow release of the gas to the targeted area is preferable over a quick burst. Metal-organic frameworks have been reported to adsorb gasotransmitter molecules. Research in this area is most advanced for nitric oxide, where a number of zeolites and MOFs have been characterised for their nitric oxide adsorption and release.

8.1.1 The M-CPO-27 structure

The structure of the M-CPO-27 series has been described in section 4.2. The structural formula of the hydrated material is $[M_2(C_8O_6H_2)(H_2O)_2]\cdot 8H_2O$ where M = Co,[1] Ni,[2] Zn,[3-5] Mg,[6, 7] Mn[8] and Fe.[9, 10] The structure contains large one-dimensional pores running parallel to the c-axis which are filled with solvent molecules from the synthesis. The sixth coordination site of the metal ion is coordinated by a solvent molecule, usually water or methanol, from the synthesis. These can be removed by heating the material

under vacuum to leave a material with unsaturated metal sites which are high energy sites and have a considerable affinity for any guest molecules.

8.1.2 Previous work on the storage and release of gasotransmitter molecules by M-CPO-27

This M-CPO-27 series has been shown to store and reverse biologically active amounts of nitric oxide.[11] A detailed study of the nitric oxide adsorption, storage and release capacities of these materials was performed by Dr Alistair McKinlay and presented evidence for variation in the uptake and release of nitric oxide depending on the metal-ion which is incorporated into the material.[12] The release properties appear to be correlated with how easy it is to dehydrate the structure initially.

The adsorption of carbon monoxide by Ni-CPO-27 has been studied by Chavan *et. al.* who characterised the adsorption using a variety of spectroscopic techniques.[13] EXAFS data indicated that the CO was stored via an interaction of the CO with the coordination vacancy left subsequent to the removal of water during the activation process. A low pressure adsorption isotherm showed a CO uptake of approximately 0.88 molecules of CO per nickel centre characterised by a differential heat of adsorption of approximately 58 kJ mol^{-1}. Infrared data indicated that the material formed monocarbonyl Ni-CO adducts through the principally σ-donation from the CO molecule, with some contribution of π-back donation from the metal centre. To date no study has been reported for any other M-CPO-27 material with hydrogen sulfide.

8.2 Aims

This chapter aims to characterise the adsorption, storage and release of the biologically active gases hydrogen sulfide and carbon monoxide by the isostructural series M-CPO-27 to determine whether these materials are suitable for storage and release of these gases for medical applications. The link between the structure of a material and the gas adsorption properties will be studied by considering adsorption using complimentary physical and structural methods. The storage and release properties of the materials will be studied using gas adsorption isotherms and release measurements. Secondly, structural studies will be used to determine the nature of the H$_2$S-adduct of Ni-CPO-27.

8.3 Synthetic details

MOFs were synthesised according to literature procedures. Synthetic procedures, characterisation and references can be found in Appendix A.

8.4 Experimental details

8.4.1 Activation and H_2S-loading onto materials

Pellets weighing no more than 20 mg of M-CPO-27 were placed in glass vials and heated overnight under dynamic vacuum (1×10^{-3} Torr) using a Buchi furnace. Co-CPO-27 and Ni-CPO-27 were heated to 150 °C. Zn-CPO-27, Mn-CPO-27 and Mg-CPO-27 were heated to 150 °C for a period of 2 hours before heating at 200 °C overnight. The materials were cooled to room temperature and exposed to 1 atmosphere pressure of H_2S (99.5%, Air Liquide) for a period of 1 hour. The excess H_2S was removed under vacuum and the samples were flame sealed under argon.

8.4.2 H_2S release measurements

The release of H_2S from the material was monitored using a Columbus Instruments Model 180C Gas Sensor. The flow rate was set to 200 ml/min with a cell pressure of approximately 8.5 Torr. The sample of MOF was removed from the sealed glass vial and placed in a specially designed sample cell which allows air to be passed over the sample and directed into the detector where the concentration of H_2S in ppb was recorded.

8.4.3 H_2S adsorption measurements

The difficulties associated with hydrogen sulfide contamination on metal surfaces meant it was not possible to do the hydrogen sulfide isotherm on materials using the in-house gas adsorption apparatus. Instead, measurements were performed in collaboration with the group of Professor Guy De Weireld, Université de Mons, Belgium, using in house-built apparatus around a high-pressure magnetic suspension balance marketed by Rubotherm. This system can withstand pressure, temperature and corrosive operating conditions. Adsorption isotherm measurements were performed at 303.15 K for pressures from vacuum up to 1 atmosphere. The adsorbent sample was exposed to H_2S (99.8%, Praxair). The gas was introduced in a stepwise manner with equilibrium assumed when the variation of weight remained below 40 µg for 30 minutes.

The sample mass variation, m_{meas}, is measured as well as pressure and temperature when the thermodynamic equilibrium is reached. The buoyancy effect of the gas phase on the adsorbent volume V_{ads} is then corrected to determine the excess adsorbed mass, m_{exc} as:

$$m_{exc} = m_{meas} + \rho_{gas}.V_{ads}$$

where the gas phase density ρ_{gas} is determined using an appropriate equation of state. The adsorbent volume, V_{ads}, is evaluated from direct helium buoyancy effect measurement and helium density is determined using a modified Benedict-Webb-Rubin EOS[14]. The pressure is measured with two pressure transmitters (MKS Baratron for measurements up to 133.3 kPa and Endress-Hauser for measurements performed up to 10 MPa). The maximum measurement error on isotherm measurement is evaluated to be 0.5 % of adsorbed measured quantities with an interval of confidence of 95%. A Helmholtz type equation of state was used for buoyancy-effect correction.[15]

After the adsorption isotherm was complete the material was reactivated by heating the sample at 150 °C for 8 hours and an identical second isotherm was performed on the material.

8.4.4 Carbon monoxide adsorption isotherms

Carbon monoxide isotherms were determined for Ni- and Co-CPO-27 using an ASAP2020 Microporosity analyser. Before each reading, samples were evacuated under dynamic vacuum (1 x 10^{-5} Torr) and activated by heating the material to 150 °C for 12 hours.

Isotherms were taken in the pressure range of 0.01 kPa to 101.4 kPa at three temperatures for each sample; 0 °C, 10 °C and 20 °C Gas was dosed to the sample incrementally, with the mass taken after the system had reached equilibrium following each dose of gas before the next dose was applied. Once atmospheric pressure was reached, the desorption isotherm was recorded incrementally by removing gas from the system. At very low pressures during the desorption, equilibriums were reached very slowly. In this case, the system waited for 4 hours for the sample to reach equilibrium and if this did not happen then the adsorption of the sample after the timeout period was taken along with the next pressure point. The temperature was maintained using a flow of water and a water bath with thermostat. Once the isotherm had reached very

low ($<$ 0.2 kPa) pressure of CO, the sample was reactivated by evacuation and heating at 150 °C for 12 hours before the next isotherm was performed.

8.4.5 PXRD characterisation of Ni-CPO-27

Ground powder samples of Ni-CPO-27 were loaded into 0.5mm borosilicate capillaries. The capillary was heated to 150 ºC under dynamic vacuum overnight to dehydrate the sample, and then cooled to room temperature. To load hydrogen sulfide onto the material, capillaries were exposed to a 1 atmosphere pressure of hydrogen sulfide. The excess H_2S was removed under vacuum, and the capillaries were placed under an argon atmosphere then flame sealed. High resolution powder X-ray diffraction data were collected on beamline I11 at Diamond Light Source, Harwell, UK. Data were collected at room temperature using a monochromated X-ray beam of wavelength 0.827439(1) Å. Thirty minute data sets were collected for the angle range of 1-50º and binned to produce data with a step size of 0.001°.

8.4.6 PDF analysis of H_2S-Ni-CPO-27

PDF data were collected at beamline 11-ID-B at the Advanced Photon Source, Argonne National Laboratory, IL, USA. A sample of Ni-CPO-27 was carefully ground to ensure homogeneity and placed in a 1 inch Kapton polyimide capillary which was sealed with 3M Scotch-Weld epoxy adhesive at one end. The sample was heated to 150 °C under vacuum overnight using a Buchi furnace and Schlenk line and cooled to room temperature. For the dehydrated sample, the capillary was put under an argon atmosphere and the end of the capillary was sealed with glue. For the hydrogen sulfide-loaded sample, the sample was exposed to a 1 atmosphere pressure of hydrogen sulfide for a period of 1 hour before the excess hydrogen sulfide was removed from the Schlenk tube under vacuum. The samples were placed under an argon environment before being removed and isolated in the polyimide capillary using epoxy. The sample was placed in the sample changer at the station and collected using the procedure outlined in chapter 7.33.

8.4.7 Biological experiments

2mm pellets of Zn-CPO-27 which had been stored in a dry argon atmosphere for 9 months were placed 2mm from a pre-contracted (U46619; 10 nM) endothelium-intact ring of porcine coronary artery in a 10 ml organ bath (37ºC; filled with Krebs buffer solution). After relaxation was complete, the MOF was removed and the bathing solution

was fully replaced. The above procedure was performed with a H$_2$S-free MOF pellet as a control.

8.5 Hydrogen sulfide adsorption and release

8.5.1 Hydrogen sulfide release measurements

MOF-delivered hydrogen sulfide has two major potential targets with different delivery mechanisms. The first is topological contact, where the MOF is held above the skin, with contact with any physiological solution, and gas release is triggered by contact with moist atmosphere. In the second situation the MOF is in direct contact with a physiological solution such as blood. The release in both cases is characterised.

The hydrogen sulfide release measurements from samples of the isostructural series M-CPO-27 which were prepared and stored for 1 day under argon and shown in Figure 8-1. Ni-CPO-27 and Co-CPO-27 and Zn-CPO-27 release significant quantities of hydrogen sulfide. The lower delivery potential of the zinc material could be associated with difficulties fully activating the sample, as have been reported before, or the fact that zinc binds particularly strongly and irreversibly to sulfur.[3, 4] The other frameworks, Mn-CPO-27 and Mg-CPO-27 show low release quantities. This may be due to incomplete activation of the materials, as has been suggested for nitric oxide release.

For any such material to be used in a medical context, the 'shelf-life' of the material under hydrogen sulfide must be determined. To do this, samples of Ni-CPO-27 and Zn-CPO-27 were prepared and stored in vials under argon for a period of 6 months and 12 months respectively. The hydrogen sulfide release after this time was analysed and compared with the results from samples stored for 1 day (Figure 8-2). Both Ni-CPO-27 and Zn-CPO-27 show release of hydrogen sulfide after prolonged storage. However, the quantity released is reduced for both framework materials. PXRD analysis of the materials (Figure 8-3, Figure 8-4) reveals that Ni-CPO-27 shows only slight loss in crystallinity after hydrogen sulfide release after 6 months of storage indicating that this material is quite resilient to chemical erosion by hydrogen sulfide.

The Zn-CPO-27 material shows much greater degradation with prolonged storage. After hydrogen sulfide release after 1 day, the crystallinity of the compound is

maintained. After 1 year of storage, the PXRD (Figure 8-4) shows few sharp peaks in the pattern, especially at low angles where the pattern is dominated by broad intensity features characteristic of an amorphous material. This indicates that structure partially amorphised by prolonged exposure of hydrogen sulfide.

PDF analysis of the Zn-CPO-27 was used to determine the amorphous product (Figure 8-5). The PDF for the as synthesised material showed discrete peaks in positions analogous to the Ni-CPO-27 material. After storage for one year followed by release of the stored H_2S, the PDF of the material showed reduced long-range order ($R_{max} = 35$ Å compared to approximately 80 Å for the as synthesised material) accounting for the broad peaks in the PXRD. At low distances, features are found in the PDF with intense peaks at 2.33 Å and 3.80 Å. When these were compared to the PDF calculated for the structure of ZnS wurtzite structure these peaks matched well. This indicates that hydrogen sulfide breaks down the material by reaction at the metal site. Peaks corresponding to the C-C bonding in the linker group are still apparent in the PDF, showing that the linker is not attacked in the process of the framework degradation. The PDF obtained after storage of 6 months under a hydrogen sulfide atmosphere indicates mixed phase between Zn-CPO-27 and ZnS. A two phase refinement of the peaks between 1.7 and 2.6 Å estimates the phase fraction of the material as 0.62(2):0.38(2) ZnS:Zn-CPO-27 after 6 months. Despite the breakdown of the material over time, the material still releases a considerable amount of hydrogen sulfide, and as is detailed in section 8.7.1, this hydrogen sulfide is still biologically active.

The alternative possible release mechanism is to directly contact the material with an aqueous solution. In this situation the toxicology of the material itself is much important. Therefore this release was done using the Zn-CPO-27 material by collaborators from the Free Radical Research Facility. The material was blended with a small amount (10%) of PTFE binder. Figure 8-6 shows the electrochemical measurement of H_2S in direct contact with foetal calf serum. An increased current is detecting indicating that hydrogen sulfide has been released. An induction period of several minutes is observed before H_2S is measured. A similar result is seen in the biological testing (section 8.7) and so this is unlikely to be an artefact of the measurement. This is not seen in the experiments with moist atmospheres and further work needs to be completed to account for this and understand fully the release mechanism.
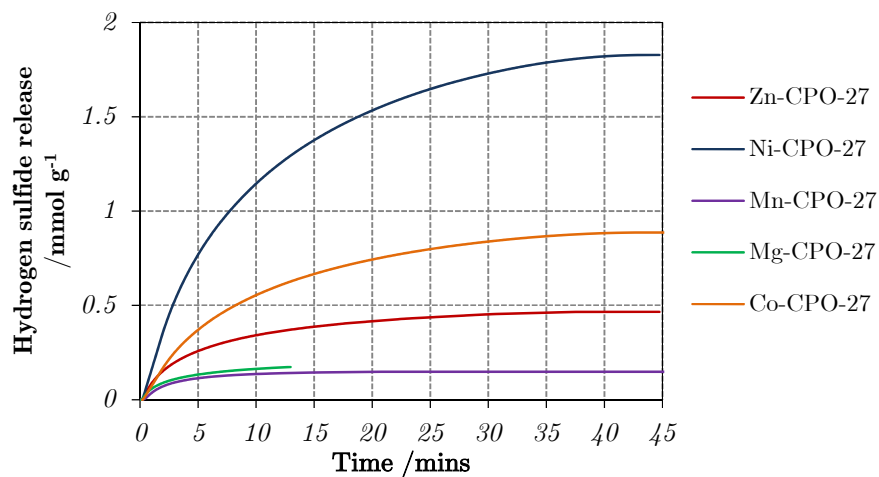
Figure 8-1: Release measurements for the M-CPO-27 isostructural series.
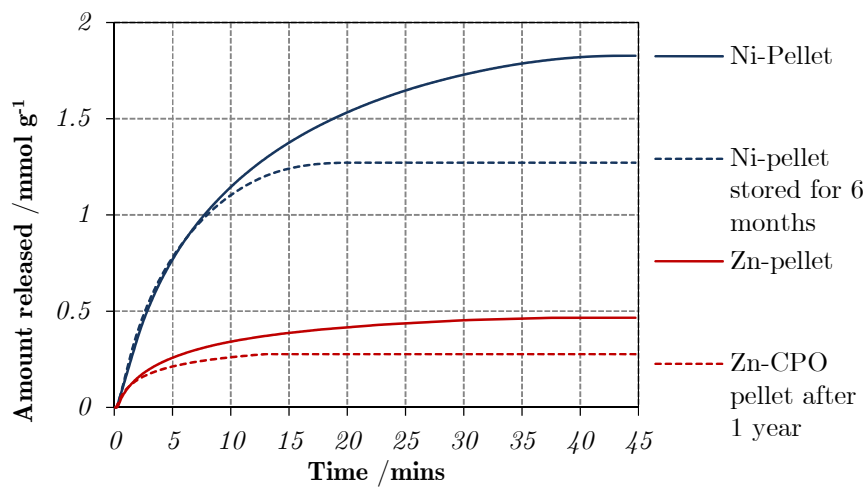

Figure 8-2: H$_2$S-release measurements for Ni-CPO-27 and Zn-CPO-27 after 1 day of storage under argon and prolonged storage under argon.
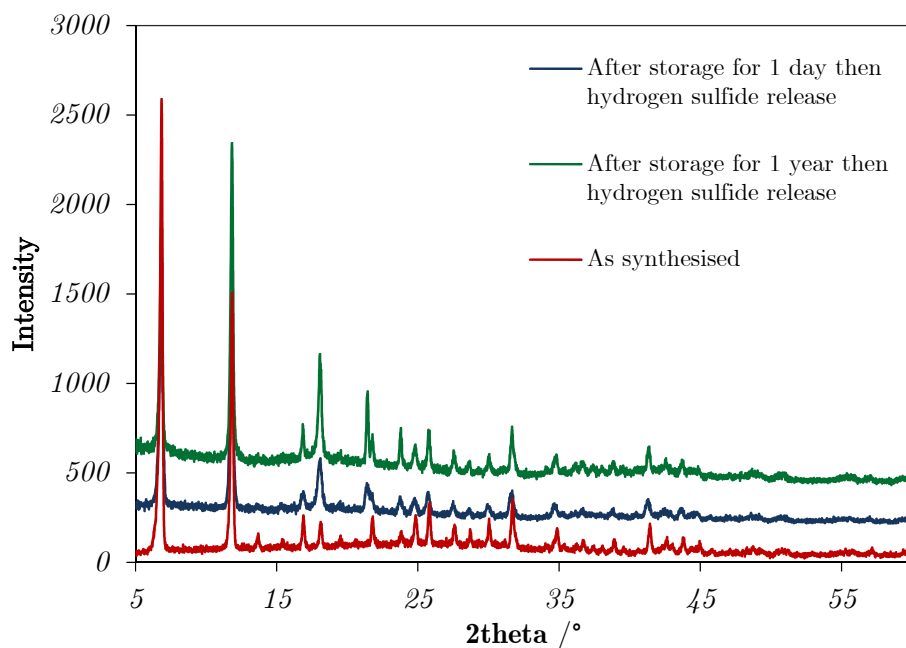
Figure 8-3: PXRD patterns for Ni-CPO-27 as synthesised (red), after H₂S release subsequent to storage for 1 day (blue) and 6 months (green). Plots are offset for clarity.
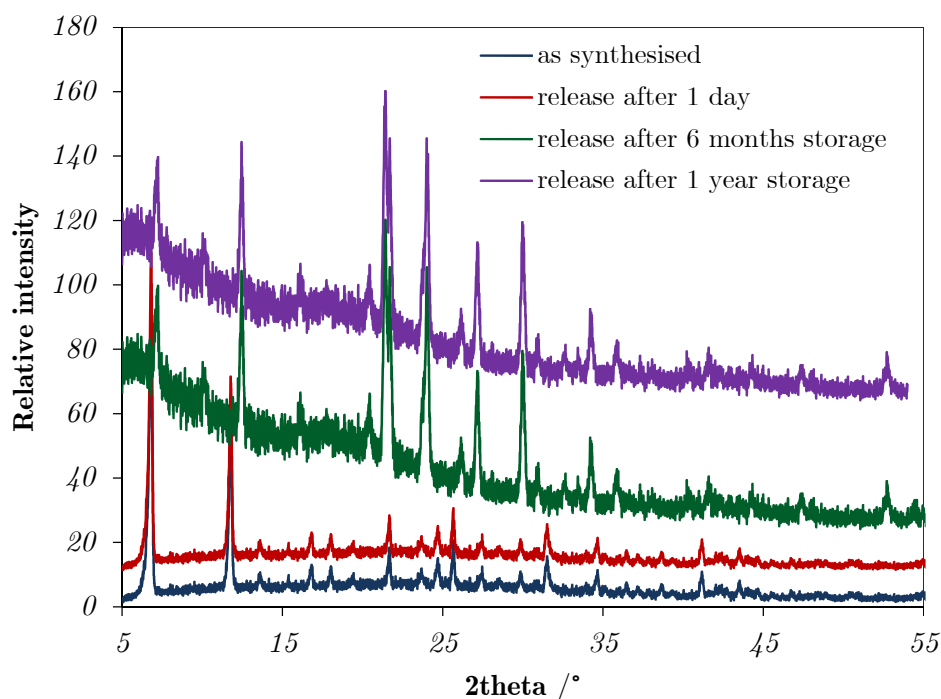

Figure 8-4: PXRD patterns for Zn-CPO-27 as synthesised (blue), after H₂S release after storage for 1 day (red), 6 months (green), and 1 year (purple). Plots are offset vertically for clarity.
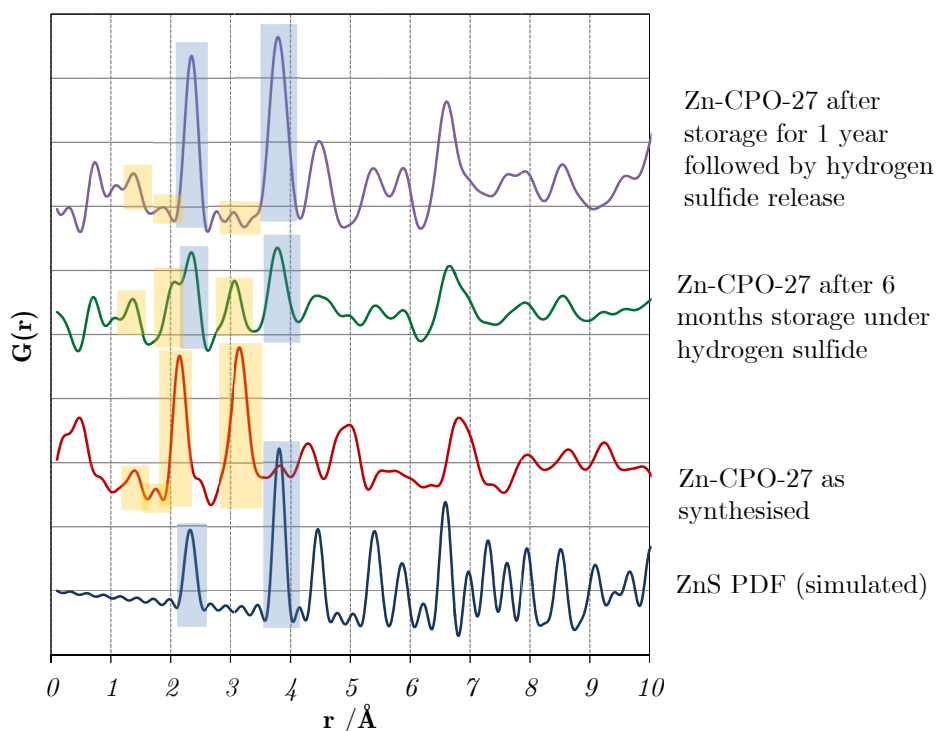
Figure 8-5: PDFs for the Zn-CPO-27 material as synthesised material and after storage for 1 year followed by H$_2$S release. Calculated PDFs for Zn-CPO-27 and ZnS (Wurtzite) are shown for comparison with experimental PDF peaks.
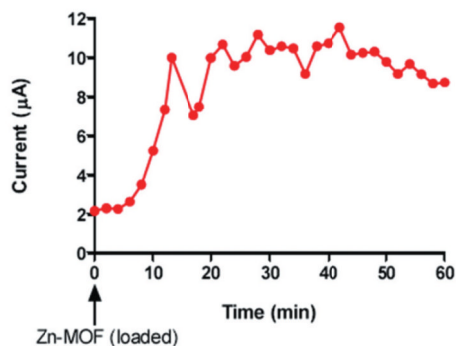
Figure 8-6: Release of H$_2$S from Zn-CPO-27, measured electrochemically in direct contact with a physiological solution (foetal calf serum).

8.5.2 Hydrogen sulfide isotherm on Ni-CPO-27

After initial release measurements were made on the materials, Ni-CPO-27 and Co-CPO-27 were chosen for further gas adsorption work. The hydrogen sulfide isotherms determined at 303.15 K are shown in Figure 8-7. Ni-CPO-27 adsorbs close to 12

264

millimoles of hydrogen sulfide per gram of material (mmol g^{-1}). Upon dosage of very low pressures of H$_2$S, there is a large uptake indicating a strong interaction between the material and H$_2$S, which is confirmed by the structural studies (see below). The amount adsorbed at very low pressures, around 6.2 mmol g^{-1}, is close to the 6.4 mmol g^{-1} adsorption expected when each metal centre interacts with one gas molecule via coordination to the unsaturated metal site left on dehydration of the material. This is the method of gas storage which has been reported for other gases in this material. The subsequent additional uptake of approximately 6 mmol g^{-1} of hydrogen sulfide can be attributed to physisorption within the pores.

After the adsorption was complete, the material was heated to 150 °C for 8 hours in order to remove the hydrogen sulfide from the framework. A repeat measurement shows a lower hydrogen sulfide uptake for the second adsorption at all pressures. The lower adsorption at low pressures of hydrogen sulfide (4.96 mmol g^{-1}) indicates that the outgassing process does not remove all of the gas adsorbed on the metal centres. These metal centres can be considered to be blocked and unavailable for adsorption. Lower adsorption at higher pressures could also indicate that some of the pores are blocked, making it impossible to get as much gas into the pores.

An adsorption isotherm for the Co-CPO-27 material was also attempted. Initial, low pressure points indicate adsorption of a comparable amount of hydrogen sulfide, 5.58 mmol g^{-1} adsorbed at 6.25 kPa pressure of hydrogen sulfide. Co-CPO-27 shows a much slower uptake of hydrogen sulfide at lower pressures. In fact, not all points of the isotherm were completed on this material because of the extended periods that the material was taking to equilibrate after every reading ($>$ 24 hours).
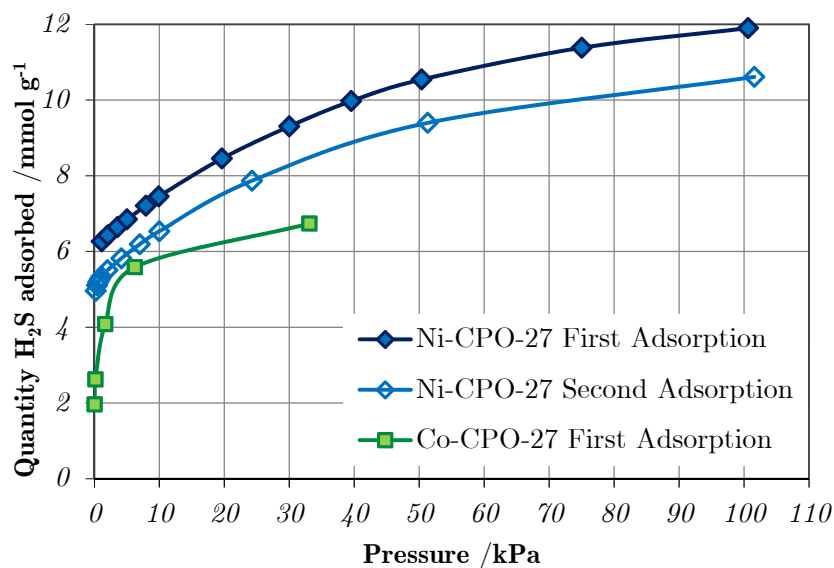
Figure 8-7: Hydrogen-sulfide adsorption isotherm for Ni-CPO-27.

8.6 The structure of the H₂S-adduct of Ni-CPO-27

In order to understand the properties of the H₂S-loaded materials it is important to probe the structural features of the material; to allow determination of how and where the gas interacts with the framework. The structure of the H₂S-adduct of Ni-CPO-27 was studied by a combination of Bragg and pair distribution function methods.

PXRD patterns for the hydrated, dehydrated and hydrogen sulfide-loaded frameworks are shown in Figure 8-8. There are significant differences between all three forms of the materials; changes in peak positions indicate that the unit cell parameters vary. Additionally, variation in peak intensity indicates structural differences between the materials.

The Rietveld refinement for the hydrated and dehydrated material are described in section 7.4 and the CIF file for the final structure can be found in Appendix E. The refinement of the hydrogen sulfide-loaded data set was based on the dehydrated crystal structure of Co-CPO-27 from single-crystal X-ray diffraction. Initially scale factor, zero point and lattice parameters were refined, followed by peak profile and finally atomic coordinates for the nickel and oxygen atoms were refined until stable and no further refinement cycles improved the fit to the data. The refinement converged without

restraints, and difference Fourier maps were produced. Using the Fourier search function of GSAS, a residual electron density peak (Q-peak) of height 3.418 electrons/Å^3 was determined at the position 0.0180, 0.3003, 0.6862. This was assigned to be the sulfur from the hydrogen sulfide. The position and occupancy of this atom was refined. The sulfur showed an occupancy of 0.910(5). The Ni-S bond length determined from the refinement was 2.5896(1)Å. This bond length is significantly longer than the Ni-O(water) bond length which is found in the hydrated form of the material (2.0813(17) Å) but consistent with the Ni-S bond length determined in hydrogen sulfide-loaded nickel zeolites.[16] This indicates this site in the material is occupied by hydrogen sulfide rather than water. Furthermore, assignment of the peak as oxygen from water results in an occupancy on the site which is greater than one, meaning that the atom which occupies this site in the material is heavier than oxygen. Anisotropic refinement of the displacement parameters of the sulfur showed no elongation towards the metal centre, indicating that there is no shared occupancy of the site with the water molecule.

The determined structure of the hydrogen sulfide-loaded material is shown in Figure 8-10. The asymmetric unit of the H_2S-adduct is shown in Figure 8-11. The analysis indicates that the H_2S is coordinated to the metal at a coordinatively unsaturated site (CUS) left after dehydration, leaving the Ni-atom in distorted octahedral geometry. The occupancy of 0.910(3) is consistent with the 1:1 correlation between uptake and site availability, consistent with the adsorption isotherm at low pressure. The small variation from the adsorption isotherm could be due to experimental procedure; it is possible that when the sample was being prepared, the remaining 9% of the bound hydrogen sulfide was removed under vacuum. No further Fourier peaks of significance were located in the channels, the largest Q-peaks left after H_2S assignment are at positions 0,0,0 and therefore likely to be a product of Fourier errors, indicating that there is little ordered physisorbed gas in the sample. Most physisorbed gas is weakly held in the material and therefore most likely to be removed from the framework when the sample was placed under vacuum prior to sealing (especially when, as noted above, some of the strongly held hydrogen sulfide was also removed under this vacuum). Any which remains is expected to be disordered throughout the pore of the material, and therefore unlikely to be located using a Fourier difference map.
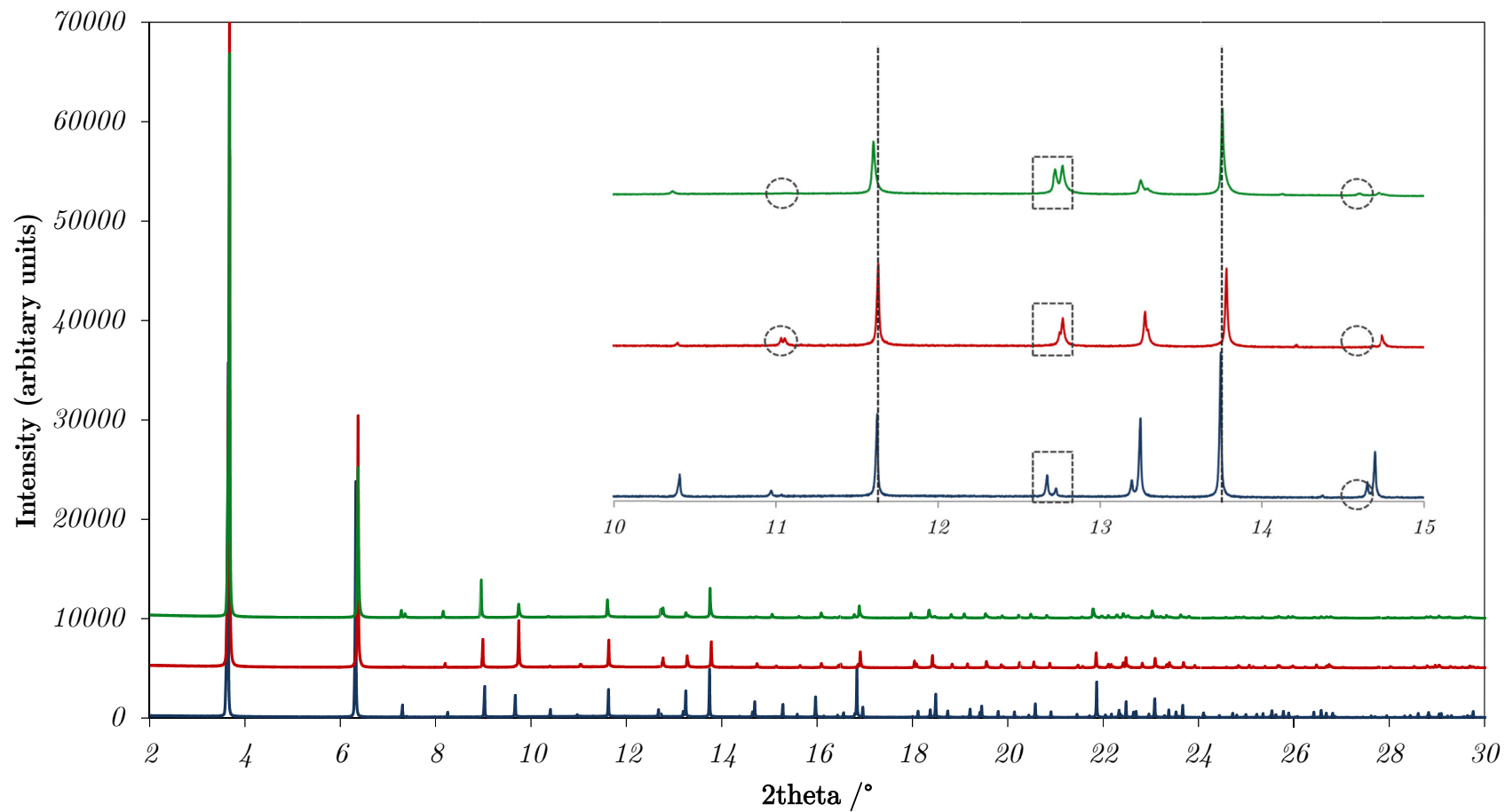
Figure 8-8: PXRD data for the hydrated (blue), dehydrated (red), and hydrogen sulfide-loaded (green) samples with 5000 intensity unit offset between the data sets. Inset shows region between 10° and 15° annotated to show distinct differences between the patterns. Dashed vertical lines highlight the change in peak positions between patterns. Circles indicate peaks which are present in one pattern but not another. Square boxes indicate change in peak intensity between patterns.
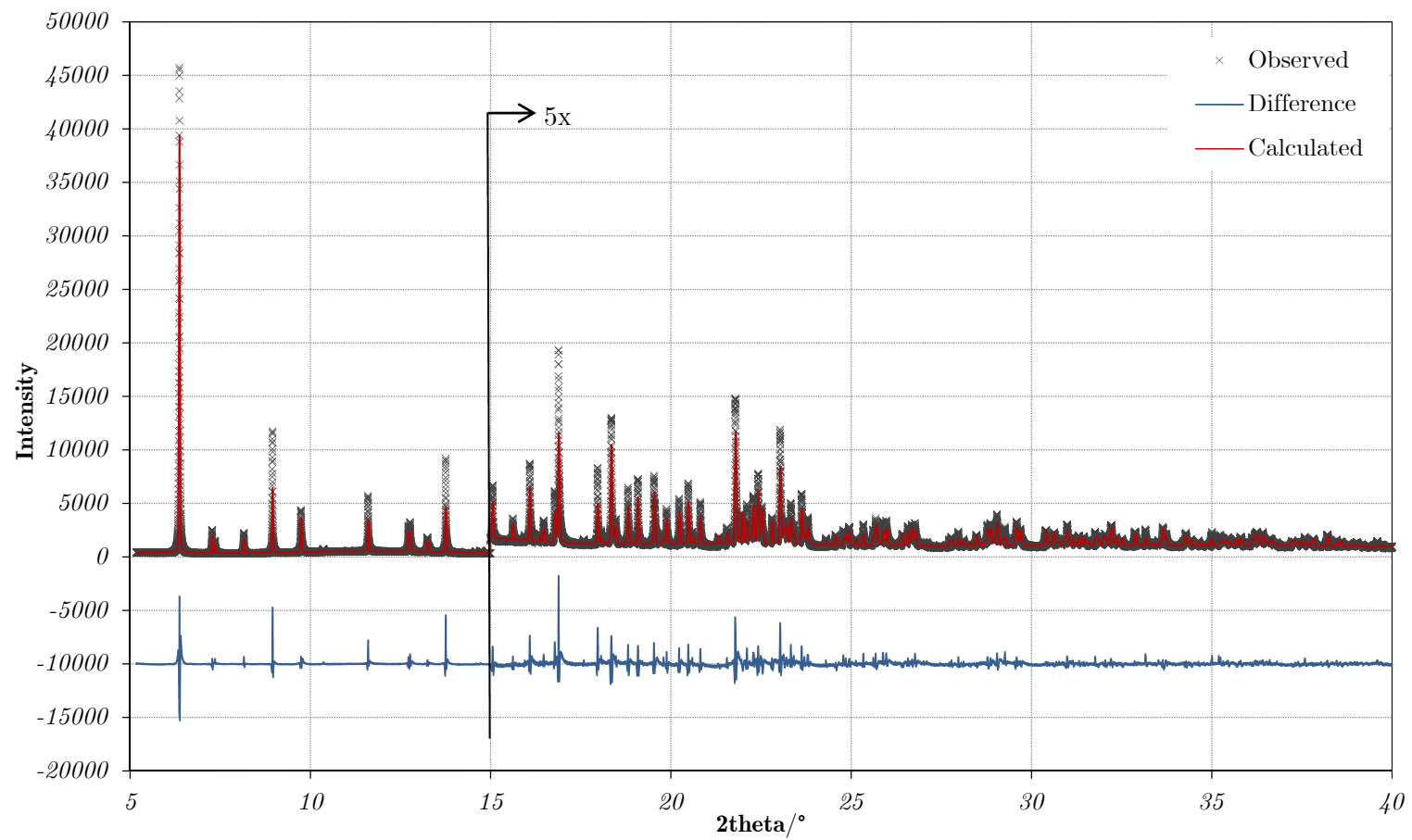
Figure 8-9: Plot of Rietveld refinement for H₂S-Ni-CPO-27. Data above 15° is amplified by a factor of 5.
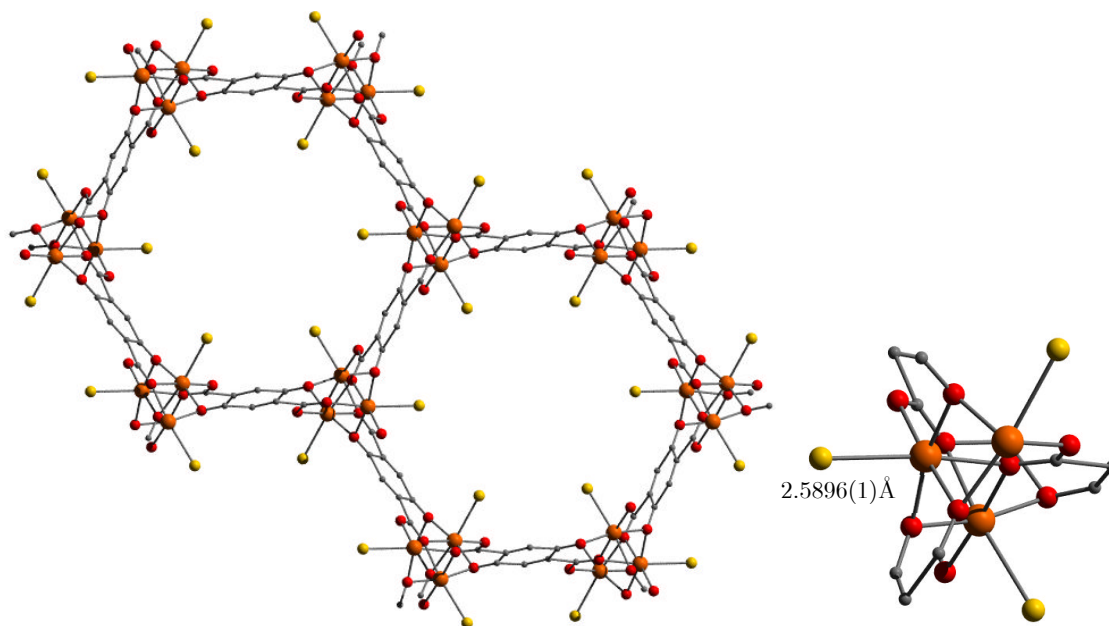
Figure 8-10: Structure of hydrogen sulfide-adduct of Ni-CPO-27 (left), Ni-coordination by hydrogen sulfide molecule (right). Carbon = grey, oxygen = red, nickel = orange, sulfur = yellow. Hydrogens on the ligand are not shown for clarity.
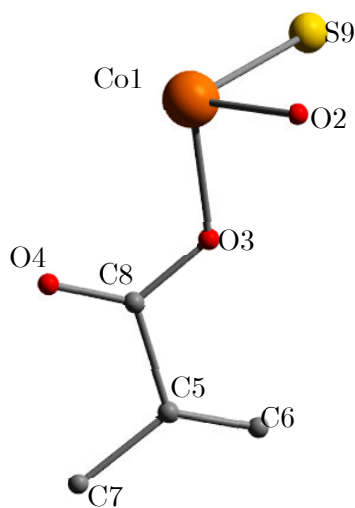

Figure 8-11: Asymmetric unit of H₂S-Ni-CPO-27.

Table 1: Details of the Rietveld refinement of hydrogen sulfide-loaded Ni-CPO−27 against synchrotron X-ray data ($\lambda = 0.827439(1)$Å)

	H₂S-loaded
a /Å	25.75145 (8)
c /Å	6.80532 (4)
V /Å³	3908.25 (2)
T /K	295
Space group	R-3
R$_w$	0.093
R$_{wp}$	0.123
R$_{exp}$	0.048
2θ range	5.01-70

Table 2: Final refinement parameters and atomic coordinates for H₂S-Ni-CPO-27.

Atom	S.O.F.	x/a	y/b	z/c	U [Å²]
Ni1	1	0.36548 (7)	0.04910 (8)	0.0179 (2)	0.03293
O2	1	0.3081 (3)	0.0558 (3)	−0.1618 (11)	0.017 (2)*
O3	1	0.3623 (3)	0.1038 (3)	−0.7713 (11)	0.031 (3)*
O4	1	0.3423 (3)	0.0400 (3)	−0.5257 (11)	0.029 (3)*
C5	1	0.3411 (5)	0.1312 (6)	−0.4555 (17)	0.015 (4)*
C6	1	0.3515 (5)	0.1806 (7)	−0.5272 (15)	0.020 (4)*
C8	1	0.3194 (5)	0.1037 (6)	−0.250 (2)	0.049 (5)*
C9	1	0.3491 (6)	0.0856 (6)	−0.5934 (17)	0.045 (5)*
S1	0.910(5)	0.01489 (18)	0.2075 (2)	0.5531 (6)	0.114 (3)*

Atom	U₁₁	U₂₂	U₃₃	U₁₂	U₁₃	U₂₃
Ni1	0.0449 (16)	0.0455 (15)	0.0089 (8)	0.0231 (16)	0.0035 (14)	−0.0005 (15)

The PDF for the dehydrated and hydrogen-sulfide loaded materials are shown in Figure 8-12. A discussion about the peak assignment in a PDF from the M-CPO-27 series is given in section 7.4. The PDFs for the dehydrated and hydrogen sulfide-loaded

materials are very similar, indicating that the main framework structure is similar, but some differences are evident. These differences are highlighted by the calculation of an experimental differential PDF (dPDF) (red line, Figure 8-12). This is calculated by subtracting the PDF for the dehydrated material from the PDF for the H_2S-loaded sample. The resulting differential curve was normalised over ripples arising from the difference in scattering power of the samples (section 6.4.6.1).

Peaks in the differential PDF arise from atom-atom distances in one material which are not present in the other material. In this case, positive peaks correspond to atom-atom distances which are present in the hydrogen sulfide-loaded material but not in the dehydrated form of the material. The only addition to the material is hydrogen sulfide gas, therefore peaks in the differential PDF are due to the interaction of the guest gas molecules with the framework.[i] Peaks in the dPDF therefore correspond to the correlations between H_2S gas and the framework, thus elucidating gas adsorption sites in the structure.

The experimental dPDF for the hydrogen sulfide-loaded system shows a sharp peak between 2.5 and 3 Å. Well-defined features such as this are indicative of a directional bonding interaction of gas molecules with the framework, rather than weakly held physisorption. A Gaussian curve was fitted to this peak using the program Fityk[19] and gave a peak maxima of 2.57(4) Å (Figure 8-13). This bond length is typical of Ni-S bonds reported in other framework materials.[16-18] This is slightly shorter than the bond length determined by Rietveld analysis.

A theoretical partial PDF for the interaction of the hydrogen sulfide gas with the framework was calculated using the model from PXRD analysis. The contribution of the hydrogen sulfide to the PDF was calculated in the range of 1 to 20 Å using PDFGui by summing interactions between the sulfur atom and all other atoms.[20] All atomic displacement parameters in the initial model were set to 0.005 Å^3. The theoretical dPDF is shown in Figure 8-12 on top of the experimental dPDF. The calculated dPDF modelling the interaction of the sulfur atom with the framework models the feature at 2.5 Å well, indicating that the Ni-S binding interaction is likely to be the principle

---

[i] This is assuming that there is not a significant change in framework-framework interactions resulting from gas adsorption which would be the case in flexible or breathing MOFs. Several studies have reported the skeleton framework of M-CPO-27 to be rigid on the adsorption of gases.

interaction responsible for gas storage in this material. The features at longer distances are also modelled well.

No other sharp peaks are visible in the experimental dPDF. There is no sharp peak observed at 2.1 Å, which is the expected distance for a Ni-O(w) bond length, indicating that there is no residual water in the material. Additionally, there does not appear to be any additional physisorbed gas molecules in *ordered* positions in the pore. Any additional gas molecules must therefore be disordered throughout the pore. The differences between the experimental and theoretical differential curves can be associated with subtle changes in the framework which occur on gas adsorption, particularly associated with the minor contributions from the gas physisorbed within the pore.

The position of the intense peaks show little change, indicating there is little change in the unit cell between the hydrated and hydrogen sulfide-loaded material. This is not unexpected as unit cell parameters show greatest change when the physisorbed gas is removed from the pores.[3]

8.6.1   The complementary nature of the two experimental methods

Here, the Rietveld and PDF analyses have used the same experimental information – the scattered intensity from a powder sample - and processed and analysed it in different ways to obtain structural information. Rietveld analysis subtracts non-Bragg scattering as background and fits the structural model in reciprocal space to consider the long-range order in the material. In contrast, PDF analysis uses all the coherent scattering intensity in real space and considers the local structure of the material. The agreement of the two methods is a form of validation for the structure solution, and differences highlight any areas where the local structure of the material may differ from the average structure. This combined Rietveld and PDF analysis has shown that hydrogen sulfide is adsorbed in the material Ni-CPO-27 via coordination to the coordinatively unsaturated nickel sites in the material. Both methods indicate that there is an interaction between the metal site and the hydrogen sulfide, with a Ni-S bond length of around 2.58 Å, though slightly different bond lengths are calculated by the two methods.
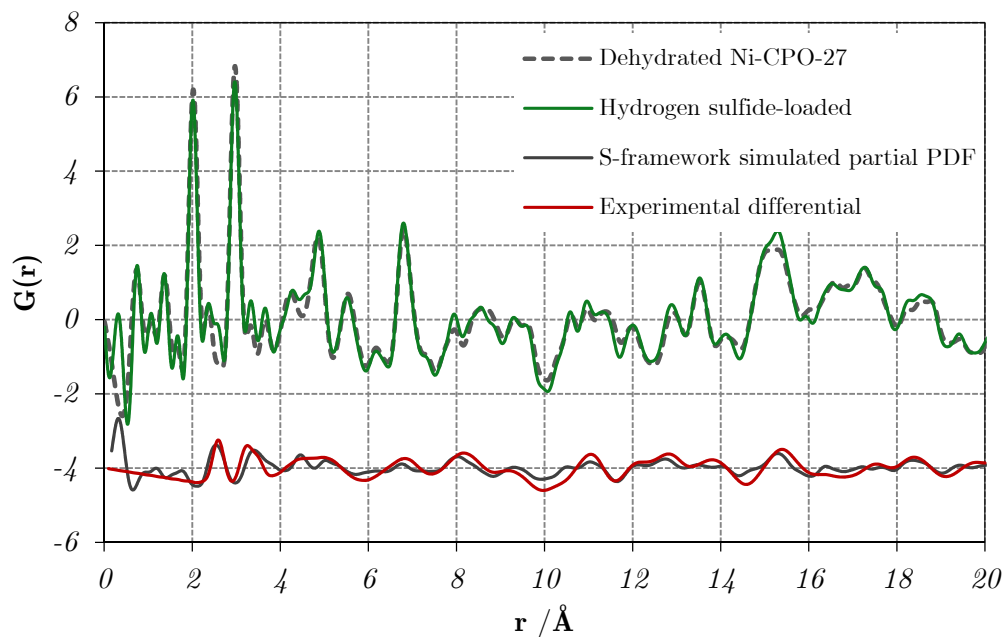
Figure 8-12: PDFs for the dehydrated (grey, dashed) and hydrogen sulfide-loaded (green) material with differential PDF underneath shown in grey. The differential PDF ($G(r)_{H2S}$ − $G(r)_{dehyd}$) is shown in grey. The theoretical S-framework partial PDF calculated from the model from Rietveld analysis is shown in red.

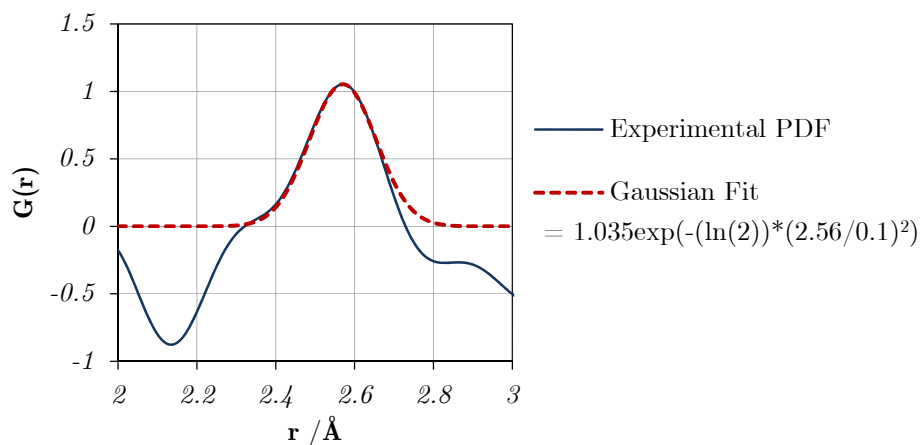**Figure 8-13: Gaussian fit of the peak at 2.5 Å.**

8.7 Preliminary biological experiments using H$_2$S-Zn-CPO-27

Preliminary biological experiments involving the H$_2$S were done via a collaboration with Professor Ian L. Megson from the Free Radical Research Facility, UHI Millennium Institute, Inverness. An investigation was carried out to investigate the vasodilatory behaviour of the hydrogen sulfide released from M-CPO-27.

8.7.1 Results

Placement of the H$_2$S-loaded Zn-CPO-27 near the porcine artery resulted in a substantial (39%) relaxation of the artery, shown in Figure 8-14. There was an induction period of 5 minutes, something which is not seen in similar reported experiments using nitric oxide as the vasodilator.[11] The relaxation was complete after approximately 15 minutes. After removal of the MOF and complete replacement of the bathing solution reversed the relaxation. Control experiments using H$_2$S-free MOF failed to cause any relaxation. This is a preliminary result but conclusively shows that the H$_2$S released from the MOF is biologically active with respect to vascular relaxation.
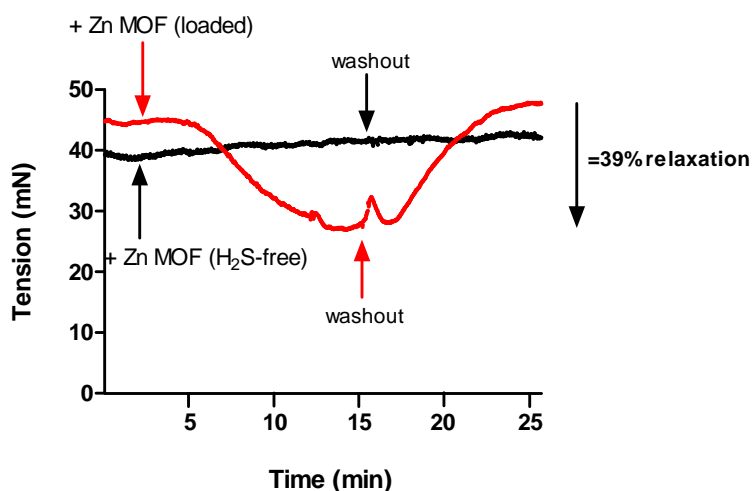

Figure 8-14: Vasodilatory behaviour of Zn-CPO-27.

8.8 Carbon monoxide adsorption and release

8.8.1 Carbon monoxide isotherms on Co-CPO-27 and Ni-CPO-27

Figure 8-15 shows isotherms for the carbon monoxide adsorption for Ni-CPO-27 (top) and Co-CPO-27 (bottom). Isotherms show that both materials adsorb significant amounts of carbon monoxide at all three temperatures. The inset of the graph in Figure 8-15 shows the isotherms at very low pressures of carbon monoxide.

Ni-CPO-27 shows a type I isotherm with respect to carbon monoxide, characteristic of a microporous material. The total adsorption of carbon monoxide at atmospheric pressure is very similar at all temperatures and the isotherms are almost completely reversible down to very low pressures of carbon monoxide. This means that the material does not hold onto the gas strongly, as no stimuli such as vacuum or heat are necessary to remove the gas from the surface. For data points taken at 1 kPa of carbon monoxide pressure the desorption slows down considerably with equilibration taking longer than 4 hours so that the time-out function on the adsorption equipment is used as explained above. This indicates that the carbon monoxide cannot be removed from the surface of the material below these pressures. The isotherms were terminated when it became clear that further evacuation would have little effect. At a desorption pressure of 0.2 kPa, the adsorbed masses of carbon monoxide on Ni-CO-27 were approximately 2.3 mmol g^{-1} at 20 °C, 2.6 mmol g^{-1} at 10 °C , and 3.7 mmol g^{-1} at 0 °C. These results indicate that some amount of carbon monoxide remains in the structure even down to low pressures. The lack of significant hysteresis in this material indicates that Ni-CPO-27 is not ideal for the storage and release of carbon monoxide. The calculated heat of adsorption for CO on Ni-CPO-27 is approximately 40 kJ mol^{-1} (Figure 8-16). This is lower than the value reported by microcalorimetry, but similar within experimental error.[13]

Co-CPO-27 also adsorbs a significant amount of CO. The uptake of CO by Co-CPO-27 is lower than that of Ni-CPO-27. This could be due to the lower surface area of the Co-CPO-27 sample (Appendix A). Co-CPO-27 shows a degree of hysteresis which is indicative of chemically adsorbed CO on the unsaturated metal ion sites. At very low pressures of CO this isotherm is reversible meaning that the carbon monoxide is almost entirely removed from the material.
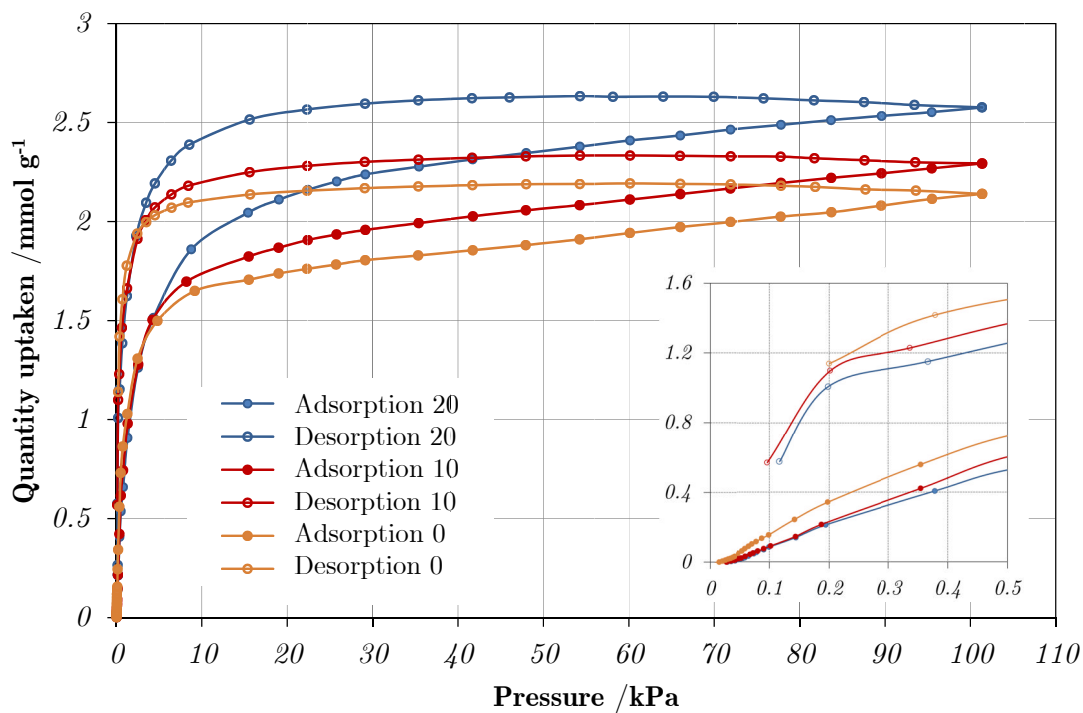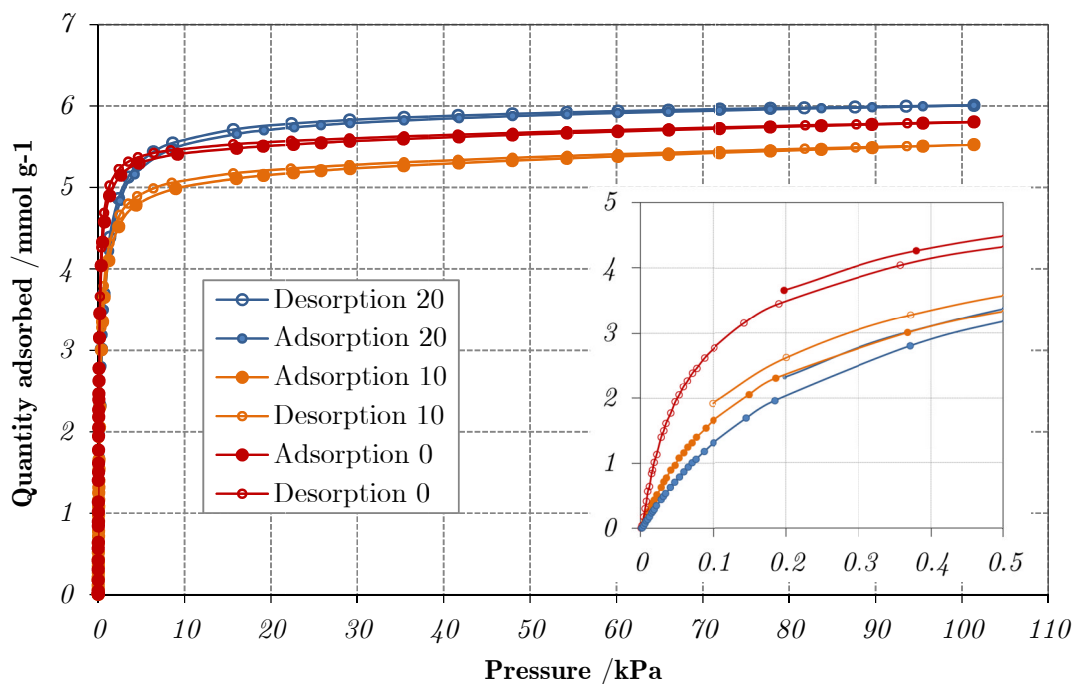
Figure 8-15: CO isotherms for Ni-CPO-27 (top) and Co-CPO-27 (bottom). Insets show the isotherms at very low carbon monoxide pressures.
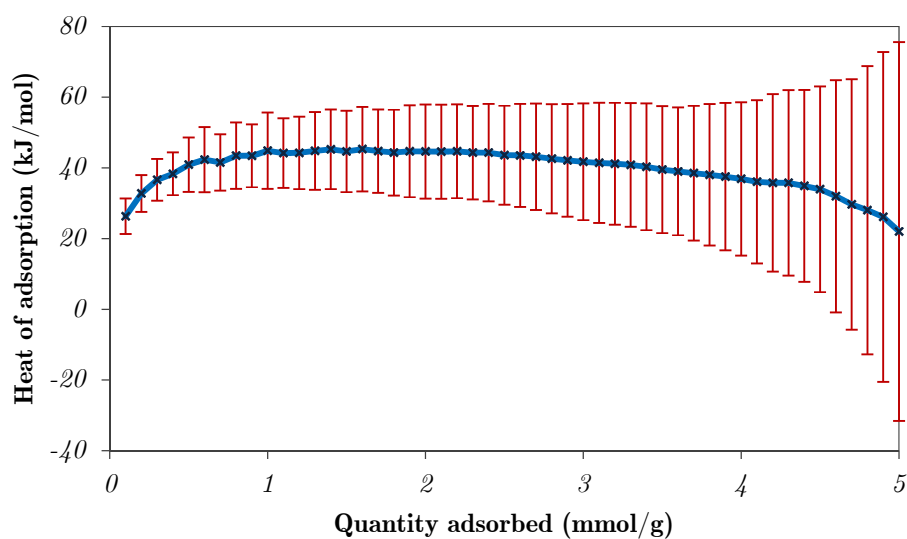
Figure 8-16: Heat of adsorption for Ni-CPO-27

8.8.2   Carbon monoxide release measurements

Carbon monoxide release measurements were performed for Ni-CPO-27 and Co-CPO-27, shown in Figure 8-17. Both materials showed release of carbon monoxide over a short timescale – release was complete after 10 minutes. PXRD patterns of the materials indicate that the structure is not degraded by the storage and release of carbon monoxide (Figure 8-18). Neither material releases the full amount of carbon monoxide which is adsorbed into the material. This could be because the material holds onto the gas too strongly, or because some of the carbon monoxide is removed in the experimental preparation.
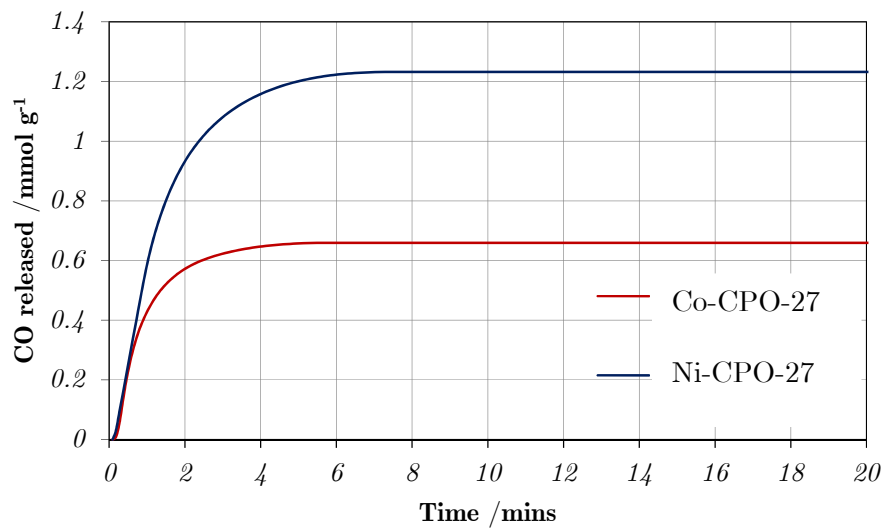
Figure 8-17: Carbon monoxide release measurements for Ni-CPO-27 and Co-CPO-27.
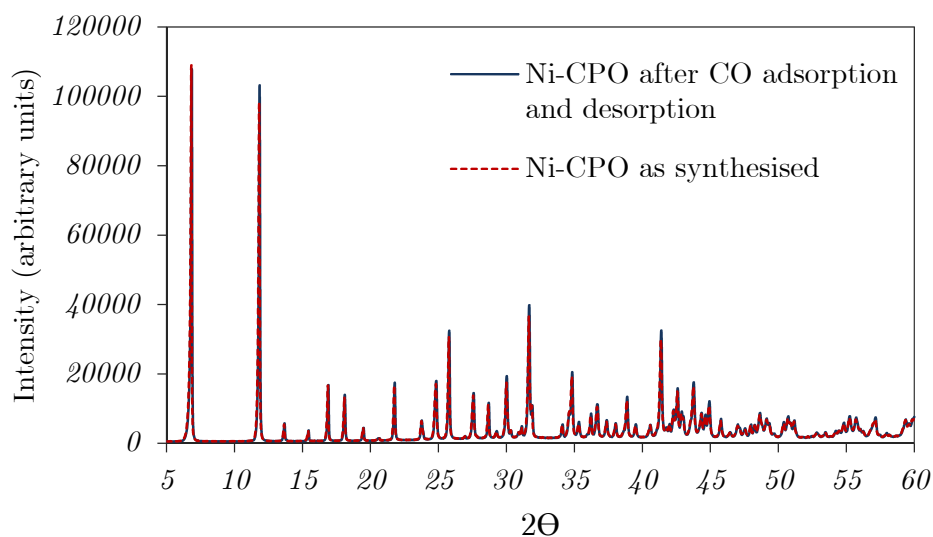

Figure 8-18: PXRD patterns for Ni-CPO-27 before and after CO release. The two traces are difficult to resolve due to their large similarities.

8.9 Discussion and conclusions

Here, we have shown the adsorption and release of hydrogen sulfide from the isostructural series of frameworks M-CPO-27. For H_2S, a 1:1 metal:gas interaction ratio gives a theoretical chemical adsorption of 6.4 mmol g^{-1} for the material. The H_2S isotherm of Ni-CPO-27 shows a sharp uptake of 6.26 mmol g^{-1} at low very pressures, which indicates that the interaction between hydrogen sulfide and nickel is strong - on par with a weak chemical bond. Structural information from powder X-ray diffraction and pair distribution function analysis indicates that the sulfur coordinates to the nickel with a Ni-S distance of approximately 2.58 Å, also indicating a bonding interaction. The 1:1 Ni-H_2S ratio determined by structural studies correlates well with adsorption at low pressures.

Despite the aggressive chemical nature of H2S in regards to metallic materials, the frameworks of both Ni-CPO-27 and Zn-CPO-27 are versatile to hydrogen sulfide storage and release. Comparison of the adsorption and release measurements for Ni-CPO-27 indicates that the chemisorbed component of the gas is incompletely released by exposure to moisture. Ni-CPO-27 shows little degradation on prolonged storage with stored H_2S indicating that this material may function well as a storage medium for the gas. In the same conditions, Zn-CPO-27 shows degradation into amorphous ZnS over the period of a year. Whilst, the hydrogen sulfide released from this material is still biologically active, the material is not ideal for storage over prolonged periods of time.

This work showed that the hydrogen sulfide release from M-CPO-27 is affected by the nature of the metal. Further work is required in this area to elucidate the relationship between metal-ion and hydrogen sulfide adsorption and release capacity through further adsorption and release measurements. Additional structural studies on the nature of H_2S-binding to the materials could help elucidate this relationship. The effect of surface area on adsorption could also be a factor in determining the quantity of gas release from the material, and this could be a useful area for further studies. Whilst, Zn-CPO-27 is non-toxic and therefore good for biological studies, Mg-CPO-27 would be ideal for biological applications. Further work could concentrate in developing this material for hydrogen sulfide release.

Preliminary biological experiments have been completed and indicate that MOF-delivered hydrogen sulfide has the expected vasodilatory effect, indicating that metal-organic frameworks could be an exciting potential delivery method for H_2S. More in depth studies would be needed to determine the reasons for this effect and to further fully ascertain how effective the hydrogen sulfide is as a vasodilator in a variety of conditions.

Initial studies indicate that a significant amount of carbon monoxide can be adsorbed by both Ni- and Co-CPO-27. Ni-CPO-27 isotherms show almost complete reversibility indicating that this material is unlikely to store significant amounts of carbon monoxide. This is further evidenced by release measurements. Co-CPO-27 shows some hysteresis, indicating that this material may be more suited to the storage of this gas. The apparent metal-dependant behaviour of the CO-adsorption is an interesting avenue for development. Whether MOF-delivered CO shows biological effects is currently being investigated.

8.10 References

1.   P. D. C. Dietzel, Y. Morita, R. Blom and H. Fjellvag, *Angew. Chem., Int. Ed.*, 2005, **44**, 6354-6358.

2.   P. D. C. Dietzel, B. Panella, M. Hirscher, R. Blom and H. Fjellvag, *Chem. Comm.*, 2006, 959-961.

3.   P. D. C. Dietzel, R. E. Johnsen, R. Blom and H. Fjellvag, *Chem. A. Eur. J.*, 2008, **14**, 2389-2397.

4.   N. L. Rosi, J. Kim, M. Eddaoudi, B. Chen, M. O'Keeffe and O. M. Yaghi, *J. Am. Chem. Soc.*, 2005, **127**, 1504-1518.

5.   J. L. C. Rowsell and O. M. Yaghi, *J. Am. Chem. Soc.*, 2006, **128**, 1304-1315.

6.   P. D. C. Dietzel, R. Blom and H. Fjellvåg, *Eur. J. Inorg. Chem.*, 2008, **2008**, 3624-3632.

7.   S. R. Caskey, A. G. Wong-Foy and A. J. Matzger, *J. Am. Chem. Soc.*, 2008, **130**, 10870-10871.

8. W. Zhou, H. Wu and T. Yildirim, *J. Am. Chem. Soc.*, 2008, **130**, 15268-15269.

9. E. D. Bloch, L. J. Murray, W. L. Queen, S. Chavan, S. N. Maximoff, J. P. Bigi, R. Krishna, V. K. Peterson, F. Grandjean, G. J. Long, B. Smit, S. Bordiga, C. M. Brown and J. R. Long, *J. Am. Chem. Soc.*, 2011, **133**, 14814-14822.

10. S. Bhattacharjee, J. S. Choi, S. T. Yang, S. B. Choi, J. Kim and W. S. Ahn, *J. Nanosci. Nanotechnol.*, 2010, **10**, 135-141.

11. A. C. McKinlay, B. Xiao, D. S. Wragg, P. S. Wheatley, I. L. Megson and R. E. Morris, *J. Am. Chem. Soc.*, 2008, **130**, 10440-10444.

12. A. C. McKinlay, PhD thesis, *University of St Andrews*, 2010.

13. S. Chavan, J. G. Vitillo, E. Groppo, F. Bonino, C. Lamberti, P. D. C. Dietzel and S. Bordiga, *J. Phys. Chem. C*, 2009, **113**, 3292-3299.

14. R. D. McCarthy and V. D. Arp, *Advances in cryogenic engineering*, New York : Plenum, 1960-, 1990.

15. E. W. Lemmon and R. Span, *J. Chem. Eng. Data*, 2006, **51**, 785-850.

16. Y. H. Yeom, Y. Kim and K. Seff, *J. Phys. Chem.*, 1996, **100**, 8373-8377.

17. Y. H. Yeom, Y. Kim, Y. W. Han and K. Seff, *Zeolites*, 1996, **17**, 495-500.

18. M. N. Bae, M. K. Song, Y. Kim and K. Seff, *Microporous Mesoporous Mat.*, 2003, **63**, 21-31.

19. M. Wojdyr, *J. Appl. Crystallogr.*, 2010, **43**, 1126-1128.

20. C. L. Farrow, P. Juhas, J. W. Liu, D. Bryndin, E. S. Bozin, J. Bloch, T. Proffen and S. J. L. Billinge, *J. Phys.: Condens. Matter*, 2007, **19**, -.

9 General implications and future directions

The main objective of this thesis was to gain a greater understanding of the way in which nitric oxide, carbon monoxide and hydrogen sulfide interact with metal-organic frameworks and to determine the potential of these frameworks as a delivery device for these gases in biological applications.

Structural studies have highlighted the role of co-coordinatively unsaturated sites in the adsorption of these gases, similar to that reported for other gases. Chapter 4 reported a high quality single-crystal structure for the nitric oxide adduct of Co-CPO-27 where nitric oxide chemisorbs to the metal centre in a bent conformation, improving the models suggested by McKinlay *et al.* and Byrne. A combined Bragg and total scattering study of the mechanism of gas adsorption in the Cu-SIP-3 framework suggested that coordination of nitric oxide to the open metal sites in the framework was responsible for the gas-uptake and selectivity. Chapter 8 reported an analysis of the structure of the hydrogen sulfide-adduct of Ni-CPO-27 which characterised the primary adsorption site as the open-metal sites on the nickel, analogous to the mechanism of nitric oxide adsorption. In conjunction with adsorption isotherms, the adsorption characteristics of the material can be rationalised. Structural evidence for the importance of CUSs indicates that future work on MOFs for storage and release of gasotransmitters should concentrate on the design and use of frameworks which feature co-coordinatively unsaturated sites on metal ions.

Hydrogen sulfide release from the M-CPO-27 frameworks was characterised and found to be dependent upon the metal ions in the framework. Further investigation is required to determine why this is the case and to determine the mechanism for release. The hydrogen sulfide released from Zn-CPO-27 was determined to have the expected biological effect in vasodilatory experiments, indicating that MOFs have potential to deliver this gas for medical applications. Ni-CPO-27 did not show any significant hysteresis in CO adsorption/desorption isotherms indicating that there is not a strong

interaction between the gas and the framework. Co-CPO-27 showed much more significant hysteresis indicating that this framework has a much greater affinity for CO. However, both frameworks showed some carbon monoxide release, indicating that these frameworks have the potential to be used as delivery materials for these gases, albeit without the same exceptional characteristics which are reported for nitric oxide.

Pair distribution function analysis has been used to analyse several metal-organic frameworks. For crystalline materials, PDF can be used as an extra verification for a structural solution; in Chapter 7, differential PDFs of hydrogen sulfide-loaded Ni-CPO-27 showed coordination of the gas to the metal site, confirming the structure resulting from the Rietveld analysis. Similarly, comparison of residual factors was able to distinguish the subtle differences between hydrated and dehydrated Ni-CPO-27 indicating that the sensitivity of real-space refinements to local distance fluctuations is useful as a comparison of potential structures and as a fingerprinting method. In areas where Bragg scattering methods do not provide an answer PDF can become the primary source of information; in Chapter 7, the secondary building unit of an unknown nanoparticle metal-organic framework was determined in order to constrain the solution from challenged powder data. In Chapter 5, PDF was used in a disordered region of a material to determine that the sulfonate group in the structure appears to move at comparatively low temperatures before the whole structure relaxes into the dehydrated regime. PDF also indicates that nitric oxide adsorption results in a structure analogous to the partially dehydrated structure. This agrees well with the single-crystal analysis where Bragg scattering from the crystal was extinguished in these conditions.

This work has demonstrated the use of *in situ* studies to track a metal-organic framework material over the full activation/adsorption/release cycle. The development of an environmental gas cell at beamline 11.3.1 achieved a high level of dehydration and good quality data, allowing a single-crystal to be tracked through adsorption of nitric oxide, the partial removal of nitric oxide using heat and full removal by exposure to moisture, where water replaces the nitric oxide on the cobalt site. *In situ* PDF studies using a flow gas cell have also allowed the structure of the NO-adduct of Cu-SIP-3 to be proposed.

In summary, this thesis aimed to determine the potential of MOFs as storage and release media for hydrogen sulfide and carbon monoxide. It was found that these

materials can adsorb and release both gases and, in the case of hydrogen sulfide, in biologically active quantities. This work also aimed to develop methods to study the adsorption of medical gases in metal-organic frameworks. It was determined that both *in situ* and *ex situ* single-crystal X-ray diffraction analysis, Rietveld analysis and pair distribution function analysis can be used to determine the structural details behind nitric oxide, carbon monoxide and hydrogen storage adsorption properties in metal-organic framework materials.

There is a great deal of potential for further work in this area. A detailed description of the opportunities arising from each study is given at the end of each chapter, but a brief summary is presented here.

The success of data collection using the environmental gas cell at beamline 11.3.1 gives potential for a large range of further work which could be performed with this cell using different gases or frameworks. Work with isostructural frameworks or different framework structures with the same metal could assess the structure/property relationship for gas adsorption and so allow the design of more task-specific frameworks in the future. For this cell to be universally applicable to MOFs and other frameworks, development of a method of keeping the cell dry throughout data collections and a strategy for low temperature data collection are essential.

PDF has great potential for application in the metal-organic framework field particularly when linked with *in situ* gas-loading studies. Flowing a gas over a framework such as Co-CPO-27 and considering the change of the PDF with time of exposure using differential PDFs could allow the gas loading process to be analysed, and integration of the differential peaks could allow quantification of the gas adsorption. If high quality data which could distinguish between Co-O and Co-NO bond distances were obtained then the release of nitric oxide from the material could be tracked in a similar manner.

The release of hydrogen sulfide and carbon monoxide from metal-organic frameworks has shown promise. Further work characterising the release of the gases is needed to determine why the isostructural frameworks of M-CPO-27 behave differently. Whilst carbon monoxide is released from pellets of M-CPO-27 it is not yet known whether this gas is biologically active, although studies have begun in collaboration with the Centre for Inflammation Research, University of Edinburgh.